In-situ Alloy Formation of Refractory Metal Alloys by Laser Powder Bed Fusion (PBF-LB/M)

In-situ Legierungsbildung von Refraktärmetalllegierungen mittels Laserstrahlschmelzen im Pulverbett (PBF-LB/M)

Der Technischen Fakultät

der Friedrich-Alexander-Universität

Erlangen-Nürnberg

zur

Erlangung des Doktorgrades Dr.-Ing.

vorgelegt von

Florian Michael Huber, M.Sc.

aus Wolfratshausen

Als Dissertation genehmigt
von der Technischen Fakultät
der Friedrich-Alexander-Universität Erlangen-Nürnberg

Tag der mündlichen Prüfung:	08.05.2024
Gutachter:	Prof. Dr.-Ing. Michael Schmidt
	Prof. Dr.-Ing. Michael Rethmeier

Vorwort

Diese Dissertation wäre ohne die Unterstützung meiner Familie und vieler Freunde, Kollegen und Unterstützer nicht möglich gewesen, bei denen ich mich an dieser Stelle herzlich bedanken möchte.

Zunächst gilt mein besonderer Dank Professor Dr.-Ing. Michael Schmidt für das entgegengebrachte Vertrauen und die stete Förderung während meiner Zeit am Lehrstuhl für Photonische Technologien der Friedrich-Alexander-Universität Erlangen-Nürnberg. Ferner möchte ich mich bei Prof. Dr.-Ing. Michael Rethmeier für die Übernahme des Zweitgutachtens sowie bei Prof. Dr.-Ing. habil. Tino Hausotte und Prof. Dr.-Ing. Peter Weidinger für die Übernahme des Prüfungsvorsitzes und des fachfremden Gutachtens am Tag meiner Promotion bedanken.

Mein Dank gilt ebenso meinen ehemaligen Kollegen vom Lehrstuhl für Photonische Technologien, die mir jederzeit mit Rat und Tat zur Seite gestanden sind. Besonders genannt seien hier die Mitglieder der Gruppe Additive Fertigung. Auch abseits der fachlichen Themen hat die Arbeit mit Euch immer sehr viel Spaß gemacht. Ich werde die Zeit mit Euch stets in guter Erinnerung behalten. Für die Hilfe beim Betrieb der PBF-LB/M-Anlagen, dem Aufbau von Systemtechnik und der ein oder anderen Störungsbehebung möchte ich mich beim Werkstattteam des LPT um Jürgen Frötsch bedanken. Ohne Eure Arbeit wäre die Durchführung der PBF-LB/M-Experimente in der vorliegenden Arbeit nicht machbar gewesen. Auch das Team des Lehrstuhlsekretariats um Vanessa Möritz sei an dieser Stelle für die rege Unterstützung beim Manövrieren durch die Untiefen der Lehrstuhlbürokratie und bei der Organisation der mündlichen Promotionsprüfung dankend erwähnt.

Nicht zuletzt gilt ein ganz großes Dankeschön meiner Familie und meinen Freunden. Insbesondere meinen Eltern Karin und Franz Huber möchte ich für ihre fortwährende Unterstützung, ihr Verständnis und ihre Geduld, die sie während dieser nicht immer einfachen Zeit aufgebracht haben, herzlich danken. Euer Rückhalt und Euer Zuspruch haben mir auch in schwierigen Phasen stets geholfen.

Abschließend möchte ich auch all den unzähligen weiteren Wegbegleitern danken, die zur Entstehung dieser Dissertation beigetragen haben – seien es die studentischen Hilfskräfte, die Kollegen aus dem SFB 814 oder die Fördergeldgeber, die die zugrundeliegenden Forschungsprojekte finanziert haben. Diese Arbeit wäre ohne die vielfältige Unterstützung, die ich erfahren habe, nicht möglich gewesen. Vielen Dank dafür!

Table of contents

Table of symbols and abbreviations

Symbol	*Unit*	*Description*
d	µm	laser spot diameter
D_{10}	µm	lower particle diameter with 10 % volume fraction
D_{50}	µm	lower particle diameter with 50 % volume fraction
D_{90}	µm	lower particle diameter with 90 % volume fraction
h	µm	hatch distance
l	µm	layer thickness
n_{abs}	-	normalized number of particles
n_{norm}	-	absolute number of particles
P_L	W	laser power
T_B	°C	build platform temperature
v_s	m/s	scan speed

Abbreviation	*Description*
Al_{eq}	aluminum equivalent
bcc	body centered cubic
DED	directed energy deposition
EDS	energy dispersive x-ray spectroscopy
EIGA	electrode induction melting inert gas atomization
hcp	hexagonal close packed
Mo_{eq}	molybdenum equivalent
PBF-LB/M	powder bed fusion of metals with laser beam
PIGA	plasma inert gas atomization
WAAM	wire arc additive manufacturing

1 Introduction

Sustainability and resource efficiency have grown to become one of the most significant factors in society and industry [1]. This development is driven on the one hand by ecological aspects such as the mitigation of climate change, but also by increasing global tensions and the associated rise in resource prices and disrupted supply chains. Considering price increases of 129.5 % for imported fossil fuels such as oil and gas in 2022 in Germany [2], the change towards regenerative alternatives and increased energy efficiency, especially in energy-intensive sectors as for instance aviation, transport or chemical industry, is not only an ecological necessity but also an economic one. This development is flanked by political measures like the extension of the EU-wide CO_2 price [3] or the ban of combustion engines by 2035 [4], but also by large-scale research programs such as Clean Aviation for low-emission aviation [5]. The disruptions this has triggered include the massive development of technologies and their scaling up from laboratory to industrial scale. Key to much of this progress are manufacturing technologies and materials engineering. Improved material properties, such as temperature or hydrogen resistance or strength-to-weight ratio, enable lighter and/or more efficient structures, while more advanced manufacturing processes facilitate economical production of highly efficient components and parts needed for a future sustainable economy.

In the field of manufacturing processes, additive manufacturing of metals using PBF-LB/M (Powder Bed Fusion of Metals with Laser Beam [6]) in particular has already made a contribution to increasing sustainability and resource efficiency over the past 20 years, as demonstrated by successful examples such as highly efficient fuel injection nozzles [7] for aircraft engines or heat exchangers for chemical industry [8]. As a result, resource savings are already being achieved today. However, the technology is still in its infancy and requires further research and development efforts to meet the expectations placed on it. This is especially true for technologically demanding areas such as aerospace. Important factors here are reproducibility and achievable quality on the one hand, and productivity and costs on the other. Both are increasingly being addressed by the industry and PBF-LB/M equipment manufacturers, as shown by new, improved machine types with optimized process gas flows and multi-laser systems [9] as well as automation approaches [10]. In addition to the available machine technology, the portfolio of materials available for PBF-LB/M, which has so far been severely limited to a few well-studied alloys, is impeding the adoption of PBF-LB/M. In the case of titanium alloys, which are particularly important for the aerospace industry, the spectrum is limited almost exclusively to the alloy Ti-6Al-4V. Exceptions are to a very small extent only α-Ti alloys related to Ti-6Al-4V, such as Ti-6Al-2Sn-4Zr-2Mo-Si, which are scarcely used. Other Ti alloys such as β-Ti alloys promise better properties for many applications but are not yet qualified for industrial use in PBF-LB/M and their processing by PBF-LB/M is also only sparsely covered in scientific literature. Further refractory metal alloys with promising properties, such as niobium, molyb-

denum or high entropy alloys comprising several refractory metal elements, are also only studied to a limited extent. This is precisely where the present work starts. The investigations provide clues on the PBF-LB/M process behavior and the resulting properties of β-Ti alloys and refractory metal high entropy alloys. This can serve as guidance for further, deeper investigations. The in-situ alloy formation approach considered in this work supports the rapid development of new alloys for PBF-LB/M with applicability to alloy development projects beyond this work. In addition, it is shown that in-situ alloy formation using PBF-LB/M is a possible approach to fabricate Ti-components with a locally adapted alloy composition and thus with locally tailored properties. This opens additional degrees of design freedom for highly efficient Ti-components. The results of this work thus support the further development of PBF-LB/M as a promising manufacturing process for future high-performance parts and are intended to contribute to more sustainable and competitive economy.

2 State of the art

2.1 Laser powder bed fusion of metals (PBF-LB/M)

Laser powder bed fusion (PBF-LB/M) is currently the most widely applied process for additive manufacturing of metals in industry as well as in research [11]. The following chapter describes the fundamental process characteristics and gives an overview of the current state of the art of in-situ alloy formation during PBF-LB/M.

Note: PBF-LB/M is still at its infancy compared to established manufacturing technologies. The standardization process is ongoing, and the terminology is continuously developing. Hence, in some journal publications which are part of this cumulative thesis the older term L-PBF is used, while in the majority of this work the term PBF-LB/M is used in accordance with the latest version of DIN EN ISO / ASTM 52900 [12]. However, both terms refer to the same process.

2.1.1 Fundamental process characteristics

PBF-LB/M [12] is an additive manufacturing technology that comprises the layer-wise fusion of metal powder. By selectively melting the powder with a laser beam within each layer and repeating the process of recoating a new powder layer and exposing it with the laser beam, the part geometry is created. The entire process is automated and based on digital data of the part to be produced.

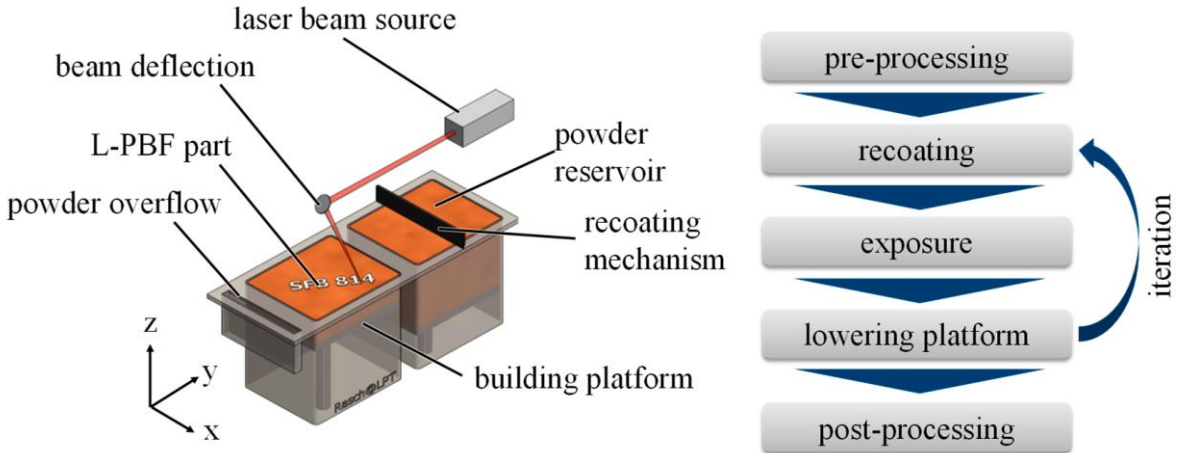

Figure 1: Schematic of the PBF-LB/M process [13]

Modern PBF-LB/M machines can operate not only one, but also multiple independent lasers to increase the build speed [14]. Typically, infrared single mode fiber lasers and galvanometer scanner optics with a resulting laser spot diameter in the process zone between 30 µm and 200

µm and a Gaussian beam profile are used for PBF-LB/M. Other laser types like frequency doubled disc lasers emitting at 515 nm that promise benefits when manufacturing certain materials such as copper which are highly reflective for infrared radiation became only very recently available [15], but are not common. Also, laser beam sources and optical systems with beam shaping capabilities and hence different beam profiles than the Gaussian profile of standard fiber lasers are currently under investigation [16]. This offers an additional degree of process control, e.g. for reducing of spatters [17] or for influencing the solidification behavior [18], but is also not yet state of the art.

To fuse the powder particles, high energy densities in the process zone are applied, which cause evaporation of the metal and, as a consequence, a high process dynamic [19]. This includes movement of the molten metal within the meltpool itself, but also the ejection of melt spatters [20] and movement of surrounding powder particles, which are affected by the evaporation driven gas jet in the vicinity of the process zone [21]. Process simulation and high speed images [22] show the formation of a so-called denudation zone at the flanks of the melt track when powder particles are dragged into the process zone by the gas movement. Besides the gas streams driven by the laser material interaction, a forced gas stream above the build plane is a necessary part of the PBF-LB/M process, as it removes detrimental process by-products like metal condensate and spatters [23].

Resulting from the complex physics behind PBF-LB/M a multitude of interdependent parameters needs to be controlled to ensure a stable process. This includes the parameters directly linked to the laser process like laser power, scan speed and beam properties, geometrical parameters describing the scan pattern like hatch distance or contour exposure and machine parameters such as build platform pre-heating temperature or gas flow rate. While a more complete description is given elsewhere (e.g. in [24]) Table 1 provides an overview of the most important PBF-LB/M process parameters, which are also subject of the investigations presented in this work. It is noted that PBF-LB/M machines are commonly calibrated in a way that the parameter values inserted into the machine control correspond with reasonable accuracy to the actual values on the build platform. E.g. losses of laser power along the optical path are compensated by correction tables, which are determined by laser power measurements. For further information please refer to relevant standards such as ISO/ASTM 52930:2021 [25].

Table 1: Selected PBF-LB/M process parameters

Parameter	Unit	Description
Laser power	W	Incident laser power on build plane
Scan speed	mm/s	Movement speed of the laser spot over the build plane
Laser spot diameter	µm	Diameter of the laser spot in the build plane
Hatch distance	µm	Distance between the middle of two melt tracks
Layer thickness	µm	Step width of the build platform movement
Build platform temperature	°C	Pre-heating temperature of the build platform

Process parameter combinations that result in the desired material quality (e.g. in terms of relative density or the absence of cracks) form the process window. Depending on the metal alloy and the quality criterions, a process window may or may not exist. Given the vast number of metal alloys that is currently in use and the complexity of the process, only a small fraction of alloys has been qualified for PBF-LB/M, yet. Also, the knowledge of the interdependencies between material properties, process behavior and PBF-LB/M parameters is still incomplete. This leaves a huge knowledge gap, that is only gradually filled by research and industry. The present work seeks to provide a contribution to this task with the focus on refractory metal alloys and especially on titanium alloys.

2.1.2 In-situ alloy formation by PBF-LB/M

In most cases, pre-alloyed metal powder is used for PBF-LB/M. This means that the powder is produced from a homogeneous metal melt and all particles in the batch have more or less the same chemical composition. For typical PBF-LB/M applications, spherical metal powders with varying particle size distributions between 5 µm and 63 µm are used. Common production processes for these metal powders are gas atomization processes like electrode induction melting inert gas atomization (EIGA) or plasma inert gas atomization (PIGA) [26]. In both cases, liquid metal is exposed to a high velocity inert gas jet which breaks up the liquid into small droplets which solidify into powder particles. High quality titanium- and nickel-alloy powders e.g. for aerospace applications, which require low impurity contents (e.g. oxygen or nitrogen) are frequently produced by plasma atomization. In this case, a plasma torch divides a metal wire into small melt droplets [27]. Other atomization techniques like water atomization [28] or ultrasonic atomization [29] can also be possible, but are of minor importance. The capacity of industrial scale atomizers ranges from a few kg to several 100 kg of metal per batch. Changing the alloy composition on an atomizer system typically requires high downtimes due to cleaning effort, which is mandatory to avoid cross contamination. Hence, powders of a limited range of standard alloys like 316L, Ti-6Al-4V or AlSi10Mg are readily available [30], but special alloys or even newly designed alloys for research activities are difficult and expansive to obtain.

Because of this, in-situ alloy formation by PBF-LB/M is an attractive option to support the development of novel alloy concepts or explore the effect of different chemical compositions on the process behavior and the resulting alloy properties. This can involve alloys which are tailored for PBF-LB/M applications or even alloys that cannot be produced by conventional casting techniques like high entropy alloys. Figure 2 shows the basic principle of in-situ alloy formation via PBF-LB/M.

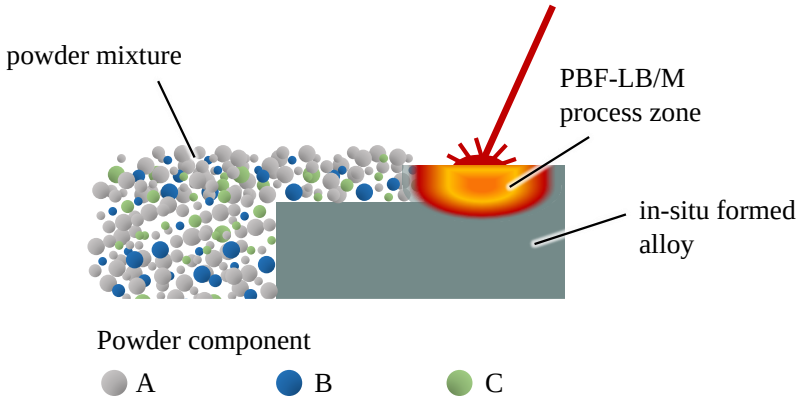

Figure 2: Principle of in-situ alloy formation via PBF-LB/M

Instead of using pre-alloyed metal powder which already has the desired alloy composition, blends of readily available metal powders with different chemical compositions are fused with the laser beam. The target composition is only formed in-situ during PBF-LB/M in the meltpool [31].

The powder blends can consist of powders with equal particle size distributions or of powders with significantly different particles size distributions, e.g. when µm sized carrier particles are loaded with nm sized particles. Examples for the later one are carbon black or WC nanoparticles on case-hardening steel 16MnCr5 carrier particles for strengthening [32] or TiC/TiB_2 nanoparticles to influence the solidification behavior of Al-alloys [33]. A special case is the application of a high energy ball mill to produce a homogeneous powder feedstock from different powder components prior to PBF-LB/M. This approach was e.g. applied in [34] for producing powder for PBF-LB/M of a high-entropy alloy particle-reinforced stainless steel. As the alloy is already formed at least to some extent by mechanical alloying during ball milling, this case is not considered as in-situ alloy formation by PBF-LB/M. Also, in-situ alloy formation with nanoparticle addition is not considered within this thesis, as only very few wt.% of nanoparticles can be coated on the carrier particles [35] and the added material is already fine dispersed, which eases the formation of a homogeneous material. Hence, the focus of this work solely rests on in-situ alloy formation with powder blends consisting of µm-sized powder particles.

Focusing on refractory metal alloys, which are subject of this work, in-situ alloy formation was applied in several research projects for investigating novel alloy concepts. Most of the research work published focuses on the development of Ti-alloys for medical applications. In this context, *Krakhmalev et al.* investigated copper addition to Ti-6Al-4V to create an alloy with antibacterial properties [36]. *Fischer at al.* modified pure Ti with 40.5 wt.% Nb, powder aiming for a biocompatible, low modulus Ti-alloy for medical implants [37]. Analogous research was published by *Zhao et al.* [38], who also investigated the material properties of an in-situ formed TiNb alloy. Also motivated by medical implants, *Duan et al.* aimed for producing a low modulus Ti alloy Ti-12Mo-6Zr-2Fe by in-situ alloy formation [39]. Despite Ti-alloys for medical applications also even more challenging alloy concepts such as shape memory alloys or refractory metal high entropy alloys are more or less successfully synthesized by PBF-LB/M and in-

situ alloy formation. *Polozov et al.* [40] investigated in-situ formation of NiTi and NiTiNb shape memory alloys [40], which partly succeeded. But the material contained a severe amount of undissolved Nb particles. Apart from own work [41], research regarding refractory metal high entropy alloys was only very recently published, e.g. by *Ron et al.* [42] or *Xu et al.* [43].

A more detailed review on in-situ alloy formation by PBF-LB/M and also by DED (Directed Energy Deposition, see also [12]) is provided by *Mosallanejad et al.* [44]. The main conclusion of this review paper is in good agreement with the overview given above. Despite a few studies like [39] showing a rather successful in-situ alloy formation with little to no remaining undissolved powder particles, other studies like [37], [38], [40] or [45] reveal severe amounts of material inhomogeneities. This demonstrates that in-situ alloy formation by PBF-LB/M is not trivial and the interdependencies between PBF-LB/M process parameters and resulting material homogeneity are not fully understood, which is the motivation for parts of the research conducted in this thesis.

2.2 Titanium

Titanium is the most important refractory metal with significant applications in industry and medicine. The following chapter provides a brief introduction to the properties and classification of titanium and its alloys to support the discussion of this work's results. Furthermore, an overview of additive manufacturing of titanium alloys is provided.

2.2.1 Unalloyed Titanium

The most important titanium containing minerals ilmenite and rutile were first described by William Gregor in 1791 and by Heinrich Klaproth in 1795, respectively. First methods to obtain metallic titanium were e.g. published by Justus von Liebig in 1842 [46]. However, it took almost one hundred years, before William Justus Kroll developed the so-called Kroll process [47] that allows the production of titanium on an industrial scale by reducing $TiCl_4$ with calcium, magnesium or sodium to elemental titanium. This process is still in use up to today. A further purification of titanium can be achieved by the Van Arkel de Boor process by reaction with iodine and a consequent decomposition of the titaniumtetraiodid vapor into elemental titanium [48]. These elaborate production processes are one of the main reasons for the high raw material costs of titanium [49] in comparison to other metallic engineering materials like steel or aluminum. Hence, for economic reasons, titanium and its alloys are in general reserved for demanding use cases, e.g. in the aerospace industry [50], in chemical engineering, and for military [51] or medical applications [52]. With a density of 4.5 g/cm³ [53] titanium is considered a light metal. Compared to steel or aluminum, it features in general an exceptional strength to weight ratio, high toughness and corrosion resistance [54]. At room temperature, titanium crystallizes in a hexagonal close packed (hcp) structure with the lattice parameters $a = 0.295$ nm and $c = 0.468$ nm (see Figure 3). At 882 °C, the hcp structure transforms to an allotropic $\alpha \rightarrow \beta$ phase transition into a body-centered cubic (bcc) structure with a lattice parameter $a = 0.332$ nm

(see Figure 4) [53]. Originating from the hcp crystal structure, α-titanium can show an anisotropic material behavior, since the Young's Modulus (E) depends on the crystal orientation, with 145 GPa for loads perpendicular to the basal plane and 100 GPa parallel to it [54]. The hcp-crystal furthermore possesses only four independent slip planes. However, according to the von Mises criterion, at least five independent slip planes are required for a homogeneous plastic deformation of polycrystals [55]. Hence, the workability of α-titanium at room temperature is rather limited [53].

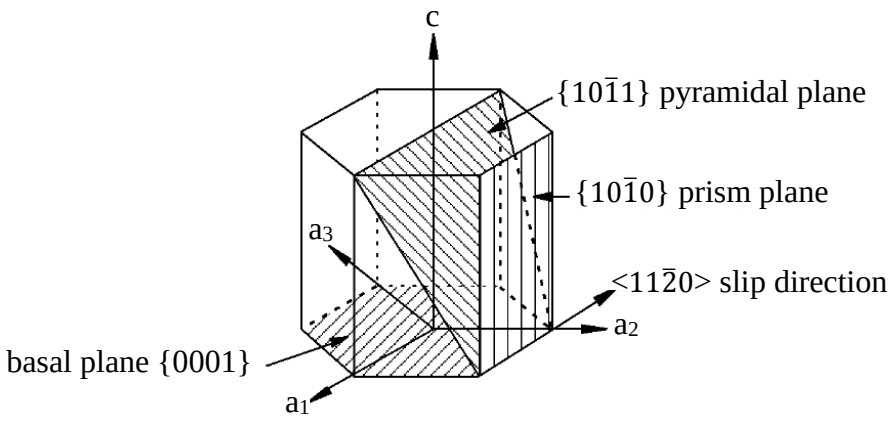

Figure 3: hcp-lattice structure of α-titan with corresponding slip planes; lattice parameters: a = 0.295 nm and c = 0.468 nm [53]

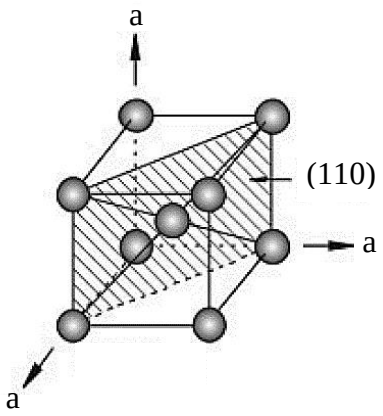

Figure 4: bcc-lattice structure of β-titan with corresponding slip planes; lattice parameter at 900 °C: a = 0.332 nm [54]

2.2.2 Titanium alloys

While pure titanium forms the hcp α-phase at room temperature, alloying elements support the formation of either α- or β-titanium and shift the transition temperature to lower or higher ranges, respectively. Higher concentrations of β-phase stabilizers in an alloy even facilitate the stabilization of the β-phase at room temperature. Intermediate contents of β-phase stabilizing elements lead to alloys that contain α- as well as β-phase. The β-phase stabilizing elements are

classified by the shape of their binary phase diagram into β-isomorphus and β-eutectoid elements [53]. Contrary to β-isomorphus elements, β-eutectoid elements bear the possibility of forming intermetallic phases at higher concentrations, which might be undesired. Figure 5 shows the effect of selected elements on the phase stability of titanium alloys.

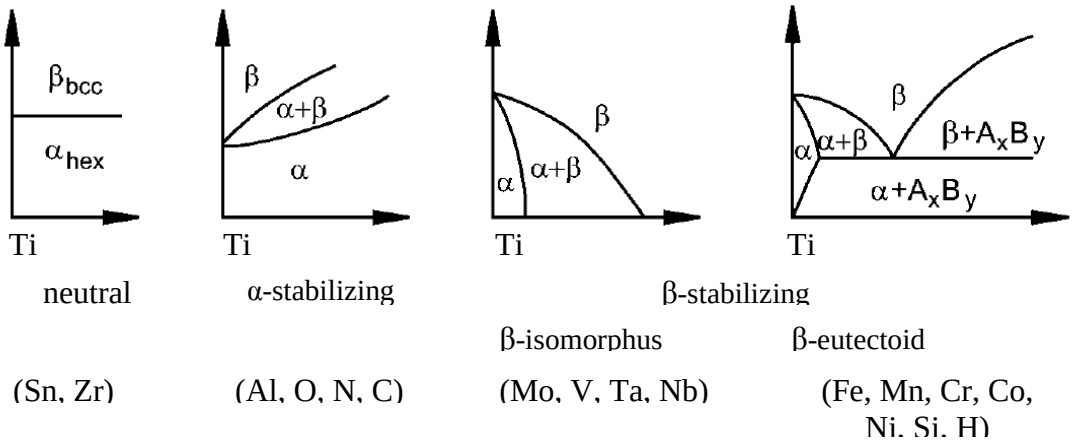

Figure 5: Influence of selected alloying elements on the phase stability of titanium alloys [54]

The tendency of a Ti-alloy to form β-phase can be estimated both by theoretical calculations and empirical formulas. Examples of theoretical approaches are the electron concentration rules by Hume-Rothery [56] or more recently calculations based on density functional theory e.g. by Tegner et al. [57] or Huang et al. [58]. Huang et al. show that the calculations are in good agreement with experiments. Smaller deviations are to be explained by model simplifications like neglection of diffusion effects or unavoidable impurities compromising the experimental results. In general, however, theoretical calculations are to be considered a valuable instrument for estimation of the phase stability of Ti-alloys [59].

Besides theoretical calculations, in engineering praxis empirical approaches like the so-called molybdenum equivalent (Mo_{eq}) are often applied as a fast and convenient way to estimate the β-phase stability of a certain alloy. The Mo_{eq} is calculated from the alloy composition according to equation (*1*).

$$Mo_{eq} = 1.0\,(wt.\%\,Mo) + 0.67\,(wt.\%\,V) + 0.44\,(wt.\%\,W) + 0.28\,(wt.\%\,Nb) + 0.22\,(wt.\%\,Ta) + 2.9\,(wt.\%\,Fe) + 1.6\,(wt.\%\,Cr) + 1.25\,(wt.\%\,Ni) + 1.7\,(wt.\%\,Mn) + 1.7\,(wt.\%\,Co) - 1.0\,(wt.\%\,Al_{eq}) \quad (1) \quad [59]$$

The factors for each element are derived by the ratio of the lowest concentration of molybdenum needed to receive solely β-phase without martensite after quenching to room temperature to the concentration needed for the respective element [59]. Aluminum is subtracted since it acts as α-stabilizer. The normalized effect of neutral and α-stabilizing elements such as O and N is taken into account by the so-called aluminum equivalent Al_{eq} which is calculated by equation (2).

(2) $$Al_{eq} = 1.0\ (wt.\%\ Al) + 0.17\ (wt.\%\ Zr) + 0.33\ (wt.\%\ Sn) + 10\ (wt.\%\ O) + 10\ (wt.\%\ N)$$ [60]

The elements Sn and Zr are considered to act more or less neutral in Figure 5, since Zr only slightly increases the transformation temperature and decreases it again at higher concentrations. Sn is actually a β-eutectoid element, but can replace Al in the Ti_3Al phase [53]. Hence, when present with Al, which is the case for most commercial alloys, Sn can support α-phase formation. This is also the reason why it is considered in equation (2) when calculating the Al_{eq} [53]. The dependency between Mo_{eq} and β-transus temperature for selected titanium alloys is shown in Figure 6. As a rule of thumb, alloys with a $Mo_{eq} > 10$ are considered metastable β-alloys, since the amount of β-stabilizers is high enough to completely suppress the formation of α-phase and α'-martensite when quenched from temperatures above the β-transus temperature to room temperature.

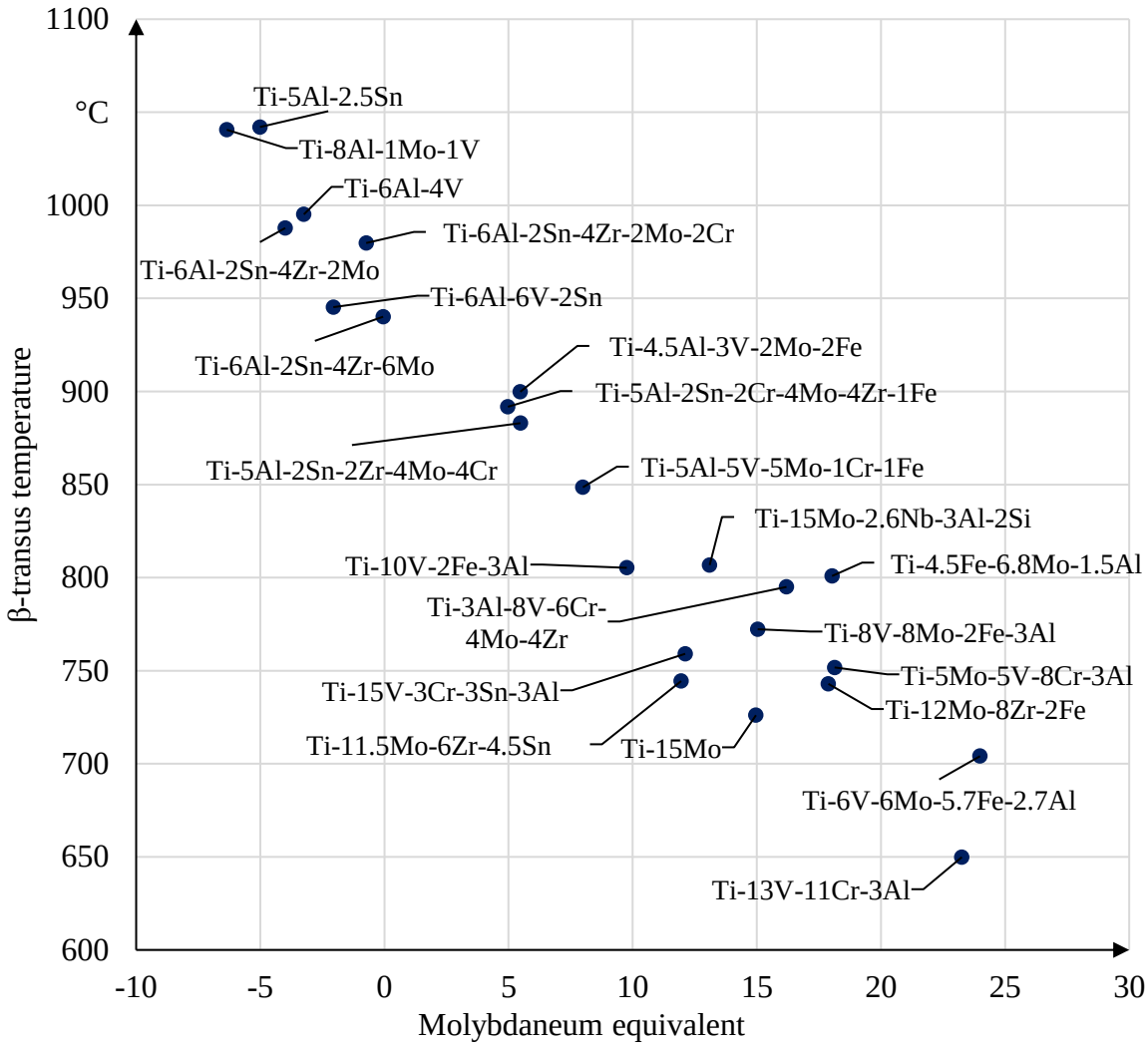

Figure 6: Dependency between Mo_{eq} and β-transus temperature of titanium alloys [61]

The properties of titanium alloys are to a major extent defined by their concentration and morphology of α- and β-phase. Consequently, it is commonly distinguished between α- and near α-, α + β and metastable β-alloys.

α- and near α-alloys

Alloys containing higher amounts of α-phase provide in general a superior resistance to plastic deformation, high corrosion resistance and originating from reduced diffusion rates due to the hcp lattice structure an increased creep resistance [54]. Furthermore, α-alloys possess a slightly lower density than β-alloys. Due to their excellent corrosion resistance and good weldability α-alloys are predominantly used in chemical engineering [53] for maritime applications in the oil and gas industry or for desalination plants [62]. For applications where mechanical strength is not the primary design criterion, the commercially pure (cp) Ti-grades 1 – 4 are applied. The sole alloying element in these alloys is oxygen, that raises from grade 1 to grade 4 [63] and increases strength (see Table 2). Even higher corrosion resistance can be achieved by alloying with small amounts of Pd or Ru. However, these elements are expensive [54]. Near α-alloys like Ti-5.8Al-4Sn-3.5Zr-0.7Nb-0.5Mo-0.35Si containing predominantly aluminum and neutral elements like Sn and Zr have been developed for high temperature applications, e.g. in aircraft engines to withstand operating temperatures of up to 600 °C [64].

α + β alloys

By far the most frequently used titanium alloy is the α + β alloy Ti-6Al-4V with a market share of over 50 % [54]. Reasons for this are the balanced material properties (see Table 2) and the fact, that it is very well investigated, which is important for safety critical applications. The properties of this group of alloys are defined by their microstructure. Depending on the processing history, an equiaxed, a fully lamellar or a bimodal microstructure as a combination of the first ones can be achieved. The application of Ti-6Al-4V is limited to temperatures below 300 °C. For higher temperatures near α-alloys are utilized. Other α + β alloys than the most common alloy Ti-6Al-4V are also used in industry, e.g. when slightly different properties are required or when the element V is replaced by less biotoxic elements like Nb for medical purposes.

Metastable and near β-alloys

Metastable and near β-alloys show a very versatile property profile and have grown in importance over time [54]. Compared to other Ti-alloys, they reach the highest strength to weight ratio, high toughness and high fatigue resistance [63]. The strength originates from the possibility of age hardening resulting in fine dispersed undeformable α-precipitations in the β-phase matrix [53]. Drawbacks of this alloy class are the increased density mainly resulting from the heavier alloying elements and a complex metallurgy, that requires a high level of control over the thermo-mechanical conditions during manufacturing to achieve the desired properties [54].

From a processing point of view, one advantage of β-alloys like Ti-1.5Al-4.5Fe-6.8Mo or Ti-15V-3Cr-3Al-3Sn is their cold workability [65]. This results from the bcc lattice structure of the β-phase and facilitates a high degree of room temperature deformation.

Table 2: Properties of selected titanium alloys

Alloy	Chemical composition	Type	E [GPa]	$R_{p0.2}$ [MPa]	R_m [MPa]	A [%]
Ti Grade 1 [63]	cp Ti, 0.2 Fe, 0.18 O	α	103	172	241	24
Ti Grade 2 [63]	cp Ti, 0.5 Fe, 0.4 O	α	103	276	345	20
TIMETAL 834 [54]	Ti-5.8Al-4Sn-3.5Zr-0.7Nb-0.5Mo-0.35Si	near α	120	910	1030	6 – 12
Ti Grade 5 [54]	Ti-6Al-4V	α + β	110 – 140	800 – 1100	900 – 1200	12 – 16
Beta C [54]	Ti-3Al-8V-6Cr-4Mo-4Zr	β	86 – 115	800 – 1200	900 – 1300	6 – 16
Ti 10-2-3 [54]	Ti-10V-2Fe-3Al	β	110	1000 – 1200	1000 – 1400	6 – 16

2.2.3 PBF-LB/M of titanium alloys

The excellent properties of titanium alloys combined with the high degree of geometrical design freedom that is facilitated by additive manufacturing technologies allow the production of high-performance parts. Furthermore, considering the high raw material costs of titanium and that conventional forming [66] and machining [67] of titanium is in general challenging, a near net shape production of titanium structures by additive manufacturing seems attractive [68]. Typical applications for additively manufactured Ti-alloys are found in the aerospace, medical and motorsport sectors, when a high strength to weight ratio at low to intermediate temperatures is required. Two examples selected from numerous successful aerospace applications are light-weight Ti-6Al-4V brackets for launch vehicles which withstand cryogenic temperatures [69] and an additively manufactured hydraulic block developed for the Airbus A380 [70]. In both cases, clear advantages of additively manufactured Ti-parts compared to their conventional counterparts could be shown. In the first case, manufacturing cost and weight are reduced [69] while in the second case, manufacturing duration is reduced by 75 % and weight is also reduced by 35 % [70]. Medical examples for PBF-LB/M of Ti-alloys are cranial [71], dental [72] or spinal [73] implants. PBF-LB/M facilitates manufacturing of patient specific implants, and the rough surface of the resulting parts support bone ingrowth. Ti-alloys are the material of choice for such implants due to their excellent chemical resistance and biocompatibility.

The most widely used and best investigated Ti-alloy for PBF-LB/M is by far Ti-6Al-4V. This accounts for industrial and medical purposes alike. The alloy is available in the two versions, namely grade 5 and grade 23, with the later one also being referred to as Ti-6Al-4V ELI (extra low interstitial) [63]. The grade 23 specification allows less interstitial impurities like H, N and O compared to grade 5 which results e.g. in an improved ductility and fracture toughness [63]. Default parameter sets for Ti-6Al-4V are available from the leading PBF-LB/M machine manufacturers for their respective machines (see Table 3). This also accounts for Ti cp (commercially pure) grades. In addition to Ti-6Al-4V and cp-Ti SLM Solutions and GE Additive provide default parameter sets for Ti-6Al-2Zr-1Mo-1V or Ti-6Al-2Sn-4Zr-2Mo respectively, which are both near α-Ti alloys that offer improved service temperatures compared to Ti-6Al-4V.

Table 3: Titanium alloys qualified by machine manufacturers

Alloy	EOS GmbH [74]	SLM Solutions AG [75]	GE Additive / Concept Laser [76]	Trumpf [77]
Ti cp	x	x	x	x
Ti-6Al-4V (grade 5 /23)	x	x	x	x
Ti-6Al-2Zr-1Mo-1V		x		
Ti-6Al-2Sn-4Zr-2Mo			x	

As shown in Table 3, currently only a very limited selection of α- or near α-Ti alloys are qualified for industrial PBF-LB/M applications by the machine manufacturers. The qualification of further α-Ti or even the metallurgically more complex metastable β-Ti alloys is subject of ongoing research [78].

PBF-LB/M of α- and α+β alloys

All Ti-alloys qualified for industrial AM machines by leading machine manufacturers are α- or α+β Ti-alloys (see Table 3). The cp-grades and the most common alloy Ti-6Al-4V are readily available and very well investigated. Research publications cover a wide range of aspects of PBF-LB/M of these alloys such as microstructure development and heat-treatment effects [79], corrosion properties of Ti-6Al-4V produced by PBF-LB/M [80] or the influence of post surface treatments on the fatigue properties [81]. Except the cp-grades and Ti-6Al-4V PBF-LB/M of other α- or α+β Ti-alloys is subject of ongoing research. The alloy Ti-6Al-2Sn-4Zr-2Mo-Si provides improved high temperature properties compared to Ti-6Al-4V and has therefore attracted some research interest. Its processability, microstructure development and potential heat-treatment routes are investigated in several research papers [82]. While good relative densities above 99.90 % are demonstrated, cold tearing occurs for unfavorable process parameter combinations with a high energy input [83]. Other commercial alloys under investigation for

PBF-LB/M suitability are e.g. Ti-6Al-2Zr-1Mo-1V [84] or Ti-6Al-7Nb [85]. Authors of other research papers on PBF-LB/M of α- and α+β Ti-alloys not only investigate processing of existing alloys but rather development of novel alloy compositions with slightly improved properties or less expensive alloying elements than Ti-6Al-4V [86]. In general, processability of this alloy class is good, as high relative densities of the sample material and no material related defects such as hot cracking are reported in literature. This correlates well with the good weldability that is associated with α- and α+β alloys [64].

PBF-LB/M of metastable and near β Ti-alloys

In contrast to α- and α+β alloys, PBF-LB/M of metastable and near β Ti-alloys is by far less researched than PBF-LB/M of α and a+β Ti-alloys [78]. Only a limited number of publications with initial parameter studies and first investigations on resulting microstructure and mechanical properties of PBF-LB/M processed commercial metastable β-alloys are available. Examples are *Qiu and Liu* [87] who published on PBF-LB/M of the alloy Ti-10V-2Fe-3Al. One year earlier, a rather similar alloy composition prepared by in-situ alloy formation was investigated in own work [13]. The findings of both publications are hard to compare due to different analysis methods of the obtained samples, but the general processability of both verry closely related alloys resulting in highly dense (> 99.5 %), crack-free samples is confirmed. Schwab et al. [88] reported a good processability and first mechanical properties for PBF-LB/M of the alloy Ti-5Al-5V-5Mo-3V. Results on PBF-LB/M of other β Ti-alloys used in industry, such as Ti-3Al-8V-6Cr-4Mo-4Zr (Beta C) [54] are not available. Though few publications address manufacturing of Ti-3Al-8V-6Cr-4Mo-4Zr by other AM processes like Wire Arc Additive Manufacturing (WAAM) [89]. Apart from engineering and aerospace alloys, PBF-LB/M of medical β Ti-alloys was reported in few publications. The main motivation is to produce alloys with low modulus and no biotoxic elements. One candidate for this is the alloy Ti-24Nb-4Zr-8Sn, which was investigated e.g. in [90]. In summary, despite first publications, information on PBF-LB/M of metastable and near β Ti-alloys is scarce and the interdependencies between alloy composition, PBF-LB/M and resulting properties are not fully understood. Given the more complex metallurgy of metastable and near β Ti-alloys compared to α- and α+β alloys [54], this is a knowledge gap that needs to be addressed to qualify existing metastable and near β Ti-alloys or even develop new alloy compositions for PBF-LB/M.

3 Aims and structure

The aim of this work is a comprehensive investigation of in-situ alloy formation of refractory metal alloys by PBF-LB/M. This includes the development of transferable process strategies that support in-situ alloy formation. The applicability of the derived strategies is subsequently verified for modification of Ti-based alloys with minor element addition and for formation of refractory metal high entropy alloys comprising up to five components.

Process strategies (Chapter 4)

As pointed out in the state-of-the-art section, in-situ alloy formation adds an additional degree of complexity compared to PBF-LB/M with pre-alloyed powder. In addition to achieving a stable laser process with low residual porosity, obtaining a homogeneous element distribution by in-situ alloy formation represents a major challenge. Consequently, it is crucial to understand influencing factors governing the homogeneity of the element distribution after in-situ alloy formation. Based on this knowledge, suitable process strategies are to be derived that support PBF-LB/M of a homogeneous material without undissolved particles or major segregations of alloying elements. Chapter 4.1 [91] addresses the fundamentals of PBF-LB/M processing of Ti within this work and provides a starting point for the following investigations. Chapter 4.2 [92] builds upon the process parameters presented in Chapter 4.1 and elucidates process strategies for in-situ alloy formation.

Hypotheses:
Under favorable conditions in the process zone, a homogeneous element distribution can be achieved by in-situ alloy formation from elemental starting powders. Influencing factors governing these conditions and hence the feasibility of successful in-situ alloying are:

- The PBF-LB/M process strategy (e.g. laser power, scan speed, exposure pattern)
- The thermo-physical material properties (e.g. melting temperature, mixing enthalpy)
- The powder properties (mainly particle size distribution)

Publications:

Customized exposure strategies for manufacturing hybrid parts by combining laser beam melting and sheet metal forming - Journal of Laser Applications, 2019 [91]

Laser Powder Bed Fusion (PBF-LB/M) process strategies for in-situ alloy formation with high-melting elements - Metals, 2021 [92]

Modification of Ti-based alloys (Chapter 5)

The development of suitable PBF-LB/M process strategies for in-situ alloy formation, in a first step, facilitates investigation of modifying a base alloy by adding limited amounts of additional elements. The aim is to examine the effects of the element addition on the process behavior and the resulting properties of titanium alloys, which are the most common refractory metal alloys that are used for engineering applications. In this context, in-situ alloy formation is considered a potentially useful tool to support the development of novel alloy concepts for PBF-LB/M. Beyond that, selectively introducing alloying elements during PBF-LB/M and subsequent in-situ alloy formation by laser powder bed fusion holds the potential to produce parts with spatially varying material properties. Hence, not only the effect of homogeneously introducing alloying elements but also the transition between areas with different alloy compositions is discussed in the following. While in chapter 5.1 [13] PBF-LB/M and in-situ alloy formation of a metastable Ti-alloy is investigated in the first place, chapter 5.2 includes a systematic study on the effect of the addition of the β-phase stabilizers Fe and V on the PBF-LB/M processability and the resulting material properties. In addition, the possibility of a defect-free transition between areas with different Ti-alloy compositions is also discussed in chapter 5.2.

Hypotheses:

- The addition of limited amounts (< 15 wt.%) of β-phase stabilizers like Fe and V facilitates the variation of the resulting properties of PBF-LB/M processed Ti-alloys in a wide range, both before and after a heat-treatment.
- The β-phase content of the PBF-LB/M processed material and to some extent the mechanical properties can be estimated by the Molybdenum equivalent.
- A defect-free transition from a highly β-stabilized Ti-alloy to a near-α base alloy is possible in PBF-LB/M parts (multi-material).

Publications:

In Situ Formation of a Metastable β-Ti Alloy by Laser Powder Bed Fusion (L-PBF) of Vanadium and Iron Modified Ti-6Al-4V - Metals, 2018 [13]

Systematic exploration of the L-PBF processing behavior and resulting properties of β-stabilized Ti-alloys prepared by in-situ alloy formation - Materials Science and Engineering A, 2021 [93]

In-situ alloy formation of refractory metal high entropy alloys (Chapter 6)

Besides modifying an existing alloy, in-situ alloy formation offers the possibility to efficiently explore the applicability of novel alloy concepts like compositionally complex or high entropy alloys for PBF-LB/M. Based on the results of the previous experiments, in-situ formation of

refractory metal high entropy alloys consisting of up to five elements with significantly different melting and boiling points is investigated. The aim is to validate the developed process strategies for in-situ alloy formation under challenging conditions and to gain knowledge on the processing behavior, the resulting microstructure, and the mechanical properties of refractory metal high entropy alloys. The results of chapter 6 are published in [41] and are discussed with respect to the scope of this work.

Hypotheses:

- The high cooling rates in the range of 10^6 K/s that are inherent to PBF-LB/M support the formation of high entropy alloys and suppress element segregation during solidification.
- By applying the developed PBF-LB/M process strategies in-situ alloy formation of refractory metal high entropy alloys from up to five elemental powders by PBF-LB/M is possible, despite significantly different melting and boiling points.
- The cooling and solidification rates are affected by the process parameters, which is reflected by microstructure and mechanical properties.

Publications:

In-Situ Alloy Formation of a WMoTaNbV Refractory Metal High Entropy Alloy by Laser Powder Bed Fusion (PBF-LB/M) - Materials, 2021 [41]

Figure 7 illustrates the structure of this work.

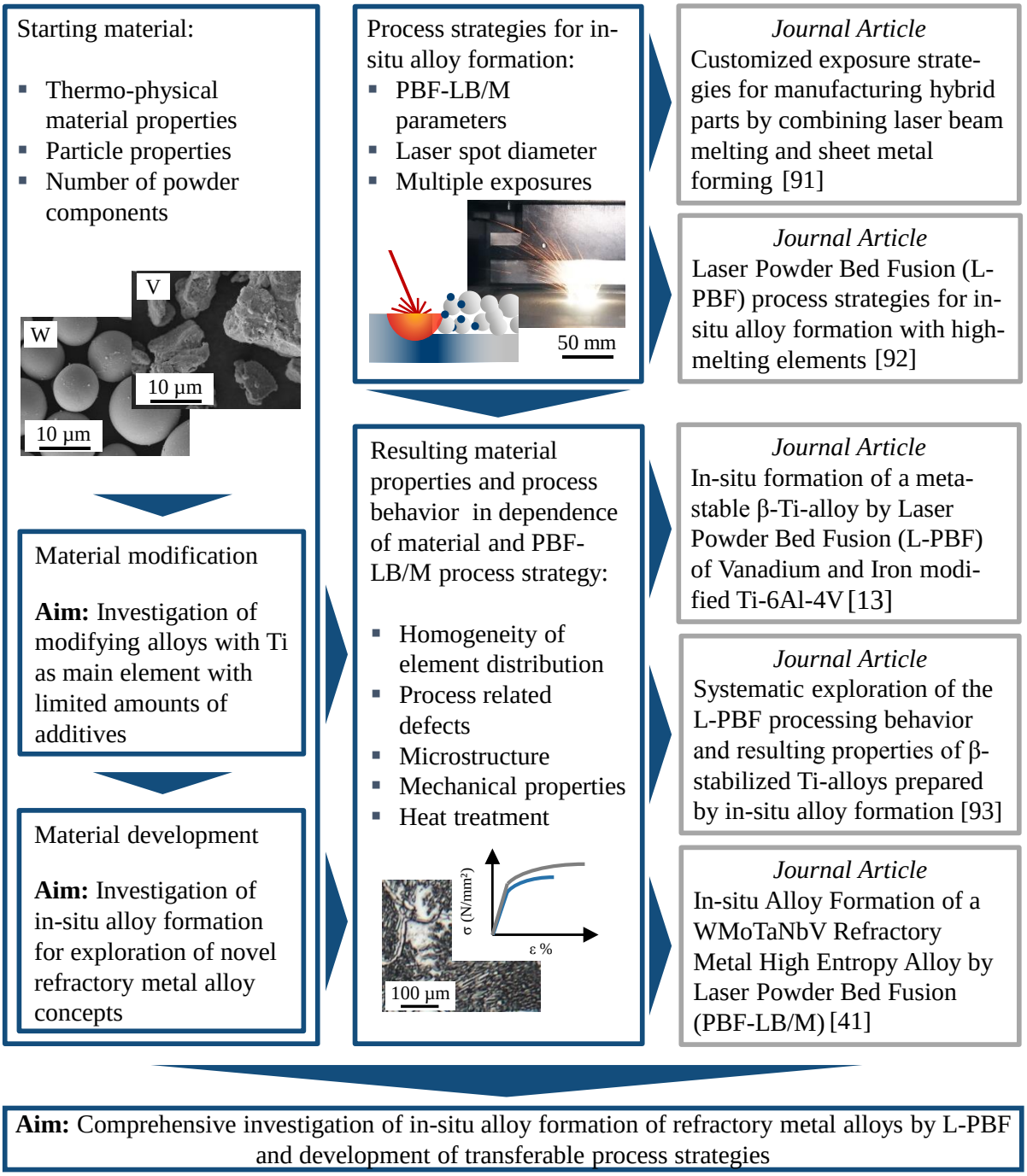

Figure 7: Illustration of the structure of this work

4 Process strategies for in-situ alloy formation

4.1 Customized exposure strategies for manufacturing hybrid parts by combining laser beam melting and sheet metal forming

Published in Journal of Laser Applications, 31 (2019)*

Florian Huber[1,2,3], Thomas Papke[2,4], Melanie Kerkien[1,4], Florian Tost[1,4], Georg Geyer[1,4], Marion Merklein[2,4] and Michael Schmidt[1,2,3]

[1] Institute of Photonic Technologies, Friedrich-Alexander Universität Erlangen-Nürnberg
[2] Collaborative Research Center 814 – Additive Manufacturing
[3] Erlangen Graduate School in Advanced Optical Technologies
[4] Institute of Manufacturing Technology, Friedrich-Alexander Universität Erlangen-Nürnberg

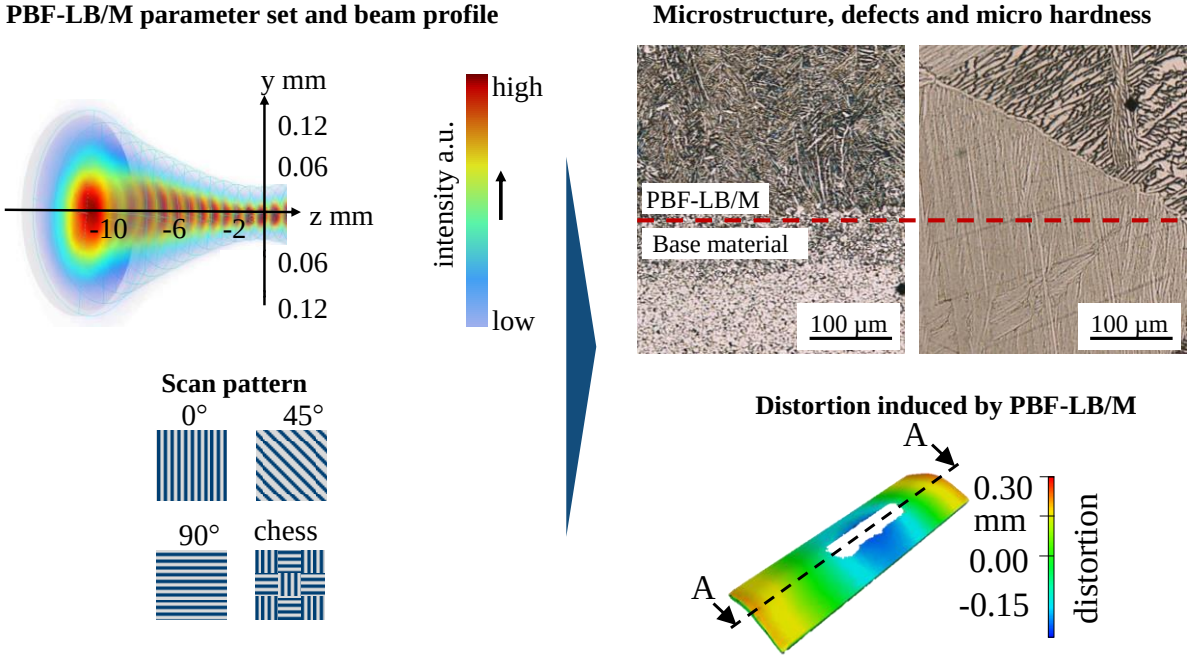

Highlights:

- Investigation of the effect of various PBF-LB/M parameter sets, beam profiles and scan patters on the resulting properties of Ti6Al4V parts including microstructure, mechanical properties and distortion
- Development of different heat treatment strategies for either preserving or altering the microstructure and hence the properties of Ti6Al4V manufactured by PBF-LB/M
- Strategies towards either homogeneous or locally different microstructures allowing for parts with tailored material properties in different part areas

*Reproduced from [91], with the permission of AIP Publishing

Customized exposure strategies for manufacturing hybrid parts by combining laser beam melting and sheet metal forming

Cite as: J. Laser Appl. **31**, 022318 (2019); https://doi.org/10.2351/1.5096115
Submitted: 14 March 2019 . Accepted: 14 March 2019 . Published Online: 01 May 2019

Florian Huber, Thomas Papke, Melanie Kerkien, Florian Tost, Georg Geyer, Marion Merklein, and Michael Schmidt

Journal of Laser Applications ARTICLE scitation.org/journal/jla

Customized exposure strategies for manufacturing hybrid parts by combining laser beam melting and sheet metal forming

Cite as: J. Laser Appl. 31, 022318 (2019); doi: 10.2351/1.5096115
Submitted: 14 March 2019 · Accepted: 14 March 2019 ·
Published Online: 1 May 2019

Florian Huber,[1,2,3] Thomas Papke,[2,4] Melanie Kerkien,[1,4] Florian Tost,[1,4] Georg Geyer,[1,4] Marion Merklein,[2,4] and Michael Schmidt[1,2,3]

AFFILIATIONS

[1]Institute of Photonic Technologies, Friedrich-Alexander-Universität Erlangen-Nürnberg, 91052 Erlangen, Germany
[2]Collaborative Research Center 814—Additive Manufacturing, 91058 Erlangen, Germany
[3]Erlangen Graduate School of Advanced Optical Technologies, 91052 Erlangen, Germany
[4]Institute of Manufacturing Technologies, Friedrich-Alexander-Universität Erlangen-Nürnberg, 91058 Erlangen, Germany

Note: This paper is part of the Special Collection: Proceedings of the International Congress of Applications of Lasers & Electro-Optics (ICALEO® 2018).

ABSTRACT

Subjects of this work are the mechanical, geometrical, and microstructural properties of hybrid parts from Ti6Al4V sheet metal bending and laser beam melting (LBM) in dependence of the extended LBM process parameters. In this context, the effects of different laser exposure strategies for the interface area to increase the reproducibility of the joint strength are investigated. Also, the effect of varying scan patterns and two different laser beam sources (Gaussian beam profile, spot size: 120 μm, maximum laser power: 400 W and irregular beam profile, spot size: 680 μm, maximum laser power: 1000 W) on the LBM process and the resulting distortion of the parts are examined. Furthermore, three heat-treatment temperatures at 450, 850, and 1050 °C were applied to the hybrid samples, resulting in variable microstructures and different mechanical properties for the sheet metal body and the LBM structure.

Key words: additive manufacturing, laser powder bed fusion (L-PBF), laser beam melting (LBM), Ti6Al4V, forming, hybrid processing, microstructure, mechanical properties

 https://doi.org/10.2351/1.5096115

I. INTRODUCTION

Titanium alloys like Ti6Al4V possess an excellent strength to weight ratio and a good corrosion resistance. Therefore, they are used for a wide range of demanding applications, for example, in aerospace and chemical industry.[1] Due to their biocompatibility, another important field of application is medical devices like implants. The combination of the excellent material properties of Ti6Al4V and the high degree of freedom in design, which is inherent to additive manufacturing (AM) technologies like laser beam melting (LBM)—also referred to as selective laser melting (SLM)—facilitates the production of advanced high-performance parts. However, the LBM process is rather expensive and slow in comparison to conventional mass production technologies like sheet metal forming, which excel at productivity and cost-efficiency. By combining sheet metal bending and LBM, the specific advantages of both processes can be exploited. Therefore, the feasibility of applying additively manufactured structures on Ti6Al4V sheet metal bodies is being investigated. In this context, the resulting properties of such hybrid parts in dependence of the LBM process strategy and a subsequent heat treatment are the subject of this work.

II. STATE OF THE ART

A. LBM of Ti6Al4V

LBM of Ti6Al4V is in general well understood,[2] and process parameters for producing almost fully dense parts are available for

numerous commercial LBM machines (e.g., Ref. 3). Additively manufactured Ti6Al4V parts are already utilized as medical implants and high-performance parts, for example, for racing applications and in the aerospace or chemical industry. Recent scientific publications are focusing, e.g., on the microstructure evolution[4] or the fatigue behavior of LBM processed Ti6Al4V.[5]

B. Typical specifications of lasers and optics used for LBM

Typically, single-mode (SM) fiber lasers with a Gaussian beam profile and output powers between 100 W (Ref. 6) and 700 W,[7] in some cases up to 1000 W,[8] are used for LBM applications. The laser spot size of commercial LBM systems is commonly in the range between 30 and 200 μm, and the layer thicknesses are between 30 and 60 μm. For increasing the build rate of LBM systems, multilaser machines are becoming more and more relevant for industrial applications.[9] A different approach for accelerating the LBM process is the use of higher laser powers and increased spot sizes. This enables the use of higher layer thicknesses and hatch distances at the tradeoff of decreased geometrical accuracy. The feasibility of processing materials with high relative density in this process regime has already been demonstrated, e.g., for AlSi10Mg (Ref. 10) and Ti6Al4V.[11]

C. Hybrid parts from LBM and conventional manufacturing technology

For producing hybrid parts from LBM and conventional manufacturing technologies, different approaches have already been proposed. Thus, a case study on building LBM structures on top of die forged base plates promises potential for weight reduction.[12] The combination of LBM and die forging was also investigated by Sizove and Bambach[13] for producing preforms for the forming process by means of additive manufacturing. A further study investigates the influence of different scan strategies on the relative density and the deviation of hybrid parts from a milled baseplate and a Ti6Al4V LBM element.[14] The general feasibility of producing hybrid parts from sheet metal, EBM (Ref. 15) and LBM (Ref. 16), respectively, has already been demonstrated in the previous work. For this purpose, two different process routes are conceivable. Both are shown in Fig. 1.

Starting with LBM followed by warm bending eases the buildup of the additive structures, but is challenging for the subsequent forming step, since the LBM structure is located in the forming zone. Starting with bending and hence building upon an uneven surface impairs the conditions for the LBM process. By applying a flexible wiper-lip, e.g., from silicon rubber, it still becomes possible to build LBM structures upon curved surfaces. In dependence of the desired hybrid part geometry, both process routes can be beneficial. However, the joint quality still shows a significant amount of scattering.[17] Hence, strategies for increasing the reproducibility of the joint quality between the baseplate and the AM element have to be identified.

Furthermore, the residual stresses induced by the LBM process[18] can be an issue since it leads to distortion of the sheet metal body. This is especially important for process route A (cf. Fig. 1), because the LBM process is the final step toward the hybrid part and, therefore, determines the geometrical accuracy.

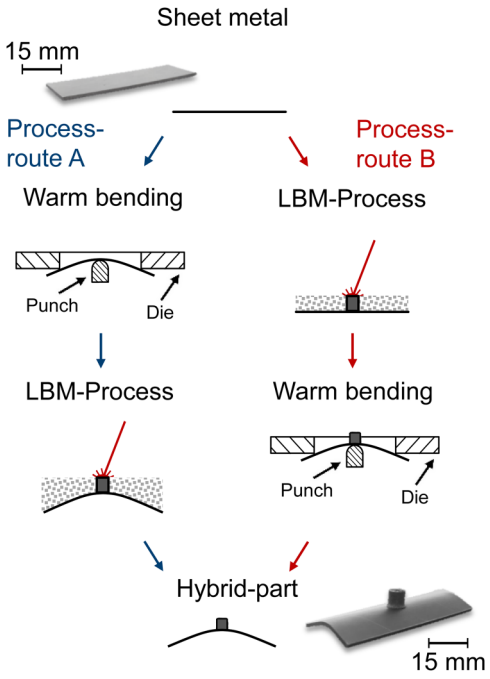

FIG. 1. Process routes for manufacturing LBM/forming hybrid parts.

For this reason, an approach for controlling the thermally induced residual stress in LBM is required.

III. METHODS

A. Experimental setup

The LBM experiments were carried out using an SLM 280^{HL} LBM machine from SLM Solutions GmbH (Germany). The basic principle of the LBM process is displayed in Fig. 2.

The SLM 280^{HL} applied in this work is equipped with two different laser beam sources. The first one is a single-mode fiber

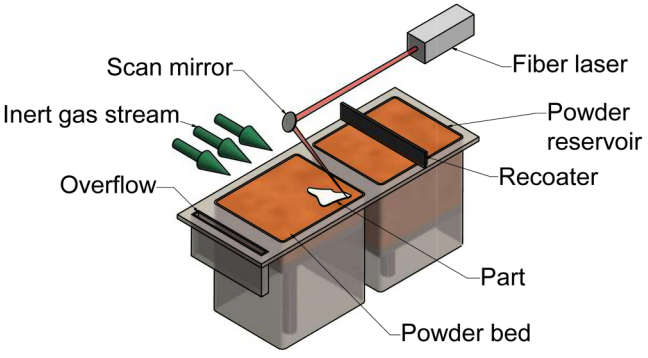

FIG. 2. Principle of the LBM process.

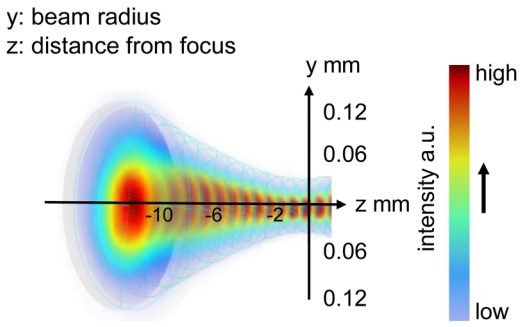

FIG. 3. Beam profile of the SM fiber laser.

laser with a Gaussian beam profile and a minimum beam diameter of approximately 80 μm (cf. Fig. 3), which represents the state of the art for LBM of Ti6Al4V. The second laser beam source is a multimode fiber laser with an irregular beam profile and a minimum beam diameter of approximately 680 μm (cf. Fig. 4). The increased spot size and laser power promises higher build rates at the tradeoff of geometrical accuracy in comparison to the single-mode fiber laser.

The Ti6Al4V powder used in this study was acquired from TLS Technik GmbH & Co. Spezialpulver KG (Germany). The chemical composition of the powder was determined by energy dispersive x-ray spectroscopy (EDS) (cf. Table I) and ranges within the specifications of DIN 17851.[19] The particle shape of the inert gas atomized powder is predominantly spherical, and the particle size ranges between 20 and 63 μm. This was verified by scanning electron microscopy imaging and static image analysis, respectively. The particle size distribution between 20 and 63 μm was chosen to facilitate a proper recoating of the power layers. For this reason, the fine particle fraction below 20 μm was removed, since it might reduce the flowability of the powder and hence the quality of the applied powder layer. The coarse fraction above 63 μm was sieved out with respect to the layer thickness of 50 μm that is used for the LBM experiments within this work.

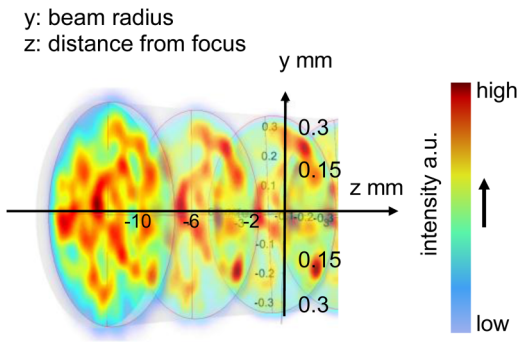

FIG. 4. Beam profile of the MM fiber laser.

TABLE I. Chemical composition of the Ti6Al4V powder used in this work (EDS measurement).

	Ti	Al	V	Fe
DIN 17851 (wt. %)	Bal.	5.50–6.75	3.5–4.5	−0.3
EDS (wt. %)	89.6	6.1	4.1	0.2
σ (wt. %)	0.1	0.1	<0.1	<0.1

The LBM parameter sets used for the experiments are listed in Table II and were experimentally developed in the previous work.[11] All parameter sets enable the production of parts with high relative densities above 99.7%.

B. Exposure strategies for the joint zone

The influence of two different exposure strategies on the joint quality of the hybrid parts and especially the reproducibility was investigated by an experimental study. For this purpose, a sample geometry consisting of a flat sheet metal baseplate with the dimensions $56 \times 20 \times 1.5$ mm^3 and a cylindrical LBM element with Ø 5×5 mm^2 were designed. The sample geometry is shown in Fig. 5. For building the LBM elements, the parameter sets D and X (cf. Table II) have been used. The altered exposures strategies were applied in the first five layers of the LBM element (height: 250 μm), since these layers are considered to be the most relevant for the joint quality. The expected asperities of the sheet metal are in the range of 100 μm and are therefore supposed to be covered reliably by the altered exposure strategies. The first altered exposure strategy comprises of a double exposure for the affected layers. For the second exposure strategy, parameter set E (cf. Table II) was applied in the joint zone. This parameter set works with a comparatively slow scan speed of 300 mm/s at 400 W laser beam power. Consequently, a 4.8 times higher line energy than with parameter set D (0.28 J/mm^3) and a three times higher line energy than with parameter set X (0.44 J/mm^3) are applied. Therefore, parameter set E promises an increased penetration depth of the melt tracks. In addition, a reference group with no special exposure strategy in the joint region was tested.

For each group, 12 samples were manufactured. The build order was randomized to exclude possible influences of the positions of the elements in the build envelop. The joint quality of the hybrid samples was assessed by shear tests. For this purpose, a

TABLE II. LBM parameters used for the experiments in this work.

	D	X	E	MM
Laser power, P_l	250 W	400 W	400 W	1000 W
Scan speed, v_s	900 mm/s	900 mm/s	300 mm/s	400 mm/s
Spot diameter, d_s	110 μm	110 μm	110 μm	680 μm
Hatch distance, h	120 μm	120 μm	120 μm	400 μm
Layer thickness	50 μm	50 μm	50 μm	100 μm
Line energy	0.28 J/mm	0.44 J/mm	1.33 J/mm	2.5 J/mm
Volume energy	46.3 J/mm^3	74.1 J/mm^3	222.2 J/mm^3	62.5 J/mm^3

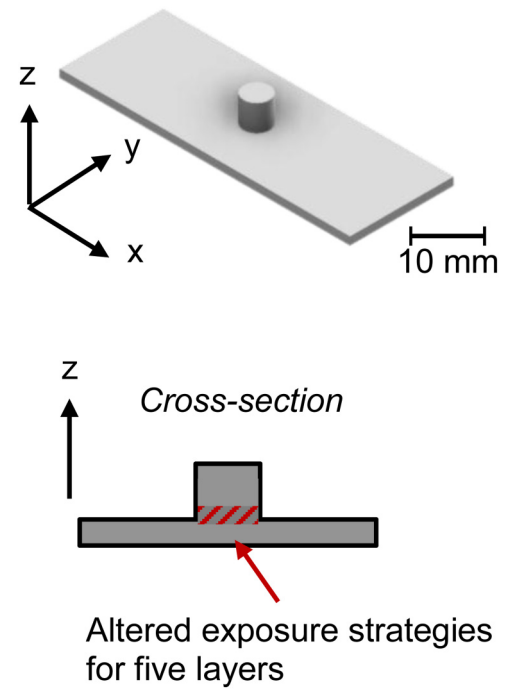

FIG. 5. Specimens for evaluating the effect of different exposure strategies on the joint quality.

universal testing machine walter + bai FS-300 with a maximum force of 300 kN was used. The tool setup for the shear tests shown in Fig. 6 was presented in prior investigations regarding the characterization of hybrid components.[20] Based on these investigations,

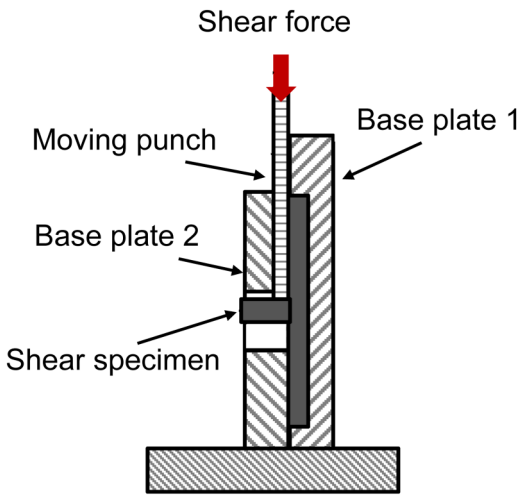

FIG. 6. Experimental setup for the shear test of the hybrid samples. Reproduced with permission from Schaub *et al.*, Key Eng. Mater. **611–612**, 609–614 (2014). Copyright 2014, Trans Tech Publications Ltd.

the punch velocity was set to 5 mm/min. Prior to the testing, the samples were heat treated at 850 °C for 2 h followed by furnace cooling to mitigate the residual stress induce by the LBM process and to adjust the microstructure of the LBM elements. This heat treatment was investigated by Vrancken *et al.*[21] for LBM parts and already applied in the previous work on hybrid parts from LBM and sheet metal.[16] The heat treatment was performed in an argon atmosphere to prevent oxidation and oxygen absorption.

C. Scan patterns for influencing the residual stress

Besides the joint quality, also the residual stress induced during the LBM process and hence the distortion of the hybrid parts is most likely influenced by the chosen exposure strategy. Therefore, the effect of different laser parameters and scan patterns on the distortion of the hybrid parts was evaluated by an experimental study. With regard to Fig. 1, process route A was used to evaluate the distortion of hybrid parts resulting from warm bending and subsequent LBM. In a first step, the Ti6Al4V sheet metals were bent. Since forming of Ti6Al4V is challenging, the bending process was conducted at elevated temperature. As shown in Ref. 22, the yield stress decreases significantly compared to room temperature even for moderate temperature of 250 °C. To realize the forming process, 250 °C was consequently chosen for the warm bending operation within this work. The samples consist of a sheet metal part with the original dimensions of $56 \times 20 \times 1.5\ \text{mm}^3$ before the bending step. The sheet metal parts were bent with a punch radius of 7 mm and a die width of 16 mm. The punch displacement was set to 4.5 mm, which results in a bending angle of about 40°. This tool combination and resulting part geometry were chosen based on prior investigations presented in Ref. 17, to increase comparability of the results. Within the second step of process route A, the LBM element with the dimensions of $20 \times 5 \times 5\ \text{mm}^3$ is placed centered on top of the sheet metal part. The bent sheet metal parts are positioned within the LBM machine by an appropriate clamping device. The resulting distortion of the hybrid parts is supposed to be influenced by the LBM process, the material properties, and the geometry of the hybrid parts (e.g., sheet thickness). This study, however, focuses on the effect of the LBM parameters. Therefore, only one sample geometry was chosen. For the first three investigated scan patterns, the orientation of the scan paths in relation to the long side of the LBM element was varied from 0° to 90° resulting in different scan vector lengths from 5 to 20 mm. The fourth scan strategy consists of a chessboard pattern with scan vectors in the length of 2.4 mm. The sample geometry and the four scan patterns are shown in Fig. 7.

For manufacturing the LBM elements, the parameter sets X, D, and MM (cf. Table II) were applied. The parameter sets X and D utilize the 400 W single-mode fiber laser of the SLM 280^{HL}. In addition, a group of samples was built with parameter set MM to investigate the impact on the residual stress of a significantly increased spot diameter and laser power in comparison to parameter set D or X. However, the hatch distance, the scan speed, and the layer thickness of MM were chosen to deposit a volume energy that is with a value of $62.5\ \text{J/mm}^3$ in the range of the parameter sets D ($46.3\ \text{J/mm}^3$) and X ($74.1\ \text{J/mm}^3$). For each combination of scan pattern and laser parameter set, three samples were built and

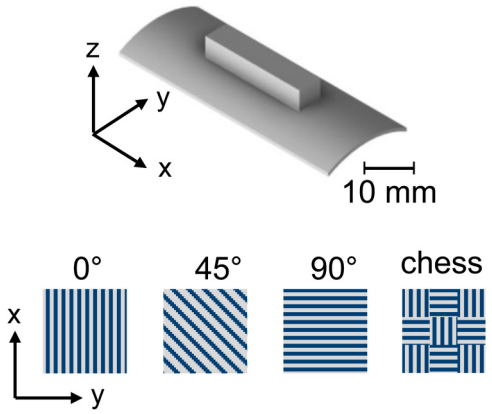

FIG. 7. Sample geometry and scan patterns.

tested. The distortion of the hybrid samples in relation to the LBM parameters and scan patterns was determined by the optical 3D measuring system ATOS provided by GOM GmbH (Germany). Prior to the LBM process, the 3D surface of each specimen after the warm bending process was measured. This geometry is used as a reference state. After the LBM process, the surface at the side of the additively manufactured element of each specimen was measured again. Between both surface topographies, a best-fit alignment was calculated. Using this approach, the geometries were oriented against each other with the overall smallest three-dimensional deviations from the reference state.

D. Heat treatment

Besides the forming operation and the LBM process itself, also the heat treatment has to be taken into account for producing Ti6Al4V hybrid parts with defined mechanical properties. Thus, a further study on the effect of three different heat-treatment temperatures for Ti6Al4V hybrid samples was performed. For this purpose, LBM elements with the geometry shown in Fig. 5 were produced and subsequently heat treated at 450, 850, and 1050 °C for 2 h followed by furnace cooling. By performing the heat treatment in an argon atmosphere, the samples were protected from oxidation and oxygen absorption. Afterward, the resulting microstructure was analyzed. For this purpose, the samples were polished with diamond suspension followed by active oxide polishing suspension (OP-S) and etched with Kroll's reagent. The hardness corresponding to the microstructures was measured using a Fischerscope® HM2000 from Helmut Fischer GmbH (Germany).

IV. RESULTS AND DISCUSSION

A. Shear tests

The results of the shear tests are plotted in Fig. 8. Each bar represents the maximum shear force averaged over 12 samples built with the same LBM parameter set and exposure strategy. No clear difference in the absolute values can be identified. However, the scattering of the results is significantly reduced by applying joint

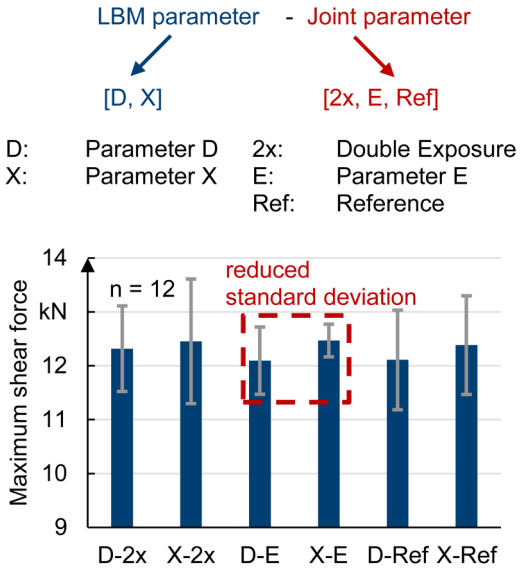

FIG. 8. Average maximum shear force in dependence of the exposure strategy for the first five layers.

parameter set E in the first five layers of the LBM element. For structures built with parameter set X, the standard deviation of the maximum shear force decreases from 915 N in the reference group to 303 N for the strategy X-E. In contrast to that, a double exposure in the first five layers has no positive effect on the scattering of the joint quality. Though the LBM parameter set E is in general inferior to D or X due to a slightly higher porosity and an increased evaporation of aluminum of up to 1 wt. % during LBM, which might decrease the mechanical properties, it shows a significantly higher penetration depth than D or X (cf. Fig. 9). This is due to the significantly higher line energy applied by parameter set E (222 J/mm^3) in comparison to D (46.3 J/mm^3) or X (74.1 J/mm^3). Since one major source of the scattering of the shear force is

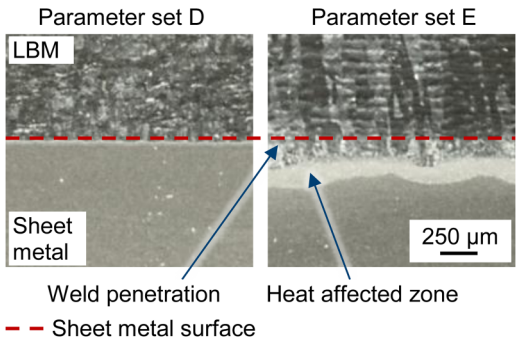

FIG. 9. Comparison of two microsections of hybrid samples built with parameter sets D and E. Influence of different scan patterns and laser parameter sets on the distortion.

presumably asperities of the sheet metal surface causing variations in the thickness of the first powder layers, an increased penetration depth is assumed beneficial for the process stability.

The high penetration depth of parameter set E in the range of 250 μm avoids bonding defects caused by variations in the powder layer thickness, and thus the scattering of the shear force can be reduced. A double exposure with the parameter sets D and X does not show this increased penetration depth, and therefore no reduction of the scattering is achieved.

For evaluating the effect of the different combinations of scan patterns and laser parameter sets on the distortion of the sheet metal, the optical 3D measurements were performed prior and after the LBM process. By comparing the measured surface topographies, the distortion caused by the LBM process is determined for the cross section along the bend line. Since the distortion was investigated for the sheet metal part, the geometry of the additively manufactured element is excluded from the evaluation. An example for this is presented in Fig. 10, which includes the equation for calculating the distortion Δz of the bent sheet metal part. For the calculation of Δz, the distortion of both ends z_1 and z_2 of the bend sheet metal part was used. Figure 11 shows the resulting values for Δz averaged over three samples for each combination of scan pattern and LBM parameter set.

It is evident that the scan strategy 0° with a scan vector length of 20 mm is inferior to the other investigated strategies in terms of residual stress and hence distortion of the sheet metal baseplate. The lowest distortion was measured for the 90° strategy with 5 mm scan vector length. This relation between scan vector length and residual stress has also been reported, e.g., by Mercelis and Kruth[23] and can be explained by the temperature gradient mechanism.[23]

The influence of the LBM parameter sets on the distortion of the sheet metal base plate appears to be rather weak in comparison to the scan strategy. This is not surprising for the parameter sets D and X, since both differ only by a factor of 1.6 in terms of laser power and intensity. Parameter set MM on the contrary consists of a significantly higher laser power and an approximately six times bigger spot diameter. Despite the higher laser power of 1 kW, the average intensity of the laser beam is less than a tenth of parameter set X.

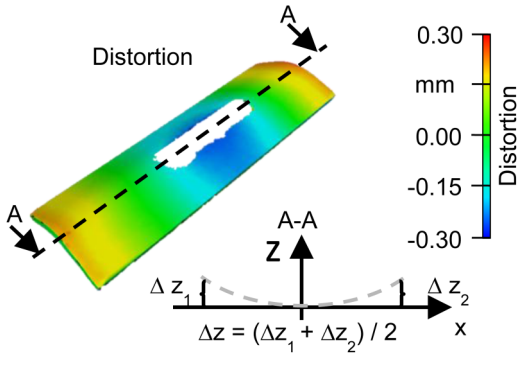

FIG. 10. Optical 3D measurement of the distortion of the hybrid samples after LBM.

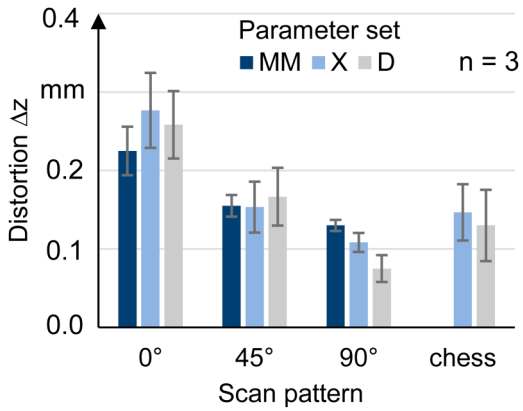

FIG. 11. Average distortion of the hybrid samples in dependence of the LBM parameters and the scan pattern.

The melt tracks of parameter set MM are approximately in the range of 800 μm and thus three times wider than those of parameter set X. However, the residual stress in the MM samples is comparable to that of the D or X samples. The reduced number of overall scan tracks resulting from the higher hatch distance and layer thickness of parameter set MM (cf. Table II) presumably equalizes the higher residual stress caused by a single weld track due to the increased welt track sizes. Consequently, the resulting distortion of the sheet metal part is again within the range of the single-mode laser parameter sets. This further proofs the feasibility of applying high laser beam powers of 1 kW and a multimode fiber laser for manufacturing hybrid parts from LBM and sheet metal forming.

B. Effect of different heat-treatment temperatures on the hybrid samples

By applying different heat-treatment temperatures at 450, 850, and 1050 °C, the microstructure and the Vickers hardness of the hybrid samples significantly changed. Figure 12 shows the resulting microstructures in the joint zone of the hybrid parts. The samples heat treated at 450 °C still show α'-martensite and columnar prior β-grains in the LBM element. This microstructure is similar to the as build condition of Ti6Al4V parts produced from LBM.[21] Also, the globular α–β microstructure that develops under the influence of plastic deformation and recrystallization[24] during hot rolling of the sheet metal appears to be unchanged compared to the original condition. The heat treatment at 850 °C, slightly below the β-transus temperature,[1] results in a decomposition of α'-martensite into a fine acicular α–β microstructure. This was also reported by Vrancken *et al.*[21] However, the microstructure of the sheet metal is still unchanged after the heat treatment at 850 °C.

In contrast to that, the microstructure of the hybrid part is homogenized by the heat treatment at 1050 °C, since a phase transition occurs while surpassing the β-transus temperature of Ti6Al4V. The resulting microstructure consists of coarse α–β grains of millimeter size. The averaged hardness values corresponding to the observed

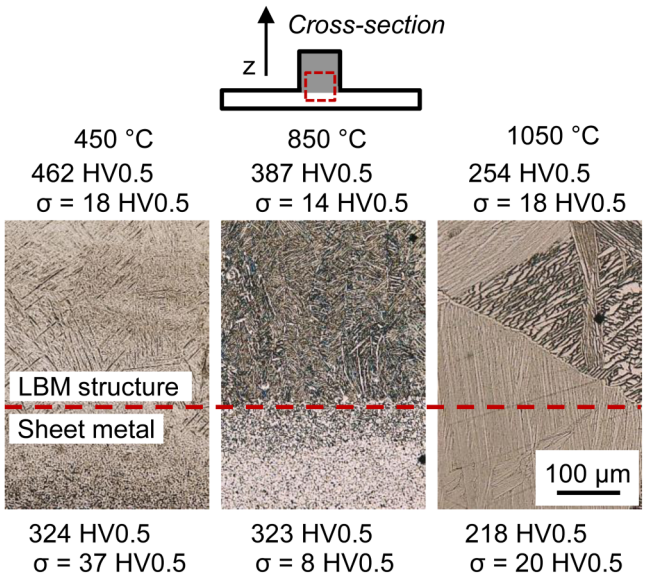

FIG. 12. Resulting microstructure in the joint zone in dependence of the applied heat treatment; averaged HV0.5 values ($n > 48$) for the sheet metal and the LBM element.

microstructures are stated in Fig. 12. The α'-martensitic microstructure shows the highest Vickers hardness with a value of 462 HV0.5 ($\sigma = 18$ HV0.5). This value significantly differs from the globular α–β microstructure of the sheet metal body, which shows an average hardness of 324 HV0.5 ($\sigma = 37$ HV0.5). The acicular α–β microstructure exhibits a slightly higher hardness of 387 HV0.5 ($\sigma = 14$ HV0.5) than the globular microstructure. The 1050 °C heat treatment generates a rather homogeneous hardness distribution within the hybrid part. The values range from 218 HV0.5 ($\sigma = 20$ HV0.5) for the sheet metal body to 254 HV0.5 ($\sigma = 18$ HV0.5) for the LBM element, respectively.

These hardness values also represent a first indicator for the formability of the hybrid samples. The high hardness of the α'-martensitic microstructure in combination with the difference between the sheet metal base and the LBM structure might decrease the formability when following process route B (cf. Fig. 1)—at least without very high forming temperatures or further heat-treatment steps. Especially with respect to process route B, the 1050 °C heat treatment on the contrary might ease the forming operation since it results in a rather homogeneous microstructure and low hardness values.

V. CONCLUSION AND OUTLOOK

This publication reports on the effects of customized exposure strategies on the joint quality of Ti6Al4V hybrid samples manufactured by LBM and sheet metal. The results indicate that LBM parameter sets with a higher line energy than otherwise preferable standard parameters (1.33 J/mm compared to 0.28 or 0.44 J/mm, respectively) have a positive impact on the reproducibility of the mechanical strength of the hybrid parts, when applied in the joint area between metal sheet and LBM structure. Shear tests showed that the standard deviation of the maximum shear force endured by the parts could be reduced by up to two-thirds in comparison to the reference group without a special exposure in the joint zone. The mean value remained at around 12 kN for all sample groups.

Furthermore, the impact of different scan patterns and laser parameter sets, including the use of two different laser beam sources (1 kW multimode fiber laser with 680 μm spot diameter and 400 W single-mode fiber laser with 110 μm spot diameter), on the geometrical distortion of the hybrid samples was investigated. The highest distortion of up to 0.28 mm was measured for an exposure strategy comprising a scan vector length of 20 mm, while exposure strategies with a shorter scan vector length significantly lowered the distortion values down to 0.08 mm. Using the 1 kW multimode laser does not have a negative effect on the distortion of the parts compared to the 400 W single-mode laser in the investigated parameter range. The measured values will be used in future work for the development and evaluation of a numerical model to predict the residual stress induced during LBM of the hybrid parts.

In addition, the impact of three heat-treatment temperatures of 450, 850, and 1050 °C on the microstructure and the Vickers hardness was analyzed. The highest hardness values of 462 HV0.5 were found for the LBM structure of the samples heat treated at 450 °C, while the sheet metal showed a hardness of 324 HV0.5. Due to the decomposition of α'-martensite, the hardness of the LBM structure dropped to 387 HV0.5 as a result of the 850 °C heat treatment. The heat-treatment temperature of 1050 °C leads to a homogenization of the microstructure of the hybrid part and the LBM structure as well as the sheet metal showing a similar coarse α–β microstructure with hardness values of 254 HV0.5 and 218 HV0.5, respectively. With respect to a subsequent forming operation of the sheet metal body, the homogeneous microstructure and the decreased hardness resulting from the 1050 °C heat treatment might be beneficial. In this context, the mechanical properties related to the different heat-treatment temperatures and microstructures will be the subject of future research.

ACKNOWLEDGMENTS

The authors want to thank the German Research Foundation (DFG) for funding Collaborative Research Center 814 (CRC 814), subproject B5. Support from the Erlangen Graduate School in Advanced Optical Technologies (SAOT) in the framework of DFG's excellence initiative is gratefully acknowledged.

REFERENCES

[1]B. Ilschner and R. F. Singer, *Werkstoffwissenschaften und Fertigungstechnik* (Springer, Heidelberg, 2005).
[2]C. Y. Yap, C. K. Chua, Z. L. Dong, Z. H. Liu, D. Q. Zhang, L. E. Loh, and S. L. Sing, "Review of selective laser melting: Materials and applications," Appl. Phys. Rev. **2**, 041101 (2015).
[3]SLM Solutions GmbH, 2017, see https://slm-solutions.de/sites/default/files/downloads/201en171023-01-001-powder_web.pdf for "SLM Solutions—3D Metals" (last accessed May 9, 2018).
[4]Y. Zhai, H. Galarraga, and D. A. Lados, "Microstructure evolution, tensile properties, and fatigue damage mechanisms in Ti-6Al-4V alloys fabricated by two additive manufacturing techniques," Procedia Eng. **114**, 658–666 (2015).

[5]V. Chastand, A. Tezenas, Y. Cadoret, P. Quaebebeur, W. Maia, and E. Charkaluk, "Fatigue characterization of Titanium Ti-6Al-4V samples produced by additive manufacturing," Procedia Struct. Integr. **2**, 3168–3176 (2016).
[6]Concept Laser GmbH, 2018, see https://www.concept-laser.de/produkte/maschinen.html; accessed 25 May 2018.
[7]SLM Solutions GmbH, 2018, see https://slm-solutions.de/produkte/maschinen/selective-laser-melting-maschine-slmr280-20; accessed 18 May 2018.
[8]Concept Laser GmbH, 2018, see https://www.concept-laser.de/home.html; accessed 18 May 2018.
[9]T. Wohlers, Wohlers Report 2016 (Wohlers Associates, Fort Collins, 2016).
[10]S. Bremen, D. Buchbinder, W. Meiners, and K. Wissenbach, "Mit selective laser melting auf dem Weg zur Serienproduktion?," Lasertechnik J. **6**, 24–28 (2011).
[11]F. Huber, M. Rasch, L. Butzhammer, M. Karg, and M. Schmidt, "Strahlschmelzen von Metallen mit unterschiedlichen Intensitäten und Belichtungsstrategien," in *Proceedings of Industriekolloquium of CRC 814—Additive Manufacturing, Nürnberg, Germany, 12 December 2017* (CRC 814, Erlangen, 2017).
[12]Rosswag GmbH, 2017, see https://www.rosswag-engineering.de/data-4/1/rosswag-umformtechnik-4-2016-036-037um.pdf; accessed 19 May 2018.
[13]I. Sizove and M. Bambach, "Hot workability and microstructure evolution of pre-forms for forgings produced by additive manufacturing," in *Proceedings of International Conference on the Technology of Plasticity, Cambridge, UK, 17–22 September 2017* (Elsevier, Amsterdam, 2017).
[14]D. Hagedorn-Hansen, M.-B. Bezuidenhout, D. Dimitrov, and G. A. Oosthuizen, "The effects of selective laser melting scan strategies on deviation of hybrid parts," S. Afr. J. Ind. Eng. **28**, 200–212 (2017).
[15]A. Schaub, M. Merklein, V. Jüchte, R. F. Singer, and C. Körner, "Funktionsintegration durch die Kombination additive Fertigungsprozesse mit der Blechumformung," in *Proceedings of Industriekolloquium of CRC 814—Additive Manufacturing, Nürnberg, Germany, 12 December 2013* (CRC 814, Erlangen, 2013).
[16]A. Schaub, B. Ahuja, M. Karg, M. Schmidt, and M. Merklein, "Fabrication and characterization of laser beam melted Ti-6Al-4V geometries on sheet metal," in *DDMC—Direct Digital Manufacturing Conference, Berlin, Germany, 12–13 March 2013* (Frainhofer Generativ, Berlin, 2014).
[17]L. Butzhammer, P. Dubjella, F. Huber, M. Aumüller, A. Baum, M. Merklein, and M. Schmidt, "Experimental investigation of a process chain combining sheet metal bending and laser beam melting of Ti-6Al-4V," in *Proceedings of World of Photonics Congress: Lasers in Manufacturing—LiM, Munich, Germany, June 26–29, 2017* (Wissenschafltiche Gesellschaft Lasertechnik e.V., Erlangen, 2017).
[18]J.-P. Kruth, J. Deckers, E. Yasa, and E. Wauthlé, "Assessing and comparing influencing factors of residual stresses in selective laser melting using a novel analysis method," J. Eng. Manuf. **226**, 980–991 (2012).
[19]DIN 17851, Titanlegierungen—Chemische Zusammensetzung, Beuth (1990).
[20]A. Schaub, V. Juechter, R. F. Singer, and M. Merklein, "Characterization of hybrid components consisting of SEBM additive structures and sheet metal of alloy Ti-6Al-4V," Key Eng. Mater. **611–612**, 609–614 (2014).
[21]B. Vrancken, L. Thijs, J.-P. Kruth, and J. Van Humbeeck, "Heat treatment of Ti6Al4V produced by selective laser melting: Microstructure and mechanical properties," J. Alloys Compd. **541**, 177–185 (2012).
[22]N. Kotkunde, A. D. Deole, A. K. Gupta, and S. K. Singh, "Comparative study of constitutive modeling for Ti–6Al–4V alloy at low strain rates and elevated temperatures," Mater. Des. **55**, 999–1005 (2014).
[23]P. Mercelis and J.-P. Kruth, "Residual stresses in selective laser sintering and selective laser melting," Rapid Prototyping J. **5**, 254–265 (2006).
[24]N. Steffansson and L. Semiatin, "Mechanisms of globularization of Ti-6Al-4V during static heat treatment," Metall. Mater. Trans. A **3**, 691–698 (2003).

Meet the Authors

Florian Huber studied Mechanical Engineering at the Technical University of Munich. Since 2016, he is working as a research assistant at the Institute of Photonic Technologies at Friedrich-Alexander-University Erlangen-Nurnberg, Germany. The primary focus of his research is on Additive Manufacturing by Laser Beam Melting in the powder bed. Within the Collaborative Research Center CRC 814—Additive Manufacturing subproject B5, he is performing research on combining Additive Manufacturing and Sheet Metal Forming.

Thomas Papke is research assistant at the Institute of Manufacturing Technology at the Friedrich-Alexander-University Erlangen-Nürnberg, Germany. He is a member of the Collaborative Research Center CRC 814—Additive Manufacturing subproject B5. Within the CRC 814, his research is focused on the process combination of Sheet Metal Forming and Additive Manufacturing and the fundamental analysis of manufacturing hybrid components.

Marion Merklein is head of the Institute of Manufacturing Technology at the Friedrich-Alexander-University Erlangen-Nürnberg, Germany. She is a member of a variety of national and international research associations (e.g., CIRP), speaker of the Collaborative Research Center TR73, and subproject leader in the Collaborative Research Center CRC814. In 2013, she received the Gottfried Wilhelm Leibniz Award for her collaborative work in the fields of material science and manufacturing technology.

Michael Schmidt studied electrical engineering at Friedrich-Alexander-University Erlangen-Nürnberg, Germany (FAU). Since 2005, he is director of the Bayerisches Laserzentrum GmbH and since 2009 head of the Institute of Photonic Technologies at FAU. Michael Schmidt is vice-speaker of the Collaborative Research Center CRC 814—Additive Manufacturing and member of several national and international research organizations such as CIRP, LIA, or SPIE.

Additional unpublished results and discussion of the publication's findings in the context of this thesis:

The overarching aim of this thesis is the investigation of in-situ alloy formation of refractory metal alloys. With regard to engineering applications, Titanium alloys are the most widely used refractory metal alloys and hence under investigation in the present work. To provide a strong basis for the in-situ alloy formation experiments, a basic understanding of the PBF-LB/M processing behavior of Titanium and its most important alloy Ti6Al4V is of essence. This includes knowledge of the interdependencies between process parameters and the resulting relative density, microstructure and mechanical properties. Furthermore, the development of heat-treatment strategies that are adapted to the requirements of PBF-LB/M is crucial. In this context, the publication *"Customized exposure strategies for manufacturing hybrid parts by combining laser beam melting and sheet metal forming"* [91] contributes to this thesis's goals by providing information on the PBF-LB/M processing behavior of Ti6Al4V and the resulting material properties in dependence of the input parameters.

The process parameter sets investigated in [91] were selected from a larger series of experiments on PBF-LB/M of Ti6Al4V. The results regarding PBF-LB/M with a multimode laser with a wide beam diameter of 680 µm in the focal plane were published in [94], while the results regarding the standard single mode laser with a nominal beam diameter of 80 µm in the focal plane are not yet published elsewhere and are consequently presented in Figure 8. The PBF-LB/M experiments were performed using a SLM 280^{HL} PBF-LB/M machine from SLM Solutions AG (Lübeck, Germany). Argon was used as shielding gas. Layer thickness, hatch distance and spot diameter on the build plane are 50 µm, 120 µm and 110 µm respectively. Test cubes with a dimension of 10 x 10 x 10 mm³ were printed and embedded in resin, cut in half and polished. The relative density of the test cubes in dependence of the PBF-LB/M parameters laser power and scan speed was determined by light microscopy and image analysis and is shown in Figure 8. The parameter sets used for investigating in-situ formation of Ti-alloys in the course of this work are to a large extent derived from this data.

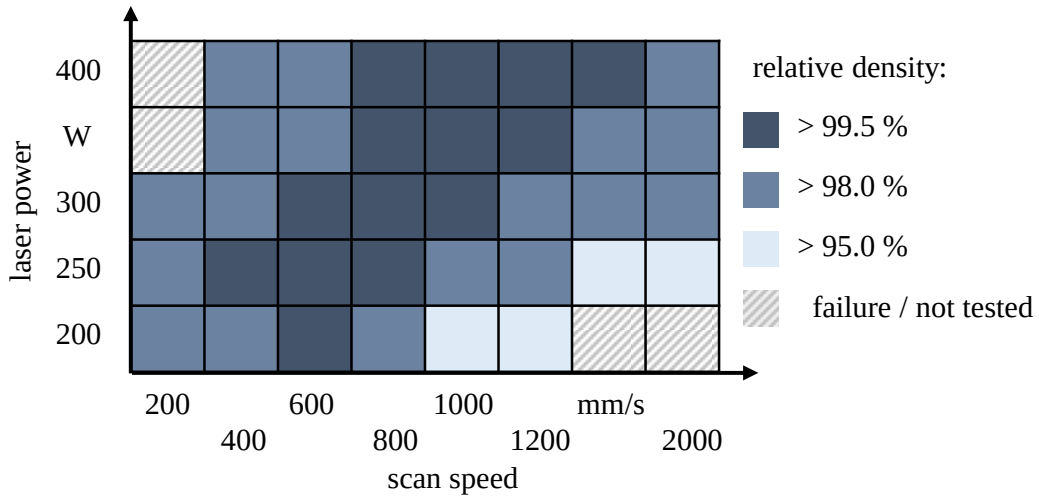

Figure 8: Relation between laser power, scan speed and relative density; material: Ti6Al4V

Besides the PBF-LB/M process itself, a subsequent heat-treatment is crucial to adjust the microstructure and mechanical properties of the final Ti6Al4V part [95]. The results presented in *"Customized exposure strategies for manufacturing hybrid parts by combining laser beam melting and sheet metal forming"* [91] demonstrate that phase transformations in Ti6Al4V hybrid parts comprising PBF-LB/M and sheet metal elements can be selectively triggered by a suitable heat-treatment, resulting in different microstructural conditions throughout a single part. By doing so, manufacturing of parts with locally different properties becomes feasible. This finding fosters the idea of even more expanding the possibilities for creating locally tailored material properties beyond the findings presented in [91]. Selectively varying the alloy composition throughout the part would provide a strong leaver to do so, since already small amounts of added elements can significantly change the material properties of many alloys [96]. This can be attractive, as different load cases and requirements (e.g. stiffness, fatigue or wear resistance) may apply in different areas of a part. A part with locally adjusted material properties could in theory better fulfill these requirements as choosing a single alloy composition, which can always only be a compromise.

The layer-wise manufacturing of the part during PBF-LB/M is predestined for local material modification, as it allows the selective introduction of additional alloying elements during the part creation. The concept of a local in-situ alloy modification by PBF-LB/M is illustrated in Figure 9.

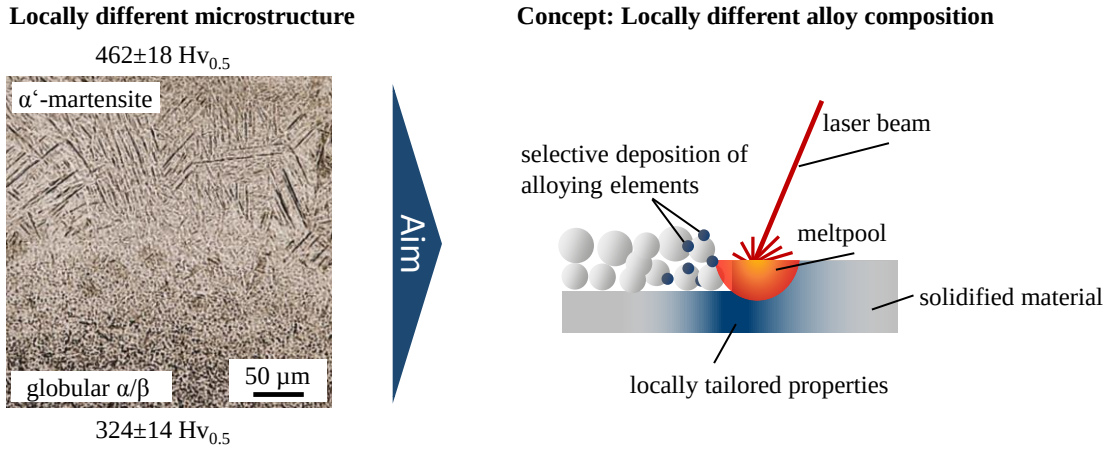

Figure 9: Concept of creating parts with locally tailored material properties by PBF-LB/M and in-situ alloy modification as continuation of the work presented in [91]

The selective deposition of the alloying element powder in the build plain is investigated elsewhere, but in general feasible (e.g. nozzle based [17] or by electrophotographic powder deposition [97]). The present work instead focuses on the laser process itself and aims for contributing to a comprehensive understanding of in-situ alloy modification by PBF-LB/M and its effect on the processing behavior and the resulting material properties of Ti-alloys. This is essential for realizing the idea of Ti-parts with locally tailored material properties manufactured by PBF-LB/M. The publication *"Customized exposure strategies for manufacturing hybrid parts by combining laser beam melting and sheet metal forming"* [91] provided inspiration and a starting point for the investigations presented in the following, thus contributing to the long-term goal of PBF-

LB/M parts with locally tailored properties. The following chapter 4.2 with the publication *"Laser Powder Bed Fusion (PBF-LB/M) process strategies for in-situ alloy formation with high-melting elements"* [41] builds upon the findings on PBF-LB/M of Ti-6Al-4V in [91], especially regarding the process parameter window for Ti-6Al-4V and investigates process strategies for in-situ alloy formation for achieving a homogeneous element distribution when adding alloying elements to Ti.

4.2 Laser Powder Bed Fusion (PBF-LB/M) process strategies for in-situ alloy formation with high-melting elements

Published in Metals, 11 (2021)

Florian Huber[1,2,3], Michael Rasch[1,2,3] and Michael Schmidt[1,2,3]

[1] Institute of Photonic Technologies, Friedrich-Alexander Universität Erlangen-Nürnberg
[2] Collaborative Research Center 814 – Additive Manufacturing
[3] Erlangen Graduate School in Advanced Optical Technologies

PBF-LB/M parameter set and scan strategy

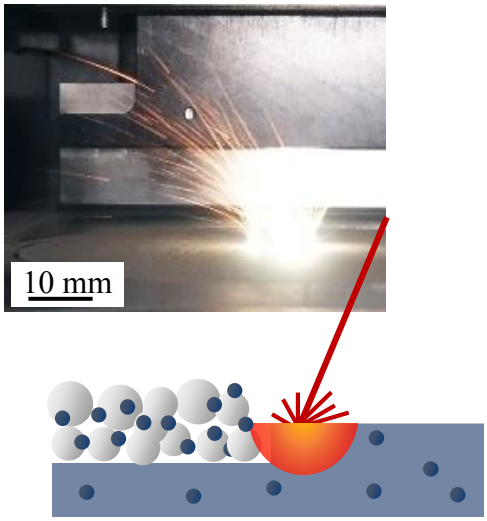

Quantification of undissolved high melting particles

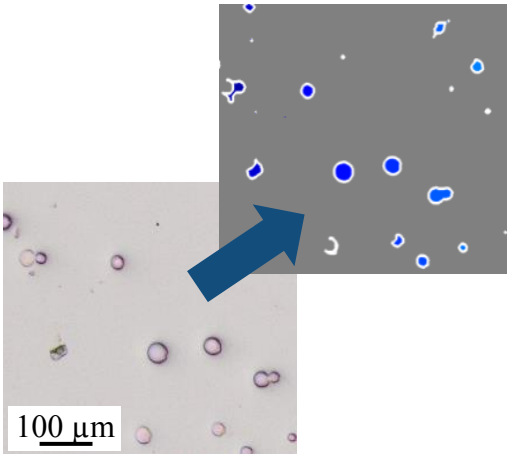

Highlights:

- Quantification of the effect of the most relevant PBF-LB/M process parameters scan speed, laser power, laser spot diameter and the exposure strategy on the dissolution of high melting particles
- Identification of the powder movement in the process zone caused by the evaporation driven gas jet above the meltpool as a major source of undissolved high melting particles; presumably reduced chance for dissolution of particles dragged into the already solidifying meltpool tail
- Effective reduction of the number of undissolved particles by double exposures and parameter sets with slow scan speeds and accordingly reduced laser power that mitigate powder movement

metals

MDPI

Article

Laser Powder Bed Fusion (PBF-LB/M) Process Strategies for In-Situ Alloy Formation with High-Melting Elements

Florian Huber [1,2,3,*], Michael Rasch [1,2,3] and Michael Schmidt [1,2,3]

[1] Institute of Photonic Technologies, Friedrich-Alexander-University Erlangen-Nürnberg (FAU), Konrad-Zuse-Straße 3/5, 91052 Erlangen, Germany; michael.rasch@lpt.uni-erlangen.de (M.R.); michael.schmidt@lpt.uni-erlangen.de (M.S.)
[2] Erlangen Graduate School in Advanced Optical Technologies (SAOT), Paul-Gordan-Straße 6, 91052 Erlangen, Germany
[3] Collaborative Research Center 814—Additive Manufacturing, Am Weichselgarten 8, 91058 Erlangen, Germany
* Correspondence: florian.huber@lpt.uni-erlangen.de

Abstract: In-situ alloy formation by Laser Powder Bed Fusion (PBF-LB/M) from mixtures of easily available elemental powders is an appealing approach for developing and qualifying new alloys for laser based additive manufacturing of metals. However, especially when dealing with high-melting elements, like W, Ta, Mo, or Nb, it is difficult to achieve a homogeneous element distribution and a complete fusion of the powder particles. The aim of this work was to understand the effects of the PBF-LB/M process parameters (laser power, scan speed, laser spot diameter) and three different single- and double-exposure strategies on the fusion of high-melting W, Ta, Mo, and Nb particles in a Ti-matrix. For this purpose, 220 samples with 10 vol.% of the high-melting particle fraction were prepared and analyzed by optical light microscopy and automated image processing, as well as by scanning electron microscopy (SEM). The results are discussed in the context of current research on the process dynamics of PBF-LB/M. Based on that process strategies to support a complete fusion of high-melting particles during in-situ alloy formation are derived. It is shown that the number of unmolten particles can be at least decreased by a factor of ten compared to the most unfavorable parameter combination. For the lower melting elements, Nb and Mo, a complete fusion without any remaining particles visible in the microsections was achieved for certain parameter combinations. The results prove the feasibility of in-situ alloy formation with high-melting alloying elements, but they also demonstrate the necessity to adjust the PBF-LB/M process strategy to achieve a complete dissolution of the alloying elements.

Keywords: additive manufacturing; laser powder bed fusion of metals (PBF-LB/M); in-situ alloying; powder consolidation; microstructure

Citation: Huber, F.; Rasch, M.; Schmidt, M. Laser Powder Bed Fusion (PBF-LB/M) Process Strategies for In-Situ Alloy Formation with High-Melting Elements. *Metals* **2021**, *11*, 336. https://doi.org/10.3390/met11020336

Academic Editor: Jon Iñaki Arrizubieta

Received: 28 January 2021
Accepted: 11 February 2021
Published: 16 February 2021

1. Introduction

Laser Powder Bed Fusion (PBF-LB/M) is currently the most widely used process for additive manufacturing of metals [1] and is gaining an increasing importance in industry and science alike [2]. Potential applications are high-value components in the aerospace industry, like fuel nozzles [3] or further engine parts [4], motor sport components [5], tool inserts with internal cooling channels [6], or medical implants [7]. The basic process principle is shown in Figure 1. Major advantages are an almost unlimited degree of design-freedom and a high flexibility of the production process. The achievable material properties are close to or even superior to conventional manufacturing [8]. However, one important drawback of PBF-LB/M, that is restricting the application of the process, is the limited variety of qualified materials. While thousands of different metal alloys are available, only a few dozens of them have been qualified for PBF-LB/M [8]. With only very few exceptions (e.g., Scalmalloy [9]), most of the alloys that are currently in use for

PBF-LB/M have been originally designed for conventional manufacturing processes, like casting. However, the PBF-LB/M process is characterized by unique thermo-mechanical conditions, like high cooling rates in the range of 10^6 K/s [10] and a cyclic re-heating during melting of consecutive scan tracks and layers. Especially the high cooling rates open up possibilities for developing and processing novel alloy classes, like bulk metallic glasses [11] or compositionally complex alloys or high entropy alloys, respectively [12]. However, the range of possible alloy compositions is vast and the availability of pre-alloyed powder is limited. The atomization of special alloys on request is possible but is expensive and time consuming, which is effectively slowing material development for PBF-LB/M. One possibility to ease material development for PBF-LB/M and facilitate high throughput investigations of novel alloy compositions is in-situ alloy formation. By using mixtures of easily available standard powders, an expensive and time-consuming atomization of pre-alloyed powder can be avoided. However, achieving a homogeneous element distribution and a complete dissolution of the powder particles during PBF-LB/M is challenging. This is especially true if the melting point of the added elements is far above the melting point of the main alloying element.

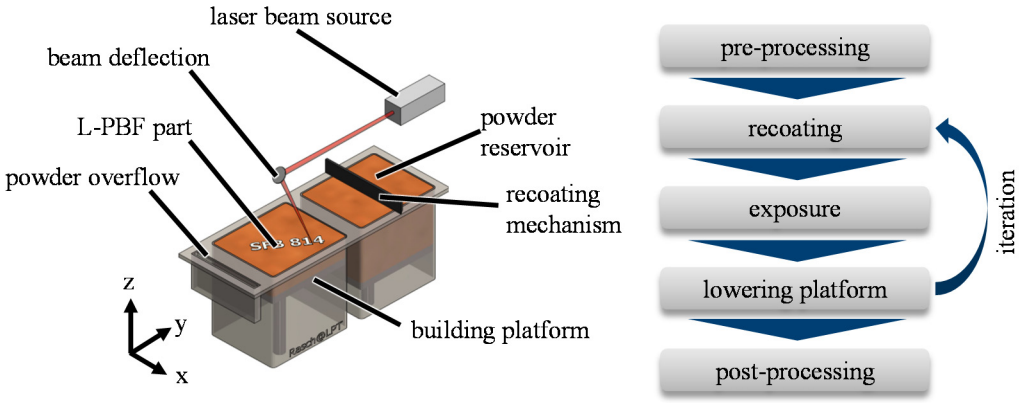

Figure 1. Schematic of the Laser Powder Bed Fusion (PBF-LB/M) process (reproduced from reference [13]).

Aota et al. [14] investigated in-situ alloy formation of 1.4307 (AISI 304L) from elemental Fe, Ni and Cr powder. They achieved a homogeneous element distribution for certain parameter combinations and concluded that the dwell time of the particles in the meltpool is crucial for achieving a complete dissolution of the particles. In addition, Chen at al. [15] obtained a fairly homogeneous element distribution by in-situ formation of a compositionally complex CoCrFeMnNi alloy. Their results show that a high volumetric energy input is favorable for in-situ alloy formation by PBF-LB/M. In contrast to these successful applications, in-situ alloy formation of Ti-based alloys proved to be more challenging. Yadroitsev et al. [16] investigated in-situ formation of Ti15Mo and Ti1.38Cu alloys. While the lower melting Cu-particles (melting point 1084 °C [17]) were completely fused, at least some of the higher melting Mo-particles (melting point 2623 °C [17]) remained undissolved. Despite the complete melting of the Cu-particles, Yadroitsev et al. [16] also report areas with increased copper content, mainly located at the fusion boundaries of consecutive melt tracks. Mosallanejad et al. [18] made similar observations in in-situ alloyed Ti5Cu samples. They also describe segregation of Cu at fusion boundaries an in addition to Yadroitsev et al. [16] also some remaining unmolten Ti-particles. Grigoriev et al. [19] investigated synthesis of Ti5Al and a Ti22Al25Nb alloys by in-situ alloy formation. They showed that PBF-LB/M with a 700 µm laser spot diameter and 950 W laser power results in a homogeneous material. Using a configuration with 70 µm beam diameter resulted in undissolved Al-particles in the Ti matrix. The Ti22Al25Nb alloy processed with the 700 µm laser spot contained unmolten Nb particles that could be removed by a heat-treatment at 1250 °C for 2 h. Polozov et al. [20] achieved similar results as Yadroitsev et al. [16] with undissolved Nb particles in Ti6Al7Nb and Ti22Al25Nb alloys that could be removed by annealing at

1250 °C and 1350 °C, respectively. Fischer et al. [21] prepared an Ti26Nb alloy by in-situ alloy formation. Their results show that the number of remaining Nb-particles is influenced by the PBF-LB/M parameter combination and that higher volumetric energy densities lead to a reduced number of remaining particles. Huang et al. [22] and Dzogbewu [23] investigated in-situ alloy formation of Ti with Ta and Mo, respectively. Both elements feature an even higher melting point than Nb, and dissolving the high melting particles proved to be challenging.

These publications show that in-situ alloy formation is an appealing and widely used method to ease material development for additive manufacturing of metals. However, despite some successful applications, e.g., for Fe-, Ni-, Cr-based alloys, defects, like an inhomogeneous element distribution and/or undissolved particles, are common. Comprehensive investigations of the interdependencies between PBF-LB/M process strategy, material/powder properties, and the resulting homogeneity of the in-situ alloyed material are currently lacking. Especially in-situ alloy formation of Ti-based alloys containing high melting elements, like Nb, Mo, or Ta, proves to be challenging and requires further investigation. The present work represents a first step in that direction.

In this context, the aim was to gain a deeper understanding of the effect of the PBF-LB/M parameters and different scan strategies on the fusion of high-melting W, Ta, Mo, and Nb particles in a Ti-matrix. For this purpose, the number of unmolten particles in PBF-LB/M is quantified in dependence of the laser power, the scan speed, the focus diameter, and the scan strategy (single and two different double exposure strategy). Based on these experiments and discussion with literature, processing strategies for successful in-situ alloy formation by PBF-LB/M with a high dissolution ratio of high melting particles are derived. It is shown that, by applying these strategies, the number of residual high melting particles can be reduced by at least a factor of ten compared to the most unfavorable PBF-LB/M parameter combination. For Mo and Nb particles, even a complete dissolution of the high melting particles was achieved.

2. Materials and Methods

Scanning electron microscopy (SEM) images of the six different powders used in this work are shown in Figure 2. The index 45 indicates the nominal upper particle size limit in µm.

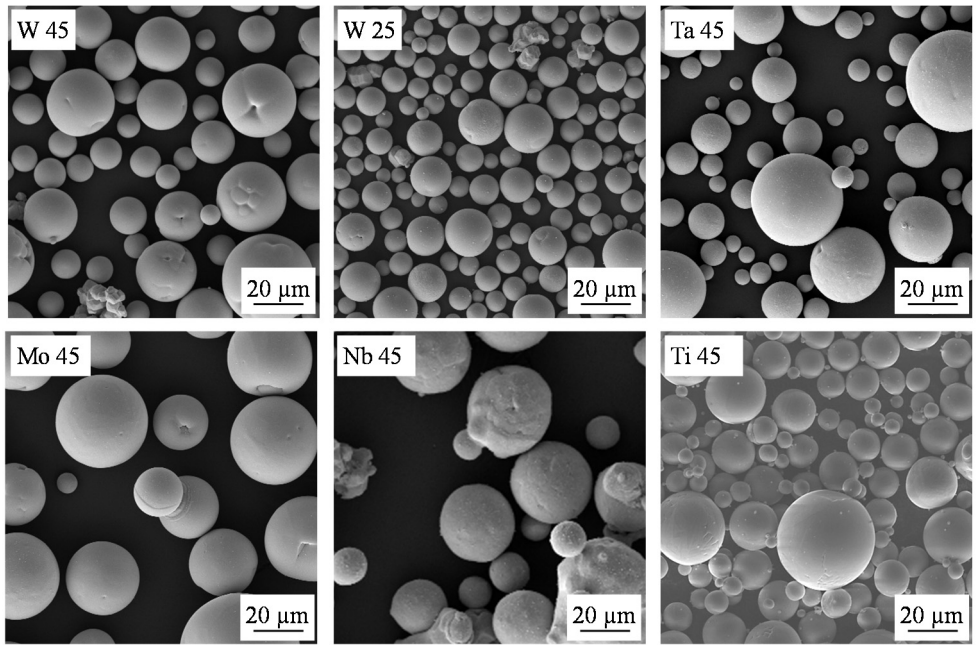

Figure 2. Scanning electron microscopy (SEM)-images of the powders used in this work; SEM type: Zeiss Merlin.

The particle shape is predominantly spherical. The plasma atomized W 45, Ta 45 and Mo 45 powder was obtained from Tekna (Sherbrooke, QC, Canada). The Ti 45 powder, which is also plasma atomized, was supplied by AP&C Advanced Powders and Coatings Inc. (Boisbriand, QC, Canada) and the argon atomized Nb 45 powder was provided by H.C. Starck Tantalum and Niobium GmbH (Goslar, Germany). The chemical purity of all powders was verified by energy-dispersive X-ray spectroscopy (EDS) and is higher than 99.8 % (metallic elements). The particle-size distribution of the powders was verified by laser diffraction measurements using a Mastersizer 3000 from Malvern Panalytical GmbH (Malvern, UK). The results are listed in Table 1.

Table 1. Particle size distribution determined by laser diffraction.

Powder	D_{10}	D_{50}	D_{90}
W 45	18.6 µm	32.4 µm	40.2 µm
Ta 45	10.5 µm	21.0 µm	39.8 µm
Mo 45	19.6 µm	30.5 µm	44.3 µm
Nb 45	18.3 µm	35.6 µm	48.4 µm
Ti 45	16.8 µm	25.6 µm	41.3 mm

For the PBF-LB/M experiments, five powder mixtures from 90 vol.% Ti 45 with 10 vol.% of each of the additional elements were prepared. The powders were mixed for 1 h in a Turbula®-mixer from Willy A. Bachofen AG (Muttenz, Switzerland) and dried in a vacuum furnace at 120 °C for 4 h to remove any moisture that might reduce flowability or interfere with the PBF-LB/M process. This procedure was empirically developed over the past years. The recoatability of the powder mixtures was verified visually inside the PBF-LB/M machine with the aid of an illumination setup (small angle illumination). All powder mixtures can be recoated to homogeneous layers without visible defects.

The PBF-LB/M parameter sets used in the following were developed experimentally and are partially derived from previous work [24]. The aim was to investigate the dissolution behavior of the high melting particles in a wide range and to ensure a relative density of more than 97%, despite the variation in chemical composition and parameter combination. The relative density >97% was verified in preliminary experiments by polished microsections. The experimental design comprises the manufacturing of three series of PBF-LB/M samples. Details are described in Table 2. Considerations regarding meltpool geometry [25,26], powder movement [27], and process dynamics [28] that led to the three series of experiments are based on previous work and literature. The intention of series 1 is to identify the effect of standard PBF-LB/M process parameters on the dissolution of high melting particles, while keeping the volumetric energy density (VED, definition given, e.g., in reference [29]) constant. The aim of series 2 was to investigate the effect of an increasing scan speed, while keeping the laser power constant. Furthermore, a parameter combination with comparably low laser power (66 W) and slow scan speeds was selected. According to literature, this results in a short meltpool tail [26], less gas and particle movement [28], and, due to the slow movement of the laser spot, a longer interaction time with the laser beam. It is assumed that this has a positive effect on the dissolution of the high melting particles in the meltpool. The main idea investigated with series 3 was that a double exposure can further reduce the number of unmolten particles. For this purpose, two different strategies were conceived. The first one comprises a straightforward double exposure, while the second strategy comprises a pre-melting step for powder fixation and the actual consolidation step for part generation. The hypothesis behind the second double exposure strategy is to prevent denudation [27] and dragging of high melting particles into the solidifying meltpool tail during the actual consolidation exposure, which is assumed to be a possible source of unmolten particles.

Table 2. Experimental design.

Paramter	Series 1	Series 2	Series 3
Description	• Constant VED (55.6 J/mm^3) • Variation of spot diameter, laser power and scanning speed	• Variation of volemtric energy density (55 – 110 J/mm^3) • Short meltpool tail • Slow scan speed	• Double exposure • Simple double exposure with repetition of printing parameters • Special double exposure with pre-melting and consolidation
Laser power	75 W, 100 W, 150 W, . . . , 400 W	66 W	75 W, 100 W, 150 W, . . . , 400 W
Laser spot diameter	70 µm, 100 µm, 200 µm	70 µm, 100 µm, 200 µm	70 µm for pre-melting: 400 µm
Scan speed	225 mm/s, 300 mm/s, 450 mm/s, . . . , 1200 mm/s	100 mm/s, 125 mm/s, . . . , 200 mm/s	225 mm/s, 300 mm/s, 450 mm/s, . . . , 1200 mm/s for pre-melting 600 mm/s
Hatch distance	120 µm	120 µm	120 µm, for pre-melting: 250 µm
Scan strategy	Single exposure	Single exposure	Double exposure: • Simple repetition • Pre-melting for powder fixation followed by consolidation

All PBF-LB/M experiments were done using an Aconity mini PBF-LB/M machine from Aconity GmbH (Herzogenrath, Germany) that is equipped with a redPower QUBE fiber laser from SPI Lasers Ltd. (Southampton, UK) with a maximum beam power of 1 kW and a wavelength of 1080 nm and an AxialSCAN-30 scanner optics from Raylase GmbH (Wessling, Germany). The sample geometry is cubic with an edge length of 6 mm. The number of undissolved particles was determined by polished microsections and light microscopy (image section 2.25 mm × 1.69 mm; 3.8 mm^2). Due to the high sample number, automated image analysis with MATLAB® was employed to detect and count the particles. While most samples have a high relative density of more than 99.5%, in dependence of the process parameters, some samples contain up to 5% defects, which could lead to misdetections. This is considered by a filter algorithm that excludes dark objects (voids) from the count. In addition, very small particles that are probably image artifacts, small defects, or dirt are not considered. This approach is visualized in Figure 3 and verified for ten selected images by manual counting. Deviations between manual counting and automated image analysis are below 5% in all cases.

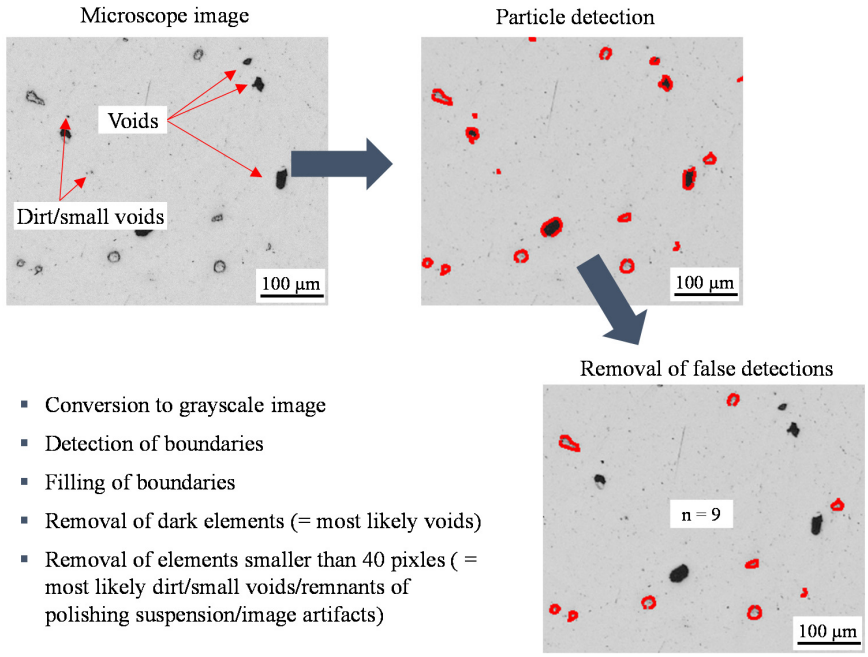

Figure 3. Detection of unmolten particles by automated image analysis.

3. Results and Discussion

The complete data set that is discussed in the following section is provided in the Appendix A section alongside this manuscript. Due to the high number of figures, only selected diagrams are shown here.

Aim of experiment series 1 (see Table 2) was to investigate the dissolution behavior of high melting particles in a Ti-matrix in dependence of standard PBF-LB/M parameters at a constant volumetric energy of 55.6 J/mm^3. The results for W 45 and Nb 45 particles are presented in Figure 4. These materials represent the highest and lowest melting particle materials investigated. Data regarding the remaining particle materials (Ta 45, Mo 45) are provided in Appendix A.

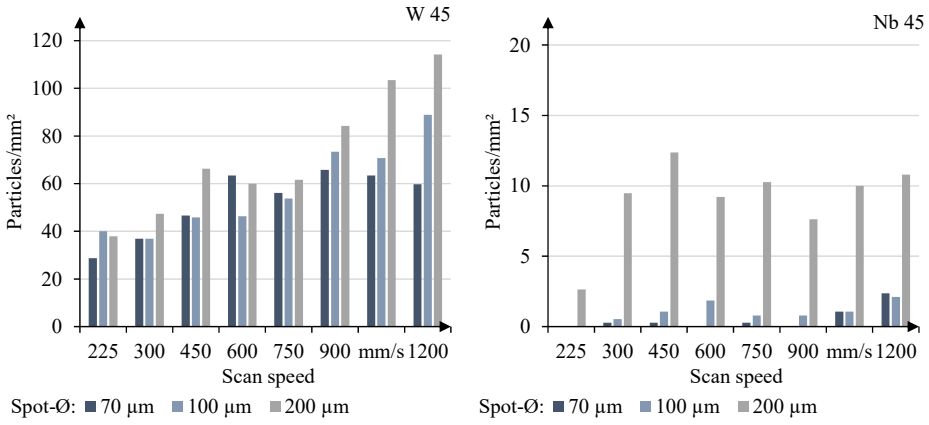

Figure 4. Results of experiment series 1 (see Table 2); constant volumetric energy density (55.6 J/mm^3), laser power scales with scan speed.

A first and rather self-evident observation is the number of undissolved particles scales with the melting point of the particle material [17] with W resulting in the highest and Nb resulting in the lowest number of undissolved particles. Despite the melting point, further interdependencies between the PBF-LB/M parameter and the number of remaining particles are evident, which are discussed in the following.

The highest number of undissolved particles (114/mm^2) was measured for W 45 at a laser spot diameter of 200 µm and a scan speed of 1200 mm/s. The relative amount of W determined by image analysis of the cross-section is 7.6 vol.%. This is slightly lower than the originally introduced 10 vol.% W but shows that only a small portion of W particles was dissolved during PBF-LB/M. In contrast to that, the slowest scan speed and the smallest spot diameter investigated resulted in 29 undissolved particles per mm^2 and, hence, a reduction by the factor four. At a constant volumetric energy, PBF-LB/M parameter combinations featuring a slow scan speed and a small spot diameter appear to be beneficial for particle dissolution. This correlation is also valid for the other investigated materials. This shows that particle dissolution is strongly governed by the PBF-LB/M parameter combination, even when keeping the volumetric energy constant. While, according to literature, a high volumetric energy proved to be beneficial [15], the present results demonstrate that this is only one aspect of many and that more complex interdependencies affect the dissolution of high melting particles in the meltpool during PBF-LB/M. Vacuum arc furnace melting experiments and theoretical considerations by Ghazal et al. [30] identify the dwell time, the temperature, and the velocity of the surrounding melt as key factors for dissolution of high melting inclusions in Ti-alloys. Quantifying these parameters for a specific PBF-LB/M parameter combination is complex and requires elaborate numeric simulations that would exceed the scope of this manuscript. However, first conclusions can be derived from current work on PBF-LB/M process physics, like Khairallah et al. [28], Matthews et al. [27], or Eschner et al. [31]. Heat and mass transport in the PBF-LB/M meltpool are driven by Marangoni convection, evaporation, and resulting recoil pressure on the meltpool surface. According to reference [27], particles around the meltpool are strongly affected by the gas flow above the laser spot that forms due to evaporation of metal and the Bernoulli effect. This is known to be the cause of powder denudation in the vicinity of the melt track. Mathews et al. [27] identified the particles affected by the gas stream as a major source of the material that is added to the meltpool and contributes to the material build up. Under standard PBF-LB/M conditions, the gas stream drags particles from all directions into the process zone, partially moves the particles upwards, and slightly towards the tail of the meltpool [32], where they are either incorporated completely into the meltpool or just stick to the part surface. In contrast to that, direct contact of particles with the liquid metal and dragging into the meltpool by capillary forces is only a minor source of material added to the meltpool [27].

With respect to the present work, it is assumed, that the meltpool temperature ranges roughly between the evaporation temperature of Ti at the impact area of the laser beam and the solidification temperature of Ti or the formed Ti-alloy, respectively, which applies for all samples of series 1. The melt velocity that is identified as a second factor for dissolution of high melting inclusions in a Ti melt is governed by Marangoni convection and recoil pressure. Smaller spot diameters, and hence higher laser beam intensities, generally result in a stronger Marangoni convection and higher recoil pressure [28], and hence higher melt velocities, which eases particle dissolution [30]. This in good agreement with Figure 4, which implies that smaller spot diameters reduce the number of undissolved particles. The third, and probably most important, factor for particle dissolution is the dwell time inside the hot meltpool. A very simple estimation would be that the dwell time can be calculated from the meltpool length and the scan speed. A slow scan speed and a long meltpool length would consequently result in longer dwell times. This seems to be at least partially true and could provide a possible explanation for the reduced number of undissolved particles at 225 mm/s compared to 1200 mm/s scan speed. Since, according to reference [26], the meltpool length is only weakly affected by the scan speed with increasing laser powder, the time the material is in a liquid state is assumed to be longer for the slower scan speeds. However, this does not explain why the size distribution of residual particles in all W 45 samples is approximately equal. The more obvious assumption would have been that samples with lower total numbers of particles also contain particles with a smaller average diameter than samples with larger numbers of particles. However, this is not true for the

present experiments. The particle size determined for 225 mm/s by manual measurement in the microscope image is 13.7 µm (σ = 9.8 µm, n = 25) and 14.0 µm (σ = 9.3 µm, n = 25) for 1200 mm/s, respectively, with both groups containing particles with a diameter in the upper quarter of the particle size distribution that was originally introduced (see Figure 5). This observation indicates that all samples contain particles that were affected by the hot meltpool for an equally short time. Considering the process physics and the findings about particle movement in the PBF-LB/M process zone by reference [27,31,32], it is likely that a major source of undissolved high melting material are particles that were either dragged by the gas stream around the hot area of the process zone into the already solidifying meltpool tail or were drawn from the side of the meltpool into the liquid metal and, hence, were not exposed to the melt for a sufficient time to be dissolved. In addition, melt velocity and temperature in the tail of the meltpool are lower than closer to the impact area of the laser beam, thus resulting in slower dissolution [33].

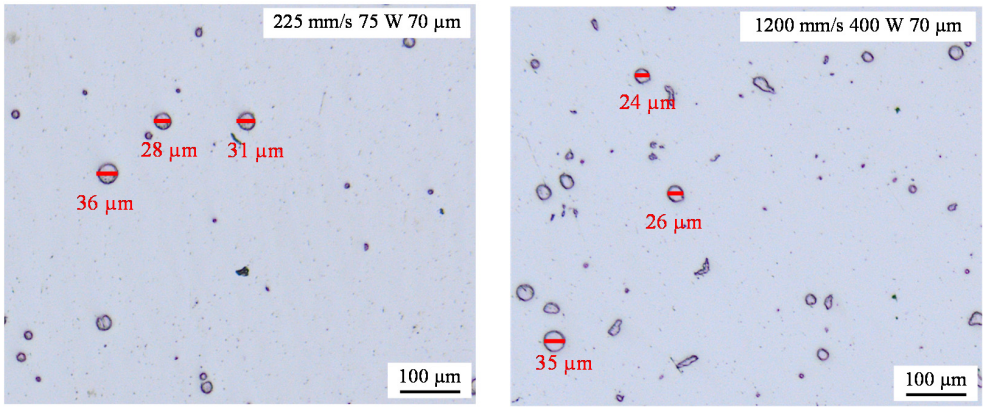

Figure 5. Polished microsection of W 45 samples with 225 mm/s scan speed and 1200 mm/s scan speed showing approximately equal particle size distributions.

To further substantiate the hypothesis that residual particles are related to denudation and particles incorporation in the meltpool tail, experiment series 2 was conceived. The laser power was set to 66 W, which is the lowest power that allows a stable operation of the laser beam source. This was done to reduce laser beam intensity in the process zone and, hence, the evaporation rate and the velocity of the consequent gas stream. This is supposed to reduce particle movement. The scan speed was varied between 200 mm/s (VED = 55 J/mm^3) and 100 mm/s (VED = 110 J/mm^3). Results for W 45 and Ta 45 are plotted in Figure 6. Nb 45 and Mo 45 are provided in Appendix A.

At equal VED (55 J/mm^3), the results at 200 mm/s and 66 W are comparable or only slightly better than the best results in series 1. With decreasing scan speed, and hence increasing VED, the number of undissolved particles drops, which is in good agreement with literature [15]. For W, the number of undissolved particles could be reduced by a factor of ten compared to the most unfavorable parameter combination (434 particles vs. 41). Interestingly, in contrast to series 1, the number of undissolved W particles is lower at a laser spot diameter of 100 µm than at 70 µm. This correlation is less clear for Ta, Mo, or Nb particles, since too few of those particles were detected to draw reliable conclusions. Apparently, two opposing effects are responsible for this observation. On the one hand, larger spot diameters reduce the strength of the vapor jet, and hence particle movement, as intended for experiment series 2. On the other hand, melt velocity is probably reduced due to less meltpool depression resulting from evaporation and a weaker Marangoni convection. In the present case, 100 µm spot diameter seems to be a good compromise between both effects, hence resulting in low numbers of undissolved particles.

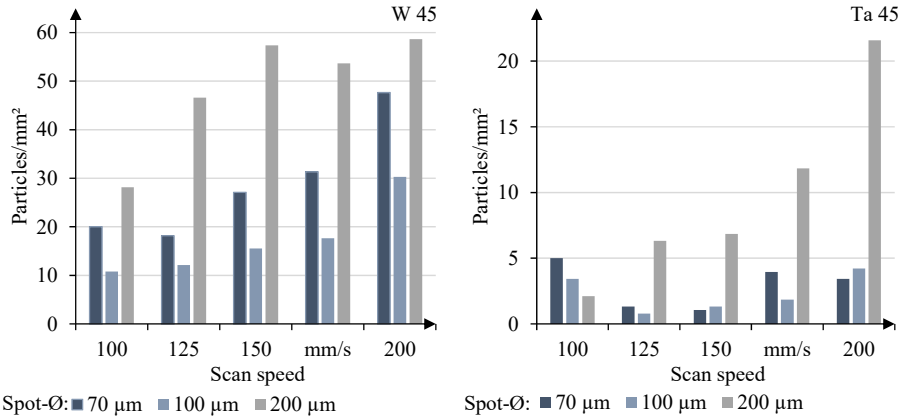

Figure 6. Results of experiment series 2 (see Table 2); constant laser power of 66 W; volumetric energy density scales with scan speed (110–55 J/mm^3).

Besides particle dissolution, a homogeneous distribution of alloying element in the material is crucial for in situ alloy formation. SEM-images shown in Figure 7 indicate that, even at equal VED and spot diameter, parameter combinations with a higher laser power/intensity and a higher scan speed result in a higher degree of homogenization due to increased mixing in the meltpool.

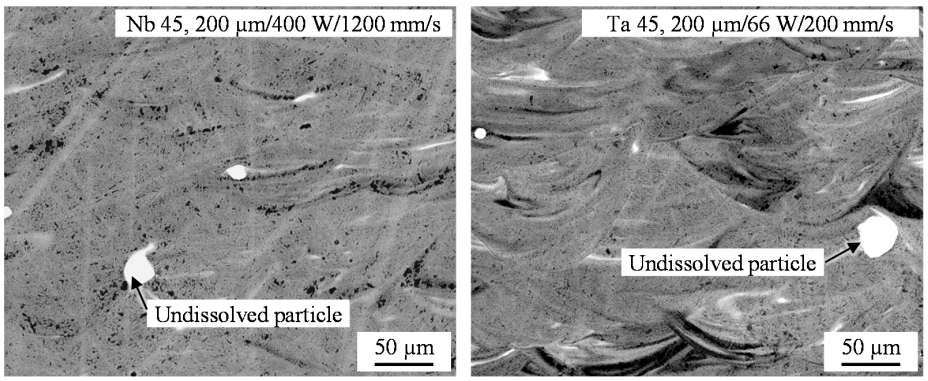

Figure 7. SEM-images of two samples from series 1 and series 2 (see Table 2) with equal volumetric energy density (VED) (55 J/mm^3); images recorded with equal SEM-settings (HV = 20 kV, I_A = 5.5 nA, CBS; FEI Helios Nanolab 600); flow marks clearly visible in the Ta 45 sample.

The low laser powder approach investigated by experiment series 2 proved to be beneficial in terms of particle dissolution but is less effective in terms of achieving a homogeneous element distribution. As a consequence, experiment series 3 was conceived to achieve good particle dissolution and improved homogenization. The hypothesis behind series 3 is that a double exposure can reduce the number of undissolved particles by two mechanisms. On the one hand, the material is melted a second time, hence increasing the average dwell time in the hot meltpool. This is also supposed to increase homogeneity of element distribution. On the other hand, a substantial number of high melting particles are already fixed inside the consolidated material during the second exposure and hence cannot be moved into the solidifying meltpool tail by the gas stream. A possible drawback of a double exposure is a higher degree of selective evaporation of elements with lower boiling point that would lead to deviations from the target concentration. This effect is described for electron beam melting, e.g., by reference [34], and is also observed for PBF-LB/M of Ti-6Al-4V in previous work [24]. Considering this, in addition to a simple repetition of identical PBF-LB/M parameters, a pre-melting step with low VED/laser beam intensity (500 µm spot diameter, 100 W laser power, 600 mm/s scan speed, 250 µm hatch) for powder fixation followed by the actual consolidation was introduced. Figure 8 shows a

microsection of a pre-melted layer with undissolved particles and incomplete fusion as a result of the low VED.

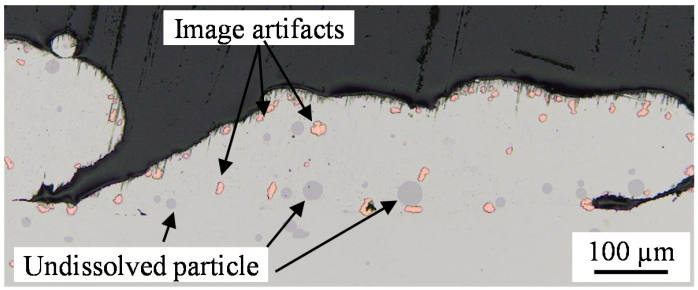

Figure 8. Pre-melted layer with low VED/laser beam intensity parameters set (500 µm spot diameter, 100 W laser power, 600 mm/s scan speed, 250 µm hatch, Ta 45).

Since little to no evaporation is expected during low laser beam intensity pre-melting, the loss of volatile elements should be approximately equal to single exposure, which could be advantageous for later in-situ alloying experiments. The results of experiment series 3 are plotted in Figure 9. Both double exposures perform equally well in terms of particle dissolution and are superior to single exposure with decreasing difference towards higher scan speeds. These findings further substantiate the assumption that particle incorporation in the meltpool tail is a main source of undissolved particles. Following the low-VED pre-melting step, few to zero particles are dissolved, but the powder is fixed in place (see Figure 8), and less particles can be dragged into the solidifying meltpool tail, during the actual layer consolidation with the second exposure. Since the sample size is small (5 mm cube) and the PBF-LB/M process is very dynamic, some degree of particle movement is still expected, which explains the remaining number of undissolved particles.

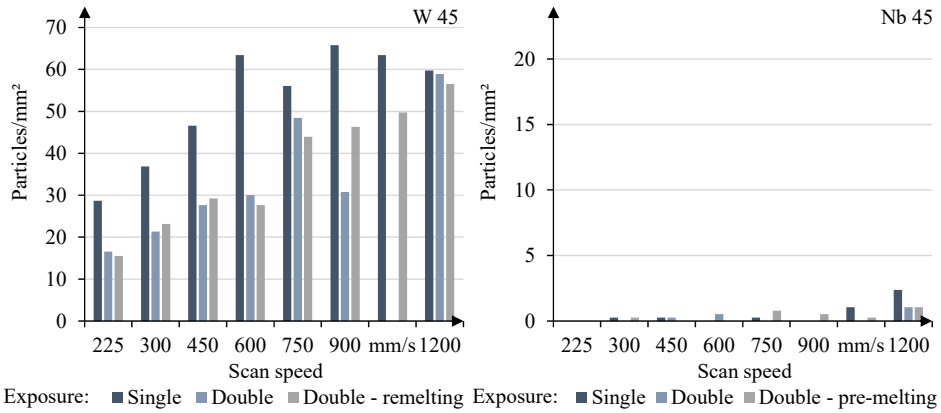

Figure 9. Results of experiment series 3 (see Table 2): single exposure, simple double exposure, double exposure with low VED pre-melting, laser power scales linearly with the scan speed (VED 55 J/mm^3), sample at 1050 mm/s not available.

4. Conclusions

The present work investigates the dissolution of high melting W, Ta, Mo, and Nb particles in a Ti matrix during the PBF-LB/M process. The following findings were obtained by own experiments and discussion with literature:

- The number of undissolved high melting particles in in-situ alloyed PBF-LB/M samples is affected by laser power, scan speed, spot diameter, and a double exposure.
- A higher volumetric energy density (VED), in general, decreases the number of undissolved particles, but the VED alone is insufficient to explain the complex interdependencies of PBF-LB/M process parameters.

- Powder movement by the gas stream in the vicinity of the PBF-LB/M process zone (denudation) was identified as a major source of undissolved high melting particles. Particles that are dragged into the colder, less turbulent, and already solidifying meltpool tail presumably cannot be dissolved anymore and remain in the material.
- Parameter combinations with low laser power and low scan speed proved to be beneficial for particle dissolution. The reasons are probably less powder movement, a shorter meltpool tail and a longer interaction time with the laser beam.
- Double exposure strategies can reduce the number of undissolved particles compared to single exposure. A low-VED pre-melting step for powder fixation proved to be equally effective in reducing the number of high melting particles than a simple double exposure with identical parameters.

In general, the number of remaining high melting particles could be at least reduced by a factor of ten compared to the least favorable parameter combination for W. In case of Mo and Nb, samples with a complete fusion of the high melting particles were obtained. These results can be of value for future research on in-situ alloy formation of Ti-based alloys, alike shape memory alloys, bulk metallic glasses, or compositionally complex alloys.

Author Contributions: Conceptualization, F.H.; methodology, F.H.; software, F.H.; investigation, F.H. and M.R.; writing—original draft preparation, F.H.; writing—review and editing, M.R. and M.S.; supervision, M.S.; funding acquisition, M.S. and F.H.; All authors have read and agreed to the published version of the manuscript.

Funding: This research was funded by the German Research Foundation (DFG), Collaborative Research Center 814, subproject B5 and A5 and the German Federal Ministry of Economic Affairs and Energy in the framework of the Aviation Research Program (LuFo V-3), project ADHEA.

Data Availability Statement: Not applicable.

Conflicts of Interest: The authors declare no conflict of interest.

Appendix A

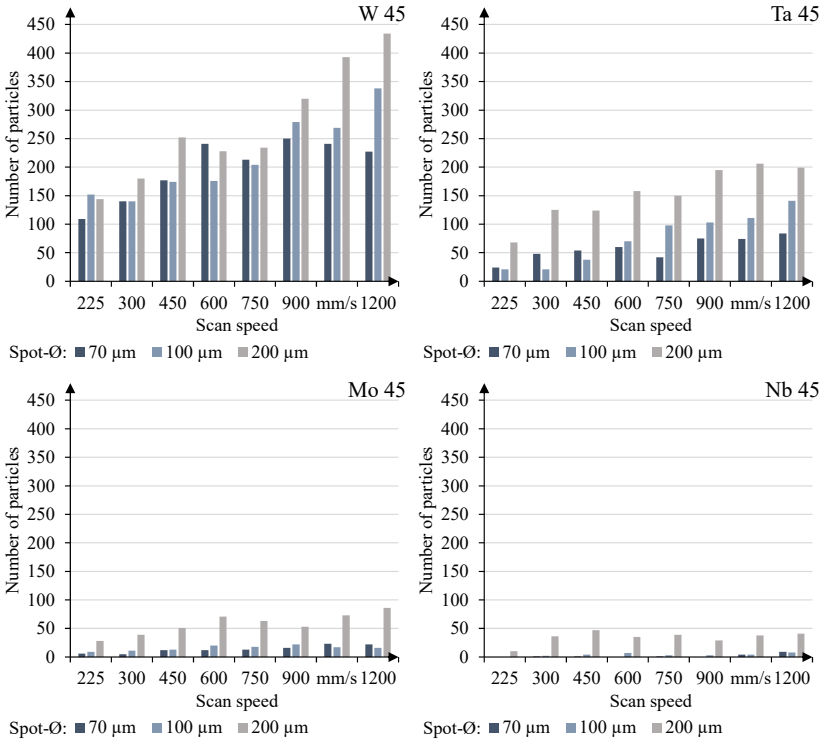

Figure A1. Results of experiments series 1 (also see Table 2); measurement area 3.8 mm^2.

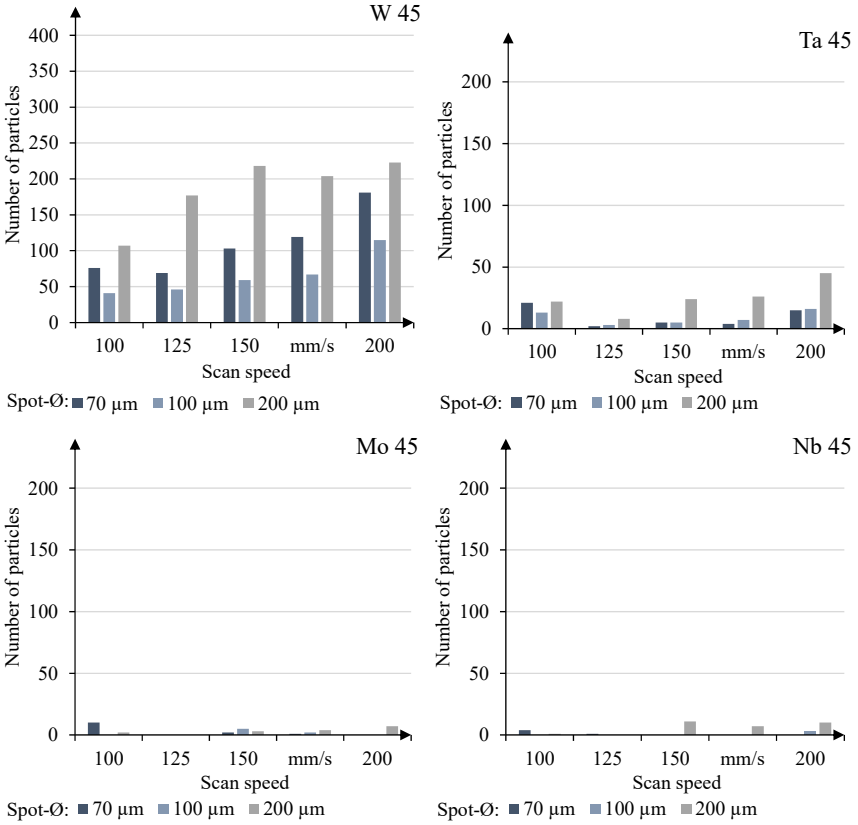

Figure A2. Results of experiments series 2 (also see Table 2); measurement area 3.8 mm^2.

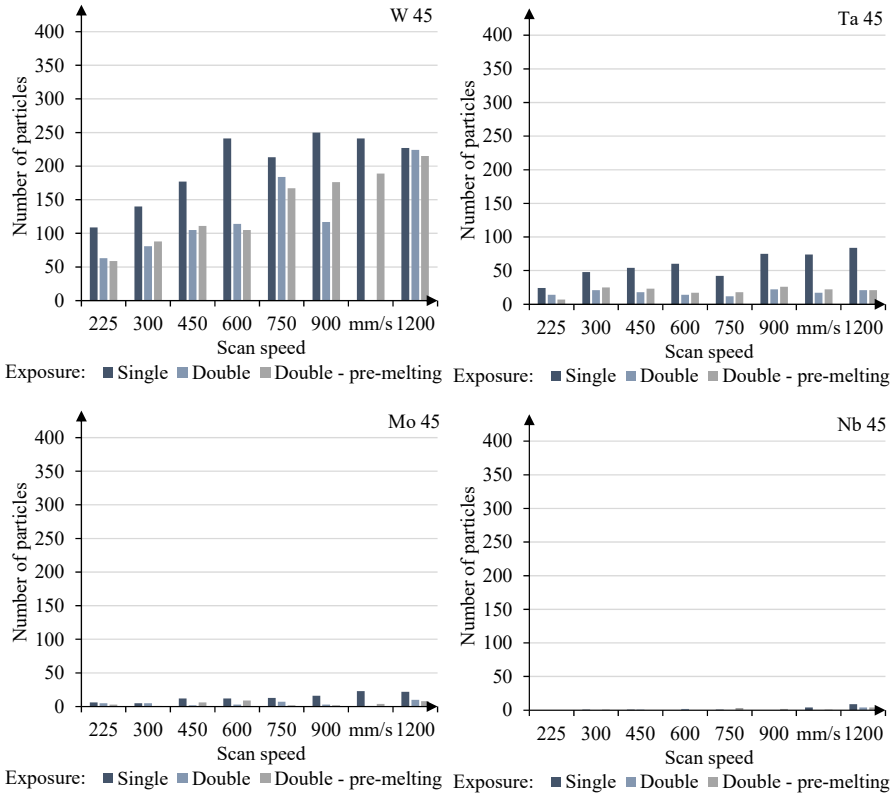

Figure A3. Results of experiments series 3 (also see Table 2); measurement area 3.8 mm^2.

References

1. Wohlers Associates, Inc. *Wohlers Associates Wohlers Report 2019*; Wohlers Associates, Inc.: Fort Collins, CO, USA, 2019; ISBN 978-0-9113332-5-7.
2. Schmidt, M.; Merklein, M.; Bourell, D.; Dimitrov, D.; Hausotte, T.; Wegener, K.; Overmeyer, L.; Vollertsen, F.; Levy, G.N. Laser based additive manufacturing in industry and academia. *CIRP Ann.* **2017**, *66*, 561–583. [CrossRef]
3. General Electric New manufacturing milestone: 30,000 additive fuel nozzles. Available online: https://www.ge.com/additive/blog/new-manufacturing-milestone-30000-additive-fuel-nozzles (accessed on 28 November 2018).
4. Liu, R.; Wang, Z.; Sparks, T.; Liou, F.; Newkirk, J. Aerospace applications of laser additive manufacturing. In *Laser Additive Manufacturing*; Elsevier: Amsterdam, The Netherlands, 2017; pp. 351–371.
5. EOS. GmbH Additive Manufacturing for Motor Sports. Available online: https://www.eos.info/en/3d-printing-examples-applications/mobility-logistics/automotive-industry-3d-printing/motor-sports (accessed on 8 February 2021).
6. Leal, R.; Barreiros, F.M.; Alves, L.; Romeiro, F.; Vasco, J.C.; Santos, M.; Marto, C. Additive manufacturing tooling for the automotive industry. *Int. J. Adv. Manuf. Technol.* **2017**, *92*, 1671–1676. [CrossRef]
7. Jang, T.-S.; Kim, D.; Han, G.; Yoon, C.-B.; Jung, H.-D. Powder based additive manufacturing for biomedical application of titanium and its alloys: A review. *Biomed. Eng. Lett.* **2020**, *10*, 505–516. [CrossRef] [PubMed]
8. Herzog, D.; Seyda, V.; Wycisk, E.; Emmelmann, C. Additive manufacturing of metals. *Acta Mater.* **2016**, *117*, 371–392. [CrossRef]
9. APWORKS. GmbH Scalmalloy. Available online: https://apworks.de/en/scalmalloy/ (accessed on 23 November 2020).
10. Hooper, P.A. Melt pool temperature and cooling rates in laser powder bed fusion. *Addit. Manuf.* **2018**, *22*, 548–559. [CrossRef]
11. Best, J.P.; Ostergaard, H.E.; Li, B.; Stolpe, M.; Yang, F.; Nomoto, K.; Hasib, M.T.; Muránsky, O.; Busch, R.; Li, X.; et al. Fracture and fatigue behaviour of a laser additive manufactured Zr-based bulk metallic glass. *Addit. Manuf.* **2020**, *36*, 101416. [CrossRef]
12. Agrawal, P.; Thapliyal, S.; Nene, S.; Mishra, R.; McWilliams, B.; Cho, K. Excellent strength-ductility synergy in metastable high entropy alloy by laser powder bed additive manufacturing. *Addit. Manuf.* **2020**, *32*, 101098. [CrossRef]
13. Huber, F.; Papke, T.; Scheitler, C.; Hanrieder, L.; Merklein, M.; Schmidt, M. In Situ Formation of a Metastable β-Ti Alloy by Laser Powder Bed Fusion (L-PBF) of Vanadium and Iron Modified Ti-6Al-4V. *Metals* **2018**, *8*, 1067. [CrossRef]
14. Aota, L.S.; Bajaj, P.; Sandim, H.R.Z.; Jägle, E.A. Laser Powder-Bed Fusion as an Alloy Development Tool: Parameter Selection for In-Situ Alloying Using Elemental Powders. *Materials* **2020**, *13*, 3922. [CrossRef]
15. Chen, P.; Li, S.; Zhou, Y.; Yan, M.; Attallah, M.M. Fabricating CoCrFeMnNi high entropy alloy via selective laser melting in-situ alloying. *J. Mater. Sci. Technol.* **2020**, *43*, 40–43. [CrossRef]
16. Yadroitsev, I.; Krakhmalev, P.; Yadroitsava, I. Titanium Alloys Manufactured by In Situ Alloying During Laser Powder Bed Fusion. *JOM* **2017**, *69*, 2725–2730. [CrossRef]
17. Haynes, W.M. *Handbook of Chemistry and Physics*; CRC Press: Boca Raton, FL, USA, 2017; ISBN 978-1-4987-5429-3.
18. Mosallanejad, M.; Niroumand, B.; Aversa, A.; Manfredi, D.; Saboori, A. Laser Powder Bed Fusion in-situ alloying of Ti-5%Cu alloy: Process-structure relationships. *J. Alloys Compd.* **2021**, *857*, 157558. [CrossRef]
19. Grigoriev, A.; Polozov, I.; Sufiiarov, V.; Popovich, A. In-situ synthesis of Ti2AlNb-based intermetallic alloy by selective laser melting. *J. Alloys Compd.* **2017**, *704*, 434–442. [CrossRef]
20. Polozov, I.; Sufiiarov, V.; Popovich, A.; Masaylo, D.; Grigoriev, A. Synthesis of Ti-5Al, Ti-6Al-7Nb, and Ti-22Al-25Nb alloys from elemental powders using powder-bed fusion additive manufacturing. *J. Alloys Compd.* **2018**, *763*, 436–445. [CrossRef]
21. Fischer, M.; Joguet, D.; Robin, G.; Peltier, L.; Laheurte, P. In situ elaboration of a binary Ti–26Nb alloy by selective laser melting of elemental titanium and niobium mixed powders. *Mater. Sci. Eng. C* **2016**, *62*, 852–859. [CrossRef] [PubMed]
22. Huang, S.; Sing, S.L.; De Looze, G.; Wilson, R.; Yeong, W.Y. Laser powder bed fusion of titanium-tantalum alloys: Compositions and designs for biomedical applications. *J. Mech. Behav. Biomed. Mater.* **2020**, *108*, 103775. [CrossRef] [PubMed]
23. Dzogbewu, T.C. Laser powder bed fusion of Ti15Mo. *Results Eng.* **2020**, *7*, 100155. [CrossRef]
24. Huber, F.; Papke, T.; Kerkien, M.; Tost, F.; Geyer, G.; Merklein, M.; Schmidt, M. Customized exposure strategies for manufacturing hybrid parts by combining laser beam melting and sheet metal forming. *J. Laser Appl.* **2019**, *31*, 022318. [CrossRef]
25. Ye, J.; Khairallah, S.A.; Rubenchik, A.M.; Crumb, M.F.; Guss, G.; Belak, J.; Matthews, M.J. Energy Coupling Mechanisms and Scaling Behavior Associated with Laser Powder Bed Fusion Additive Manufacturing. *Adv. Eng. Mater.* **2019**, *21*, 1–9. [CrossRef]
26. Heigel, J.C.; Lane, B.M.; Levine, L.E. In Situ Measurements of Melt-Pool Length and Cooling Rate During 3D Builds of the Metal AM-Bench Artifacts. *Integrating Mater. Manuf. Innov.* **2020**, *9*, 31–53. [CrossRef]
27. Matthews, M.J.; Guss, G.; Khairallah, S.A.; Rubenchik, A.M.; Depond, P.J.; King, W.E. Denudation of metal powder layers in laser powder bed fusion processes. *Acta Mater.* **2016**, *114*, 33–42. [CrossRef]
28. Khairallah, S.A.; Anderson, A.T.; Rubenchik, A.; King, W.E. Laser powder-bed fusion additive manufacturing: Physics of complex melt flow and formation mechanisms of pores, spatter, and denudation zones. *Acta Mater.* **2016**, *108*, 36–45. [CrossRef]
29. Caiazzo, F.; Alfieri, V.; Casalino, G. On the Relevance of Volumetric Energy Density in the Investigation of Inconel 718 Laser Powder Bed Fusion. *Materials* **2020**, *13*, 538. [CrossRef]
30. Ghazal, G.; Chapelle, P.; Jardy, A.; Jourdan, J.; Millet, Y. Dissolution of High Density Inclusions in Titanium Alloys. *ISIJ Int.* **2012**, *52*, 1–9. [CrossRef]
31. Eschner, E.; Staudt, T.; Schmidt, M. Correlation of spatter behavior and process zone formation in powder bed fusion of metals. *CIRP Ann.* **2020**, *69*, 209–212. [CrossRef]

32. Ly, S.; Rubenchik, A.M.; Khairallah, S.A.; Guss, G.; Matthews, M.J. Metal vapor micro-jet controls material redistribution in laser powder bed fusion additive manufacturing. *Sci. Rep.* **2017**, *7*, 1–12. [CrossRef] [PubMed]
33. Rasch, M.; Roider, C.; Kohl, S.; Strauß, J.; Maurer, N.; Nagulin, K.Y.; Schmidt, M. Shaped laser beam profiles for heat conduction welding of aluminium-copper alloys. *Opt. Lasers Eng.* **2019**, *115*, 179–189. [CrossRef]
34. Klassen, A.; Forster, V.E.; Juechter, V.; Körner, C. Numerical simulation of multi-component evaporation during selective electron beam melting of TiAl. J. *Mater. Process. Technol.* **2017**, *247*, 280–288. [CrossRef]

Additional unpublished results and discussion of the publication's findings in the context of this thesis:

Compared to conventional PBF-LB/M in-situ alloy formation adds an additional degree of difficulty as not only a dense part without common lack of fusion or deep penetration welding defects, but also a complete fusion of all particle fractions needs to be ensured. While chapter 4.1 provides a basic understanding of the effect of the PBF-LB/M process parameters on the resulting properties of Ti6Al4V parts manufactured from pre-alloyed powder, the publication *"Laser Powder Bed Fusion (PBF-LB/M) process strategies for in-situ alloy formation with high-melting elements"* [92] explicitly addresses the dissolution of high melting particles in a Ti-matrix during in-situ alloy formation by PBF-LB/M.

Achieving a full dissolution of all employed powder components is crucial for successful in-situ alloy formation. However, this is not trivial. Especially when the difference of the melting points of the respective alloying elements is large, undissolved high melting particles are commonly observed in literature. Considering findings on in-situ alloy formation reported in literature as well as own experiments, smaller differences in the melting points of the employed elemental powders cause almost no undissolved particles. For example, Aota et al. [98] report a full dissolution of mixtures of Fe, Ni and Cr powder, with Fe being the main alloying element. The melting points of the three elements are 1538 °C, 1455 °C and 1907 °C respectively [99], thus resulting in a difference of 369 K between the melting point of the main alloying element and the highest melting element Cr and 452 K between the melting points of the lowest melting and the highest melting element in the blend. Similar results were obtained by Chen et al. [100], who investigated in-situ alloy formation of a 3d transition metal high entropy alloy from Co, Cr, Fe, Mn and Ni. Also, the dissolution of Vanadium (melting point 1910 °C [99]) in a titanium matrix (melting point 1668 °C [99]) is possible without further measures [13]. Consequently, melting point differences in the range of approximately 300 – 450 K apparently do not impose severe difficulties in dissolving powder particles by PBF-LB/M during in-situ alloy formation.

Despite the low melting point of Al (660 °C [99]) Grigoriev et al. [101] also observed occurrence of undissolved Al-particles in a Ti-matrix. These are most likely attributed to the stable oxide shell surrounding the Al-particles that needs to be dissolved too. The melting point of Al_2O_3 is 2054 °C [102] and therefore considerably higher than the melting point of the Ti-matrix. High melting point differences in general increase the difficulty of in-situ alloy formation and cause undesired undissolved high melting particles in the PBF-LB/M parts. Further examples are Yadroitsev et al. [45], Grigoriev et al. [101] or Polozov et al. [103] who report undissolved Mo- or Nb-particles respectively remaining in the Ti-based matrix after PBF-LB/M and in-situ alloy formation. The melting point differences in these cases are 955 K for Ti-Mo and 809 K for Ti-Nb, respectively. By contrast, the findings in *"Laser Powder Bed Fusion (PBF-LB/M) process strategies for in-situ alloy formation with high-melting elements"* [92] demonstrate that a complete dissolution of Mo and Nb particles in a Ti-matrix by PBF-LB/M and in-situ alloys formation

is still possible, if suitable PBF-LB/M process strategies are employed. This finding was confirmed for Ti-Nb by *Huang et al.* who also successfully demonstrated nearly complete dissolution of Nb particles in a Ti-matrix [104]. They used a top hat laser beam profile instead of a Gaussian beam profile, which reduces peak intensity and probably process dynamics. The successful parameter combination included rather high laser power and a slow-moving laser spot [104]. Hence, their findings are in good agreement with the findings in *"Laser Powder Bed Fusion (PBF-LB/M) process strategies for in-situ alloy formation with high-melting elements"* [92]. For even higher melting point differences, no full dissolution of high melting particles could be achieved in [92]. However, the number of residual high melting particle inclusions can at least be minimized by adjusting the PBF-LB/M process strategy accordingly [92].

In summary, in-situ alloy formation of Ti-alloys with a complete dissolution of high melting particles is possible if melting point differences higher than approximately 450 K are avoided. Melting point differences in the range between 450 K and 955 K require adjusted PBF-LB/M process strategies. Differences greater than 955 K will most likely cause undissolved particle inclusions.

The previous discussion regarding melting point differences refers to powder blends comprising powders with an approximately equal particle size distribution. To increase the dissolution ratio of high melting particles, an obvious idea is to reduce the size of the high melting particles. An extreme case would be the application of nanoparticles. The effect of melting point depression of metallic nanoparticles is well known [105] and nanosized particles imply very small melting paths that need to be overcome to fully dissolve a particle. This would, in theory, be beneficial for in-situ alloy formation. However, nanoparticulate alloying elements are not considered in the framework of this thesis for the following two reasons: First, refractory metals like V or Nb in general have a high affinity for oxygen. Nanoparticulate powders possess a vast surface area that is available for reactions with the surrounding gas. This imposes a safety hazard and the oxygen intake can strongly affect the resulting properties of Ti-alloys [54], thus spoiling the results. A save and oxygen-free handling of metallic nanoparticulate powders would require elaborate equipment and prohibit a practical application of this work's results. Second, nanoparticles have a tendency to agglomerate and to impede recoatabilty of the powder blend when applied in higher concentrations. This limits the maximum amount of nanoparticles that can be deployed. Depending on the desired effect, this is in some cases acceptable. E.g. even small amounts of grain refining nanoparticles are highly effective in tuning the properties of Al-alloys [106] and the properties of additively manufactured steels are very sensitive to small additions of carbon nanoparticles [107]. However, considering typical Ti-alloys [64] or even more refractory metal high entropy alloys [108], which are subject of this work, higher amounts of alloying elements >> 5 wt.% are required. This prohibits the use of nanoparticles in this work. Consequently, only µm-sized particles are considered.

To investigate the effect of a size reduction of the high melting particles on the dissolution ratio, the experiments described in *"Laser Powder Bed Fusion (PBF-LB/M) process strategies for in-situ alloy formation with high-melting elements"* [92] are repeated with a W powder comprising particles with approximately half the median size of the W powder used in [92], but still in the µm scale. Table 4 contains the particles size distribution of the two W powders. The experimental procedure matches the one described in [92].

Table 4: Particle size distribution of the W powder used in [92] *and the smaller sized W powder used for the following experiments*

	D_{10}	D_{50}	D_{90}
W 45	18.6 µm	32.4 µm	40.2 µm
W 25	8.6 µm	14.0 µm	23.1 µm

As shown in Figure 10, the total number of undissolved W particles is higher, when working with the W 25 powder compared to the W 45 powder. However, a direct comparison of the absolute number of particles is misleading. Both powder mixtures comprise 10 vol.% W (based on solid material, not apparent density). This implicates, that the initial number of W 25 particles in the powder blend was about eight times higher (assuming half the particle size) compared to the W 45 blend. Inversely, eight residual particles in the W 25 sample approximately correspond to one W 45 in terms of undissolved W volume / mass. Pre-condition for the later statement is that the size relation between W 25 and W 45 is not severely altered during PBF-LB/M. Figure 10 and more detailed findings in [92], however, support that assumption.

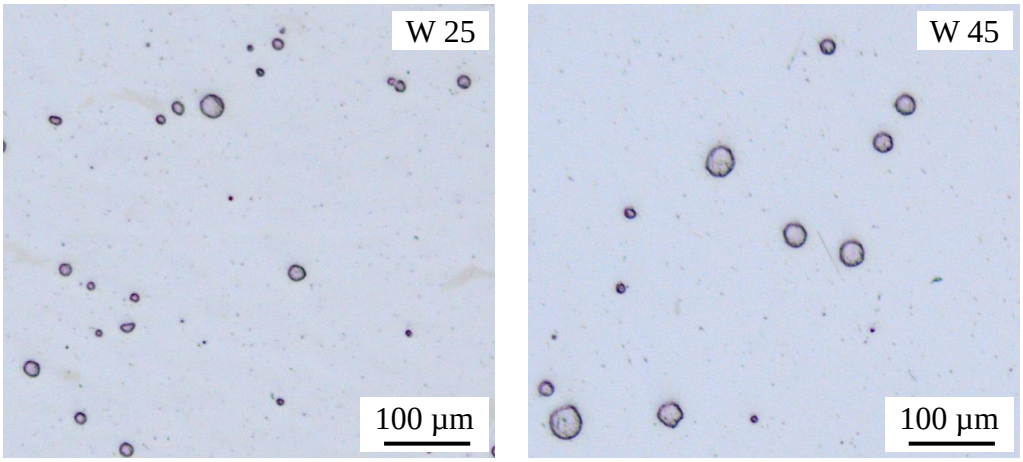

Figure 10: Undissolved W-particles in a Ti-matrix; 10 vol.% W in the powder blend; scan speed: 225 mm/s; laser power: 75 W; laser spot diameter: 70 µm; left: W-powder with a D_{50} of 14.0 µm; right: W-power with a D_{50} of 32.4 µm

To facilitate comparison between W 25 and W 45 the number of W particles counted in the W 25 samples is normalized to the median particle size of the W 45 powder by using equation (3):

(3) $$n_{norm}(W25) = n_{abs}(W25) \times \frac{D_{50}(W25)^3}{D_{50}(W45)^3}$$

According to Table 4, D_{50}(W25) = 14.0 µm and D_{50}(W45) = 32.4 µm. n_{abs} is the absolute number of W 25 particles and n_{norm} is the normalized number. The normalized number of undissolved W particles in a cross-section area of 3.8 mm² in W 25 and W 45 samples in dependence of the PBF-LB/M parameters are plotted in Figure 11. The normalized number of undissolved W 25 particles is considerably lower compared to the W 45 powder. This indicates that despite the higher absolute number of residual particles, a smaller particle size of the high melting particles increases the dissolution ratio in the matrix in terms of mass / volume. With respect to in-situ alloy formation, considerations regarding mass / volume of undissolved particles are in general more important than the absolute number of undissolved particles. In summary, the application of smaller particle fractions for in-situ alloy formation is considered beneficial, as long as powder recoatability and oxidation are not an issue.

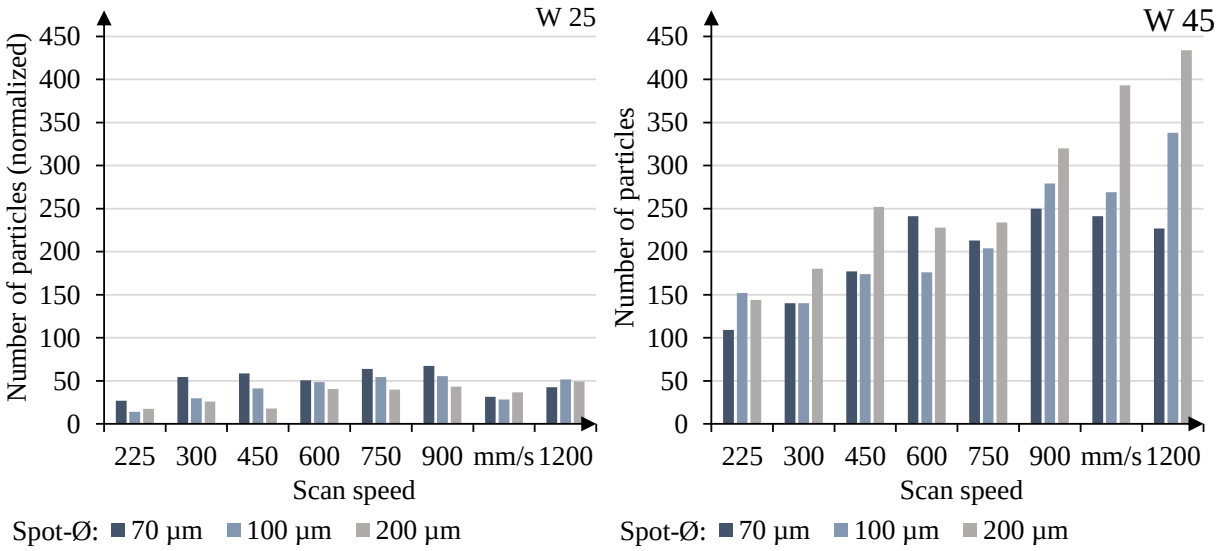

Figure 11: Number of undissolved W-particles in dependence of the PBF-LB/M parameter set and the particle diameter; measurement area 3.8 mm², constant volumetric energy density (55.6 J/mm³); laser power scales proportionally to the scan speed; number of particles in sample W 25 normalized to ensure comparability with sample W 45

When comparing the effect of the PBF-LB/M process parameters on the number of undissolved high melting particles, differences between W 25 and W 45 become visible (see Figure 10). The slowest scan speed of 225 mm/s at a laser power of 75 W still results in the lowest number of undissolved particles. However, in contrast to the W 45 experiments, the laser spot diameter of 70 µm has an adverse effect on particle dissolution when compared to a 100 µm or 200 µm spot diameter. This finding again stresses the conclusion drawn in [92] that the number of undissolved particles is subject to the complex interplay between PBF-LB/M parameter set, meltpool dynamics and powder movement in the process zone. As discussed in [92] it is assumed that two opposing effects affect the particle dissolution ratio:

First, a larger meltpool dimension, higher meltpool temperatures and increased melt velocity are beneficial for dissolution of high melting particles [109]. Consequently, high power, high speed and high laser intensity parameter sets would be preferable.

Second, powder movement in the process zone and so-called denudation [21] can lead to a deposition of high melting particles into the already solidifying and less turbulent meltpool tail, thus resulting in undissolved particles. Lower laser intensities, laser powers and accordingly reduced scan speeds reduce the powder movement [22] and also the meltpool length. Furthermore, lower scan speeds and laser powers change the angle of the vapor jet and hence the particle movement above the process zone to a more upward or even forward direction [20]. Altogether, this is assumed to reduce the chance that high melting particles are deposited into the meltpool tail and thus remain undissolved.

Figure 12 illustrates the findings on particle movement in the PBF-LB/M process zone based on own experiments and literature sources (e.g. [19]) The number of undissolved particles remaining in the PBF-LB/M part is assumed to be defined by the superposition of the two opposing main effects described above. Altering the average particle size and hence the particle mass affects the interaction between the gas jet above the process zone and the high melting particles. The velocity of the gas jet is probably severely affected by the laser intensity and hence the laser spot diameter. Changing the W powder from W 45 to W 25 apparently shifts the local minimum of residual unmolten W to the disadvantage of the 70 µm spot diameter to 100 µm or even 200 µm spot diameter.

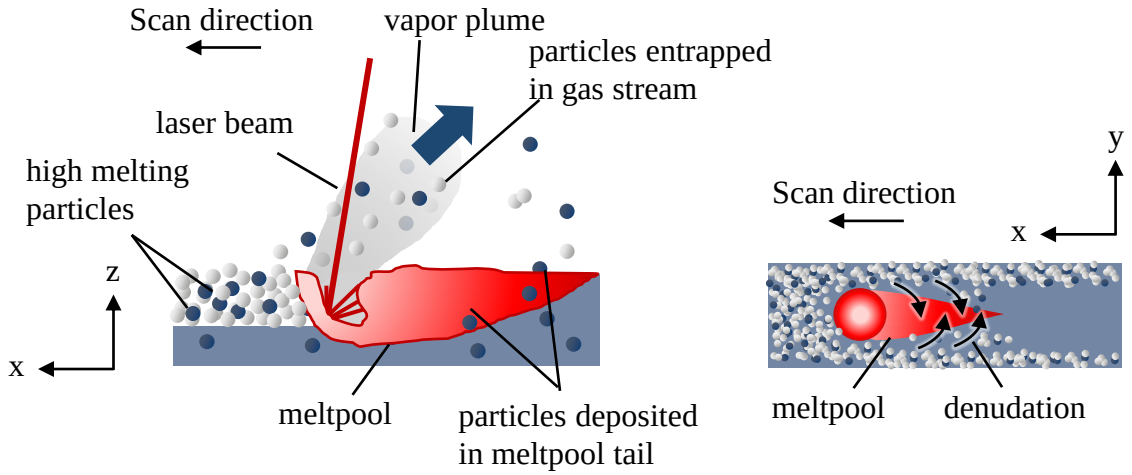

Figure 12: Schematics of particle entrainment and powder denudation phenomena related to the gas jet above the PBF-LB/M process zone; various sources: own experiments on dissolution of high melting particles [92], *simulation and high speed imaging of denudation and particle movement* [21], *multiphase flow simulation of denudation and spattering* [110], *simulation, high speed and schlieren imaging of particle dynamics in PBF-LB/M* [22]

The findings presented in *"Laser Powder Bed Fusion (PBF-LB/M) process strategies for in-situ alloy formation with high-melting elements"* [92] elucidate the interdependencies between the

powder and material properties, the PBF-LB/M parameter set and the number of undissolved particles following PBF-LB/M and in-situ alloy formation. This information is taken up in the following chapters 5 and 6 and is used for the selection of possible alloying elements for the modification of Ti-alloys and for the development of PBF-LB/M process strategies for the in-situ alloy formation of refractory metal high entropy alloys.

In summary the working hypothesis formulated in chapter 3 are confirmed by the investigations presented in chapter 4:

Discussion of initial hypotheses:

The number of undissolved high melting particles in LPB-LB/M samples produced by in-situ alloy formation is severely affected by the PBF-LB/M parameters scan speed, laser power, laser spot diameter and exposure pattern. The findings indicate that the complex interplay between meltpool dynamics, powder denudation and powder entrainment phenomena needs to be taken into account when developing suitable strategies to mitigate the occurrence of undissolved particles. Adjusted PBF-LB/M parameter sets and multiple exposures are found to be beneficial for the dissolution of high melting particles.

Besides the PBF-LB/M parameters, the thermo-physical properties of the elements applied are an important factor for the success of in-situ alloy formation. An estimate based on own experiments and literature sources suggests that complete dissolution of the powder particles during in-situ alloy formation is most likely to succeed when the melting point differences between the alloying elements are smaller than 450 K. Higher differences between 450 K and 955 K necessitate adjusted process strategies, while melting point differences greater than 955 K will most likely result in residual undissolved high melting particles in the PBF-LB/M part. However, the number of the undissolved inclusions can still be reduced by the adjusted process strategies.

Reducing the size of high melting particles used for in-situ alloy formation is considered beneficial. It is shown that a smaller median particle size reduces the amount of undissolved W in a Ti matrix in terms of mass / volume content. However, it is furthermore shown, that different particle sizes affect the interactions in the PBF-LB process zone. Hence, when developing PBF-LB/M parameter sets to mitigate occurrence of undissolved particles, the particle size distribution needs to be taken into account. Different particle size distributions of high melting alloying elements will necessitate slightly different PBF-LB/M parameter sets to minimize occurrence of undissolved high melting particles.

5 Modification of Ti-based alloys by in-situ alloy formation

5.1 In Situ Formation of a Metastable β-Ti Alloy by Laser Powder Bed Fusion (L-PBF) of Vanadium and Iron Modified Ti-6Al-4V

Published in Metals, 8 (2018)

Florian Huber[1,2,3], Thomas Papke[2,4], Christian Scheitler[1,2,3], Lukas Hanrieder[1], Marion Merklein[2,3,4] and Michael Schmidt[1,2,3]

[1] Institute of Photonic Technologies, Friedrich-Alexander Universität Erlangen-Nürnberg
[2] Collaborative Research Center 814 – Additive Manufacturing
[3] Erlangen Graduate School in Advanced Optical Technologies
[4] Institute of Manufacturing Technology, Friedrich-Alexander Universität Erlangen-Nürnberg

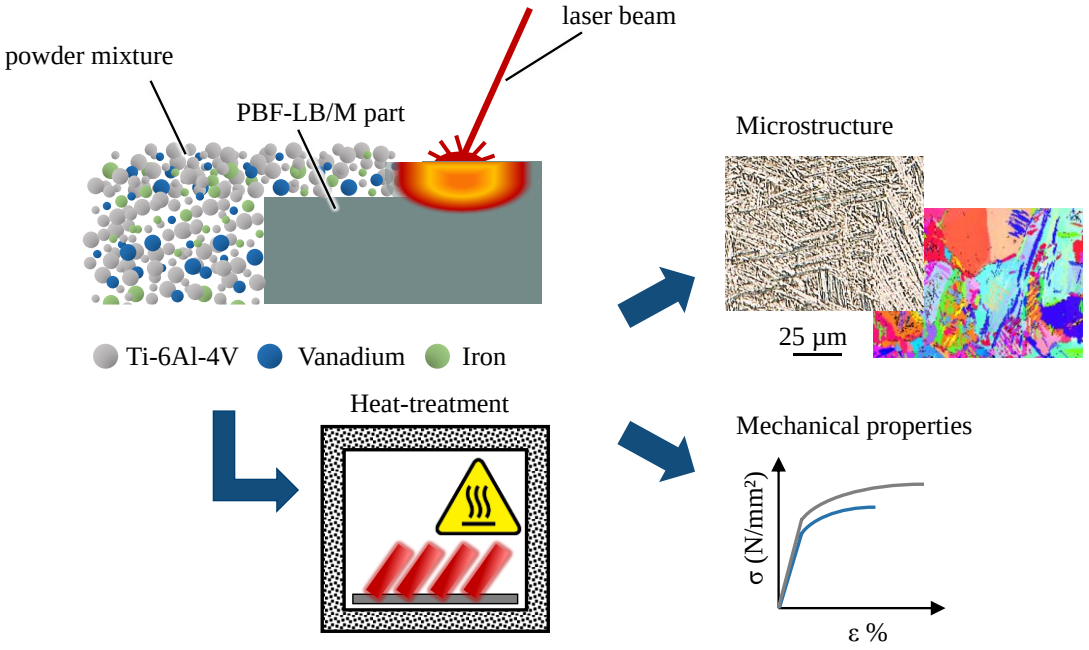

Highlights:

- Demonstrating the feasibility of modifying a Ti6Al4V base alloy by addition of β-phase stabilizers via in-situ alloy formation and PBF-LB/M
- Homogeneous α/β microstructure with a β-phase content > 60 % obtained by PBF-LB compared to a pure α'-martensitic structure when using unmodified Ti6Al4V
- Considerably increase in ductility compared to pure Ti6Al4V
- High cooling rates (~10^6 K/s) inherent to PBF-LB/M contribute to a higher ratio of metastable β-phase compared to furnace cooling with slower cooling rates (~10 K/s)
- Confirmation of the suitability of the elements V and Fe for in-situ alloy formation with Ti6Al4V and the potential to alter the resulting material properties in a wide range
- Investigation of the effect of different heat-treatments on the material properties
- In Situ Formation of a Metastable -Ti Alloy by Laser Powder Bed Fusion (L-PBF) of Vanadium and Iron Modified Ti-6Al-4V

metals

MDPI

Article

In Situ Formation of a Metastable β-Ti Alloy by Laser Powder Bed Fusion (L-PBF) of Vanadium and Iron Modified Ti-6Al-4V

Florian Huber [1,2,3,*], Thomas Papke [3,4], Christian Scheitler [1,2,3], Lukas Hanrieder [1], Marion Merklein [3,4] and Michael Schmidt [1,2,3]

1 Institute of Photonic Technologies, Friedrich-Alexander-University Erlangen-Nürnberg (FAU), Konrad-Zuse-Straße 3/5, 91052 Erlangen, Germany; sekretariat@lpt.uni-erlangen.de (C.S. & L.H. & M.S.)
2 Erlangen Graduate School in Advanced Optical Technologies (SAOT), Paul-Gordan-Straße 6, 91052 Erlangen, Germany
3 Collaborative Research Center 814—Additive Manufacturing, Am Weichselgarten 8, 91058 Erlangen, Germany; thomas.papke@fau.de (T.P.); sabine.wittmann@fau.de (M.M.)
4 Institute of Manufacturing Technology, Friedrich-Alexander-University Erlangen-Nürnberg (FAU), Egerlandstraße 11–13, 91058 Erlangen, Germany
* Correspondence: florian.huber@lpt.uni-erlangen.de; Tel.: +49-09131-85-23241

Received: 27 November 2018; Accepted: 13 December 2018; Published: 14 December 2018

Abstract: The aim of this work is to investigate the β-Ti-phase-stabilizing effect of vanadium and iron added to Ti-6Al-4V powder by means of heterogeneous powder mixtures and in situ alloy-formation during laser powder bed fusion (L-PBF). The resulting microstructure was analyzed by metallographic methods, scanning electron microscopy (SEM), and electron backscatter diffraction (EBSD). The mechanical properties were characterized by compression tests, both prior to and after heat-treating. Energy dispersive X-ray spectroscopy showed a homogeneous element distribution, proving the feasibility of in situ alloying by LPBF. Due to the β-phase-stabilizing effect of V and Fe added to Ti-6Al-4V, instead of an α'-martensitic microstructure, an α/β-microstructure containing at least 63.8% β-phase develops. Depending on the post L-PBF heat-treatment, either an increased upsetting at failure (33.9%) compared to unmodified Ti-6Al-4V (28.8%), or an exceptional high compressive yield strength (1857 ± 35 MPa compared to 1100 MPa) were measured. The hardness of the in situ alloyed material ranges from 336 ± 7 HV0.5, in as-built condition, to 543 ± 13 HV0.5 after precipitation-hardening. Hence, the range of achievable mechanical properties in dependence of the post-L-PBF heat-treatment can be significantly expanded in comparison to unmodified Ti-6Al-4V, thus providing increased flexibility for additive manufacturing of titanium parts.

Keywords: laser powder bed fusion (L-PBF); additive manufacturing; titanium alloys; microstructure; compression test

1. Introduction

Laser powder bed fusion (L-PBF), also referred to as selective laser melting (SLM) or laser beam melting (LBM), is currently the most widely used technique for additive manufacturing of metals [1]. Figure 1 shows a basic schematic of the process. Especially for demanding applications, e.g., in the aerospace industry [2] or for medical implants [3] titanium alloys are of particular interest. The most important titanium alloy for L-PBF applications is Ti-6Al-4V [4]. L-PBF of Ti-6Al-4V is, in general, well understood and standard parameter sets are available for numerous commercial L-PBF systems (e.g., EOS M 290 [5] or SLM 280 [6]). Recent scientific publications focus, for example, on the microstructure evolution [7] or the fatigue behavior [8] of Ti-6Al-4V processed by L-PBF. However,

the usage of alternative titanium alloys for L-PBF is rather uncommon. Reasons for this are an elaborate development of process parameters for new alloys and the limited availability of suitable pre-alloyed powders as starting material for L-PBF. The atomization of special alloys on demand is possible, but generally linked with high costs. One approach for developing new Ti alloys for L-PBF is in situ alloying from heterogeneous powder mixtures made from commercially available standard powders. Aiming for an increased wear resistance, Gu [9] reported a similar approach for producing metal matrix composites. For this purpose, SiC and commercially pure Ti powder were blended using a ball mill. After L-PBF, the resulting parts showed an elevated microhardness (>980 HV0.3) and wear resistance in comparison to pure Ti. With respect to antibacterial properties, Macpherson et al. [10] published a study on adding Cu and Ag to Ti-6Al-4V by in situ alloying. Energy dispersive X-ray spectroscopy (EDS) measurements showed a homogeneous distribution of the added elements after L-PBF. Also motivated by medical applications, Sing et al. [11] investigated in situ alloying of Ti with 50 wt % Ta, and showed that a microstructure predominantly consisting of β-phase evolved. However, no heat-treatments were performed to adjust the mechanical properties and to remove the internal stress induced during L-PBF, and the homogeneity of the element distribution after L-PBF was partly not investigated. Furthermore, with respect to load-bearing applications, e.g., in the aerospace industry, alloy compositions different than those described in the abovementioned works, are required. Due to their exceptional mechanical properties and, especially, their high cycle fatigue strength, metastable β-Ti alloys, like Ti-10V-2Fe-3Al, are becoming increasingly important for aircraft parts [12]. Thus, aim of this work is to investigate the modification of Ti-6Al-4V with the β-phase-stabilizing elements, V and Fe, by means of heterogeneous powder mixtures and in situ alloying during L-PBF. Following L-PBF, different heat-treatments were conceived and applied to the in situ alloyed samples. Subsequently, the resulting element distribution, as a criterion for a successful in situ alloy formation, as well as the microstructure and the mechanical properties, were analyzed.

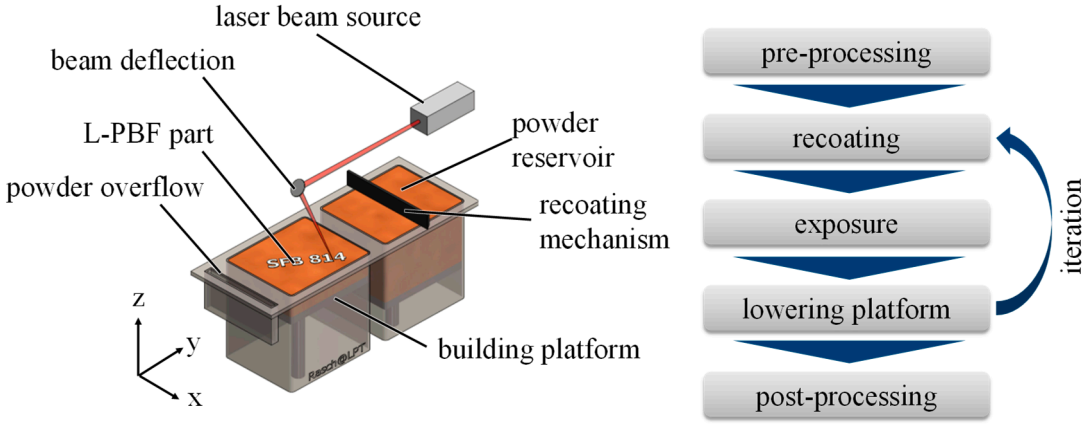

Figure 1. Schematic of the L-PBF process.

2. Materials and Methods

The predominantly spherical Ti-6Al-4V with a particle size distribution of 15–45 µm, used in this work, was obtained from AP&C Advanced Powders and Coatings Inc. (Boisbriand, QC, Canada). The irregular-shaped V and Fe powders, also with a nominal particle size distribution of <45 µm, were provided by PMCtec GmbH (Leun Germany) and NMD GmbH (Heemsen, Germany), respectively. The chemical composition of the powders was analyzed by EDS and are listed in Table 1. Figure 2 shows scanning electron images (SEM) of the powders. For the L-PBF experiments, the Ti-6Al-4V powder was blended with commercially pure Fe and V powder (ratio: 91.67 Ti-6Al-4V/2.00 Fe/6.33 V). The mixing procedure was experimentally developed and comprises vibration sieving to break up potential agglomerates, and subsequent mixing for two hours in a Turbula®-mixer from Willy A. Bachofen AG (Muttenz, Switzerland). The intention was to achieve a relative element

distribution throughout the heterogeneous powder mixture close to the commercial metastable β-alloy Ti-10V-2Fe-3Al. Since an exact Al concentration of the target alloy is not achievable by adding Fe and V to Ti-6Al-4V powder, the resulting nominal elemental distribution is 82.5 Ti/10 V/2 Fe/5.5 Al and, therefore, shows a slightly higher aluminum content than the target alloy. Despite the non-spherical particle shape of the Fe and V powders, the powder system obtained from the mixing procedure can be recoated to homogeneous layers without significant imperfections. This was verified visually by an illumination setup and a high-resolution camera.

Table 1. Chemical composition of the powder batches used in this study determined by EDS analysis.

Material	Ti	Al	V	Fe	Si
Specification Ti-6Al-4V (wt %) [13]	bal.	5.5–6.75	3.5–4.5	0.0–0.3	-
Ti-6Al-4V (wt %)	89.3	6.3	4.2	0.2	-
Fe (wt %)	-	-	-	99.8	0.1
V (wt %)	-	-	99.9	-	-
standard deviation < 0.1 wt %					

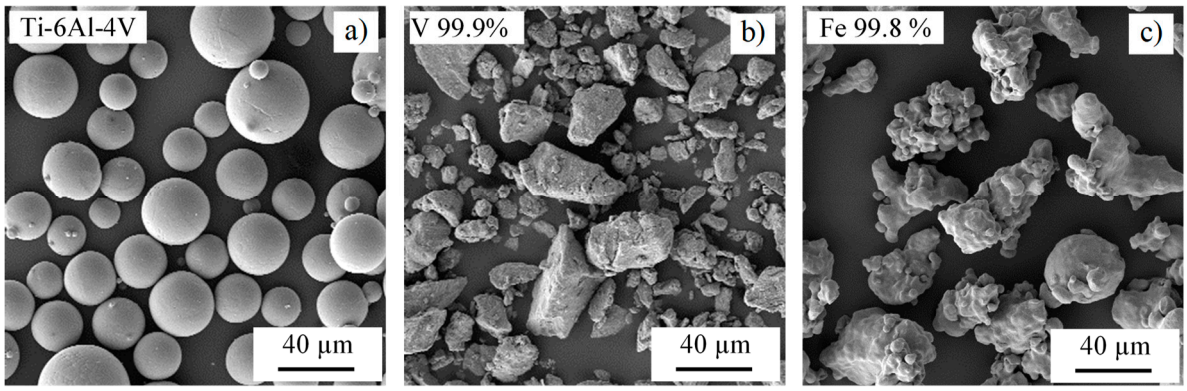

Figure 2. SEM images of the powders used in this work: (**a**) Ti-6Al-4V powder, (**b**) V powder, (**c**) Fe powder.

To analyze the effect of the addition of V and Fe to Ti-6Al-4V by in situ alloying on the microstructure and the mechanical properties, 30 cylindrical samples with the dimensions Ø 7.5 mm × 19 mm were manufactured using a SLM 50 L-PBF-machine from Realizer GmbH (Borchen, Germany). Eighteen samples were built with Ti-6Al-4V powder modified with V and Fe, while 12 samples have been built with non-modified Ti-6Al-4V powder as reference group. The parameter sets used for manufacturing the specimens are listed in Table 2. The parameters were experimentally developed and facilitate the production of parts with relative densities above 99.9%. For each powder material, the parameter set facilitating the highest relative densities was selected from a series of 36 test samples, that were built with varying scan speeds (300, 600, and 900 mm/s), spot diameters (40 and 70 µm), and hatch distances (60, 90, and 120 µm). The highest relative densities for the Ti-6Al-4V + 2Fe + 6V powder mixture are achievable with a reduced spot diameter compared to unmodified Ti-6Al-4V. This is probably due to the altered chemical composition.

Table 2. Parameter sets used for manufacturing the samples.

Material	Laser Power	Scan Speed	Spot Diameter	Hatch Distance	Layer Thickness
Ti-6Al-4V	100 W	600 mm/s	70 µm	60 µm	30 µm
Ti-6Al-4V + 2Fe + 6V	100 W	600 mm/s	40 µm	60 µm	30 µm

Following the L-PBF process, a group of six samples of each material was heat-treated at 850 °C for two hours, and cooled in the furnace. This heat-treatment, which was developed for Ti-6Al-4V from L-PBF, was derived from Vrancken et al. [14], and also applied in previous work [15]. All heat-treatments were performed in a furnace constantly flushed with argon to reduce oxidation and oxygen absorption. Furthermore, an additional heat-treatment for a group of six Ti-6Al-4V + 2Fe + 6V samples was conceived. It comprised a solution heat-treatment at 1050 °C (above β-transus temperature) for 20 min, followed by water quenching and annealing at 500 °C for eight hours. These values were partially derived from [12]. The intention of this heat-treatment is to dissolve the microstructure developed during L-PBF by the occurring phase transition related to the temperatures above β-transus temperature, and the subsequent water quenching. For achieving a strengthening effect, the homogeneous precipitation of fine dispersed α-phase within the β-phase matrix by the annealing at 500 °C is proposed. The heat-treatments used in this work are summed up in Table 3. The S 1050 °C + PH heat-treatment was not applied to the unmodified Ti-6Al-4V reference samples, since, without the presumed β-phase-stabilizing effect of the Fe and V addition, the formation of α'-martensite, instead of β-phase, that would be required for the precipitation-hardening after water quenching, is to be expected.

Table 3. Heat-treatments applied to the specimens.

AN 850 °C	Annealed at 850 °C, 2 h
S 1050 °C + PH	Solution heat-treated at 1050 °C, 20 min; water quenched; precipitation-hardened at 500 °C, 8 h

The resulting microstructure in dependence of the alloy composition and the heat-treatment condition was characterized by analyzing metallographically prepared cross-sections by means of EDS, scanning electron imaging (SEM), and electron backscatter diffraction (EDSB). For this purpose, the specimens were grinded and polished with 3 µm diamond suspension, followed by a polishing step with active oxide polishing suspension (OPS) and hydrogen peroxide. To reveal the microstructure, the samples were cleaned in an ultrasonic bath and etched with Kroll's reagent (H_2O, HNO_3, HF) for 8 s and investigated by optical microscopy. The mechanical properties were characterized by compression tests and hardness measurements. The microhardness was measured using a KB 30 S device from Hegewald & Peschke Meß- und Prüftechnik GmbH (Nossen, Germany). For determining the compression properties, five samples of each group have been processed to specimens with the dimensions Ø 6 mm × 9 mm by successive turn-milling and grinding. Further information on the experimental setup is given in prior work [16]. The tests were performed in accordance with DIN 50106 [17].

3. Results and Discussion

One criterion for the success of the in situ alloying approach, by means of heterogeneous powder mixtures and L-PBF, is to accomplish the desired elemental distribution homogeneously throughout the L-PBF part. This was investigated by EDS. As shown in Figure 3, after annealing at 850 °C, only minor inhomogeneity is visible, and the elements are evenly distributed across the part. The original powder particles with a size of 1 to 45 µm are completely fused and mixed, and no unmelted areas consisting of pure V, Fe, or Ti-6Al-4V are visible. A significant demixing effect of the powder particles during powder handling or recoating was not observed, as the element concentration in the resulting parts was found to be homogeneous. The resulting alloying element concentration was determined to be 81.9 ± 0.06 wt % titanium, 10.8 ± 0.05 wt % vanadium, 2.0 ± 0.03 wt % iron, and 5.2 ± 0.06 wt % aluminum, and is therefore close to the expected 82.5 Ti/10 V/2 Fe/5.5 Al composition. The slightly lower amount of aluminum, in comparison to the calculated value of 5.5 wt %, presumably originates from aluminum evaporation during L-PBF, that was also observed in previous work [18]. The EDS results demonstrate the general feasibility of in situ alloying for developing new Ti alloys for L-PBF applications.

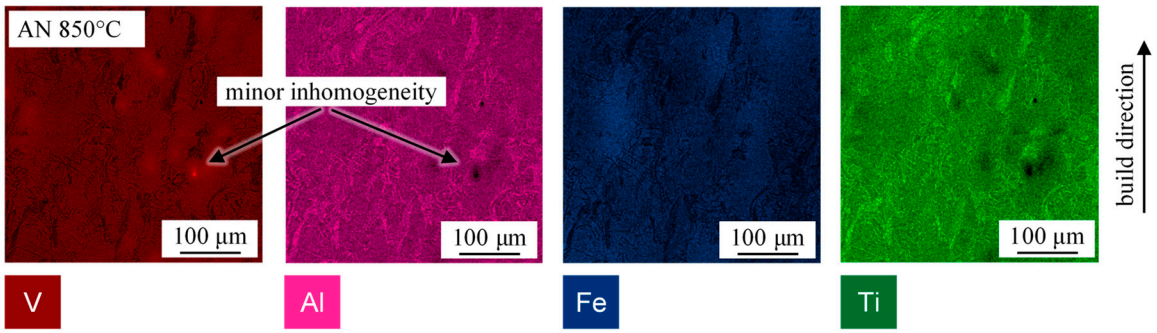

Figure 3. EDS analysis of the in situ alloyed Ti-6Al-4V + 2Fe + 6V material; from left to right: elemental mapping for the elements V, Al, Fe, and Ti.

The resulting microstructure in dependence of the alloy composition and the heat-treatment is shown in Figure 4. In as-built condition, the Ti-6Al-4V reference samples consist of an α'-martensitic microstructure with elongated, columnar prior β-grains, and a hardness of 424 ± 11 HV0.5. The α'-martensite is formed due to the high cooling rates in the range of 106 K/s [19], that are related to the L-PBF process. This is well in accordance with literature (e.g., [20]). A heat-treatment at 850 °C leads to a decomposition of the α'-martensite into fine acicular α-phase surrounded by β-phase, while the prior β-grains remain visible, since the β-transus temperature of Ti-6Al-4V at around 960 °C [12] is not exceeded. The hardness is reduced to 364 ± 14 HV0.5, due to the change in microstructure. The amount of β-phase was determined to be 15% by EBSD measurements.

V and Fe addition to Ti-6Al-4V, by means of in situ alloying, results in a significant change in the microstructure compared to unmodified Ti-6Al-4V reference samples. No α'-martensite is formed during L-PBF of the in situ alloyed samples, and the hardness is with 336 ± 7 HV0.5, significantly lower than the hardness of the unmodified alloy in as-built condition, with 424 ± 11 HV0.5. Instead, a microstructure consisting of intertwined α- and β-grains evolves (Figures 4 and 5). EBSD measurements show the presence of at least 63.8% β-phase and 26.6% α-phase (9.6% unresolved areas, presumed to be predominantly α-phase) in as-built condition. The β-phase-stabilizing effect of the elements V and Fe [12] can, therefore, be confirmed for the L-PBF process.

Heat-treatment of the Ti-6Al-4V + 2Fe + 6V samples at 850 °C results in cellular β-grains with α-phase located at the grain boundaries and acicular α-phase platelets inside the β-grains (Figures 4 and 5). Due to the microstructural changes, it is assumed that a complete phase transition takes place during the 850 °C heat-treatment, and the as-built microstructure is dissolved. This indicates that the β-transus temperature of the in situ alloyed material is reduced below 850 °C by the β-phase-stabilizing effect the alloying elements V and Fe (see also β-transus temperature of the commercial alloy Ti-10V-2Fe-3Al at 800 °C [21]). During the subsequent cooling, from 850 °C to room temperature in the furnace, a more equilibrium material state evolves than during the L-PBF process, that comprises cooling rates in the range of 106 K/s [19]. Due to the lower cooling rates, slightly less β-phase with a share of 57.8% is obtained after the 850 °C heat-treatment, than directly after L-PBF. Solution heat-treatment at 1050 °C, and subsequent water quenching and precipitation heat-treatment leads, as intended, to very fine, homogeneously distributed nm-scale α-precipitations inside cellular β-grains (Figures 4 and 5). The very high hardness of 534 ± 13 HV0.5, measured for the sample, presumably originates from these precipitations, and indicates a high mechanical strength.

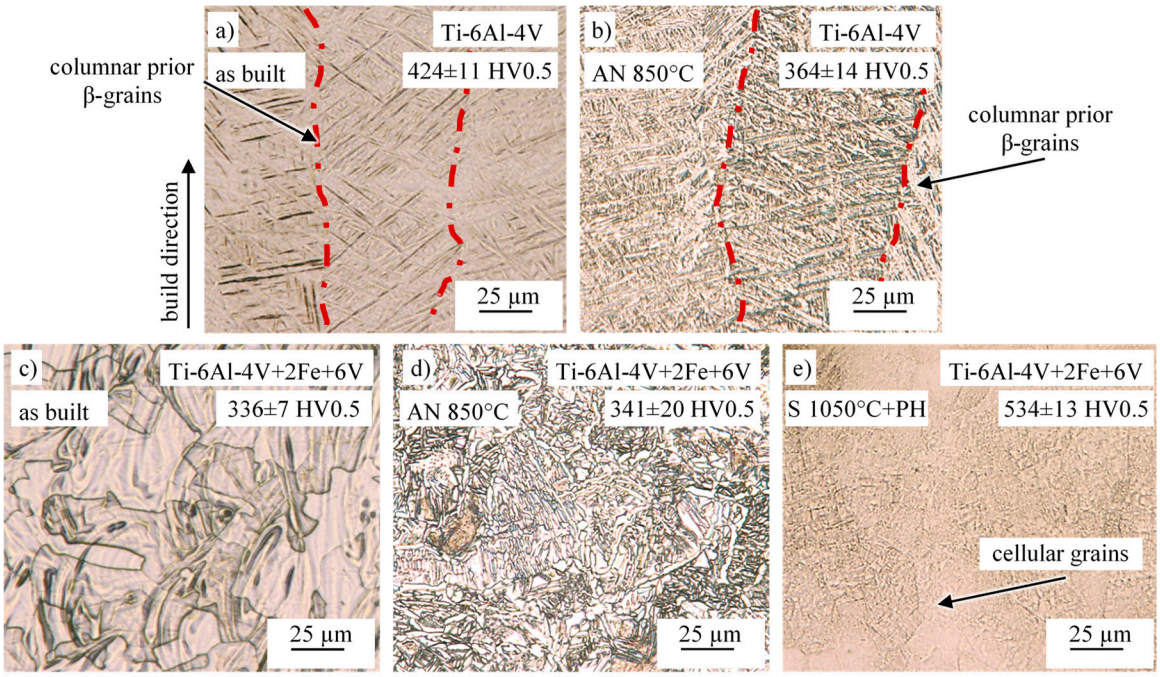

Figure 4. Resulting microstructure and microhardness (n = 8) in dependence of the alloy composition and the heat-treatment (oxide polishing suspension (OPS)-polished and etched with Kroll's reagent): (**a**) Ti-6Al-4V as-built, (**b**) Ti-6Al-4V heat-treated at 850 °C, (**c**) Ti-6Al-4V + 2Fe + 6V as-built, (**d**) Ti-6Al-4V + 2Fe + 6V heat-treated at 850 °C, (**e**) Ti-6Al-4V + 2Fe + 6V solution heat-treated at 1050 °C and precipitation-hardened.

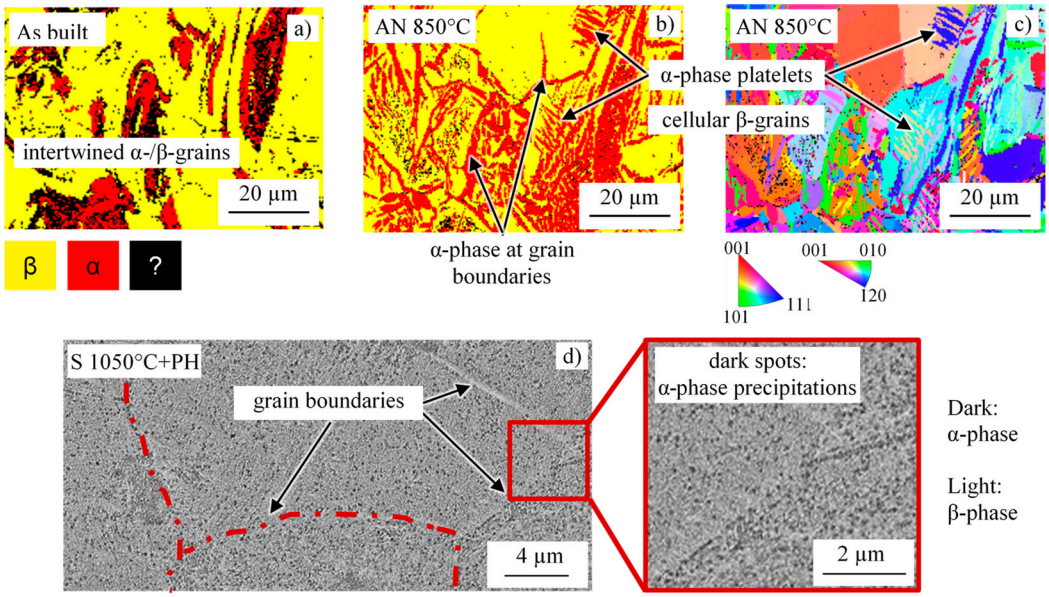

Figure 5. (**a**,**b**): EBSD phase-mapping, (**c**): EBSD inverse pole figure (ipf) map corresponding to (**b**,**d**): SEM images of the in situ alloyed Ti-6Al-4V + 2Fe + 6V samples.

The effect of in situ alloying and the heat-treatments on the mechanical properties of the material was investigated by compression tests. The resulting mean compressive yield stresses ($\sigma_{d0.2}$) out of five samples, which are evaluated at a plastic upsetting of 0.2%, are shown in Figure 6 (left). Furthermore, $\varepsilon_{dtM,min}$, representing the minimal upsetting at failure measured in each group of five samples, is plotted in Figure 6 (right). The failure is characterized by the break of the specimen under pressure load. In as-built condition, the Ti-6Al-4V + 2Fe + 6V material reaches a slightly lower yield strength

than the Ti-6Al-4V reference group, but the minimal upsetting at failure increases from 17.2% to 25.2% as a consequence of the in situ alloying. The 850 °C heat-treatment increases the minimal upsetting at failure for pure Ti-6Al-4V, as well as for the modified alloy, due to microstructural changes shown in Figures 4 and 5. The in situ alloyed and 850 °C heat-treated samples again show a higher upsetting at break of 33.9% compared to 25.2% of the Ti-6Al-4V reference group. This behavior can be explained by the increased amount of β-phase (from 15% to 58%) resulting from in situ alloying with the β-phase-stabilizing elements V and Fe (Figure 5). The β-phase provides a higher amount of slip planes due to its body-centered cubic (bcc) structure in comparison to the hexagonal close-packed (hcp) structure of the α-phase [12] and, therefore, the ductility and, hence, the upsetting at fracture increases.

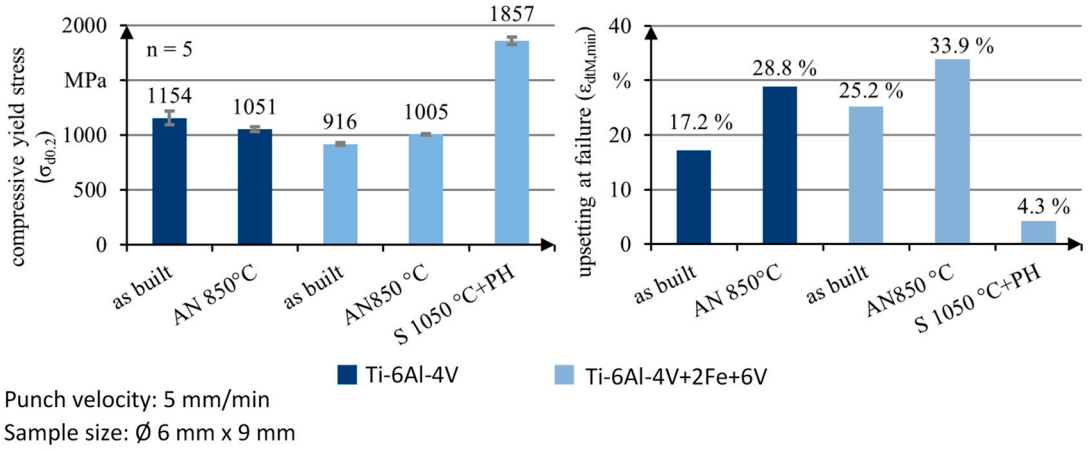

Figure 6. Compressive yield stress and minimal upsetting at failure out of five samples in dependence of the alloy composition and the heat-treatment. (**Left**): compressive yield stress; (**right**): upsetting at failure.

In contrast to that, the 1050 °C heat-treatment results in an exceptional high compressive yield stress of 1857 ± 35 MPa for the in situ alloyed Ti-6Al-4V + 2Fe + 6V samples. This value significantly surpasses Ti-6Al-4V and, also, the commercial alloy Ti-10V-2Fe-3Al at a similar heat-treatment state with a compressive yield stress of 1145 MPa [21]. This is probably related to the strengthening effect of the nm-scale α-precipitations observed in Figure 5. A possible explanation for the higher compressive yield stress in comparison to Ti-10V-2Fe-3Al is the α-phase-stabilizing effect of the higher amount of aluminum of the in situ alloyed Ti-6Al-4V + 2Fe + 6V material. Additionally, oxygen, that might have been taken up during L-PBF, could act as α-phase stabilizer. This could possibly lead to an increased amount of α-phase precipitations compared to forged and heat-treated commercial Ti-10V-2Fe-3Al, and might explain the elevated compressive yield stress. However, the upsetting at fracture of the 1050 °C heat-treated Ti-6Al-4V + 2Fe + 6V shows a comparable low value of 4.3%, which is significantly below the values measured for Ti-6Al-4V, but is in good agreement with an elongation at break of 4.0% specified for the commercial alloy Ti-10V-2Fe-3Al with a similar heat-treatment state [21]. As a result of the modification of Ti-6Al-4V with V and F, the range of achievable mechanical properties in dependence of the heat-treatment is significantly expanded.

4. Conclusions

In summary, this publication describes the modification of Ti-6Al-4V with the β-phase-stabilizing elements V and Fe by means of heterogeneous powder mixing and in situ alloying during L-PBF. The β-phase-stabilizing effect of the elements Fe and V, and the general feasibility of in situ alloying for the swift development of new alloys for L-PBF-applications, are confirmed. The results demonstrate the possibility of obtaining a metastable β-Ti alloy close to the commercial alloy Ti-10V-2Fe-3Al from Ti-6Al-4V, V, and Fe powder without the need for expensive atomization of customized pre-alloyed powder. EBSD analysis shows a β-phase content of at least 63.8% in as-built condition, whereas

unmodified Ti-6Al-4V develops an α'-martensitic microstructure. In dependence of the post-L-PBF heat-treatment either an increased minimum upsetting at failure of 33.9%, in comparison to 28.8% for unmodified Ti-6Al-4V, or an exceptional high compressive yield strength of 1857 $\pm$ 35 MPa in comparison to about 1100 MPa for unmodified Ti-6Al-4V, can be achieved. The hardness of the in situ alloyed material ranges from 336 $\pm$ 7 HV0.5, in as-built condition, to 543 $\pm$ 13 HV0.5 after precipitation-hardening. Modification of Ti-6Al-4V with Fe and V consequently expands the range of mechanical properties that can be achieved in dependence of the heat-treatment. This provides additional flexibility for developing sophisticated titanium parts with tailored material properties.

Author Contributions: F.H. wrote the paper. F.H. developed the methodology and designed the experiments. F.H. performed the experiments together with L.H. T.P. performed the compression test and provided his expertise regarding the interpretation of the same. C.S. contributed additional expertise regarding the discussion of the results and the preparation of the manuscript. M.M. and M.S. supervised the work.

Funding: This research was funded by the German Research Foundation (DFG), Germany [Collaborative Research Center 814: Additive Manufacturing, Subproject B5; Erlangen Graduate School in Advanced Optical Technologies (SAOT)].

Acknowledgments: We acknowledge support by the German Research Foundation (DFG) and Friedrich-Alexander-Universität Erlangen-Nürnberg (FAU) within the funding program Open Access Publishing.

Conflicts of Interest: The authors declare no conflict of interest.

References

1. Wohlers, T.; Caffrey, T.; Campbell, I. *Wohlers Report 2016 Published*; Wohlers Associates, Inc.: Fort Collins, CO, USA, 2016; ISBN 9780991333226.
2. Uhlmann, E.; Kersting, R.; Klein, T.B.; Cruz, M.F.; Borille, A.V. Additive manufacturing of titanium alloy for aircraft components. *Procedia CIRP* **2015**, *35*, 55–60. [CrossRef]
3. Rotaru, H.; Schumacher, R.; Kim, S.-G.; Dinu, C. Selective laser melted titanium implants: a new technique for the reconstruction of extensive zygomatic complex defects. *Maxillofac. Plast. Reconstr. Surg.* **2015**, *37*, 12. [CrossRef]
4. Dutta, B.; Froes, F.H. *Additive manufacturing of Titanium Alloys: State of the Art, Challenges and Opportunities*; Butterworth-Heinemann: Oxford, UK, 2015; ISBN 9780128047828.
5. EOS GmbH No Title. Available online: https://www.eos.info/material-m (accessed on 10 September 2018).
6. SLM Solutions GmbH No Title. Available online: https://slm-solutions.com/products/accessories-and-consumables/slmr-metal-powder (accessed on 11 September 2018).
7. Zhai, Y.; Galarraga, H.; Lados, D.A. Microstructure evolution, tensile properties, and fatigue damage mechanisms in Ti-6Al-4V alloys fabricated by two additive manufacturing techniques. *Procedia Eng.* **2015**, *114*, 658–666. [CrossRef]
8. Chastand, V.; Tezenas, A.; Cadoret, Y.; Quaegebeur, P.; Maia, W.; Charkaluk, E. Fatigue characterization of Titanium Ti-6Al-4V samples produced by additive manufacturing. *Procedia Struct. Integr.* **2016**, *2*, 3168–3176. [CrossRef]
9. Gu, D. *Laser Additive Manufacturing of High-Performance Materials*; Springer: Heidelberg, Germany, 2015.
10. Macpherson, A.; Li, X.; McCormick, P.; Ren, L.; Yang, K.; Sercombe, T.B. Antibacterial titanium produced using selective laser melting. *JOM* **2017**, *69*, 2719–2724. [CrossRef]
11. Sing, S.L.; Yeong, W.Y.; Wiria, F.E. Selective laser melting of titanium alloy with 50 wt% tantalum: Microstructure and mechanical properties. *J. Alloys Compd.* **2016**, *660*, 461–470. [CrossRef]
12. Leyens, C.; Peters, M. *Titanium and Titanium Alloys: Fundamentals and Applications*; John Wiley & Sons: Hoboken, NJ, USA, 2003; ISBN 3527305343.
13. DIN 17851. *Titanium Alloys; Chemical Composition*; Deutsches Institut für Normung E.V. (DIN): Berlin, Germany, 1990.
14. Vrancken, B.; Thijs, L.; Kruth, J.P.; Van Humbeeck, J. Heat treatment of Ti6Al4V produced by selective laser melting: microstructure and mechanical properties. *J. Alloys Compd.* **2012**, *541*, 177–185. [CrossRef]
15. Butzhammer, L.; Dubjella, P.; Huber, F.; Schaub, A.; Aumüller, M.; Petrunenko, O.; Merklein, M.; Schmidt, M. Experimental Investigation of a Process Chain Combining Sheet Metal Bending and Laser Beam Melting of Ti-6Al-4V. In Proceedings of the Lasers in Manufacturing Conference, Munich, Germany, 26–29 June 2017.

16. Papke, T.; Junker, D.; Schmidt, M.; Kolb, T.; Merklein, M. Bulk Metal Forming of Additively Manufactured Elements. In Proceedings of the 5th International Conference on New Forming Technology, Bremen, Germany, 18–21 September 2018.
17. DIN 50106. *Testing of Metallic Components—Compression Test at Room Temperature*; Deutsches Institut für Normung E.V. (DIN): Berlin, Germany, 2016.
18. Huber, F.; Rasch, M.; Butzhammer, L.; Karg, M.; Schmidt, M. Strahlschmelzen von Metallen mit unterschiedlichen Intensitäten und Belichtungsstrategien. In Proceedings of the 5. Industriekolloquium des Sonderforschungsbereichs 814—Additive Fertigung, Nürnberg, Germany, 12 December 2017.
19. Mukherjee, T.; Wei, H.L.; De, A.; DebRoy, T. Heat and fluid flow in additive manufacturing—Part II: Powder bed fusion of stainless steel, and titanium, nickel and aluminum base alloys. *Comput. Mater. Sci.* **2018**, *150*, 369–380. [CrossRef]
20. Xu, W.; Brandt, M.; Sun, S.; Elambasseril, J.; Liu, Q.; Latham, K.; Xia, K.; Qian, M. Additive manufacturing of strong and ductile Ti-6Al-4V by selective laser melting via in situ martensite decomposition. *Acta Mater.* **2015**, *85*, 74–84. [CrossRef]
21. Titanium Metals Corporation Timetal® 10-2-3. Available online: http://www.timet.com/assets/local/documents/datasheets/metastablebetaalloys/10-2-3.pdf (accessed on 11 September 2018).

5.2 Systematic exploration of the L-PBF processing behavior and resulting properties of β-stabilized Ti-alloys prepared by in-situ alloy formation

Published in Materials Science and Engineering A 818 (2021)

Florian Huber[1,2,3], Thomas Papke[2,4], Constantin Kauffmann[1,4], Richard Rothfelder[1,2,3], Pavel Krakhmalev[5], Marion Merklein[2,3,4] and Michael Schmidt[1,2,3]

[1] Institute of Photonic Technologies, Friedrich-Alexander Universität Erlangen-Nürnberg
[2] Collaborative Research Center 814 – Additive Manufacturing
[3] Erlangen Graduate School in Advanced Optical Technologies
[4] Institute of Manufacturing Technology, Friedrich-Alexander Universität Erlangen-Nürnberg
[5] Department of Engineering and Physics, Karlstad University

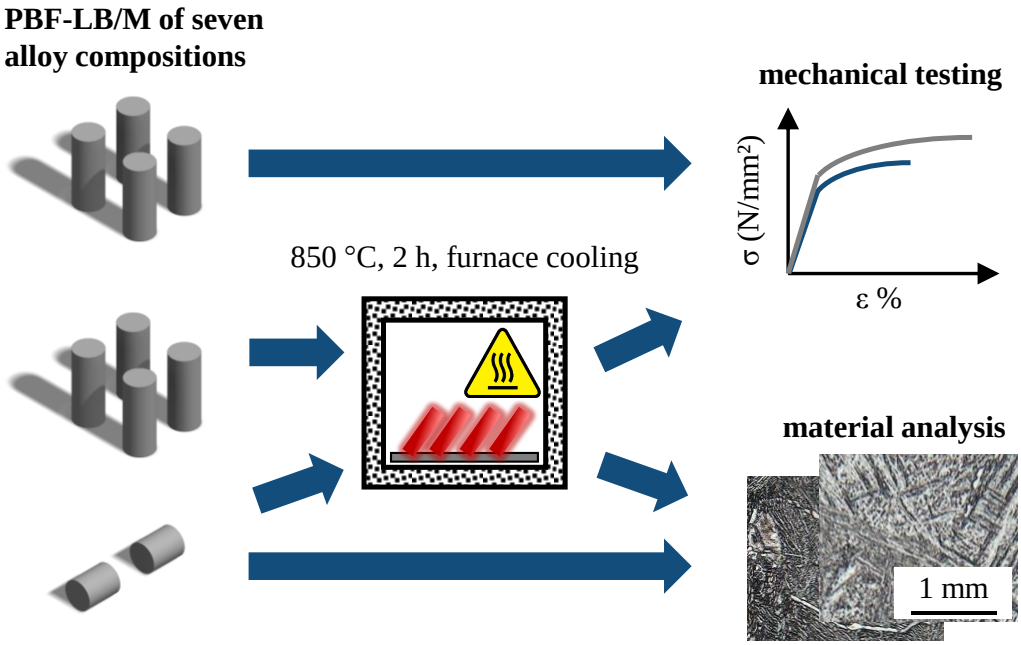

Highlights:

- Molybdenum equivalent suitable as an indicator for the β-phase stability of Ti-alloys processed by PBF-LB/M
- No negative impact of in-situ alloy formation on the homogeneity of the element distribution throughout single parts and across the whole build platform
- β-phase content adjustable between 0 % and more than 95 % in dependence of the Fe and V content
- Identification of ω-phase formation as the cause for detrimental embrittlement of the material in certain Mo_{eq} ranges
- Only slight change of the alloy's thermo-physical properties by adding Fe and V allowing for processing of different compositions and handling transition zones between part areas with different alloy compositions without laborious PBF-LB/M parameter development

Materials Science & Engineering A 818 (2021) 141374

Contents lists available at ScienceDirect

Materials Science & Engineering A

journal homepage: www.elsevier.com/locate/msea

Systematic exploration of the L-PBF processing behavior and resulting properties of β-stabilized Ti-alloys prepared by in-situ alloy formation

Florian Huber [a,b,c,*], Thomas Papke [c,d], Constantin Kauffmann [a], Richard Rothfelder [a,b,c], Pavel Krakhmalev [e], Marion Merklein [b,c,d], Michael Schmidt [a,b,c]

[a] Institute of Photonic Technologies, Friedrich-Alexander-Universität Erlangen-Nürnberg, Konrad-Zuse-Straße 3/5, 91052, Erlangen, Germany
[b] Erlangen Graduate School in Advanced Optical Technologies, Friedrich-Alexander-Universität Erlangen-Nürnberg, Paul-Gordan-Straße 6, 91052, Erlangen, Germany
[c] Collaborative Research Center 814: Additive Manufacturing, Friedrich-Alexander-Universität Erlangen-Nürnberg, Am Weichselgarten 9, 91058, Erlangen, Germany
[d] Institute of Manufacturing Technology, Friedrich-Alexander-Universität Erlangen-Nürnberg, Egerlandstraße 13, 91058, Erlangen, Germany
[e] Department of Engineering and Physics, Karlstad University, 651 88, Karlstad, Sweden

ARTICLE INFO

Keywords:
Additive manufacturing
Laser powder bed fusion (L-PBF)
Titanium alloys
Laser materials processing
In-situ alloy formation
Mechanical properties

ABSTRACT

Aim of this work is to gain a comprehensive understanding of the effects of an increasing β-phase stability of Ti-alloys on the L-PBF processing behavior. For this purpose, seven different Ti-alloys with an increasing concentration of the β-phase stabilizing elements Fe and V were prepared by L-PBF and in-situ alloy formation. The Molybdenum equivalent (Mo_{eq}) of the examined alloys, as a measure of β-phase stability, was varied systematically between −3.3 and 25. It is shown that a homogeneous distribution of elements is achievable by in-situ alloying. The experiments prove that the investigated alloys can be processed by a single L-PBF parameter set with high relative density above 99.8%. This finding is substantiated by calculated thermo-physical material properties and an analytical model. To understand the underlying metallurgical effects governing the L-PBF results, the samples were investigated extensively by EDS, EBSD, XRD, light microscopy and compression tests. The β-phase fraction varies in dependence of the Mo_{eq} between 0% and 99%. Because of rapid solidification inherent in L-PBF a Mo_{eq} of 10 is sufficient to receive more than 90% β-phase. The same amount of β-phase after furnace cooling was only observed in alloys with Mo_{eq} of 20 or more. While all alloy compositions can be processed with high relative density of over 99.8%, alloys with a Mo_{eq} between 15 and 20 show a brittle material behavior in as-built state, resulting in cracking during L-PBF. This behavior is attributed to the formation of ω-phase during L-PBF. In contrast, the highest β-stabilized alloy with a nominal Mo_{eq} of 25 exhibits a very high ductility with a fracture strain exceeding 50%.

1. Introduction

Currently, the most relevant process for additive manufacturing of metals is Laser Powder Bed Fusion (L-PBF) [1], which is also referred to as Selective Laser Melting (SLM) or Laser Beam Melting (LBM). The basic principle of the process, as shown in Fig. 1, comprises an iteration of powder recoating, selective consolidation with a laser beam and lowering of the build platform. This layerwise manufacturing approach facilitates an almost unlimited degree of design freedom and allows the production of complex geometries. For manufacturing of high performance parts e.g. in the aerospace industry [2] or for medical applications [3] additive manufacturing of titanium alloys is of interest. The alloy Ti–6Al–4V is by far the most widely used titanium alloy for L-PBF applications [4]. Reasons for this are its balanced material properties, the fact, that it is very well investigated ([5] or [6]) and standard processing parameters are available for a majority of commercial L-PBF machines (e.g. GE Additive M2 series [7] or SLM Solutions SLM 280 [8]). Ti–6Al–4V is an α-β Ti-alloy [9], which forms an α′-martensitic structure when processed by L-PBF [10]. This is due to the high cooling rates which are inherent to L-PBF thus limiting diffusion processes. In Ref. [11] a cooling rate in the range of 10^6 K/s was determined by numerical simulations. This value is in good agreement with experimental measurements in Ref. [12], that show cooling rates between 1–40 × 10^6 K/s. By applying a heat-treatment below the β-transus temperature of

* Corresponding author. Institute of Photonic Technologies, Friedrich-Alexander-Universität Erlangen-Nürnberg, Konrad-Zuse-Straße 3/5, 91052, Erlangen, Germany.
E-mail address: florian.huber@lpt.uni-erlangen.de (F. Huber).

https://doi.org/10.1016/j.msea.2021.141374
Received 9 December 2020; Received in revised form 26 March 2021; Accepted 29 April 2021
Available online 13 May 2021

the alloy, the α′-martensite decomposes into a fine microstructure consisting of acicular α-Ti and some remaining β-phase [5], thus increasing the ductility of the material. The mechanical properties of Ti–6Al–4V processed by L-PBF are comparable or in some aspects even superior to conventionally manufactured material. Qiu et al. report a 0.2% yield strength of >1000 MPa for as-built samples [13]. However, the fracture strain reaches only 7%–10%, probably because of the martensitic microstructure. Heat-treating and hot isostatic pressing respectively slightly reduces the 0.2% yield strength to 925 MPa–1000 MPa but leads to a significant increase in fracture strain to 15%–18% [13]. Current research on laser powder bed fusion of Ti–6Al–4V investigates for example the effect of oxygen intake during manufacturing on the mechanical properties [14] or the evolution of residual stress in dependence of the process parameters [15].

Additive manufacturing of Ti-alloys other than Ti–6Al–4V is significantly less investigated. Some studies focus on L-PBF of the commercially pure (cp) grades [17]. Mainly for biomedical applications, L-PBF of Ti–6Al–7Nb is investigated, since it features a superior biocompatibility than Ti–6Al–4V due to the absence of Vanadium [18]. However, Ti–6Al–7Nb is an α-β Ti-alloy like Ti–6Al–4V and possess rather similar properties. In contrast to that, metastable β-Ti alloys would be of interest since they reach a superior strength to weight ratio due to the possibility of precipitation hardening and feature a superior room temperature ductility resulting from the body centered cubic (bcc) crystal structure [9]. Because of this, the application of metastable β-Ti-alloys like Ti–10 V–2Fe–3Al in the aerospace industry is increasing [19]. Metastable β-Ti alloys are Ti-alloys that contain a sufficient amount of β-stabilizing elements to obtain only β-phase after quenching from a temperature above β-transus to room temperature [20]. As shown in Fig. 2 β-phase stabilizing elements are classified in β-isomorphous elements like Nb or V and β-eutectoid elements that tend to form intermetallic phases at higher concentrations like Fe and Cr [9].

Both, empirical and theoretical approaches can be used to predict the affinity of an alloy to form either β-Ti or α-Ti [21]. Theoretical approaches date back to the electron concentration rules proposed by Hume-Rothery [22]. In more recent work e.g. Tegner et al. [23] apply density functional theory calculations to determine the single-phase stability in dependence of the alloying element. Huang et al. [24] present ab initio calculations of formation energies of transition metal solutes in the α-, β- and ω-phases of Ti also based on density functional theory. This data is used to derive stabilization energies and respective phase diagrams and to assess the β-stabilization strength of the investigated alloying elements. The calculated values are in good agreement with experimental data, but still show some quantitative discrepancies, which become larger for weaker β-phase stabilizers like Zr. Huang et al. [24] explain these differences by unavoidable model simplifications, neglection of diffusion effects and discrepancies in experiments like impurities. Also, the formation of intermetallic and martensitic phases is not taken into account. Nevertheless, theoretical calculations can be a valuable tool for predicting the single-phase stability of α-, β-, and ω-Ti-phases [25].

Besides theoretical approaches, in engineering praxis empirical models are established to conveniently predict the β-phase stability of a certain alloy. The so-called molybdenum equivalent (Mo_{eq}) can be used to evaluate the affinity of an alloy to form β-Ti rather than α-Ti. An established version of the Mo_{eq} is calculated by the following formula:

$$Mo_{eq} = 1.0\,(wt.\%\ Mo) + 0.67\,(wt.\%\ V) + 0.44\,(wt.\%\ W) + 0.28\,(wt.\%\ Nb) + 0.22\,(wt.\%\ Ta) + 2.9\,(wt.\%\ Fe) + 1.6\,(wt.\%\ Cr) + 1.25\,(wt.\%\ Ni) + 1.7\,(wt.\%\ Mn) + 1.7\,(wt.\%\ Co) - 1.0\,(wt.\%\ Al)$$

The factors for each element are determined by dividing the concentration of Mo needed to receive only β-phase after quenching by the concentration need for a specific element. The aluminum concentration is subtracted since aluminum stabilizes α-Ti. Similar to the Mo_{eq} an aluminum equivalent can be calculated, that considers the effect of neutral and α-stabilizing elements [26]:

$$Al_{eq} = 1.0\,(wt.\%\ Al) + 0.17\,(wt.\%\ Zr) + 0.33\,(wt.\%\ Sn) + 10\,(wt.\%\ O) + 10\,(wt.\%\ N)$$

According to Refs. [25,27] alloys with a Mo_{eq} greater than ten are considered metastable β-Ti alloys. Besides the formula presented above, different versions of Mo_{eq} have been proposed, that are more accurate in certain cases. Especially the contribution of weaker β-stabilizers like Zr is still subject of ongoing investigations. Based on experimental data, in Jiang et al. [28] a consideration of Zr as weak β-stabilizer with a factor of 0.31 and a slightly increase of the factor for Nb to 0.33 is proposed. Wang et al. [21] showed, that their variant of the Mo_{eq}, which is derived from the slope of boundary lines between the β and (α+β) phase zones in binary Ti-M phase diagrams is more accurate for low-E β-Ti-alloys like Ti–24Nb–4Zr-7.9Sn than the older formula. Despite slightly different factors for most alloying elements a strong difference to the formula presented above is the consideration of Zr and additionally Sn as β-stabilizers, which is in accordance with theoretical calculations by Huang [24]. However, since only Al, V and in limited amounts Fe are used as alloying elements in the present work and Zr and Sn are not present, the different formulas for Mo_{eq} provide rather similar results, which are also in good agreement with theoretical calculations. Consequently, since it is the most prominent one, widely used in literature and sufficiently evaluated for the alloy class investigated in the present work, the older Mo_{eq} formula reported by Bania [27] is used in the following.

These considerations show that (metastable) β-Ti-alloys possess a more complex metallurgy compared to α- and near α-Ti-alloys, which is one of their drawbacks. As a consequence, the weldability is decreased and processing requires a higher level of control of the thermo-mechanical conditions [9]. This might be one reason why there is only little work on L-PBF of metastable β-Ti-alloys. Zopp et al. [29] investigated processing of the metastable β-Ti-alloy Ti–5Al–5Mo–5V–3Cr in a single study. It is shown, that L-PBF of Ti–5Al–5Mo–5V–3Cr with high

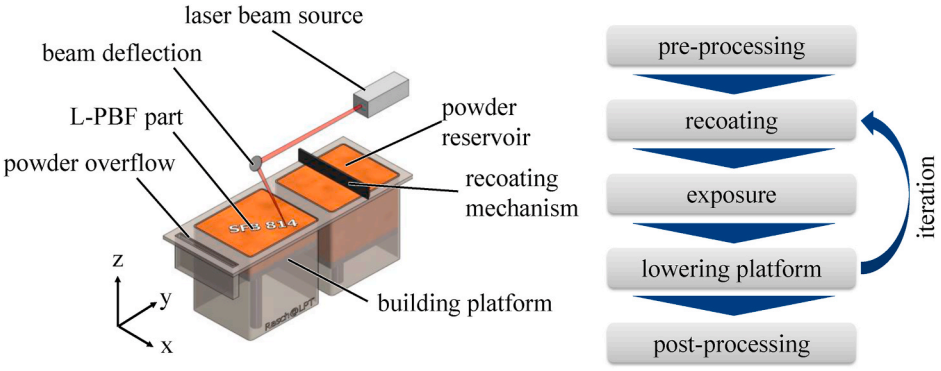

Fig. 1. Schematic of the L-PBF process (reproduced from Ref. [16]).

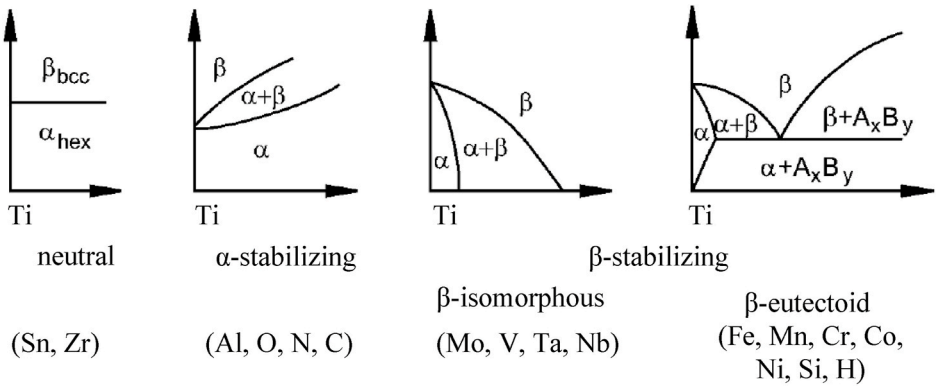

Fig. 2. Influence of selected alloying elements on the phase stability of titanium alloys according to [9].

relative density above 99.9% is possible, but no material properties were published. In a previous study we investigated in-situ alloy formation from powder mixtures of an alloy close to the commercial metastable β-Ti-alloy Ti–10 V–2Fe–3Al [30]. In contrast to other studies on in-situ formation of Ti-alloys by Polozov et al. [31], Sing et al. [32] or Yadroitsev et al. [33] no unmolten particles were detected in our samples [30]. By adding 50 wt % Tantalum, Sing et al. [32] showed, that samples consisting completely of β-phase and some remaining unmolten Tantalum could be manufactured by L-PBF, thus increasing ductility and reducing the Young's modulus. Yadroitsev et al. [33] investigated in-situ alloy formation of a TiMo15 alloy from elemental powders. However, they also observed unmolten Mo-particles and an inhomogeneous Mo-distribution. Similar results were reported by Wang et al. [37], who investigated in-situ alloy formation of Ti–35Nb from elemental powders. No complete dissolution of the Nb-particles was achieved during L-PBF. However, annealing at 1000 °C lead to a significant increase in material homogeneity. Krakhmalev et al. [34] examined the addition of 1 wt% copper to Ti6Al4V ELI mainly motivated by biomedical applications. Though, a complete melting of the copper particles was demonstrated, they observed segregations of copper resulting in areas with increased copper content between 20 wt% and 35 wt%. Because of the β-phase stabilizing effect of Cu these areas consisted of β-Ti rather than α′-martensite like the areas with lower Cu concentration. Also aiming for medical implants some research groups investigated the suitability of low-E β-Ti-alloys for L-PBF. Examples are Zhang et al. [35], who successfully demonstrated L-PBF of pre-alloyed Ti–24Nb–4Zr–8Sn or Hafeez et al. [36], who also worked with pre-alloyed powder and investigated the phase transformation behavior of a Ti–35Nb–2Ta–3Zr alloy fabricated by L-PBF.

Despite these first studies a comprehensive understanding regarding L-PBF of β-stabilized Ti-alloys is still lacking. In particular in as-built condition strong deviations from conventionally processed β-Ti-alloys are expected because of the high cooling rates inherent to L-PBF [12] and the consequent re-heating during layerwise manufacturing. Current research on in-situ alloy formation of Ti-based materials in many cases reports unmolten particles or other material inhomogeneities. L-PBF of low-E β-Ti-alloys is addressed by some research groups. Especially the L-PBF processing behavior of Ti-alloys with intermediate β-phase stabilization in the Mo_{eq}-range between 5 and 20 is barely investigated. Consequently, further research is necessary.

In this context, the aim of the present work is to gain a comprehensive understanding of L-PBF of β-stabilized Ti-alloys containing Al, Fe and V as main alloying elements. For this purpose, seven alloy compositions with a nominal Mo_{eq} (as an indicator for β-phase stability) ranging from −3.3 to 25 were prepared by L-PBF and in-situ alloy formation. The samples were extensively characterized by compression tests, light microscopy, EDS (energy dispersive X-ray spectroscopy), XRD (x-ray diffraction) and EBSD (electron backscatter diffraction). In this context, the following research questions were investigated:

- Effect of in-situ alloying on the homogeneity of the element distribution
- Effect of the increasing addition of β-phase stabilizing elements on the processability of Ti-alloys
- Interdependencies between the alloy composition, the unique conditions during the L-PBF process and the resulting microstructural and mechanical properties
- Effect of a heat-treatment featuring significantly lower cooling rates than the material faces during L-PBF on the microstructure and the mechanical properties
- Value of the Mo_{eq} for predicting the phase composition and the resulting material properties in as-built condition as well as in heat-treated condition
- Conclusions for the further development of (metastable) β-Ti alloys for L-PBF

2. Methods

To avoid an elaborate atomization of pre-alloyed powder, seven different alloy compositions were prepared by in-situ alloying from mixtures of easily available standard-powders. The variation of the Mo_{eq} was realized by addition of the β-phase stabilizers Fe and V. The general feasibility of this approach and particularly the homogeneity of the resulting distribution of the alloying elements is confirmed by previous investigations [30]. Both elements were chosen since they have melting points in a similar range Ti (Iron: 1538 °C [38]; Vanadium: 1910 °C [38], Titanium: 1668 °C, [38]), thus lowering the risk of unmolten particles and extensive evaporation. Fe has a very strong effect on β-phase stability, however, bears the risk of embrittlement due to formation of intermetallic phases at higher concentrations [20]. Hence, V was added as second β-stabilizer to keep the Fe concentration needed to achieve the highest Mo_{eq} of 25 below 5 wt%. Starting from the commercial alloy Ti–6Al–4V with a Mo_{eq} of −3.3 the Mo_{eq} was increased to 10 by adding Fe and V. The powder mixtures with Mo_{eq} values between 15 and 20 were prepared with commercially pure Ti-powder (grade 2) since Al acts as α-stabilizer and reduces the Mo_{eq}. As discussed in the introduction section the formula for the Mo_{eq} reported by Bania [27] is

Table 1
Investigated powder mixtures and calculated element concentration in wt.% (deviations from 1 due to mathematical rounding).

Notation	Ti wt.%	Al wt.%	V wt.%	Fe wt.%	Mo_{eq}
Ti Mo_{eq}-3.3	90.00	6.00	4.00	0	−3.32
Ti Mo_{eq}5	83.83	5.59	9.08	1.51	4.86
Ti Mo_{eq}7	82.51	5.50	9.96	2.04	7.08
Ti Mo_{eq}10	80.09	5.34	12.06	2.52	10.03
Ti Mo_{eq}15	88.16	–	8.85	2.99	14.60
Ti Mo_{eq}20	83.86	–	11.98	4.16	20.09
Ti Mo_{eq}25	79.88	–	15.12	5.01	24.65

used in the present work, since it is the most prominent one in literature. The exact compositions of the seven powder systems are listed in Table 1.

The plasma atomized Ti–6Al–4V and Ti grade 2 powders were obtained from AP&C Advanced Powders and Coatings Inc. (Boisbriand, QC, Canada). The water atomized Fe and milled V powders that were used for in-situ alloying were provided by PMCtec GmbH (Leun, Germany) and NMD GmbH (Heemsen, Germany), respectively. The particle size distribution was determined by laser diffraction with a Mastersizer 3000 from Malvern Panalytical GmbH (Kassel, Germany) (see Table 2).

The particle shape was verified by SEM images (Zeiss Merlin, Carl Zeiss Microscopy GmbH, Germany), which are shown in Fig. 3.

The chemical composition of the four powders was checked by EDS (Zeiss Merlin with AzTec advanced EDS system) for the metallic elements and inert gas fusion (ONH analyzer, Eltra GmbH, Germany) for oxygen. All values are within the specification (see Table 3).

For preparing the powder mixtures, the powders were vacuum dried in a lab furnace at 120 °C for 8 h to remove any moisture. This step was followed by sieving for breaking up possible agglomerates (mesh size 75 µm). The mixing itself was performed with a Turbula-mixer from Willy A. Bachofen AG (Muttenz, Switzerland) for a duration of 2 h. This procedure was experimentally developed and already successfully applied e.g. in Ref. [16]. The recoatability of the powder mixtures was tested visually by a camera system and small angle illumination (defects in the power layer visible because of shading). In addition the homogeneity of the resulting element distribution in the in-situ alloyed L-PBF samples has to be investigated to rule out possible segregation effects. Following a build job, the powder mixtures were recycled by sieving with a lab sieving machine from Haver & Boecker (Oelde, Germany) with a mesh opening of 90 µm and mixing for 1 h in the Turbula-mixer. Both steps were performed in argon atmosphere.

To investigate processing behavior, resulting microstructure and mechanical properties in dependence of the alloy composition nine cylindrical samples with the dimensions Ø 7.5 mm × 19 mm were produced for each powder mixture resulting in 63 samples in total. The samples were manufactured using an Aconity mini L-PBF machine from Aconity GmbH (Herzogenrath, Germany), which is equipped with a redPower QUBE single mode fiber laser from SPI Lasers Ltd. (Southampton, United Kingdom) with a maximum beam power of 1 kW and a wavelength of 1080 nm and an AxialSCAN-30 scanner optics from Raylase GmbH (Wessling, Germany). The minimum beam diameter on the build platform is 70 µm. Since titanium has a strong oxygen-affinity and interstitial oxygen acts as α-stabilizer in titanium, the oxygen content in the processing gas (Argon) was kept below 100 ppm for the whole duration of the build job. The L-PBF parameter set, which was experimentally developed and used for all alloy compositions, is listed in Table 4.

Eight of the nine samples made from each powder composition were designated for compression tests and the remaining sample was investigated by metallographic methods. Four of the compression-test samples along with a half-section of the metallography sample were heat-treated, while the remaining four samples and the other half-section of the metallography sample were investigated in as-built condition. This experimental approach is illustrated in Fig. 4.

The heat-treatment, which is partially derived from Ref. [5], comprised an annealing at 850 °C for 2 h followed by furnace cooling. To protect the samples from oxygen the furnace was constantly flushed with argon. The intention of this heat-treatment was to remove residual stress induced during L-PBF [40] and to reach a more equilibrium material condition compared to as-built samples, that faced very high cooling rates in the range of 10^6 K/s [12] during L-PBF.

Compression tests were chosen to measure the mechanical properties resulting from L-PBF. In general tensile tests would be preferable for material characterization of Ti-alloys. However, with respect to the present study, compression tests require smaller sample sizes and hence allow the production of more samples. Aim of this work is not to investigate/optimize one specific alloy, but rather explore the L-PBF process behavior of β-stabilized Ti-alloys in a wide range to lay the foundation for further investigations. Consequently, compression tests better match the requirements of such screening investigations, while still providing reasonable information on the mechanical properties. Tensile tests are planned for future work, based on the results of the present investigations. The samples for compression tests were turned to a cylindrical shape of Ø 6 mm × 9 mm. The end surfaces were grinded. For the compression tests the setup consisting of tungsten carbide tools was mounted in a universal testing machine from Walter + Bai AG (Löhningen, Switzerland) with a maximum possible force of 300 kN. To keep friction between tool and specimen low, a Teflon® foil was used. The compressive load was induced by a linear movement of the upper tool, which is moved with a constant velocity of 5 mm/min. Force and displacement of the tool were recorded for evaluation of stress strain curves. The tests stopped when the specimen breaks or is compressed to 50% of the initial height. Consequently, higher degrees of sample deformation cannot be measured, which is relevant for highly ductile β-Ti alloys. The tests were performed in accordance with DIN 50106 [41]. Hardness measurements (HV1) were carried out on polished microsections with five measurement points per sample.

The relative density, microstructure and resulting alloy composition was analyzed by metallographic microsections, energy dispersive x-ray spectroscopy (EDS), electron backscatter diffraction (EBSD) and x-ray diffraction (XRD) respectively. For this purpose, the samples were embedded in epoxy resin, sectioned by disc-cutting, grinded with SiC grinding paper, polished with 3 µm diamond suspensions and finished with active oxide polishing suspension (OPS) and hydrogen peroxide. To investigate the microstructure by optical microscopy, the samples were etched with Kroll's reagent (H_2O, HNO_3, HF). The x-ray diffraction measurements were performed using a Panalytical Empyrean x-ray diffractometer equipped with a cobalt-anode (λ = 1.7902 Å). The diffraction patterns were analyzed with data sets from the databases ICSD FIZ 2016–1, COD 2019 HS-4.5 and PDF-2 2004. A Zeiss Merlin SEM (Carl Zeiss Microscopy GmbH, Germany) equipped with a Wave 700 EBSD system and an AzTec Advanced EDS system with XMax50 detector (Oxford Instruments, UK) were used for SEM/EDS/EBSD-analysis. Quantitative EDS-measurements are either line scans (5 mm length/100 layers, n = 1000) or area scans (5 measurement areas, 400 × 400 µm^2).

Table 2
Particle size distribution determined by laser diffraction.

Material	D_{10}	D_{50}	D_{90}	Particle shape
Ti grade 2	21 µm	35 µm	48 µm	spherical
Ti–6Al–4V	25 µm	43 µm	61 µm	spherical
Fe	28 µm	47 µm	68 µm	spattered
V	8 µm	24 µm	53 µm	angular

3. Results and discussion

3.1. Homogeneity of the element distribution

Despite the non-spherical particle shape of the Fe and V powder, the recoatability of all powder mixtures is not impaired, which was verified visually by an illumination setup and a camera system (small angle illumination and shading). A demixing of the powder components during handling which might occur under unfavorable conditions [39] was not observed. Nevertheless, before the microstructure and the mechanical properties are discussed, it is necessary to verify that a homogeneous element distribution with the desired concentrations throughout the samples was achieved, since fluctuations in the element concentration might affect the results. This is particularly relevant when preparing samples by in-situ alloying. As pointed out in the state of the art section, unmolten particles as reported by Polozov et al. [31],

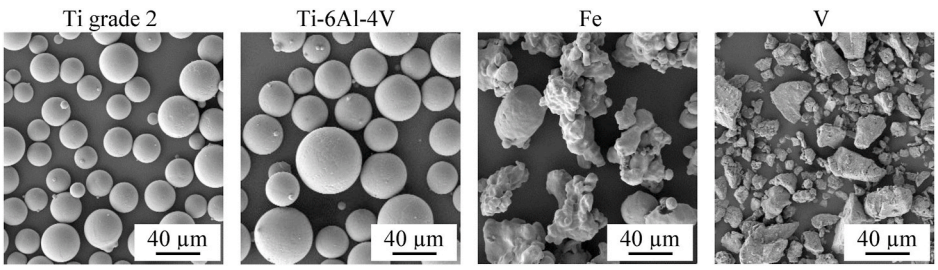

Fig. 3. SEM images of the four powders used for preparing the powder mixtures.

Table 3
Chemical composition of the powders, determined by EDS and inert gas fusion respectively.

	Ti	Al	V	Fe	Si	O*
Ti grade 2	99.8	–	–	0.1	–	0.12
Ti–6Al–4V (wt.%)	89.4	6.4	4.1	0.1	–	0.11
Fe (wt.%)	–	–	–	99.8	0.1	0.09
V (wt.%)	–	–	99.9	–	–	n.a.

Standard deviation < 0.1 wt%, * determined by inert gas fusion.

Table 4
L-PBF parameter set for manufacturing the samples.

Laser power	Scan speed	Spot diameter	Hatch distance	Layer thickness
400 W	1200 mm/s	100 µm	120 µm	50 µm

Yadroitsev et al. [33] or Sing et al. [32] are a major source of such inhomogeneities. Also possible segregation effects during melting/solidifying as described in Refs. [33,34] for the addition of Cu to Ti6Al4V need to be excluded. According to Yadroitsev et al. [33] these segregations are predominantly found at fusion boundaries and form because of different melt viscosities and/or densities. A further effect, that could also lead to an inhomogeneous element distribution is the segregation of the different powders during handling or recoating [39] which also needs to be ruled out for all powder mixtures. For this purpose, the element composition is measured in dependence on the build height and the build platform position and is compared to the target concentration. Fig. 5 shows the concentration of the relevant elements Ti, Fe, Al and V in relation to the build height (5 mm, 100 layers) for an in-situ alloyed Ti Mo_{eq}25 sample and for a sample made from pre-alloyed Ti–6Al–4V powder as reference. The measurements show, that the in-situ alloyed sample has a comparable homogeneity of the element distribution as the sample made from pre-alloyed powder. The standard deviation of the element Ti is 0.93% (n = 1000) for the pre-alloyed powder and 0.98% (n = 1000) for the in-situ alloyed powder and thus in a similar range. No strong peaks for the alloying elements Fe and V are visible for sample Ti Mo_{eq}25 thus proving the complete melting of the powder and a successful mixing in the molten pool. Also, the etched microsections in Fig. 11 do not show any sign of unmolten particles or segregation effects

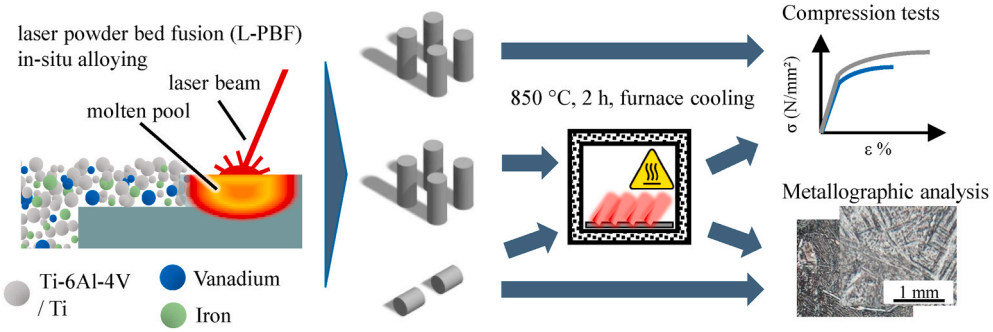

Fig. 4. Experimental approach.

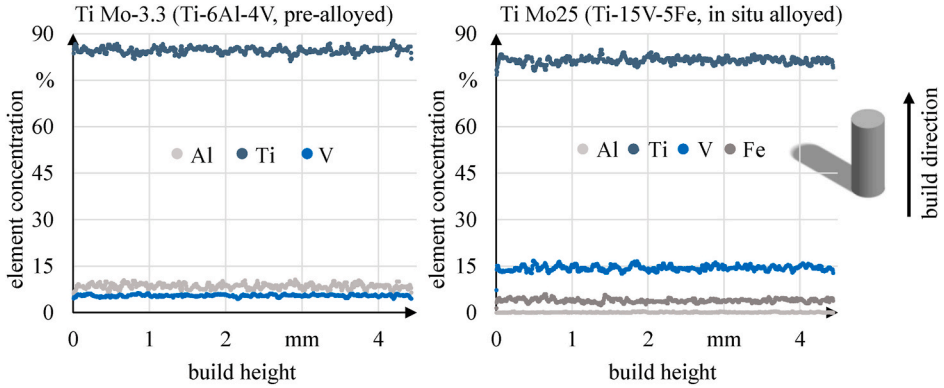

Fig. 5. EDS line scan to determine the element concentration over 5 mm build height (100 layers) of a Ti–6Al–4V sample (pre-alloyed) and an in-situ alloyed Ti Mo_{eq}25 sample, both in as-built state.

during melting and solidifying. Compared to the aforementioned studies which discuss alloying with high melting elements like Niobium [31], Molybdenum [33] or Tantalum [32] we investigated alloying with the elements Vanadium and Iron, which have melting points close to Titanium [38]. This eases in-situ alloying and supports a homogeneous distribution of elements throughout the L-PBF part. Also, no inclination of the element concentrations over build height was observed. This indicates that no demixing of the powder occurred and in-situ alloying has no negative effect on the element homogeneity, at least in this case and at least in build direction. Similar measurements for the other alloy compositions investigated in this study confirm this conclusion.

To further substantiate the hypothesis of a fairly homogeneous element distribution resulting from in-situ alloying a qualitative EDS area scan of a Ti Mo_{eq}7 sample and a cross-section of a single weld track obtained from the parameter set listed in Table 4 is shown in Fig. 6. The sample section in Fig. 6 a) covers multiple layers (layer-thickness: 50 µm). Hence, element segregation at fusion boundaries would be clearly visible, if present. Based on simple assumptions one could argument, that the meltpool size needs to be big enough to contain at least one powder particle of the added alloying elements. Considering the average particle size provided in Table 2 and the meltpool dimensions shown in Fig. 6 b), this is verified for the present work. The base material used for the single weld track was Ti grade 1. Nevertheless, it is safe to assume that the actual meltpool dimensions during L-PBF of the investigated alloys are in a similar range or with respect to the material properties and the boundary conditions of the process even slightly bigger. The meltpool length cannot be obtained from the cross section. However, under usual process conditions the meltpool length is significantly bigger than the meltpool width [42], thus resulting in a meltpool that is big enough to contain at least one particle of the added elements for all investigated conditions. Besides particle incorporation in the meltpool the weld track size clearly shows, that the material is remelted multiple times during L-PBF (layerthickness: 50 µm, hatch distance: 120 µm), thus further homogenizing the in-situ alloyed material.

Since at this point an inhomogeneous element distribution is only ruled out for a single sample, there is still the need to verify that no segregation of the powder systems in the build plane occurred, thus causing concentration variations between multiple samples on build platform. Possible reasons for this could be influences during processing, like recoating or powder transportation by the gas stream. To investigate this matter, six cubical samples (dimension: 6 mm × 6 mm x 6 mm) were built randomly distributed across the build platform (see Fig. 7) with the Ti Mo_{eq}7 powder system. EDS-measurements (area scan, 3 mm × 3 mm) on cross-sections of this cubes presented in Table 5 are very close to each other and no deviations from the target concentration can be observed. Hence, influences of the recoating process or the gas stream are either very small or not present at all. The same measurements were also done for the Ti Mo_{eq}25 powder system, which led to similar results. Based on this data it is concluded, that in-situ alloying had no negative impact on the homogeneity of the element distribution neither in build direction nor in the build plane.

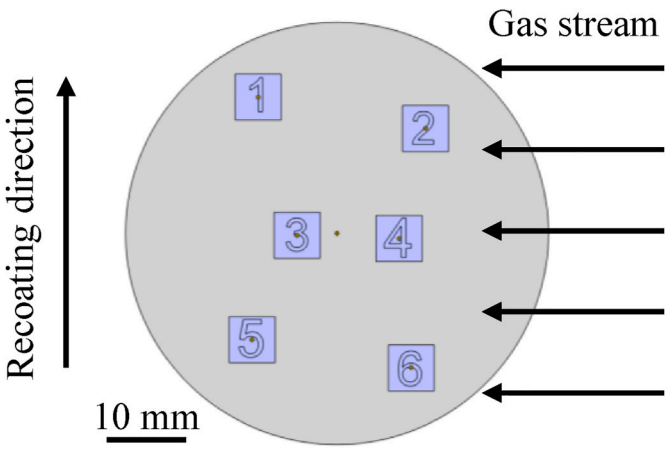

Fig. 7. Distribution of the samples from Table 5 across the build platform.

Table 5
Element composition in dependence of the position on the build plate measured by EDS area scans of polished cross sections (average of five measurement areas of 400 × 400 µm^2 with standard deviation); in brackets: target values.

Number	Ti wt.%	Al wt.%	V wt.%	Fe wt.%
1	82.7 ± 0.1 (82.5)	5.2 ± 0.2 (5.5)	10.0 ± 0.2 (10.0)	2.1 ± 0.1 (2.0)
2	82.6 ± 0.2 (82.5)	5.5 ± 0.1 (5.5)	9.9 ± 0.1 (10.0)	1.9 ± 0.1 (2.0)
3	82.8 ± 0.1 (82.5)	5.3 ± 0.2 (5.5)	10.1 ± 0.1 (10.0)	1.9 ± 0.0 (2.0)
4	82.7 ± 0.2 (82.5)	5.4 ± 0.1 (5.5)	9.8 ± 0.1 (10.0)	2.0 ± 0.1 (2.0)
5	82.6 ± 0.3 (82.5)	5.3 ± 0.1 (5.5)	10.2 ± 0.2 (10.0)	2.1 ± 0.1 (2.0)
6	82.7 ± 0.2 (82.5)	5.2 ± 0.2 (5.5)	10.2 ± 0.2 (10.0)	1.8 ± 0.1 (2.0)

The results of the EDS line scans on samples made from each of the investigated alloy compositions are summarized in Table 6. The achieved compositions are close to the target compositions. However, a small amount of V and especially of Fe was lost during processing. Possible reasons for this are selective element evaporation during L-PBF as previously measured for Ti–6Al–4V e.g. in Ref. [43] or a selective loss of certain powder fractions during handling, sieving and processing. The alloying element with the lowest boiling point present in the samples is

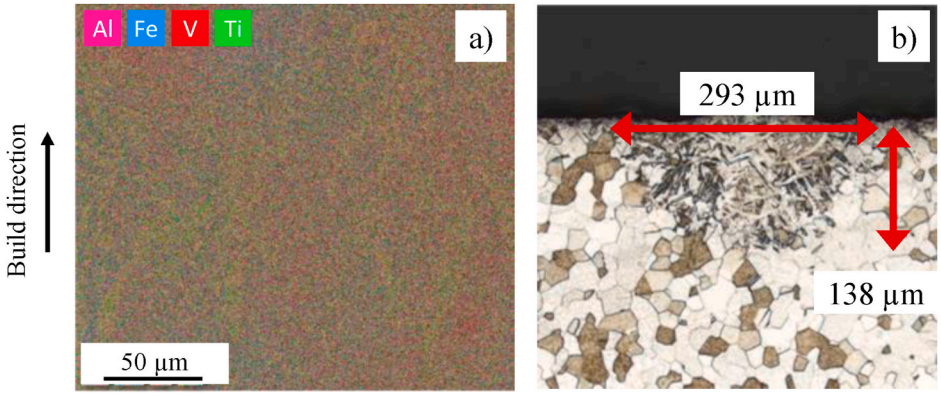

Fig. 6. a): Qualitative EDS area scan of an in-situ alloyed Ti Mo_{eq}7 sample; b) Meltpool dimensions of a single weld track obtained from the parameter set shown in Table 4 in Ti grade 1 sheet metal (thickness: 2 mm).

Table 6
Actual element concentrations in as build sample measured by EDS line scans (length 4.5 mm, n = 1000); target values from Table 1 in brackets.

Notation	Ti wt.%	Al wt.%	V wt.%	Fe wt.%	Mo_{eq}
Ti Mo_{eq}-3.3	89.7 (90.0)	6.0 (6.0)	4.1 (4.0)	0.1 (0.0)	−3.0 (−3.3)
Ti Mo_{eq}5	84.3 (83.8)	5.7 (5.6)	8.9 (9.1)	1.2 (1.5)	3.8 (4.9)
Ti Mo_{eq}7	82.6 (82.5)	5.5 (5.5)	9.9 (10.0)	1.9 (2.0)	6.7 (7.1)
Ti Mo_{eq}10	80.4 (80.1)	5.4 (5.3)	11.5 (12.0)	2.3 (2.5)	8.8 (10.0)
Ti Mo_{eq}15	89.5 (88.1)	0.1 (0.0)	8.2 (8.9)	2.8 (3.0)	13.5 (14.7)
Ti Mo_{eq}20	85.2 (83.9)	0.1 (0.0)	11.5 (12.0)	3.2 (4.2)	17.0 (20.1)
Ti Mo_{eq}25	81.5 (79.9)	0.1 (0.0)	14.4 (15.1)	4.1 (5.0)	21.4 (24.7)

Al (2470 °C [38]). Hence, if selective evaporation during L-PBF would be the reason for the loss of alloying elements, it is to be assumed that Al suffers the highest concentration losses. However, according to Table 6 no such Al loss is evident for neither alloy composition that contained Al. An effect of the process parameters on evaporation is excluded for this specific study, since all samples were built with the same parameter set (see Table 4). Consequently, it is concluded, that losses during sieving of the powder mixtures prior or in-between build jobs are responsible for the reduced Fe content. This assumption is supported by the particle shape and size of the water atomized Fe powder shown in Fig. 3 and Table 2 respectively, which might reduce the penetrability through a sieve compared to the other powder fractions. The slightly lower V content might be due to the extremely fine fractions of the milled V powder (see Fig. 3), which are more prone to being affected by the gas stream during processing or which might also be lost during handling and sieving. Despite these minor deviations, it is shown that in-situ alloy formation in L-PBF is successful and a homogeneous element distribution in build direction as well as in the build plane was achieved. The actual element concentrations in the resulting L-PBF samples are very close to the target concentrations.

3.2. Mechanical properties

Having verified the element composition of the samples, the mechanical properties are discussed in the following. It is pointed out, that the aim of the heat-treatment was to achieve a thermodynamically stable material condition to support the investigations. Hence, the values do not reflect the full potential of (metastable) β-Ti alloys. For this purpose, solution annealing and quenching followed by precipitation hardening would be a more promising approach [20]. It is also noted that comparing the compression test results with tensile properties from literature should be done with caution. E.g. Gao et al. [44] report differences in the compressive and tensile properties for alloys with intermediate β-stabilization with a Mo_{eq} between 9 and 16, that contain metastable phases. The reasons for this are differences in the stress induced phase transformation in dependence of the load direction. This behavior has to be analyzed in subsequent work by investigating the tensile properties of selected alloys. The yield strength and fracture stain/maximum strain is discussed here. Typical stress/strain curves of selected samples are attached in appendix section A1.

One result of the compression tests is the yield strength representing the stress when the material starts to plastify. The values plotted in Fig. 8 show that the yield strength is influenced by the alloy composition and the heat-treatment condition. Comparability of the results of Ti Mo_{eq}15 and Ti Mo_{eq}20 is limited due to the formation of single large sized cracks during L-PBF. This is a direct result of the alloy composition and the conditions during L-PBF and couldn't be avoided. The reasons for this behavior are investigated and discussed in the following section on microstructure formation. In the reference state (Ti Mo_{eq}-3.3 or Ti–6Al–4V respectively), the compression yield strength is 1254 ± 12 MPa, which is in accordance with investigations in Ref. [45]. In comparison, the yield strength increased for Ti Mo_{eq}5 (1384 ± 66 MPa) and Ti Mo_{eq}7 (1439 ± 66 MPa), but it decreased significantly for Ti Mo10 (957 ± 25 MPa). The highest yield strength was reached for Ti Mo_{eq}15 at 1682±88 MPa, whereas it decreased again for Ti Mo_{eq}20 and Ti Mo_{eq}25 compared to Ti Mo_{eq}15. In case of Ti Mo_{eq}15 and Ti Mo_{eq}20 the spread was relatively high compared to the other parameter combinations. This indicates possible defect formation during L-PBF of the alloys Ti Mo_{eq}15 and Ti Mo_{eq}20. In as-built condition only the yield strength of the alloys Ti Mo_{eq}10 and Ti Mo_{eq}25 was lower than the yield strength of the reference alloy Ti6Al4V (Ti Mo_{eq}-3.3). An increase of Mo_{eq} does not result in a linear relation of yield strength and alloy composition. In the first instance, this seems to contradict the working hypothesis, that a higher Mo_{eq} of a given Ti-alloy promotes the formation of β-phase also during L-PBF and consequently increases the ductility of L-PBF processed material. This indicates that more complex metallurgical mechanisms govern the evolution of the mechanical properties in dependence of the alloy composition, which are discussed in the course of this work. The heat-treatment performed at 850 °C in general decreased the yield strength. Only the alloys Ti Mo_{eq}25 and Ti Mo_{eq}10 showed almost no change in mechanical properties following the heat-treatment. This

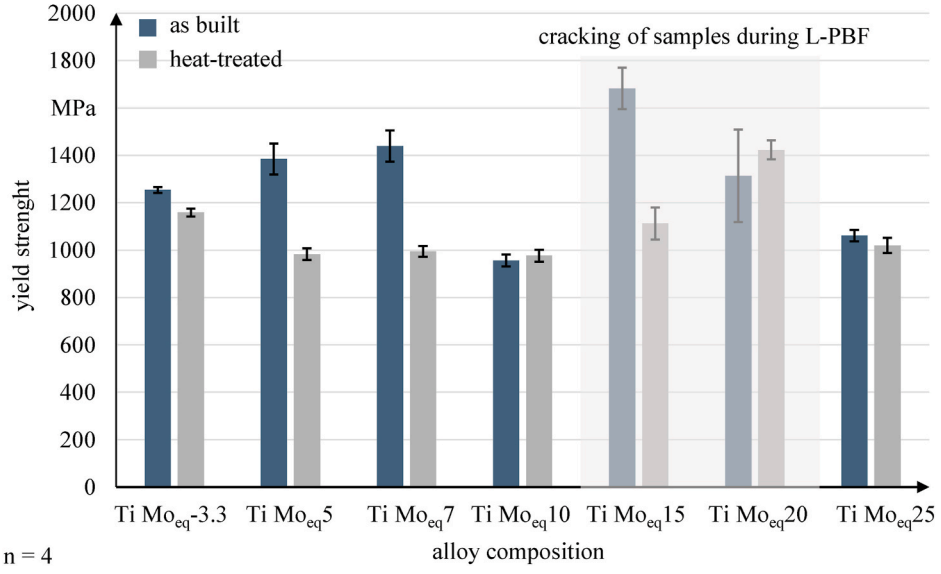

Fig. 8. Compression yield strength in dependence of the alloy composition (see Table 6) and the heat-treatment; cracking of Ti Mo_{eq} 15 and Ti Mo_{eq} 20 during L-PBF (see Fig. 10).

raises the assumption that no major change in the microstructure occurred during the heat-treatment of these alloys.

The fracture strain/maximum strain of the investigated alloys in as-built and in heat-treated condition indicating the point when the material breaks or the preset limit of 50% strain is reached is plotted in Fig. 9.

With a fracture strain of 0.18 ± 0.01 in as-built condition the reference alloy Ti Mo_{eq}-3.3 is again in good accordance with values reported in literature [45]. The addition of the β-phase stabilizing elements V and Fe resulted in a significant drop in fracture strain for the alloys Ti Mo_{eq}5 and Ti Mo_{eq}7. Ti Mo_{eq}10 showed again a very ductile material behavior with a fracture strain of 0.30 ± 0.03 and surpassed the reference alloy Ti Mo_{eq}-3.3. The fracture strain of the alloys Ti Mo_{eq}15 and Ti Mo_{eq}20 scatters in a wide range thus substantiating the assumption, that severe material defects are present in the samples. Alloy Ti Mo_{eq}25 exhibited a very ductile material behavior with a fracture strain of at least 0.50. However, for Ti Mo_{eq}25 the specimens do not break but the maximum upset of the test is reached, which is set to 0.5 (pre-defined end of test). Tensile tests, which are planned for selected alloys in future work, are required to determine the actual fracture strain. The heat-treatment in general increased the fracture strain, which is well in accordance with the reduced yield strength. The most significant increase in fracture strain was observed for the samples Ti Mo_{eq}5 and Ti Mo_{eq}7. This raises the assumption, that the low fracture strain in as-built condition is related to the thermal conditions during L-PBF. Very high fracture strain values were also measured for the alloys Ti Mo_{eq}10 and Ti Mo_{eq}25 in heat-treated condition. Since the measurements stopped at a maximum strain of 0.50 it cannot be determined whether the heat-treatment leads to an increase in fracture strain of alloy Ti Mo_{eq}25. Additional information on the mechanical properties of the material is provided in form of hardness measurements (HV1) in appendix section A2. The results are in good agreement with the compression tests and facilitate at least some degree of comparability for the crack affected samples Ti Mo_{eq}15 and Ti Mo_{eq}20. To gain an understanding of the effects observed in the compression test data further results are presented in the following.

3.3. Microstructure

The L-PBF processed material were analyzed extensively by metallographic methods, EBSD and x-ray diffraction, to get information on the microstructure and the element composition and distribution. The resulting findings are discussed in the following. First of all, light microscopy images (shown in Fig. 10) are investigated. All samples show a high relative density above 99.8% and are free of typical defects related to L-PBF [42] like lack of fusion, defects caused by spatters and deep penetration welding defects. In contrast to cracking, which is in general related to metallurgical effects, these kinds of defects are governed to a great extent by thermo-physical material properties and the laser parameters (e.g. power, scan speed, spot size).

An interesting finding of the present study is, that obviously all alloy compositions could be processed with high relative density using the same parameter set (see Table 4). In Ref. [46] Ye et al. discuss the laser-beam/matter interaction and the scaling behavior associated with L-PBF. One major finding of this study is that the process behavior and especially the meltpool depth normalized by the beam diameter d^* occurring during L-PBF are highly related to the melting enthalpy H_m and absorptivity A of the material and the so called thermal diffusion length L_{th} which is a function of the thermal diffusivity D_{th}, the scan speed v and the beam diameter r [46]:

$$d^* = K\beta L_{th} \tag{1}$$

With K being a constant prefactor compensating the differences between the actual meltpool and the simplified model [46] and the normalized enthalpy β being a function of A, H_m, r, v, D_{th} and the laser power P_L [46]:

$$\beta = \frac{AP_L}{\pi H_m \sqrt{D_{th} v r^3}} \tag{2}$$

Ye et al. evaluated the theoretical findings with experimental results for the alloys Ti6Al4V, In625 and 316 L [46]. Their data shows a good fit between theory and experiment for process parameters relevant for L-PBF ($R^2 = 0.98$). Comparing the results of the present study and the findings of Ye at al. it can be concluded that alloys with a similar thermal diffusion length L_{th}, absorptivity A and specific melting enthalpy H_m are

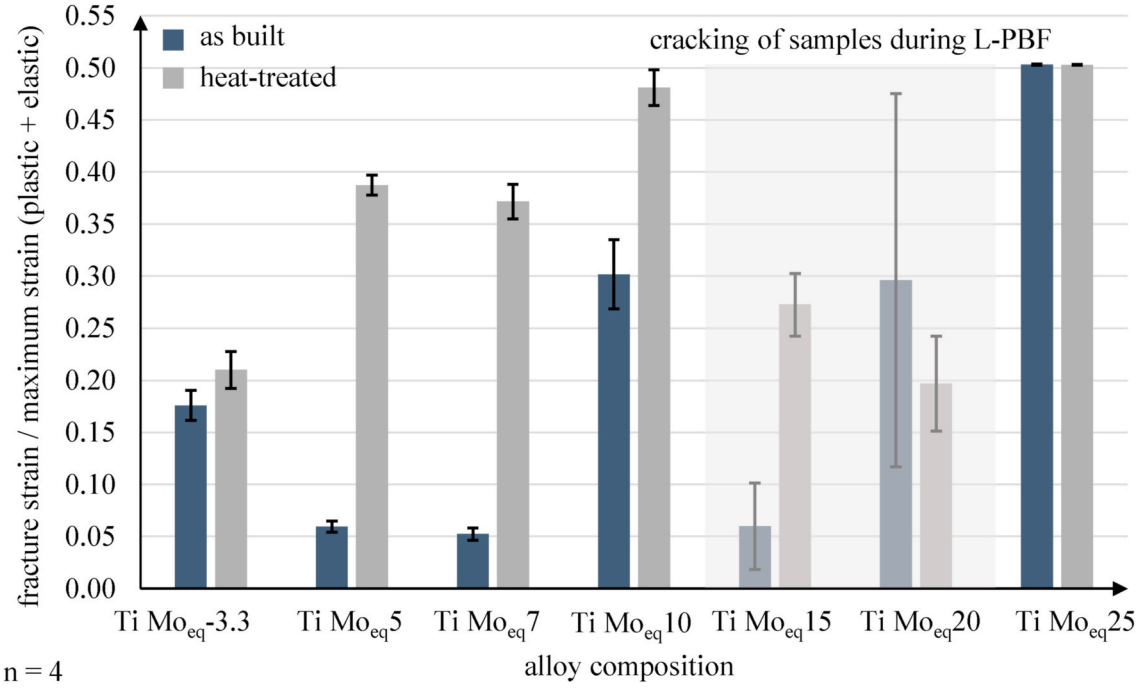

Fig. 9. Fracture strain/Maximum strain obtained by compression tests in dependence of the alloy composition (see Table 6) and the heat-treatment; cracking of Ti Mo_{eq} 15 and Ti Mo_{eq} 20 during L-PBF (see Fig. 10).

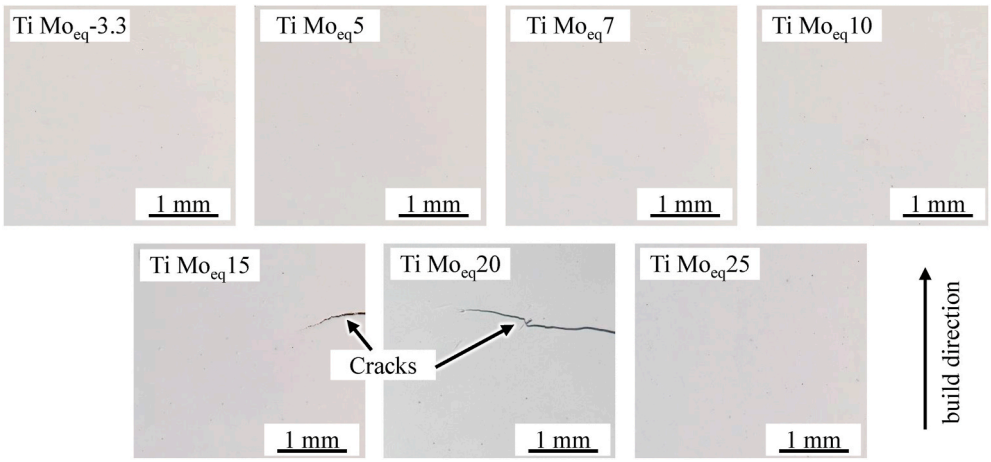

Fig. 10. Microsections of L-PBF samples with varying alloy composition (see also Table 6).

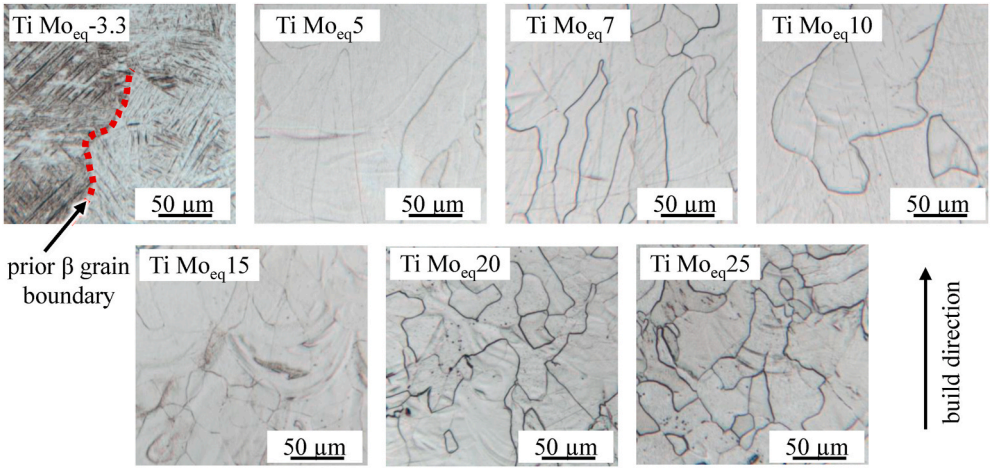

Fig. 11. Microstructure in as-built condition in dependence of the alloy composition (see also Table 6).

processable by L-PBF using similar parameter sets. In return, alloys with different material-specific thermo-physical parameters would show a different process behavior and require different process parameters.

The thermal diffusivity D_{th} and the specific melting enthalpy H_m for the alloys Ti Mo$_{eq}$-3.3 and Ti Mo$_{eq}$25 that feature the greatest differences regarding the alloy composition in our study are compared with stainless steel 316 L. 316 L is a common L-PBF alloy, but shows a different process behavior than Ti6Al4V and requires significantly different process parameters for producing sound parts [47]. The values for all three alloys are listed in Table 7. The thermal diffusivity and the specific melting enthalpy are calculated using the software JMatPro Version 11.2 (Sente Software Ltd., United Kingdom) [48]. The effective absorptivity, that was determined for L-PBF conditions, was taken from Ref. [46] for Ti Mo$_{eq}$-3.3 (Ti6Al4V) and 316 L and estimated for Ti Mo$_{eq}$25. Despite the considerable differences in the alloy composition between Ti Mo$_{eq}$-3.3 and Ti Mo$_{eq}$25 the calculated thermal diffusivity and specific melting enthalpy differ only about 13% and 9% respectively. Compared with the stainless steel 316 L, these differences are small. This explains the overlapping process window for all investigated alloys. A more general conclusion resulting from this considerations is that at least when alloying with Fe, Al and V the alloy composition and hence the material properties (see Figs. 8 and 9) of the resulting material can be varied in a wide range, while maintaining comparable thermo-physical properties and consequently a comparable process behavior. Hence, for future applications of derivatives of the investigated alloys, no extensive process development but rather a slight adaption of existing process parameter sets for Ti6Al4V is expected.

Table 7
Thermal diffusivity and specific melting enthalpy of the alloys Ti Mo$_{eq}$-3.3, Ti Mo$_{eq}$25 and for comparison 316 L calculated with JMatPro [48], Absorptivity from Ref. [46].

	Thermal diffusivity (m^2/s)	Specific melting enthalpy (J/cm^3)	Absorptivity
Ti Mo$_{eq}$-3.3	10.6×10^{-6}	6433	0.26
Ti Mo$_{eq}$25	9.37×10^{-6}	5899	~0.26
316 L	5.38×10^{-6}	8058	0.28

However, despite the absence of fusion defects, a few large cracks, perpendicular to the build direction, starting from the contour of the samples are observed for the alloy compositions Ti Mo$_{eq}$15 and Ti Mo$_{eq}$20 (see Fig. 10). This is in good accordance with the compression test data plotted in Figs. 8 and 9 that shows a strong spread of the results, hence indicating material defects.

Solidification cracking, as described e.g. in Ref. [49], is excluded as cause of the cracking due to the size, number and direction of the cracks. Instead cold cracking as a result of a brittle material behavior and the internal stress induced by the L-PBF process [50] is assumed to be the reason for cracking of the alloys Ti Mo$_{eq}$15 and Ti Mo$_{eq}$20. The reasons for this brittle material behavior are discussed in the following sections.

Fig. 11 shows the microstructure of all seven alloys in as-built condition, while the heat-treated condition is depicted in Fig. 12. The

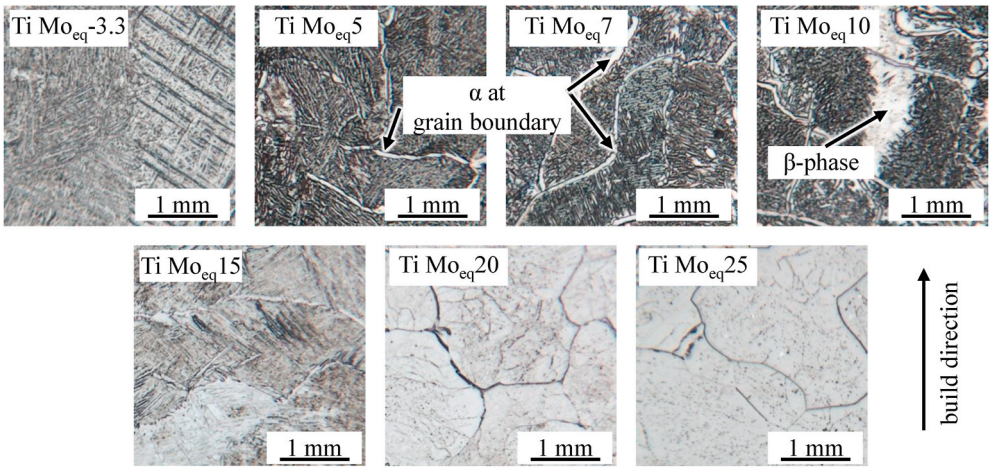

Fig. 12. Microstructure after heat-treating at 850 °C in dependence of the alloy composition (see also Table 6).

reference alloy Ti Mo_{eq}-3.3 forms a typical α′-martensitic structure with a super-structure of columnar prior β-grains still visible. An obvious effect of the addition of β-phase stabilizing elements is the suppression of α′-martensite formation during L-PBF. Even the lowest alloyed sample Ti Mo_{eq}5 does not show any sign of the typical needlelike martensitic structure. Compared to the heat-treated samples, the further interpretation of the as-built microstructures shown in Fig. 11 is challenging. The etching only reveals dark grain boundaries and at least for the alloys Ti Mo_{eq}5 and Ti Mo_{eq}15 weak shadows of the meltpools formed by the laser during L-PBF. An explanation for the brittle material behavior of the samples Ti Mo_{eqeq}15 and Ti Mo_{eq}20 as well as for the low fracture strain of the samples Ti Mo_{eq}5 and Ti Mo_{eq}7 in as-built condition (see Fig. 9) cannot be identified in the microsections. To shed light on these effects, further investigations by EDX, EBSD and XRD are presented in the following.

After a heat-treatment at 850 °C and furnace cooling the α′-martensite of alloy Ti Mo_{eq}-3.3 decomposes into fine acicular α-Ti and a small amount of β-phase. The columnar structure of the prior β-grains is still visible after the heat-treatment thus indicating that no recrystallization and no phase change took place and the β-transus temperature of Ti6Al4V was not exceeded. The decomposition of α′-martensite leads to a slight reduction in yield strength and to an increase in ductility, as shown in Figs. 7 and 8. This is well in accordance with the literature [5]. The addition of β-phase stabilizing elements causes in all cases a decrease of the β-transus temperature below the heat-treatment temperature at 850 °C. This is indicated by the microstructural changes during the heat-treatment that are related to recrystallization and formation of new grains. As a result of the heat-treatment at 850 °C and the, compared to the L-PBF process, very slow cooling rates in the furnace, the material is transformed into a more thermodynamically stable condition. The alloys Ti Mo_{eq}5 to Ti Mo_{eq}15 show accumulations of α-phase at β-grain boundaries as well as segregation of α-phase inside the β-grains (see Fig. 13, Ti Mo_{eq}10 HT). It is estimated, that the thickness of the α-regions decreases with increasing Mo_{eq}. This assumption is also supported by the EBSD-measurements. As suggested by the initial working hypothesis, the amount of α-phase appears to decrease with increasing Mo_{eq}. The Ti Mo_{eq}20 and Ti Mo_{eq}25 samples consist almost completely of β-phase (see also Fig. 15). These microstructural properties are mirrored by the compression yield strength and the fracture strain, showing the highest ductility for the highest β-stabilized alloy Ti Mo_{eq}25 with a fracture strain of more than 0.50 (no fracture, pre-defined end of test). Since the cracks cannot be healed during the heat-treatment, the ductility of the defective samples Ti Mo_{eq}15 and Ti Mo_{eq}20 is reduced, despite the high amount of β-phase.

Fig. 13 shows EBSD phase maps of selected samples, while the phase fractions determined by EBSD for all alloys in as build condition as well as in heat-treated condition are summarized in Fig. 14 and Fig. 15 respectively.

In some samples (e.g. Ti Mo_{eq}7 as-built) parts of the scan area could not be resolved by EBSD. The reasons for this are presumably very fine microstructural features and/or strong lattice distortions due to rapid solidification or residual stress induced by the L-PBF process. Since in as-built condition the etched microsections and EBSD images are hard to interpret, XRD-measurements are performed on these samples to gain additional information. Looking at the XRD diffraction patterns plotted in Fig. 16 the unresolved areas are to a vast majority α or α-‘ martensite for the reference alloy Ti Mo_{eq}-3.3 and probably a more or less equal amount of α- and β-phase in the samples Ti Mo_{eq}5 and Ti Mo_{eq}7. The relative intensity of the α-phase peaks of the alloys Ti Mo_{eq}5 and Ti Mo_{eq}7 indicate in any case a higher α-phase fraction in Ti Mo_{eq}5 compared to Ti Mo_{eq}7.

The EBSD measurements as well as the XRD measurements do not distinguish between α-Ti and α’-martensite, since α′-martensite has a very similar lattice structure as α-Ti that is only distorted by alloying elements replacing Ti on lattice positions [51]. However, the etched microsections depicted in Fig. 11 show no indication of α′-martensite in

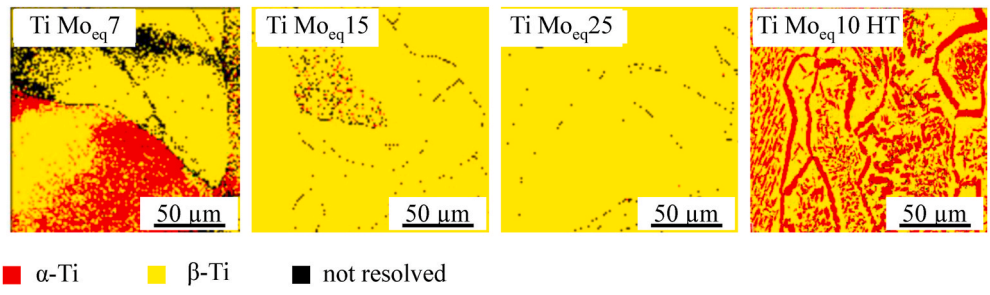

Fig. 13. EBSD phase maps of the samples Ti Mo_{eq}7, Ti Mo_{eq}15 and Ti Mo_{eq}25 in as-built condition and the Ti Mo_{eq}10 sample in heat-treated condition.

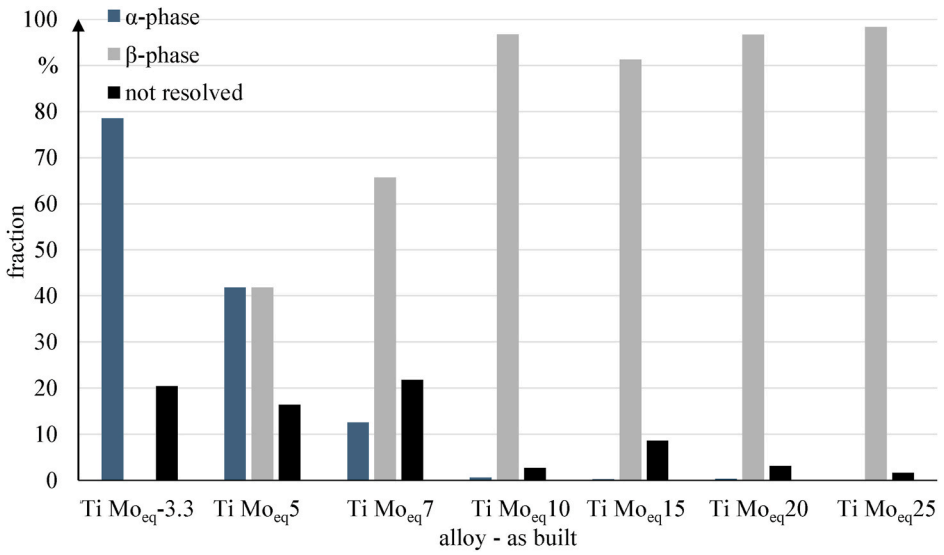

Fig. 14. Phase fractions determined by EBSD in dependence of the alloy composition in as-built condition.

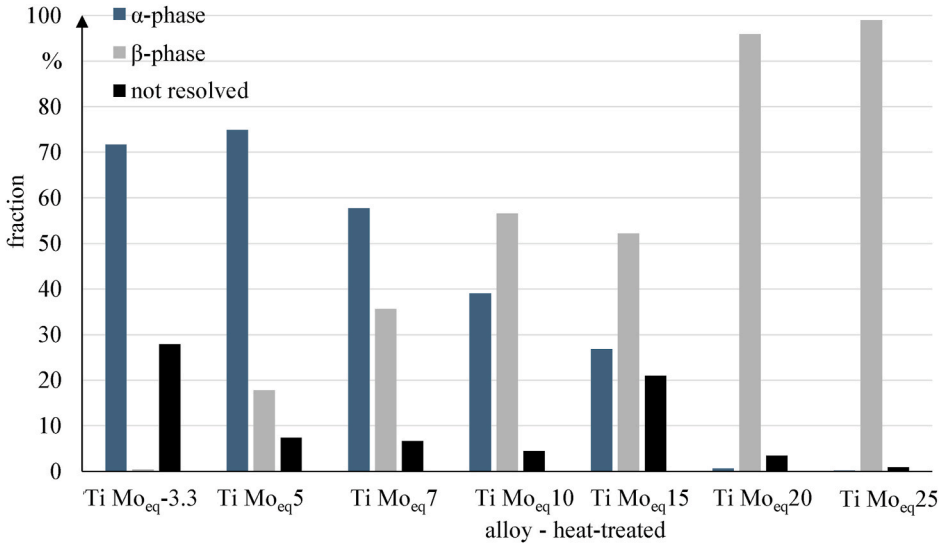

Fig. 15. Phase fractions determined by EBSD in dependence of the alloy composition in heat-treated condition.

any sample other than Ti Mo_{eq}-3.3. The XRD-measurements together with the EBSD measurements confirm the original hypothesis that an increasing Mo_{eq} leads to an increase of β-phase. This is true for the heat-treated samples as well as for the as-built samples. The β-phase fraction of the heat-treated samples is in general lower than in the as-built samples. To achieve a β-phase fraction of more than 90% in as-built condition a Mo_{eq} of 10 is sufficient, while at least a Mo_{eq} of 20 is necessary to reach the same amount of β-phase in heat-treated condition. This is probably due to the very high cooling rates in the range of 10^6 K/s featured by L-PBF [12] that limit diffusion processes and increase the amount of β-phase retained after cooling. The repeated heating and cooling related to neighboring and overlying scan vectors during L-PBF represents some sort of in process heat-treatment, but the dwell time of each pass of the laser beam appears to be too short to cause extensive phase transformations neither of α′-martensite in Ti Mo_{eq}-3.3 nor of β-phase in the other alloys. The high strength and low ductility of the samples Ti Mo_{eq}5 and Ti Mo_{eq}7 observed in the compression test data (see Figs. 8 and 9) in as-built condition is presumably a result of residual stress, a high amount of lattice distortion of the β-phase due to rapid solidification and probably most important beginning α-phase formation in the β-phase matrix. This highly disordered material state is visible in the EBSD-image of Ti Mo_{eq}7 in Fig. 13. Despite the high amount of unresolved areas, the images show, that regions of remaining β-phase and regions that are at least partially transformed to α-phase are intertwined into each other. This microstructure is probably a result of rapid solidification and consequent reheating during L-PBF. This extremely unordered and only partially transformed material condition is presumably the reason for the low ductility and high strength observed during the compression tests. The β-phase stability of the alloy Ti Mo_{eq}10 is high enough to avoid α-phase formation during L-PBF almost completely, as shown in Fig. 14.

This is in good agreement with the threshold for almost complete β-phase stabilization in quenched Ti-alloys reported by Bania et al. [27], thus proving the applicability of the Mo_{eq} for estimating the phase composition of Ti-alloys processed by L-PBF. Because of the high ratio of β-phase the fracture strain of alloy Ti Mo_{eq}10 is with a value of 0.30 ± 0.03 by far higher than the fracture strain of the alloy Ti Mo_{eq}7 and also, due to the increased ductility of the β-phase compared to the α-phase higher than for the reference alloy Ti Mo_{eq}-3.3. Furnace cooling, featuring significantly lower cooling rates than L-PBF however leads to

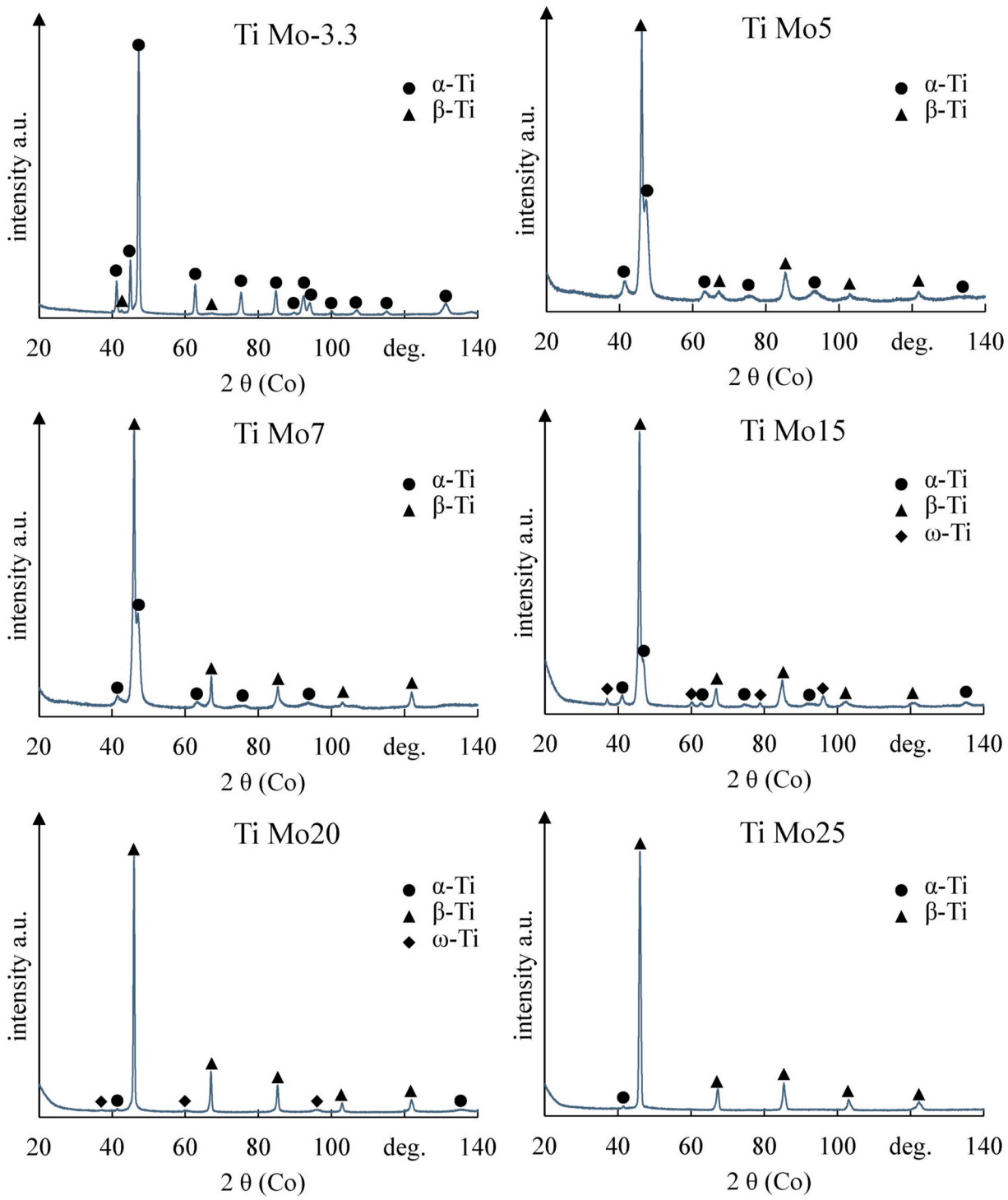

Fig. 16. X-ray diffraction patterns of the samples Ti Mo_{eq}-3.3, Ti Mo_{eq}5, Ti Mo_{eq}7, Ti Mo_{eq}15, Ti Mo_{eq}20 and Ti Mo_{eq}25, all in as-built condition.

about 40% α-phase (see Figs. 15 and 12) for the alloy Ti Mo_{eq}10.

This metastable material condition of the alloy Ti Mo_{eq}10 after L-PBF offers the promising option of combining the mandatory stress relief heat-treatment after L-PBF with a precipitation hardening to tune the material properties as desired, e.g. by further increasing the mechanical strength. Considering the heat-treating recommendations for related commercial alloys (e.g. TIMETAL® 10-2-3) [52] it is assumed that an aging heat-treatment in the temperature range between 500 °C and 600 °C and hence below the β-transus temperature of the alloy would foster α-phase precipitations inside the β-phase matrix, that have a strengthening effect. By varying the heat-treating time, the number and size of the α-phase precipitations and hence the mechanical strength can be controlled. At the same time, the temperature should be high enough to reduce the internal stress induced by L-PBF. A costly and elaborate solution annealing at high temperatures and a subsequent quenching which is the standard heat-treatment strategy for metastable β-Ti alloys [9] would not be necessary to achieve desirable mechanical properties.

Compared to Ti Mo_{eq}10 the alloys Ti Mo_{eq}15 and Ti Mo_{eq}20 show, despite the higher amount of β-phase stabilization, again a very brittle material behavior. This contradicts the simple assumption that a high amount of β-phase results in increased ductility. The reason for this, lies in the formation of ω-Ti during L-PBF in the Mo_{eq} range between 15 und

20. The hexagonal ω-phase can form under certain conditions in Ti- or Zr- alloys [53] and is clearly identified by the characteristic peaks in the XRD patterns of the alloys Ti Mo_{eq}15 and Ti Mo_{eq}20 in as-built condition (see Fig. 16). In contrast to α-phase precipitates in a β-phase matrix, which are in some cases even desired, the ω-phase has a deteriorating effect on the material properties. The coherent or semicoherent ω-phase inside the β-phase matrix induces a planar dislocation distribution thus effectively supporting early crack formation and material embrittlement [54]. According to Refs. [51,55] ω-phase forms by transformation of β-phase. Both, an athermal and an isothermal mechanism are possible. The athermal transformation is either induced by rapid cooling from the β-phase field [56] or by deformation/stress [57]. Isothermal formation of ω-phase can occur in the temperature range between 350 °C and 550 °C [54]. Especially Ti-alloys with intermediate β-phase stabilization (as it is the case for Ti Mo_{eq}15 and Ti Mo_{eq}20) tend to form ω-phase. With respect to the present work, it is hard to determine the underlying ω-phase formation mechanism. Considering the complex thermal conditions during L-PBF and the internal stress induced by the laser process, all three mechanisms are plausible. Owing to the small meltpool dimensions in the range of a few 100 µm, high cooling rates of 10^6 K/s are common during L-PBF [12]. This supports the hypothesis of an athermal ω-phase formation. However, also an isothermal formation seems possible, since it can be assumed, that temperatures between 350 °C and 550 °C are reached multiple times during the melting of neighboring and overlying scan vectors, thus the dwell time is estimated to be only in the ms-range. Since at this point no mechanism can be excluded, further investigations are necessary, to determine the actual process that leads to ω-phase formation.

For Ti-alloys with an intermediate degree of β-phase stabilization the formation of orthorhombic α''-martensite instead of hexagonal α′-martensite is reported in literature [58], which might affect the material properties [59]. Kazantseva et al. [60] showed by TEM-measurements that along with α′-martensite also a small amount of a''-martensite is formed during L-PBF of Ti6Al4V ELI. With respect to the present study, no orthorhombic phase could be detected by XRD. Hence, it is assumed that the amount of α''- martensite in as-built samples is at least small. However, further investigations e.g. by TEM-measurements are necessary to investigate the presence of α''-martensite in L-PBF samples with greater precision. Besides the formation during L-PBF, the β → α''-martensite phase transformation might still occur during compression testing and could consequently affect the test results. This stress induced phase transformation finds e.g. application in the development of Titanium alloys with superelastic material properties [61]. This material behavior is characterized by double yielding [62]. With respect to the compression test performed in the present work, no clear sign of double yielding was observed. However, in case of Ti Mo_{eq}15 and Ti Mo_{eq}20 scattering of the results is high due to crack formation during L-PBF. In addition the increasing cross section during compression testing complicates analysis. Consequently, the presence of high amounts of α''-martensite in as built condition can be ruled out, but further investigations specifically addressing the topic of stress induced α''-martensite formation in L-PBF samples are required.

The alloy Ti Mo_{eq}25 is again free of ω-phase due to the high degree of β-phase stabilization. Also only a negligible amount α-phase is present in the sample Ti Mo_{eq}25 indicating an almost fully β-stabilized alloy. Consequently, a high maximum strain of at least 0.50 (predefined end of test) is observed and no cracking during L-PBF of occurs. When designing future metastable β-Ti alloys, an intermediate β-phase stabilization with a Mo_{eq} ranging between 15 and 20 should be avoided or further measures like the addition of a small amount of α-stabilizers like Al [20] should be taken into account, to avoid the detrimental formation of ω-Ti during L-PBF.

4. Summary and conclusion

Seven Ti-alloys with an increasing amount of the β-phase stabilizers Fe and V were prepared by L-PBF and in-situ alloy formation. The Molybdenum equivalent (Mo_{eq}) as an indicator for the β-phase stability of a given alloy composition was varied from −3.3 to 25 and the L-PBF manufactured samples were investigated. Based on the results, the following conclusions are drawn:

- The Mo_{eq} can be a useful guideline for estimating the amount of β-phase in L-PBF processed Ti-alloys. A prediction of the resulting material properties only based on the Mo_{eq} is, however, difficult because more complex metallurgical effects (e.g. ω-phase formation) play an important role.
- Already the lowest addition of Fe and V (Mo_{eq} 5) suppressed the formation of at least the majority of α′-martensite, which is otherwise typical for L-PBF of Ti6Al4V (Mo_{eq} −3.3) and increased the amount of retained β-phase. This proves, that already small additions of alloying elements can significantly alter the resulting material properties of L-PBF processed materials.
- A Mo_{eq} of 10 is sufficient to retain more than 90% β-phase after L-PBF, thus increasing the fracture strain to 0.26. This metastable material condition offers the promising opportunity of tailoring the material properties by precipitation strengthening (formation of α-phase) directly after L-PBF without the need of an elaborate solution annealing and quenching as it is necessary in conventional processing routes for metastable β-Ti alloys.
- Following a heat-treatment at 850 °C and furnace cooling, thus applying a significantly lower cooling rate than during L-PBF, a Mo_{eq} of at least 20 is necessary to receive more than 90% β-phase. This demonstrates the sensitivity of the investigated alloys to the cooling rate.
- The Mo_{eq} region between 15 and 20 results in ω-phase precipitation and a detrimental embrittlement of the material resulting in cracking during L-PBF despite a high amount of β-phase. Without further measures to avoid ω-phase formation the Mo_{eq} range between 10 and 20 should be avoided when designing future alloys for L-PBF applications. This also demonstrates that the Mo_{eq} alone is unsuited for predicting material properties.
- A Mo_{eq} of 25 is sufficient to avoid ω-phase formation and to receive a very ductile material consisting almost completely of β-phase and featuring a very high fracture strain exceeding 0.50.
- In-situ alloy formation of Ti–Al–V–Fe alloys with a high homogeneity of the element distribution is possible. Common defects like incomplete mixing in the meltpool or undissolved particles can be avoided. In the future, this facilitates an efficient development of L-PBF specific alloys.
- When alloying Ti with Fe, Al and V the alloy composition and hence the resulting mechanical properties can be varied in a wide range, while still maintaining comparable thermo-physical properties and hence a similar process behavior and similar process parameters. This indicates that future derivatives of the investigated alloys can be processed by L-PBF without the necessity of an elaborate process development, but rather a slight adaption of existing parameter sets for Ti6Al4V.

The investigations prove that β-stabilized Ti-alloys are a very versatile class of materials with promising properties. The alloys are in general suitable for L-PBF. However, they possess a complex metallurgy that needs to be considered when selecting alloy compositions for L-PBF applications. A prediction of material properties only based on the Mo_{eq} not possible. However, the Mo_{eq} can provide a first lead for estimating the β-phase stability even in as built condition of β-stabilized Ti-parts manufactured by L-PBF.

CRediT authorship contribution statement

Florian Huber: Conceptualization, Methodology, Investigation, Writing – original draft. **Thomas Papke:** Investigation, Writing – review

& editing. **Constantin Kauffmann:** Investigation. **Richard Rothfelder:** Writing – review & editing. **Pavel Krakhmalev:** Writing – review & editing. **Marion Merklein:** Writing – review & editing, Supervision, Funding acquisition. **Michael Schmidt:** Writing – review & editing, Supervision, Funding acquisition.

Declaration of competing interest

The authors declare no conflict of interest.

Acknowledgements

The authors gratefully acknowledge funding by the German Research Foundation (DFG): Collaborative Research Center 814: Additive Manufacturing - Subproject B5 and Erlangen Graduate School in Advanced Optical Technologies (SAOT). Funding by the German Federal Ministry for Economic Affairs and Energy in the framework of the Aviation Research Program for project ADHEA is acknowledged. The authors also want to thank Prof. Dr.-Ing. Ulrich Tetzlaff for supporting us with XRD-measurements.

Appendix

A1: Compressive stress/strain curves

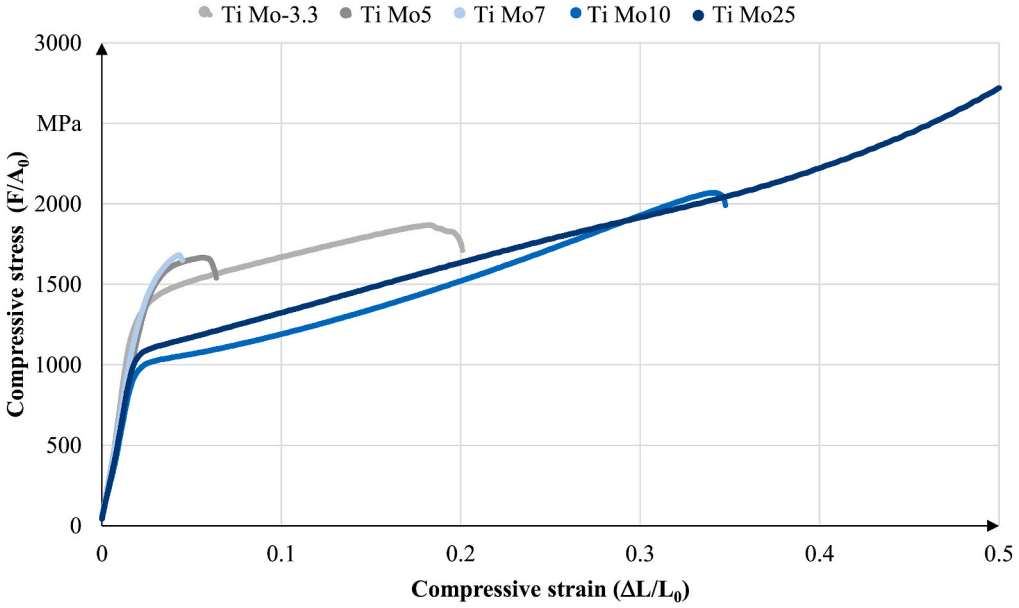

A1 – Fig. 1. Compressive stress/strain curves of typical samples; as built condition; sample geometry: Ø 6 mm × 9 mm; F: force; A_0: initial cross-section area, L_0: initial length

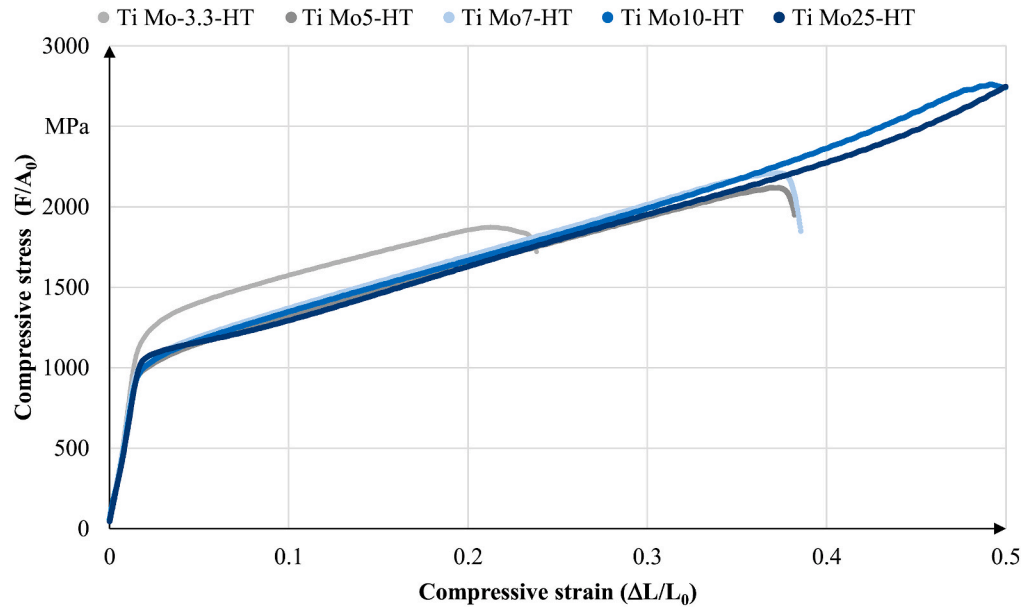

A1 – Fig. 2. Compressive stress/strain curves of typical samples; heat-treated condition (850 °C for 2 h); sample geometry: Ø 6 mm × 9 mm; F: force; A0: initial cross-section area, L0: initial length

A2: Hardness measurements

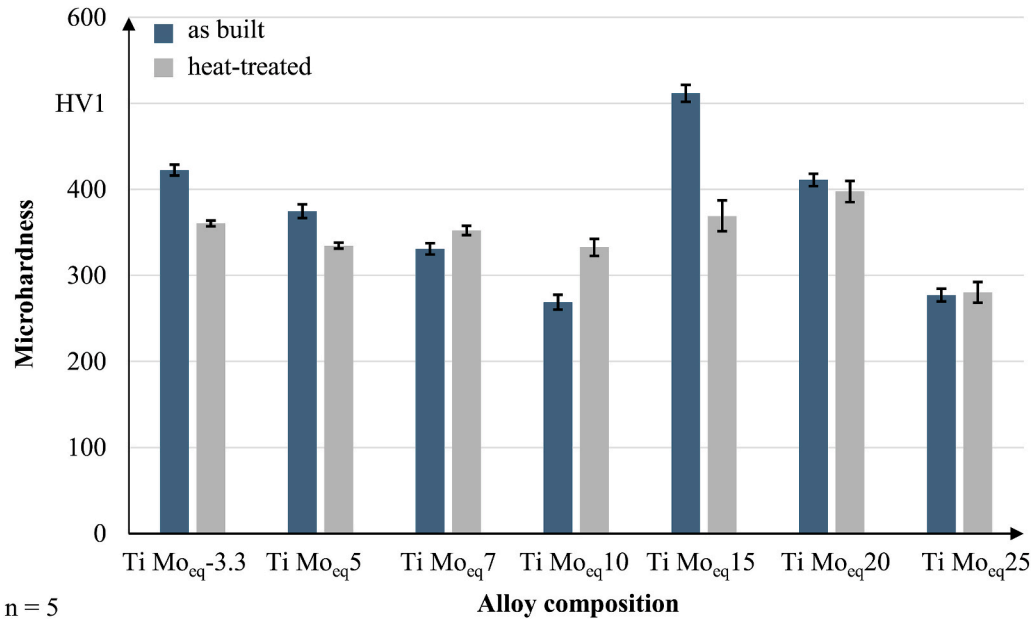

A2 – Fig. 1. Microhardness (HV1) in dependence of the alloy composition; mean value and standard deviation of five measurement points

References

[1] Wohlers Associates, Wohlers Report 2019, Wohlers Associates, Inc., 2019.
[2] E. Uhlmann, R. Kersting, T.B. Klein, M.F. Cruz, A.V. Borille, Additive manufacturing of titanium alloy for aircraft components, Procedia CIRP 35 (2015) 55–60, https://doi.org/10.1016/j.procir.2015.08.061.
[3] F.H. (Sam) Froes, Titanium for medical and dental applications—an introduction, Elsevier Inc. (2018), https://doi.org/10.1016/b978-0-12-812456-7.00001-9.
[4] B. Dutta, F.H. Froes, Additive manufacturing of titanium alloys, Adv. Mater. Process. 172 (2014) 18–23, https://doi.org/10.1016/b978-0-12-804782-8.00001-x.
[5] B. Vrancken, L. Thijs, J.P. Kruth, J. Van Humbeeck, Heat-treatment of Ti6Al4V produced by selective laser melting: microstructure and mechanical properties, J. Alloys Compd. 541 (2012) 177–185, https://doi.org/10.1016/j.jallcom.2012.07.022.
[6] A.M. Beese, B.E. Carroll, Review of mechanical properties of Ti-6Al-4V made by laser-based additive manufacturing using powder feedstock, JOM 68 (2016) 724–734, https://doi.org/10.1007/s11837-015-1759-z.
[7] G. Additive, GE Additive M2 series, (n.d.). https://www.ge.com/additive/additive-manufacturing/machines/m2series5 (accessed February 17, 2020).
[8] SLM Solutions Group AG, Metal Powder Brochure, (n.d.). https://www.slm-solutions.com/fileadmin/user_upload/Metal_Powder_1912_02_Web.pdf.
[9] C. Leyens, M. Peters, Titanium an titanium alloys. https://doi.org/10.1002/3527602119, 2003.
[10] L. Thijs, F. Verhaeghe, T. Craeghs, J. Van Humbeeck, J.-P. Kruth, A study of the microstructural evolution during selective laser melting of Ti–6Al–4V, Acta Mater. 58 (2010) 3303–3312, https://doi.org/10.1016/j.actamat.2010.02.004.
[11] T. Mukherjee, H.L. Wei, A. De, T. DebRoy, Heat and fluid flow in additive manufacturing – Part II: powder bed fusion of stainless steel, and titanium, nickel and aluminum base alloys, Comput. Mater. Sci. 150 (2018) 369–380, https://doi.org/10.1016/j.commatsci.2018.04.027.
[12] P.A. Hooper, Melt pool temperature and cooling rates in laser powder bed fusion, Addit. Manuf. 22 (2018) 548–559, https://doi.org/10.1016/j.addma.2018.05.032.
[13] C. Qiu, N.J.E. Adkins, M.M. Attallah, Microstructure and tensile properties of selectively laser-melted and of HIPed laser-melted Ti-6Al-4V, Mater. Sci. Eng. 578 (2013) 230–239, https://doi.org/10.1016/j.msea.2013.04.099.
[14] K. Dietrich, J. Diller, S. Dubiez-Le Goff, D. Bauer, P. Forêt, G. Witt, The influence of oxygen on the chemical composition and mechanical properties of Ti-6Al-4V during laser powder bed fusion (L-PBF), Addit. Manuf. 32 (2020), 100980, https://doi.org/10.1016/j.addma.2019.100980.
[15] N.C. Levkulich, S.L. Semiatin, J.E. Gockel, J.R. Middendorf, A.T. DeWald, N. W. Klingbeil, The effect of process parameters on residual stress evolution and distortion in the laser powder bed fusion of Ti-6Al-4V, Addit. Manuf. 28 (2019) 475–484, https://doi.org/10.1016/j.addma.2019.05.015.
[16] F. Huber, T. Papke, C. Scheitler, L. Hanrieder, M. Merklein, M. Schmidt, In situ formation of a metastable β-Ti alloy by laser powder bed fusion (L-PBF) of vanadium and Iron modified Ti-6Al-4V, Metals 8 (2018) 1067, https://doi.org/10.3390/met8121067.
[17] D. Gu, Y.C. Hagedorn, W. Meiners, G. Meng, R.J.S. Batista, K. Wissenbach, R. Poprawe, Densification behavior, microstructure evolution, and wear performance of selective laser melting processed commercially pure titanium, Acta Mater. 60 (2012) 3849–3860, https://doi.org/10.1016/j.actamat.2012.04.006.
[18] E. Łyczkowska, P. Szymczyk, B. Dybała, E. Chlebus, Chemical polishing of scaffolds made of Ti–6Al–7Nb alloy by additive manufacturing, Arch. Civ. Mech. Eng. 14 (2014) 586–594, https://doi.org/10.1016/j.acme.2014.03.001.
[19] B.M. Peters, J. Kumpfert, C.H. Ward, C. Leyens, Titanium Alloys for Aerospace Applications, 2003, pp. 419–427, https://doi.org/10.1002/adem.200310095.
[20] G. Lütjering, J.C. Williams, Titanium, second ed., Springer, Heidelberg, 2007.
[21] Q. Wang, C. Dong, P.K. Liaw, Structural stabilities of β-Ti alloys studied using a new Mo equivalent derived from [β/(α + β)] phase-boundary slopes, Metall. Mater. Trans. A Phys. Metall. Mater. Sci. 46 (2015) 3440–3447, https://doi.org/10.1007/s11661-015-2923-3.
[22] C.W. Hume-Rothery, William Smallman, R. Haworth, The Structure of Metals and Alloys, The Metals and Metallurgy Trust of the Institute of Metals and the Institution of Metallurgists, 1969.
[23] B.E. Tegner, L. Zhu, G.J. Ackland, Relative strength of phase stabilizers in titanium alloys, Phys. Rev. B Condens. Matter 85 (2012) 3–6, https://doi.org/10.1103/PhysRevB.85.214106.
[24] L.F. Huang, B. Grabowski, J. Zhang, M.J. Lai, C.C. Tasan, S. Sandlöbes, D. Raabe, J. Neugebauer, From electronic structure to phase diagrams: a bottom-up approach to understand the stability of titanium–transition metal alloys, Acta Mater. 113 (2016) 311–319, https://doi.org/10.1016/j.actamat.2016.04.059.
[25] R.P. Kolli, A. Devaraj, A review of metastable beta titanium alloys, Metals 8 (2018) 1–41, https://doi.org/10.3390/met8070506.
[26] H.W. ROSENBERG, Titanium alloying IN theory and practice, in: Sci. Technol. Appl. Titan., Elsevier, 1970, pp. 851–859, https://doi.org/10.1016/B978-0-08-006564-9.50095-6.
[27] P.J. Bania, Beta titanium alloys and their role in the titanium industry, JOM (J. Occup. Med.) 46 (1994) 16–19, https://doi.org/10.1007/BF03220742.
[28] B. Jiang, Q. Wang, D. Wen, F. Xu, G. Chen, C. Dong, L. Sun, P.K. Liaw, Effects of Nb and Zr on structural stabilities of Ti-Mo-Sn-based alloys with low modulus, Mater. Sci. Eng. 687 (2017) 1–7, https://doi.org/10.1016/j.msea.2017.01.047.
[29] C. Zopp, S. Blümer, F. Schubert, L. Kroll, Processing of a metastable titanium alloy (Ti-5553) by selective laser melting, Ain Shams Eng. J. 8 (2017) 475–479, https://doi.org/10.1016/j.asej.2016.11.004.
[30] F. Huber, T. Papke, C. Scheitler, L. Hanrieder, M. Merklein, M. Schmidt, In situ formation of a metastable β-Ti alloy by laser powder bed fusion (L-PBF) of vanadium and Iron modified Ti-6Al-4V, Metals 8 (2018) 1067, https://doi.org/10.3390/met8121067.
[31] I. Polozov, V. Sufiiarov, A. Popovich, D. Masaylo, A. Grigoriev, Synthesis of Ti-5Al, Ti-6Al-7Nb, and Ti-22Al-25Nb alloys from elemental powders using powder-bed fusion additive manufacturing, J. Alloys Compd. 763 (2018) 436–445, https://doi.org/10.1016/j.jallcom.2018.05.325.

[32] S.L. Sing, W.Y. Yeong, F.E. Wiria, Selective laser melting of titanium alloy with 50 wt% tantalum: microstructure and mechanical properties, J. Alloys Compd. 660 (2016) 461–470, https://doi.org/10.1016/j.jallcom.2015.11.141.
[33] I. Yadroitsev, P. Krakhmalev, I. Yadroitsava, Titanium alloys manufactured by in situ alloying during laser powder bed fusion, JOM (J. Occup. Med.) 69 (2017) 2725–2730, https://doi.org/10.1007/s11837-017-2600-7.
[34] P. Krakhmalev, I. Yadroitsev, I. Yadroitsava, O. de Smidt, Functionalization of biomedical Ti6Al4V via in situ alloying by Cu during laser powder bed fusion manufacturing, Materials 10 (2017), https://doi.org/10.3390/ma10101154.
[35] L.C. Zhang, D. Klemm, J. Eckert, Y.L. Hao, T.B. Sercombe, Manufacture by selective laser melting and mechanical behavior of a biomedical Ti–24Nb–4Zr–8Sn alloy, Scripta Mater. 65 (2011) 21–24, https://doi.org/10.1016/j.scriptamat.2011.03.024.
[36] N. Hafeez, S. Liu, E. Lu, L. Wang, R. Liu, W. Lu, L.-C. Zhang, Mechanical behavior and phase transformation of β-type Ti-35Nb-2Ta-3Zr alloy fabricated by 3D-Printing, J. Alloys Compd. 790 (2019) 117–126, https://doi.org/10.1016/j.jallcom.2019.03.138.
[37] J.C. Wang, Y.J. Liu, P. Qin, S.X. Liang, T.B. Sercombe, L.C. Zhang, Selective laser melting of Ti–35Nb composite from elemental powder mixture: microstructure, mechanical behavior and corrosion behavior, Mater. Sci. Eng. 760 (2019) 214–224, https://doi.org/10.1016/j.msea.2019.06.001.
[38] W.M. Haynes, Handbook of Chemistry and Physics, 2017.
[39] M.C.H. Karg, M. Rasch, K. Schmidt, S.A.E. Spitzer, T.F. Karsten, D. Schlaug, C. R. Biaciu, A.I. Gorunov, M. Schmidt, Laser alloying advantages by dry coating metallic powder mixtures with SiOx nanoparticles, Nanomaterials 8 (2018), https://doi.org/10.3390/nano8100862.
[40] J.-P. Kruth, J. Deckers, E. Yasa, R. Wauthlé, Assessing and comparing influencing factors of residual stresses in selective laser melting using a novel analysis method, Proc. Inst. Mech. Eng. Part B J. Eng. Manuf. 226 (2012) 980–991, https://doi.org/10.1177/0954405412437085.
[41] DIN 50106: Testing of Metallic Components - Compression Test at Room Temperature, 2016.
[42] S.A. Khairallah, A.T. Anderson, A. Rubenchik, W.E. King, Laser powder-bed fusion additive manufacturing: physics of complex melt flow and formation mechanisms of pores, spatter, and denudation zones, Acta Mater. 108 (2016) 36–45, https://doi.org/10.1016/j.actamat.2016.02.014.
[43] F. Huber, T. Papke, M. Kerkien, F. Tost, G. Geyer, M. Merklein, M. Schmidt, Customized exposure strategies for manufacturing hybrid parts by combining laser beam melting and sheet metal forming, J. Laser Appl. 31 (2019), 022318, https://doi.org/10.2351/1.5096115.
[44] P. Gao, J. Fan, F. Sun, J. Cheng, L. Li, B. Tang, H. Kou, J. Li, Crystallography and asymmetry of tensile and compressive stress-induced martensitic transformation in metastable β titanium alloy Ti–7Mo–3Nb–3Cr–3Al, J. Alloys Compd. 809 (2019), https://doi.org/10.1016/j.jallcom.2019.151762.
[45] J. Tong, C.R. Bowen, J. Persson, A. Plummer, Mechanical properties of titanium-based Ti–6Al–4V alloys manufactured by powder bed additive manufacture, Mater. Sci. Technol. 33 (2017) 138–148, https://doi.org/10.1080/02670836.2016.1172787.
[46] J. Ye, S.A. Khairallah, A.M. Rubenchik, M.F. Crumb, G. Guss, J. Belak, M. J. Matthews, Energy coupling mechanisms and scaling behavior associated with laser powder bed fusion additive manufacturing, Adv. Eng. Mater. 21 (2019) 1–9, https://doi.org/10.1002/adem.201900185.
[47] SLM Solutions GmbH, SLM 280 Standard Process Parameters, 2018.
[48] JMatPro, (n.d.). https://www.sentesoftware.co.uk/jmatpro.
[49] G. Marchese, G. Basile, E. Bassini, A. Aversa, M. Lombardi, D. Ugues, P. Fino, S. Biamino, Study of the microstructure and cracking mechanisms of hastelloy X produced by laser powder bed fusion, Materials 11 (2018), https://doi.org/10.3390/ma11010106.
[50] A.S. Wu, D.W. Brown, M. Kumar, G.F. Gallegos, W.E. King, An experimental investigation into additive manufacturing-induced residual stresses in 316L stainless steel, Metall. Mater. Trans. A Phys. Metall. Mater. Sci. 45 (2014) 6260–6270, https://doi.org/10.1007/s11661-014-2549-x.
[51] M. Motyka, K. Kubiak, J. Sieniawski, W. Ziaja, Phase transformations and characterization of α + β titanium alloys, Elsevier, 2014, https://doi.org/10.1016/B978-0-08-096532-1.00202-8.
[52] Timet Titanium Metals Corporation, TIMETAL 10-2-3 Property datasheet, 49 (n.d.) 2–3. http://www.timet.com/assets/local/documents/datasheets/metastablebetaalloys/10-2-3.pdf.
[53] D. De Fontaine, N. Paton, J. Williams, The omega phase transformation in titanium alloys as an example of displacement controlled reactions, Acta Metall. 19 (1971) 1153–1162, https://doi.org/10.1016/0001-6160(71)90047-2.
[54] G. Lütjering, J.C. Williams, A. Gysler, Microstructure and mechanical properties OF titanium alloys, in: Microstruct. Prop. Mater., WORLD SCIENTIFIC, 2000, pp. 1–77, https://doi.org/10.1142/9789812793959_0001.
[55] D. Choudhuri, Y. Zheng, T. Alam, R. Shi, M. Hendrickson, S. Banerjee, Y. Wang, S. G. Srinivasan, H. Fraser, R. Banerjee, Coupled experimental and computational investigation of omega phase evolution in a high misfit titanium-vanadium alloy, Acta Mater. 130 (2017) 215–228, https://doi.org/10.1016/j.actamat.2017.03.047.
[56] C.W. Dawson, S.L. Sass, As-quenched form of the omega phase in Zr- Nb alloys, OR Trans. 1 (1970) 2225–2233.
[57] T.S. Kuan, R.R. Ahrens, S.L. Sass, The Stress-induced omega phase transformation in Ti-V alloys, Metall. Trans. A. 6 (1975) 1767–1774, https://doi.org/10.1007/BF02642306.
[58] J.C. Williams, B.S. Hickman, Tempering behavior of orthorhombic martensite in titanium alloys, Metall. Trans. 1 (1970) 2648–2650, https://doi.org/10.1007/BF03038403.
[59] W.F. Ho, C.P. Ju, J.H. Chern Lin, Structure and properties of cast binary Ti-Mo alloys, Biomaterials 20 (1999) 2115–2122, https://doi.org/10.1016/S0142-9612(99)00114-3.
[60] N. Kazantseva, P. Krakhmalev, M. Thuvander, I. Yadroitsev, N. Vinogradova, I. Ezhov, Martensitic transformations in Ti-6Al-4V (ELI) alloy manufactured by 3D Printing, Mater. Char. 146 (2018) 101–112, https://doi.org/10.1016/j.matchar.2018.09.042.
[61] D.C. Zhang, Y.F. Mao, M. Yan, J.J. Li, E.L. Su, Y.L. Li, S.W. Tan, J.G. Lin, Superelastic behavior of a B-type titanium alloy, J. Mech. Behav. Biomed. Mater. 20 (2013) 29–35, https://doi.org/10.1016/j.jmbbm.2013.01.015.
[62] T. Grosdidier, M.J. Philippe, Deformation induced martensite and superelasticity in a β-metastable titanium alloy, Mater. Sci. Eng. 291 (2000) 218–223, https://doi.org/10.1016/S0921-5093(00)00921-7.

Additional unpublished results and discussion of the publication's findings in the context of this thesis:

The publication *"Systematic exploration of the L-PBF processing behavior and resulting properties of β-stabilized Ti-alloys prepared by in-situ alloy formation"* [93] takes up the approach of in-situ alloy formation of metastable β-Ti alloys with Fe and V as β-phase stabilizers that is proposed in [13]. While in [13] only a single alloy composition is investigated, the aim of [93] is to gain a more comprehensive understanding of the effect of in-situ alloy formation with Fe and V additions on the PBF-LB/M process behavior and the resulting properties of Ti-alloys. For this purpose, seven alloy compositions with an increasing degree of β-phase stabilization were processed by PBF-LB/M and the resulting properties were analyzed extensively by light and electron microscopy, x-ray diffraction, compression tests and hardness measurements.

The findings of the publication "*Systematic exploration of the L-PBF processing behavior and resulting properties of β-stabilized Ti-alloys prepared by in-situ alloy formation"* [93] prove that a defect-free processing of five of the investigated seven alloy compositions is possible. The remaining two compositions with an intermediate degree of β-phase stabilization and Ti grade 2 as base alloy suffer from a detrimental ω-phase embrittlement, resulting in cracking during LBF-LB/M (see Figure 13). With respect to the idea of employing in-situ alloy formation for producing Ti-parts with locally different properties, this would pose a serious problem in the manufacturing of transitions between areas with a high degree of β-phase stabilization and areas with a lower degree of β-phase stabilization. Mixing effects during PBF-LB/M would inevitably lead to zones with unfavorable alloy compositions that are prone to ω-phase formation and hence cracking. For this reason, additional measures to avoid ω-phase formation under PBF-LB/M conditions are required.

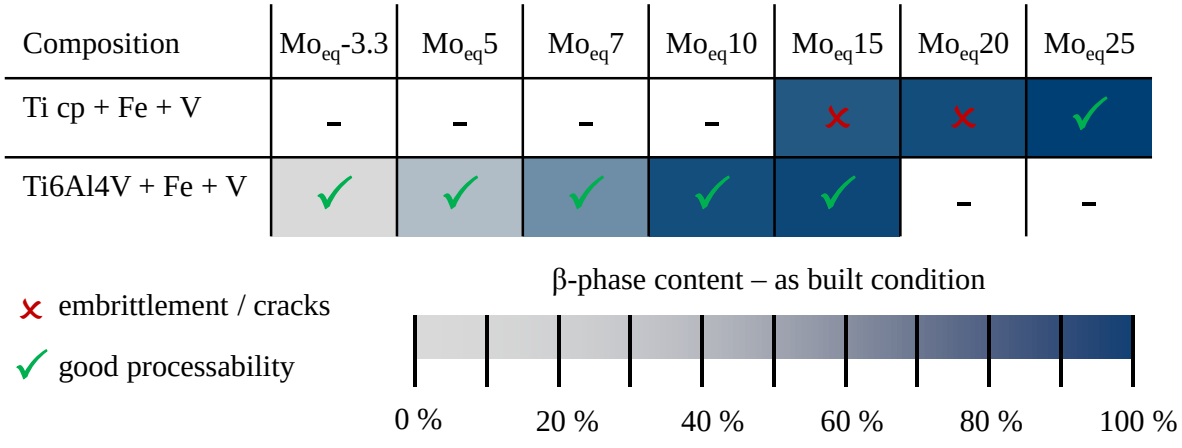

Figure 13: Processability by PBF-LB/M and β-phase content in as built condition in dependence of the Mo_{eq}; data partially extracted from [93]

According to literature [54] one possibility to influence ω-phase formation in Ti-alloys is an Al-addition. To verify this approach, an eighth alloy composition with a Mo_{eq} of 15, but Ti6Al4V instead of Ti grade 2 was investigated in addition to the experiments in [93]. Powder

preparation, PBF-LB/M processing and sample analysis matche the procedures described in [93]. As intended, the Al-content effectively mitigates ω-phase formation or at least shifts it to regions with a higher Fe and V content, thus facilitating a crack free processing. The absence of ω-phase is confirmed by an x-ray diffraction measurement that is displayed in Figure 14. EBSD-measurements show a β-phase content in as-built condition of 98.7 %.

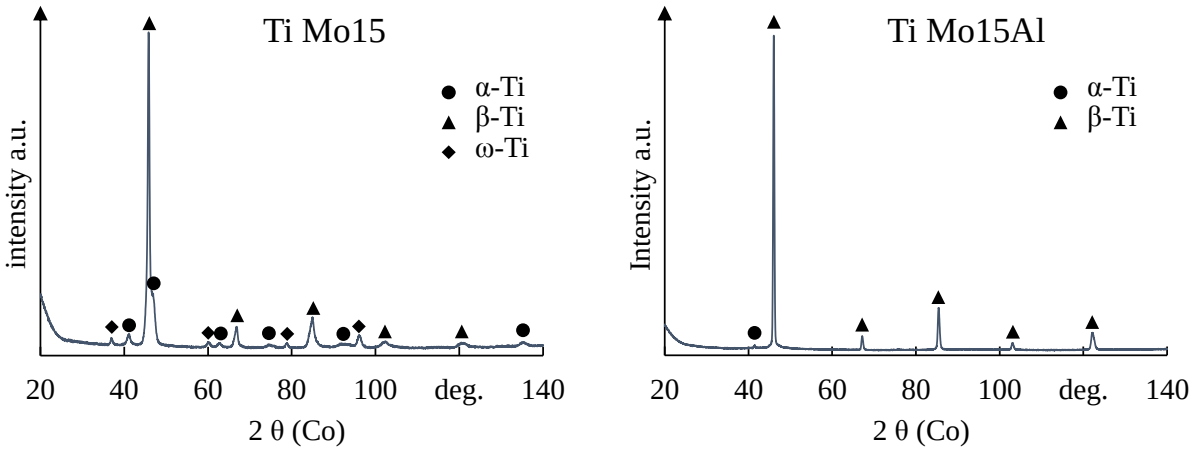

Figure 14: x-ray diffraction patterns of two samples with a Mo_{eq} of 15; left: pure Titanium (grade 2) alloyed with Fe and V [93] *with clearly visible ω-phase peaks, right: Ti6Al4V alloyed with Fe and V without ω-phase*

These results demonstrate that a defect-free transition between areas with a high degree of β-phase stabilization and areas with a low degree of β-phase stabilization is feasible when using Ti6Al4V as base alloy and Fe and V as β-phase stabilizers (see Figure 15). When comparing the property profiles of the α-β Ti-alloy Ti-6Al-4V and the β Ti-alloy Ti-10V-2Fe-3Al (see [64]), which is close to the β Ti-alloy in Figure 15, strong property differences in terms of strength, ductility and modulus can be achieved in a single part.

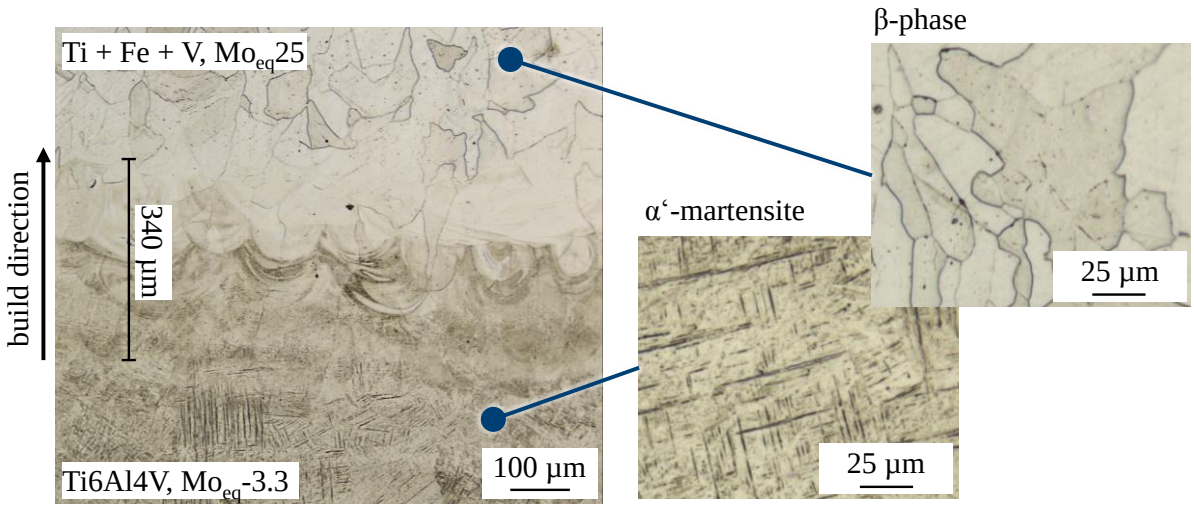

Figure 15: Defect-free transition between fully α'-martensitic and fully β-phase microstructure in a single PBF-LB/M part; as-built condition; both sections produced with identical PBF-LB/M parameters (see [93], *Table 4)*

Moreover, the experiments presented in [93] show that processing of all investigated alloy compositions is possible with the same set of PBF-LB/M process parameters. In addition to the experiments, this is verified in [93] by an empirical process model developed by *Ye et al.* [112] and calculation of the corresponding thermo-physical properties of the different alloy composition with the software J-Mat pro [113]. The necessary amounts of Fe and V to produce even high degrees of β-phase stabilization do not severely change the alloy's thermo-physical properties, thus resulting in overlapping PBF-LB/M process windows. This is important for manufacturing parts with locally varying alloy compositions. It proves that a whole part can be fused with a single set of PBF-LB/M parameters. This renders developing different parameter sets for every alloy composition, or in the worst-case elaborate exposure strategies to ensure a defect-free transition between areas with different alloy compositions unnecessary.

Up to now, only studies on multi-material parts consisting of alloys of different alloy classes have been published. Examples are PBF-LB/M of 316L and Ti-6Al-4V with copper as interlayer [114] or Ti/Al multi-material parts. However, in both publications brittle intermetallic phases and cracking is reported for the transition zone, which is a yet unsolved problem for PBF-LB/M of multi-material parts with different and in most cases incompatible alloys.

Another option for creating parts with locally different properties but with only one alloy composition is by controlling the temperature fields during PBF-LB/M e.g. by parameter adjustment [115] or by introducing certain geometrical features that affect the heat distribution from the PBF-LB/M process zone [116]. This can either affect the solidification of the material or induce local tempering effects. Beyond scientific samples, this is however difficult to transfer to actual parts and the effect on the material properties is limited.

Compared to both approaches published in literature for creating parts with locally different properties, namely multi-material with different alloy classes and local temperature control during single alloy PBF-LB/M the approached demonstrated here for Ti-alloys provides a middle way. Since only compatible alloys of the same class are joined, cracks and brittle phases in the transition zone are avoided, in contrast to multi material approaches. Compared to single alloy PBF-LB/M the range of possible property variations and hence the benefit for real parts is greater. This finding is unique compared to the state of the art and is considered a promising approach for future research and possibly industrial applications.

In summary, the initial working hypotheses formulated in chapter 3 are verified to a large extent by the investigations presented in chapter 5.1 and chapter 5.2:

Discussion of initial hypotheses:

The addition of the β-phase stabilizers Fe and V provides a powerful leaver to adjust the properties of Ti-alloys in a wide range. In agreement with the results of chapter 4.2 a complete

dissolution of both Fe and V in the Ti-matrix is feasible. In dependence on the alloy composition and the heat-treatment, the compression yield strength can be tuned to a value between 1857 ± 35 MPa and 957 ± 25 MPa. The fracture strain reaches values from 4.3 % to more than 50 % (pre-defined end of test).

The Molybdenum equivalent is a suitable rule of thumb to estimate the β-phase content of Ti-alloys processed by PBF-LB/M. Due to high cooling rates in the range of 10^6 K/s inherent to PBF-LB/M a Mo_{eq} of 10 is sufficient to retain more than 90 % β-phase. However, statements about resulting mechanical properties solely based on the Mo_{eq} are only possible to a limited extent, as more complex metallurgical effects like the formation of the ω-phase can have a strong effect.

It is successfully demonstrated that a defect-free transition from areas with a highly β-stabilized Ti-alloy to a near-α base alloy is possible in PBF-LB/M. Moreover, the findings prove that PBF-LB/M of the near-α Ti-alloy and all β-stabilized Ti-alloys is possible with the same PBF-LB/M parameter set. This indicates that manufacturing of multi-alloy Ti-parts is possible even without the necessity for developing multiple PBF-LB/M parameter sets or special exposure strategies for the transition zone between two different alloy compositions.

6 In-Situ Alloy Formation of a WMoTaNbV Refractory Metal High Entropy Alloy by Laser Powder Bed Fusion (PBF-LB/M)

Published in Materials, 14 (2021)

Florian Huber[1,2,3], Dominic Bartels[1,2,3] and Michael Schmidt[1,2,3]

[1] Institute of Photonic Technologies, Friedrich-Alexander Universität Erlangen-Nürnberg
[2] Collaborative Research Center 814 – Additive Manufacturing
[3] Erlangen Graduate School in Advanced Optical Technologies

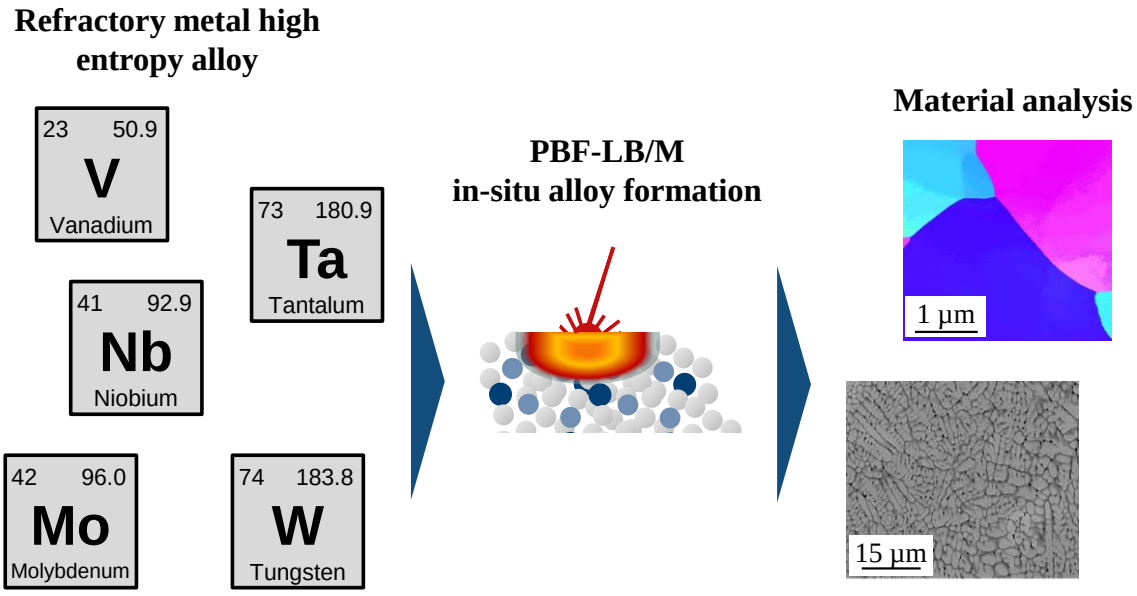

Highlights:

- Formation of a single bcc-phase proving successful formation of a refractory metal high entropy alloy by PBF-LB/M
- Confirmation of the process strategies developed in chapter 4 for in-situ alloy formation of refractory metal high entropy alloys from up to five powder components
- Solidification mode, resulting microstructure and hardness of the refractory metal high entropy alloy WMoTaNbV adjustable by the PBF-LB/M parameter combination

materials

MDPI

Article

In-Situ Alloy Formation of a WMoTaNbV Refractory Metal High Entropy Alloy by Laser Powder Bed Fusion (PBF-LB/M)

Florian Huber [1,2,*], Dominic Bartels [1,2] and Michael Schmidt [1,2]

[1] Institute of Photonic Technologies, Faculty of Engineering, Friedrich-Alexander Universität Erlangen-Nürnberg (FAU), Konrad-Zuse-Straße 3/5, 91052 Erlangen, Germany; dominic.bartels@lpt.uni-erlangen.de (D.B.); sekretariat@lpt.uni-erlangen.de (M.S.)

[2] Erlangen Graduate School in Advanced Optical Technologies (SAOT), Friedrich-Alexander Universität Erlangen-Nürnberg, Paul-Gordan-Straße 6, 91052 Erlangen, Germany

* Correspondence: florian.huber@lpt.uni-erlangen.de

Abstract: High entropy or multi principal element alloys are a promising and relatively young concept for designing alloys. The idea of creating alloys without a single main alloying element opens up a wide space for possible new alloy compositions. High entropy alloys based on refractory metals such as W, Mo, Ta or Nb are of interest for future high temperature applications e.g., in the aerospace or chemical industry. However, producing refractory metal high entropy alloys by conventional metallurgical methods remains challenging. For this reason, the feasibility of laser-based additive manufacturing of the refractory metal high entropy alloy $W_{20}Mo_{20}Ta_{20}Nb_{20}V_{20}$ by laser powder bed fusion (PBF-LB/M) is investigated in the present work. In-situ alloy formation from mixtures of easily available elemental powders is employed to avoid an expensive atomization of pre-alloyed powder. It is shown that PBF-LB/M of $W_{20}Mo_{20}Ta_{20}Nb_{20}V_{20}$ is in general possible and that a complete fusion of the powder mixture without a significant number of undissolved particles is achievable by in-situ alloy formation during PBF-LB/M when selecting favorable process parameter combinations. The relative density of the samples with a dimension of $6 \times 6 \times 6$ mm^3 reaches, in dependence of the PBF-LB/M parameter set, 99.8%. Electron backscatter diffraction (EBSD) and transmission electron microscopy (TEM) measurements confirm the presence of a single bcc-phase. Scanning electron microscopy (SEM) images show a dendritic and/or cellular microstructure that can, to some extent, be controlled by the PBF-LB/M parameters.

Keywords: additive manufacturing; laser powder bed fusion; PBF-LB/M; laser beam melting (LBM); in-situ alloy formation; high entropy alloys (HEA); refractory metals

Citation: Huber, F.; Bartels, D.; Schmidt, M. In-Situ Alloy Formation of a WMoTaNbV Refractory Metal High Entropy Alloy by Laser Powder Bed Fusion (PBF-LB/M). *Materials* **2021**, *14*, 3095. https://doi.org/10.3390/ma14113095

Academic Editors: Volker Schulze and Frederik Zanger

Received: 25 May 2021
Accepted: 2 June 2021
Published: 4 June 2021

1. Introduction

High entropy alloys and related compositions are a relatively young concept for designing alloys. The formation of such multi component alloys was reported independently by Cantor et al. [1] and the research group around J.-W. Yeh in 2004 [2–4]. In contrast to most conventional alloys, high entropy alloys do not possess a single main alloying element but comprise a composition of multiple principal elements. The exact definition of high entropy alloys varies from source to source. The most common definition includes alloys consisting of at least five elements with a concentration between 5% and 35% each [5]. Other definitions demand a configurational entropy of at least 1.5 R [6]. However, both definitions are overlapping in large parts. Additionally, further criterions like the formation of a single phase solid solution were suggested [7]. These definitions are discussed extensively in recent review papers [7] and books [6,8]. The focus of the present work lies on the alloy $W_{20}Mo_{20}Ta_{20}Nb_{20}V_{20}$, which is considered a high entropy alloy in agreement with all these criterions. The majority of publications on high entropy alloys is focused on 3d transition metal alloys based on the CoCrFeMnNi alloy and its derivatives first reported by Cantor et al. [1]. Recent publications demonstrate successful

PBF-LB/M of this group of alloys [9,10], investigate the effect of C [11] and N [12] additions, or examine the wear resistance [13]. Besides PBF-LB/M, different additive manufacturing processes such as wire arc additive manufacturing [14], electron beam melting [15,16] or laser liquid phase sintering [17] of 3d transition metal high entropy alloys are subjects of ongoing research. In contrast to that, refractory metal high entropy alloys are by far less investigated [7]. First results on the alloys WMoTaNb and WMoTaNbV were reported by Senkov et al., in 2010 [18] and 2011 [19], respectively. Refractory metal high entropy alloys possess a wide range of material properties depending on the alloy compositions and are especially interesting for high temperature applications [19]. Since the first publications different refractory metal high entropy alloy compositions and alloy design approaches were investigated with the aim to increase e.g., room temperature ductility [20] or to decrease the density of the alloys by replacing heavy elements like Ta and W by lighter elements. Senkov et al. reported a beneficial effect of an Al addition on the mechanical properties of MoNbTaTiZr and HfNbTaTiZr refractory metal high entropy alloys [21], while also reducing the density of the alloy. Also with the aim of decreasing the density, the properties of four alloys of the CrNbTiVZr system are discussed in [22]. In [23] different heat-treatments for modifying the microstructure of $Al_{0.5}NbTa_{0.8}Ti_{1.5}V_{0.2}Zr$ with the aim of increasing the ductility at room temperature are reported. A comprehensive overview of current research activities regarding development of refractory metal high entropy alloys can be found in respective review papers [7,24,25].

Despite first investigations, currently only a small fracture of the possible compositions of refractory metal high entropy alloys is investigated. One reason for this is the laborious preparation of samples. Due to the high melting temperatures, the wide range of melting points of refractory metals (e.g., Vanadium at 1910 °C [26] vs. Tungsten at 3422 °C [26]), and the tendency to segregate during solidification, manufacturing of refractory metal high entropy alloys is challenging. Samples are commonly prepared by vacuum arc melting [18,19] or in the case of thin films by magnetron sputtering [27]. Some alloys are also prepared by casting [23] and subsequent homogenization heat treatments with long durations (>>1 day) in a furnace.

Considering this, laser powder bed fusion (PBF-LB/M) is an appealing approach for manufacturing refractory metal high entropy alloys with high throughput. The intensity of modern high power laser beam sources is sufficient to effortlessly melt even tungsten [28]. Furthermore, small meltpool dimensions of a few hundred µm and high cooling rates in the range of 10^6 K/s [29] during PBF-LB/M are presumed to mitigate segregation of elements during solidification which is of importance with regard to refractory metal high entropy alloys [18]. In addition, by adjusting the process parameters and scan strategies, the energy input can be controlled very precisely. Starting material for PBF-LB/M are metal powders. Novel alloys can be produced either by atomization of pre-alloyed powder or by in-situ alloy formation during PBF-LB/M from mixtures of commonly available elemental powders [30]. The later approach supports material development and high throughput investigations as the desired alloy composition can easily be produced by mixing of powder components without the need of an expensive powder atomization [30]. This, however, requires careful PBF-LB/M process development, since despite successful application of in-situ alloy formation even for high entropy alloys (e.g., [31]), unmolten particles and an inhomogeneous distribution of elements might occur. This is especially crucial if the difference between the melting points of the alloying elements is large, as is the case for refractory metal high entropy alloys [32].

Laser processing of refractory metal high entropy alloys was first demonstrated by Dobbelstein et al., in 2016 [33] by means of directed energy deposition (DED) and in-situ alloy formation. Very comprehensive results of their work are also published in [34]. In contrast to conventional DED, Dobbelstein et al. are not welding continuous weld seams but stack spot welds onto each other to form cylindrical samples, which limits the geometries that can be manufactured. Also, a re-melting step without powder flow is necessary for homogenization of the element distribution and to avoid unmolten particles.

Further research on DED of refractory metal high entropy alloys is published by Moorhead et al. [35] or Li et al. [36], who also successfully demonstrated the formation of refractory metal high entropy alloys by DED.

PBF-LB/M of refractory metal high entropy alloys is even less investigated. First results are published by Zhang et al. [37] for the alloy WMoNbTa. However, only small-scale SEM-images and basic corrosion resistance measurements are shown and further research is necessary to understand the effect of the PBF-LB/M processing conditions on the material properties and the homogeneity of the element distribution after in-situ alloy formation. In this context, the aim of the present work is to explore processing of the refectory metal high entropy alloy $W_{20}Mo_{20}Ta_{20}Nb_{20}V_{20}$ by PBF-LB/M and to examine the influence of the process parameters on the resulting microstructural properties.

2. Materials and Methods

Though there are more recent refractory metal high entropy alloys with superior properties reported in the literature [7], the alloy $W_{20}Mo_{20}Ta_{20}Nb_{20}V_{20}$ was selected for this work's experiments. Since the concept of refractory metal high entropy alloys is comparably young, and the number of possible alloy combinations is vast, there are only single publications on most of the different alloy combinations, thus providing only limited information per alloy. $W_{20}Mo_{20}Ta_{20}Nb_{20}V_{20}$ is one of the first refractory metal high entropy alloys developed by Senkov et al. [18] and therefore also one of the best investigated ones. Consequently there are at least a few publications available that allow a comparison with the results and support discussion.

For the experiments, a heterogeneous mixture of five single element powders was used to prepare the WMoTaNbV samples. The specifications of the powders used for the PBF-LB/M experiments were chosen based on literature and our own experience. To facilitate PBF-LB/M in the first place, it is mandatory that the powder mixture has sufficient flowability and can be recoated to thin layers [38,39], typically ranging between 20 µm and 100 µm for PBF-LB/M. Furthermore, a low oxygen content of the powders is considered beneficial for manufacturing refractory metal high entropy alloys [34]. Among other factors, the recoatability is determined by particle size and particle shape [38]. Spherical powder particles are in general superior to irregular shaped particles with respect to flowability and are consequently preferable. Also very small particle fractions (<10 µm) should be avoided as they might impair recoatability and bear difficulties with respect to occupational safety [40]. Based on these criteria W-, Mo-, and Ta-powder was purchased from Tekna Plasma Europe SAS (Mâcon, France). The Nb-powder was provided by H.C. Starck Tantalum and Niobium GmbH (Goslar, Germany). Spherical V-powder could unfortunately not be obtained. Hence, milled V-powder from NMD New Materials Development GmbH (Heemsen, Germany) was used. Scanning electron images of the different powder fractions are shown in Figure 1.

All powder particles except the V-powder are predominantly spherical and show a good flowability. The irregular shaped, milled V-powder has a lower flowability than spherical powder. Preliminary recoating test nevertheless proved a sufficient recoatability of the blend for all five powders. The particle size determined by laser diffraction using a Mastersizer 3000 from Malvern Panalytical (Malvern, UK) is listed in Table 1. For the high-melting elements W and Ta a smaller D_{90} (23.1 µm and 36.1 µm respectively) was chosen to ease fusion during PBF-LB/M and to avoid undissolved particles. Since selective evaporation of lower boiling alloying elements is a common phenomenon in PBF-LB/M [41], the amount of Vanadium, which has the lowest boiling point in the WMoNbTaV system [26], in the initial powder mixture was increased by a factor of 1.5 compared to the other alloying elements to pre-compensate the expected evaporation of V during PBF-LB/M. All powders were dried in a vacuum furnace at 120 °C for 8 h and subsequently mixed for 1 h in a Turbular-mix from Willy A. Bachofen AG (Mutenz, Switzerland).

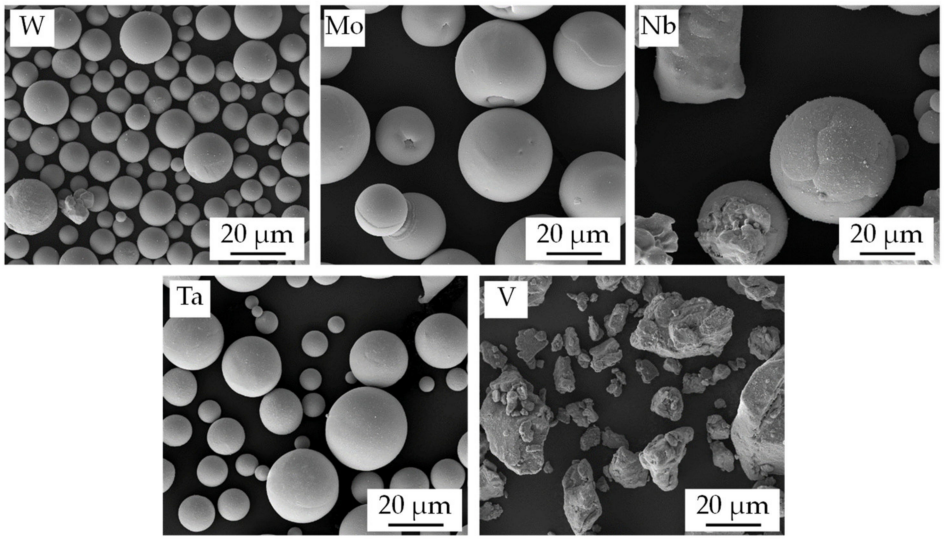

Figure 1. SEM-images of the metal powders used for in-situ alloy formation; W, Mo and Ta powder plasma atomized, Nb powder argon atomized, V powder milled.

Table 1. Particle size distribution of the powders used for in-situ alloy formation; determined by laser diffraction; mean value with standard deviation from five single measurements.

Powder	D_{10}	D_{50}	D_{90}
W	8.6 ± 0.1 µm	14.0 ± 0.2 µm	23.1 ± 0.5 µm
Mo	19.6 ± 0.3 µm	30.5 ± 0.7 µm	44.3 ± 0.7 µm
Nb	18.7 ± 0.1 µm	35.5 ± 0.4 µm	63.1 ± 0.3 µm
Ta	10.5 ± 0.2 µm	21.0 ± 0.6 µm	36.1 ± 0.7 µm
V	7.8 ± 0.4 µm	24.2 ± 0.1 µm	52.5 ± 1.1 µm

A PBF-LB/M machine of the type AconityMINI (Aconity GmbH, Herzogenrath, Germany) was used for manufacturing cubic samples with an edge length of 6 mm on molybdenum substrate plates obtained from Plansee SE (Reutte, Austria). The machine is equipped with a redPower QUBE single mode fiber laser from SPI Lasers Ltd. (Southamton, UK) featuring an operating wavelength of 1080 nm and a maximum power of 1 kW. The scanner optics used is an AxialScan-30 from Raylase GmbH (Wessling, Germany). The minimal beam diameter on the substrate plate is 70 µm. Argon was used as shielding gas. The oxygen content of the process gas was constantly kept below 25 ppm during PBF-LB/M processing to keep oxygen intake low. PBF-LB/M process parameters were developed experimentally. The following results and discussion section focuses on the two parameter sets described in Table 2. The two parameter sets were chosen based on a preliminary screening study in which we varied laser power, scan speed and hatch distance in a wide range from 100 W to 600 W, 100 mm/s to 1600 mm/s and 45 µm to 180 µm. Both parameter sets were selected for this work because they allow manufacturing of PBF-LB/M samples with high relative densities over 99.5% and represent different areas of the process window with maximum difference in terms of laser power, scan speed and hatch distance to support investigation and discussion of possible effects of the laser parameter set on the material properties. The low laser power/low scan speed parameter set PBF-LB/M B was furthermore derived from previous work on in-situ alloy formation strategies with high melting particles and is assumed to support dissolution of W in the meltpool [32].

Table 2. PBF-LB/M parameter sets used in this work.

Parameter Set	Laser Power	Scan Speed	Spot Diameter	Hatch	Layer Thickness
PBF-LB/M A	600 W	800 mm/s	200 µ	120 µm	50 µm
PBF-LB/M B	200 W	100 mm/s	200 µm	45 µm	50 µm

The PBF-LB/M samples were separated from the build platform, embedded in epoxy resin, grinded with diamond grinding pads and polished with 3 µm diamond suspensions and oxide polishing suspension with hydrogen peroxide. The preparation depth is in the range of 3 mm and hence in the middle of the 6 mm cubic samples. Samples for transmission electron microscopy (TEM) were subsequently manufactured with a focused ion beam (FIB). The samples were analyzed by optical light microscopy, scanning electron microscopy (SEM), energy dispersive X-ray spectroscopy (EDX), electron backscatter diffraction (EBSD), transmission electron microscopy (TEM) and micro hardness measurements. Relative density values were determined by optical light microscopy and image analysis.

3. Results and Discussion

Figure 2 shows polished microsections of samples built with parameter set PBF-LB/M A and PBF-LB/M B (see Table 2). While the samples exhibit a high relative density of 99.8% in case of parameter set PBF-LB/M A and 99.5% in case of parameter set PBF-LB/M B, both samples still contain defects.

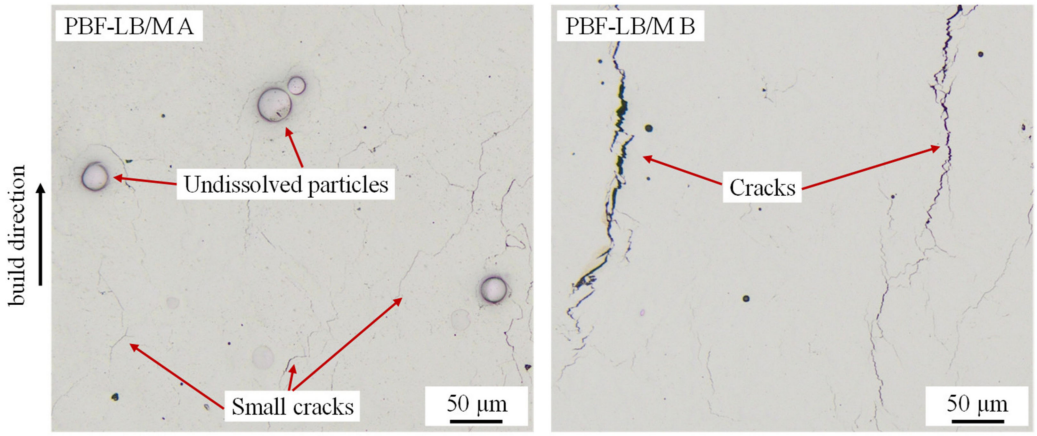

Figure 2. Microsections of WMoNbTaV-samples manufactured with parameter set PBF-LB/M A (**left**) and PBF-LB/M B (**right**).

These are essentially cracks, mostly perpendicular to the build direction, and undissolved particles. PBF-LB/M A results in considerably smaller cracks than PBF-LB/M B but contains undissolved powder particles which were identified as tungsten particles by EDS measurements. Tungsten has the highest melting point of the alloy's elements [26] and consequently is the hardest to dissolve during PBF-LB/M. Undissolved particles are a common phenomenon related to in-situ alloy formation by PBF-LB/M, especially if alloying elements with very different melting points are combined. E.g., Yadroitsev et al. [42] report undissolved Mo particles in Ti-alloys produced by in-situ alloy formation and PBF-LB/M while the lower melting Cu was completely dissolved in the Ti-matrix. Fischer at al. [43] made similar observations with undissolved Nb particles in a Ti matrix. However, they also reported a parameter dependence of the amount of remaining high melting particles. These interdependencies between the PBF-LB/M process parameters and the amount of undissolved high melting particles at in-situ alloy formation are discussed extensively in one of our previous publications [32]. According to [32] a high volumetric energy input, slow scan speeds, and accordingly reduced laser power support the dissolution of high melting elements at in-situ alloy formation by PBF-LB/M. The reasons

for this are a higher degree of re-melting, a longer interaction time with the laser beam, and a more favorable powder movement during PBF-LB/M [32]. These relationships apparently also apply for in-situ alloy formation of refractory metal high entropy alloys in the present work. Parameter set PBF-LB/M B comprises a considerably lower scan speed (100 mm/s vs. 800 mm/s) but, despite the lower laser power, a higher volumetric energy density (889 J/mm^3 vs. 125 J/mm^3) than parameter set PBF-LB/M A. This facilitates the dissolution of the high melting W particles, thus leading to less undissolved particles as shown in Figure 2. This finding is in good agreement with the results in [32] regarding the dissolution of high melting particles.

While the sample built with parameter set PBF-LB/M B contains less undissolved particles, parameter set PBF-LB/M A is superior to PBF-LB/M B in terms of cracking. In comparison to parameter set PBF-LB/M B much smaller cracks are apparent in sample PBF-LB/M A. Cracking during PBF-LB/M is a common process-related defect and can have multiple causes. One mechanism, the so called hot cracking, which is related to the solidification of the alloy, is often reported for PBF-LB/M of e.g., Al wrought alloys like the EN AW 6xxx [44] or EN AW 2xxx [45] series. However, based on the crack structure visible in Figure 2, hot cracking is excluded as the main cause of the cracks appearing in WMoTaNbV samples. Instead, cracking of the already solidified material due to internal stress induced by the PBF-LB/M process and an insufficient ductility of the material at lower temperatures is assumed to be the cause for the cracks. According to the results of Zou et al. [46] and Senkov et al. [19] the alloy WMoTaNb possesses only a very limited degree of ductility and fracture toughness at room temperature. While the WMoTaNb grains themselves are comparably crack resistant according to [46], O and N impurities aggregate at grain boundaries and cause embrittlement. This material behavior probably also applies for the alloy WMoTaNbV that is investigated in the present work. The brittle grain boundaries in combination with the internal stress induced during PBF-LB/M consequently lead to cracking of the samples during processing. The different crack patterns in dependence of the parameter set PBF-LB/M A and PBF-LB/M B with wider cracks in the PBF-LB/M B samples are a result of the smaller hatch distance (45 µm vs. 120 µm) and the higher volumetric energy density applied (889 J/mm^3 vs. 125 J/mm^3) compared to parameter set PBF-LB/M A. According to the temperature gradient mechanism model that describes the formation of internal stress during PBF-LB/M [47,48] both factors together are assumed to cause higher stress values and consequently wider cracks. Based on these findings, a high temperature (>600 °C) build-platform heating device and/or high purity powder with low O and N content are suggested for crack-free PBF-LB/M of WMoTaNbV. Nevertheless, it is demonstrated that successful in-situ alloy formation of refractory metal high entropy alloys with nearly complete dissolution of the highest melting particles is possible, if favorable parameter combinations are selected. More recently developed refractory metal high entropy alloys like $Al_{10}Nb_{15}Ta_5Ti_{30}Zr_{40}$ [49] promise an increased room temperature ductility and hence crack-free processing by PBF-LB/M even without high temperature build-platform heating, which needs to verified in future work.

The grain and phase structure of a PBF-LB/M B sample was analyzed by EBSD measurements, which are shown in Figure 3. The sample consists entirely of a single bcc high entropy phase, which is in agreement with the results of Senkov et al. for vacuum arc molten WMoTaNbV [18,19]. This confirms the feasibility of producing refractory metal high entropy alloys by PBF-LB/M and in-situ alloy formation. The average grain size determined by the linear intercept method is 16.3 µm. This is more than a factor of four smaller than the 80 µm reported by Senkov et al. for vacuum arc molten samples. The smaller grain size can be attributed to the high cooling rates in the range of 10^6 K/s during the PBF-LB/M process [50].

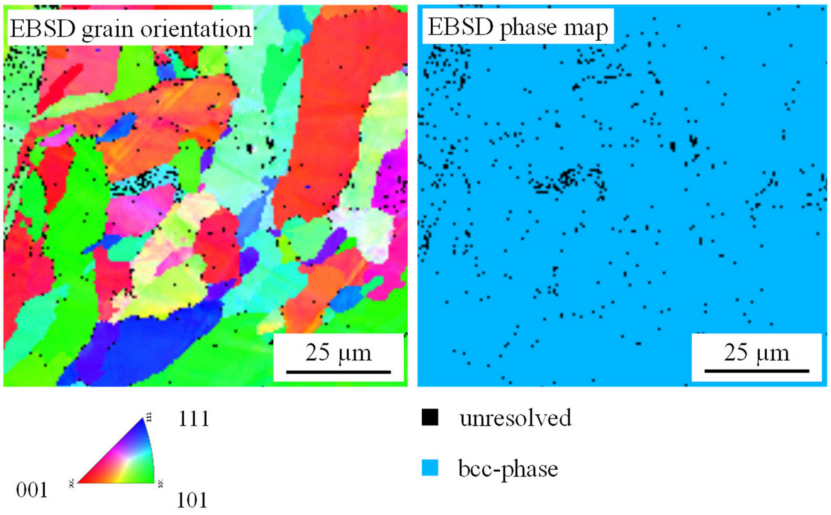

Figure 3. EBSD grain orientation map and EBSD phase map of sample PBF-LB/M B.

SEM images reveal an influence of the process parameters and the PBF-LB/M specific solidification conditions on the microstructure. As visible in Figure 4 inter layer boundaries are clearly distinguished by coarser structures. According to [51] temperature gradients in the liquid and growth rates are smaller at the outer contours of the meltpool compared to the inner regions, explaining the coarser structures (see also Figure 5). This demonstrates the sensitivity of the alloy to the solidification conditions and offers the chance to influence material properties by adjusting the PBF-LB/M process conditions/parameters.

This effect is even more evident when comparing the parameter sets PBF-LB/M A and PBF-LB/M B. Based on the process parameters it is safe to assume that the material is subject to higher growth rates R when processed with parameter set PBF-LB/M A compared to parameter set PBF-LB/M B. This is due to the eight times higher scan speed that correlates to some extent with the growth rate [51]. Based on simplified considerations it can further be assumed that the temperature gradient in the liquid is higher for parameter set PBF-LB/M B than for parameter set PBF-LB/M A. The upper temperature of the meltpool is defined by the evaporation temperature of the alloy's components while the lowest temperature in the meltpool is defined by the solidification range of the alloy. This is equally true for both parameter sets. Considering the differences in the process parameter sets, PBF-LB/M A features larger meltpool dimensions than PBF-LB/M B. Consequently, it is assumed that the temperature gradient in the liquid G is larger for parameter set PBF-LB/M B. According to the literature [52,53] the solidification mode and also the structure size is determined by R and G. While higher growth rates R and lower temperature gradients G in the liquid favor a columnar dendritic solidification, lower growth rates R and higher temperature gradients in the liquid G favor cellular solidification.

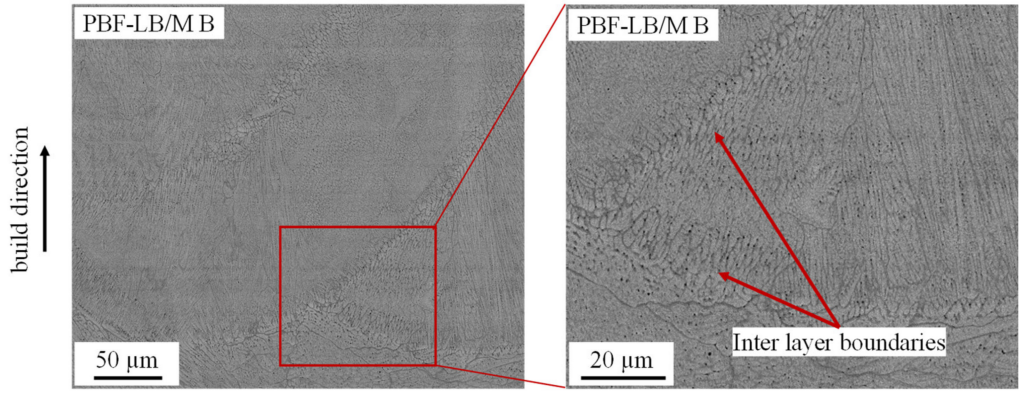

Figure 4. Backscattered electron (BSE) images of sample PBF-LB/M B showing visible melt tracks with coarser structures at the inter layer boundaries.

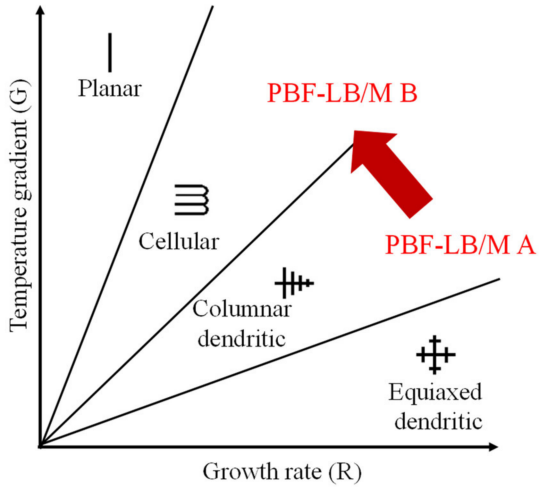

Figure 5. Effect of temperature gradient in the liquid G and growth rate R on the solidification mode and the structure size [52,53].

This effect can clearly be seen in Figure 6. Parameter set PBF-LB/M A features a larger structure size and more distinct secondary dendrites, while the material processed with parameter set PBF-LB/M B solidifies in an almost cellular structure with only a few secondary dendrites. These different solidification modes also affect the material properties. The microhardness of the PBF-LB/M A sample with the coarser structure is 561 ± 17 HV0.1 (n = 9) while the microhardness of the PBF-LB/M B sample is 614 ± 21 HV0.1 (n = 9).

Due to their complex alloy composition and a tendency for segregation, the distribution of the alloy's elements is of particular interest when it comes to refractory metal high entropy alloys. For this reason, the samples were analyzed by EDS and TEM-EDS respectively. As shown in Figure 7 Vanadium, which is the lowest melting element [54] in the WMoTaNbV alloy, is concentrated in the interdendritic areas, while the intradendritic areas lack Vanadium.

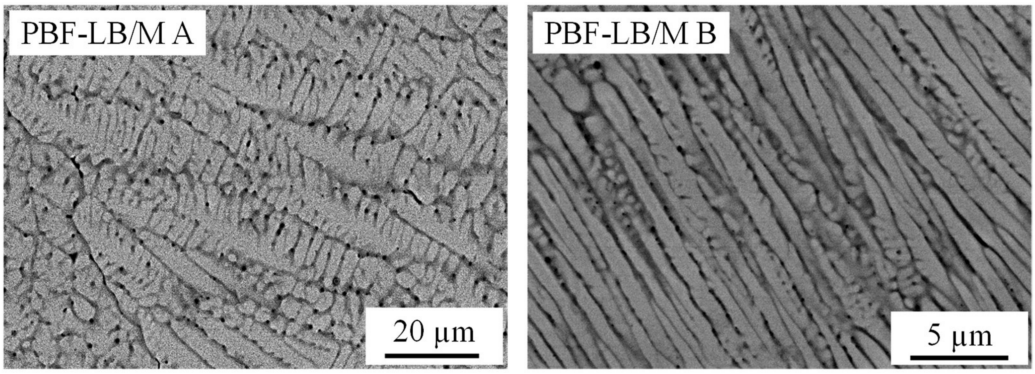

Figure 6. Backscattered electron (BSE) images of the microstructure of sample PBF-LB/M A (**left**) and sample PBF-LB/M B **(right)**.

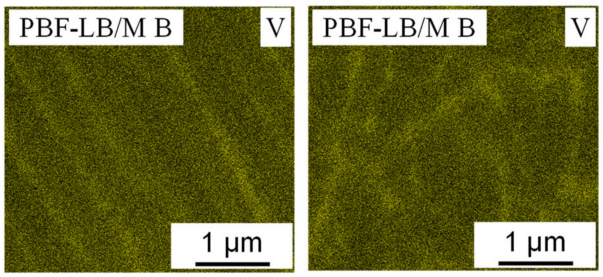

Figure 7. Qualitative EDS maps of the element Vanadium in a PBF-LB/M B sample showing a Vanadium surplus in the interdendrtic areas.

Quantitative EDS point measurements (see Table 3) confirm the vanadium surplus in the interdendritic areas. Nb and Mo are almost equally distributed between inter- and intradendritic regions, while Ta and especially W are predominantly located in the intradendritic areas. These findings are in agreement with results of Senkov et al. [18] who prepared WMoTaNbV samples by vacuum arc melting. Compared to vacuum arc molten samples [18,19] the homogeneity of the element distribution achieved by PBF-LB/M is still very good, which can be attributed to the higher solidification rates and temperature gradients inherent to PBF-LB/M.

Table 3. Quantitative point measurements in the interdendritic area and the intradendritic area of a PBF-LB/M B sample, respectively; mean value and standard deviation of 6 measurements each.

Position	V	Nb	Mo	Ta	W
Interdentritic at. %	21.8 ± 1.2	20.7 ± 0.4	17.0 ± 0.3	21.1 ± 0.2	15.5 ± 1.3
Intradendritic at. %	11.6 ± 1.6	22.0 ± 0.2	20.1 ± 0.8	23.8 ± 0.5	22.6 ± 0.7
n = 6					

A PBF-LB/M A sample was analyzed by TEM-EDS with similar results as already observed for parameter set PBF-LB/M B with EDS. Figure 8 shows qualitative TEM-EDS measurements of the element distribution. Mo and Nb are almost equally distributed between interdendritic and intradendritic areas, while there is a considerable W and a weak Ta surplus in the intradendritic regions. V is predominantly concentrated in the interdendritic areas of the material.

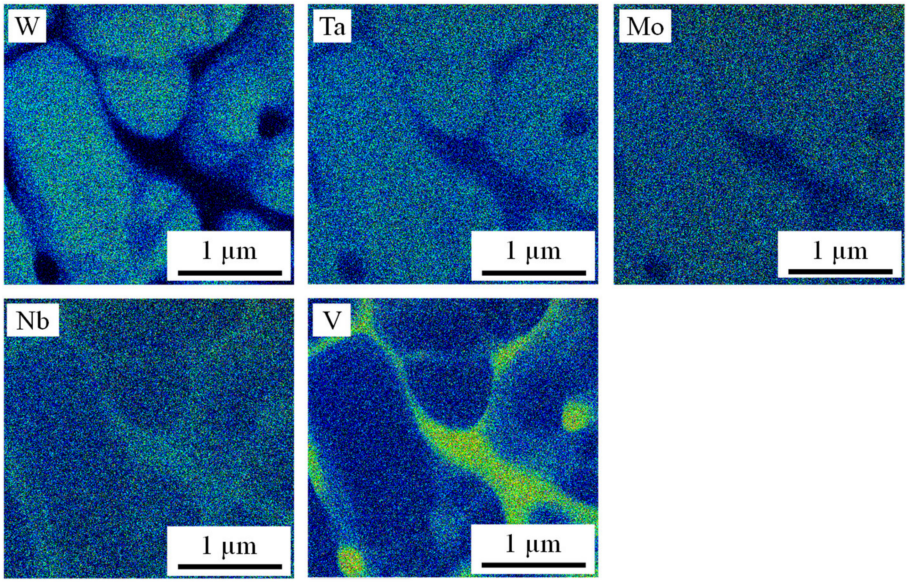

Figure 8. Qualitative TEM-EDS measurements showing the element distribution in a PBF-LB/M A sample.

4. Summary and Conclusions

In the present work, in-situ alloy formation of a WMoTaNbV refractory metal high entropy alloy by PBF-LB/M additive manufacturing is investigated. Samples manufactured with two different parameter sets were analyzed by light and electron microscopy, EBSD, EDS and TEM-EDS. Although high relative densities over 99.8% and a single bcc high entropy phase were achieved, the samples still contained cracks and undissolved W particles. The cracks are a result of the alloy's low room temperature ductility and can probably be avoided by applying a high temperature heating device or by selecting different alloy compositions with more favorable room temperature properties. It is demonstrated that the number of undissolved high melting particles can be greatly reduced by choosing PBF-LB/M parameter sets with slow scan speeds and accordingly reduced laser power. It is furthermore shown that the PBF-LB/M parameters affect the solidification mode and the resulting microhardness of the alloy. This demonstrates that the alloy WMoTaNbV is sensitive to the processing conditions which are determined by the PBF-LB/M parameters. Besides the mere alloy composition, this opens up opportunities to modify the resulting properties of related additively manufactured refractory metal high entropy alloys. Though, no completely defect free samples were produced the results still demonstrate the general feasibility of in-situ formation of refractory metal high entropy alloys by PBF-LB/M. High cooling rates related to PBF-LB/M mitigate segregation of the elements during solidification without the need of time consuming vacuum arc melting. The possibility of in-situ alloy formation by PBF-LB/M could therefore be a valuable tool to facilitate high throughput investigations that are key to identify application-relevant alloys within the vast number of possible alloy compositions inherent to the high entropy concept—not only for 3d transition metal alloys but also for refractory metal based high entropy alloys.

Author Contributions: Conceptualization, F.H.; methodology, F.H.; investigation, F.H. and D.B.; writing—original draft preparation, F.H.; writing—review and editing, D.B. and M.S.; supervision, M.S.; funding acquisition, M.S. and F.H. All authors have read and agreed to the published version of the manuscript.

Funding: This research was funded by the German Federal Ministry of Economic Affairs and Energy in the framework of the Aviation Research Program (LuFo V-3), project ADHEA. TEM-access was provided by the European Union via the program ESTEEM3.

Institutional Review Board Statement: Not applicable.

Informed Consent Statement: Not applicable.

Data Availability Statement: Not applicable.

Acknowledgments: The authors gratefully acknowledge funding of the Erlangen Graduate School in Advanced Optical Technologies (SAOT) by the Bavarian State Ministry for Science and Art.

Conflicts of Interest: The authors declare no conflict of interest.

References

1. Cantor, B.; Chang, I.T.H.; Knight, P.; Vincent, A.J.B. Microstructural development in equiatomic multicomponent alloys. *Mater. Sci. Eng. A* **2004**, *375–377*, 213–218. [CrossRef]
2. Yeh, J.-W.; Chen, S.-K.; Lin, S.-J.; Gan, J.-Y.; Chin, T.-S.; Shun, T.-T.; Tsau, C.-H.; Chang, S.-Y. Nanostructured High-Entropy Alloys with Multiple Principal Elements: Novel Alloy Design Concepts and Outcomes. *Adv. Eng. Mater.* **2004**, *6*, 299–303. [CrossRef]
3. Yeh, J.-W.; Lin, S.-J.; Chin, T.-S.; Gan, J.-Y.; Chen, S.-K.; Shun, T.-T.; Tsau, C.-H.; Chou, S.-Y. Formation of simple crystal structures in Cu-Co-Ni-Cr-Al-Fe-Ti-V alloys with multiprincipal metallic elements. *Metall. Mater. Trans. A* **2004**, *35*, 2533–2536. [CrossRef]
4. Hsu, C.-Y.; Yeh, J.-W.; Chen, S.-K.; Shun, T.-T. Wear resistance and high-temperature compression strength of Fcc $CuCoNiCrAl_{0.5}Fe$ alloy with boron addition. *Metall. Mater. Trans. A Phys. Metall. Mater. Sci.* **2004**, *35*, 1465–1469. [CrossRef]
5. Zhang, Y.; Yang, X.; Liaw, P.K. Alloy design and properties optimization of high-entropy alloys. *JOM* **2012**, *64*, 830–838. [CrossRef]
6. Gao, M.C.; Yeh, J.-W.; Liaw, P.K.; Zhang, Y. (Eds.) *High-Entropy Alloys*; Springer International Publishing: Basel, Switzerland, 2016; ISBN 978-3-319-27011-1.
7. Miracle, D.B.; Senkov, O.N. Acta Materialia A critical review of high entropy alloys and related concepts. *Acta Mater.* **2017**, *122*, 448–511. [CrossRef]
8. Murty, B.S.; Yeh, J.W.; Ranganthan, S.; Bhattacharjee, P.P. *High-Entropy Alloys*; Elsevier: Amsterdam, The Netherlands, 2019; ISBN 9780128160671.
9. Park, J.M.; Choe, J.; Kim, J.G.; Bae, J.W.; Moon, J.; Yang, S.; Kim, K.T.; Yu, J.-H.; Kim, H.S. Superior tensile properties of 1%C-CoCrFeMnNi high-entropy alloy additively manufactured by selective laser melting. *Mater. Res. Lett.* **2020**, *8*, 1–7. [CrossRef]
10. Park, J.M.; Choe, J.; Park, H.K.; Son, S.; Jung, J.; Kim, T.-S.; Yu, J.-H.; Kim, J.G.; Kim, H.S. Synergetic strengthening of additively manufactured (CoCrFeMnNi)99C1 high-entropy alloy by heterogeneous anisotropic microstructure. *Addit. Manuf.* **2020**, *35*, 101333. [CrossRef]
11. Klimova, M.; Shaysultanov, D.; Semenyuk, A.; Zherebtsov, S.; Stepanov, N. Effect of carbon on recrystallised microstructures and properties of CoCrFeMnNi-type high-entropy alloys. *J. Alloys Compd.* **2021**, *851*, 156839. [CrossRef]
12. Klimova, M.; Shaysultanov, D.; Semenyuk, A.; Zherebtsov, S.; Salishchev, G.; Stepanov, N. Effect of nitrogen on mechanical properties of CoCrFeMnNi high entropy alloy at room and cryogenic temperatures. *J. Alloys Compd.* **2020**, *849*, 156633. [CrossRef]
13. Joseph, J.; Haghdadi, N.; Annasamy, M.; Kada, S.; Hodgson, P.D.; Barnett, M.R.; Fabijanic, D.M. On the enhanced wear resistance of CoCrFeMnNi high entropy alloy at intermediate temperature. *Scr. Mater.* **2020**, *186*, 230–235. [CrossRef]
14. Osintsev, K.A.; Konovalov, S.V.; Glezer, A.M.; Gromov, V.E.; Ivanov, Y.F.; Panchenko, I.A.; Sundeev, R.V. Research on the structure of $Al_{2.1}Co_{0.3}Cr_{0.5}FeNi_{2.1}$ high-entropy alloy at submicro- and nano-scale levels. *Mater. Lett.* **2021**, *294*, 129717. [CrossRef]
15. Shiratori, H.; Fujieda, T.; Yamanaka, K.; Koizumi, Y.; Kuwabara, K.; Kato, T.; Chiba, A. Relationship between the microstructure and mechanical properties of an equiatomic AlCoCrFeNi high-entropy alloy fabricated by selective electron beam melting. *Mater. Sci. Eng. A* **2016**, *656*, 39–46. [CrossRef]
16. Lyu, P.; Peng, T.; Miao, Y.; Liu, Z.; Gao, Q.; Zhang, C.; Jin, Y.; Guan, Q.; Cai, J. Microstructure and properties of CoCrFeNiMo0.2 high-entropy alloy enhanced by high-current pulsed electron beam. *Surf. Coat. Technol.* **2021**, *410*, 126911. [CrossRef]
17. Zhou, S.; Liang, Y.-J.; Zhu, Y.; Wang, B.; Wang, L.; Xue, Y. Ultrashort-time liquid phase sintering of high-performance fine-grain tungsten heavy alloys by laser additive manufacturing. *J. Mater. Sci. Technol.* **2021**, *90*, 30–36. [CrossRef]
18. Senkov, O.N.; Wilks, G.B.; Miracle, D.B.; Chuang, C.P.; Liaw, P.K. Refractory high-entropy alloys. *Intermetallics* **2010**, *18*, 1758–1765. [CrossRef]
19. Senkov, O.N.; Wilks, G.B.; Scott, J.M.; Miracle, D.B. Mechanical properties of $Nb_{25}Mo_{25}Ta_{25}W_{25}$ and $V_{20}Nb_{20}Mo_{20}Ta_{20}W_{20}$ refractory high entropy alloys. *Intermetallics* **2011**, *19*, 698–706. [CrossRef]
20. Qi, L.; Chrzan, D.C. Tuning Ideal Tensile Strengths and Intrinsic Ductility of bcc Refractory Alloys. *Phys. Rev. Lett.* **2014**, *112*, 115503. [CrossRef] [PubMed]
21. Senkov, O.N.; Senkova, S.V.; Woodward, C. Effect of aluminum on the microstructure and properties of two refractory high-entropy alloys. *ACTA Mater.* **2014**, *68*, 214–228. [CrossRef]
22. Senkov, O.N.; Senkova, S.V.; Miracle, D.B.; Woodward, C. Mechanical properties of low-density, refractory multi-principal element alloys of the Cr–Nb–Ti–V–Zr system. *Mater. Sci. Eng. A* **2013**, *565*, 51–62. [CrossRef]
23. Soni, V.; Senkov, O.N.; Gwalani, B.; Miracle, D.B.; Banerjee, R. Microstructural Design for Improving Ductility of An Initially Brittle Refractory High Entropy Alloy. *Sci. Rep.* **2018**, *8*, 8816. [CrossRef] [PubMed]
24. Miracle, D.; Miller, J.; Senkov, O.; Woodward, C.; Uchic, M.; Tiley, J. Exploration and Development of High Entropy Alloys for Structural Applications. *Entropy* **2014**, *16*, 494–525. [CrossRef]

25. Senkov, O.N.; Miracle, D.B.; Chaput, K.J.; Couzinie, J.-P. Development and exploration of refractory high entropy alloys—A review. *J. Mater. Res.* **2018**, *33*, 3092–3128. [CrossRef]
26. Haynes, W.M. *Handbook of Chemistry and Physics*; Taylor & Francis: Boca Raton, FL, USA, 2017; ISBN 978-1-4987-5429-3.
27. Kim, H.; Nam, S.; Roh, A.; Son, M.; Ham, M.-H.; Kim, J.-H.; Choi, H. Mechanical and electrical properties of NbMoTaW refractory high-entropy alloy thin films. *Int. J. Refract. Met. Hard Mater.* **2019**, *80*, 286–291. [CrossRef]
28. Iveković, A.; Omidvari, N.; Vrancken, B.; Lietaert, K.; Thijs, L.; Vanmeensel, K.; Vleugels, J.; Kruth, J.-P. Selective laser melting of tungsten and tungsten alloys. *Int. J. Refract. Met. Hard Mater.* **2018**, *72*, 27–32. [CrossRef]
29. Heigel, J.C.; Lane, B.M.; Levine, L.E. In Situ Measurements of Melt-Pool Length and Cooling Rate During 3D Builds of the Metal AM-Bench Artifacts. *Integr. Mater. Manuf. Innov.* **2020**, *9*, 31–53. [CrossRef]
30. Huber, F.; Papke, T.; Scheitler, C.; Hanrieder, L.; Merklein, M.; Schmidt, M. In Situ Formation of a Metastable β-Ti Alloy by Laser Powder Bed Fusion (L-PBF) of Vanadium and Iron Modified Ti-6Al-4V. *Metals* **2018**, *8*, 1067. [CrossRef]
31. Chen, P.; Li, S.; Zhou, Y.; Yan, M.; Attallah, M.M. Fabricating CoCrFeMnNi high entropy alloy via selective laser melting in-situ alloying. *J. Mater. Sci. Technol.* **2020**, *43*, 40–43. [CrossRef]
32. Huber, F.; Rasch, M.; Schmidt, M. Laser Powder Bed Fusion (PBF-LB/M) Process Strategies for In-Situ Alloy Formation with High-Melting Elements. *Metals* **2021**, *11*, 336. [CrossRef]
33. Dobbelstein, H.; Thiele, M.; Gurevich, E.L.; George, E.P.; Ostendorf, A. Direct Metal Deposition of Refractory High Entropy Alloy MoNbTaW. *Phys. Proc.* **2016**, *83*, 624–633. [CrossRef]
34. Dobbelstein, H.; George, E.P.; Gurevich, E.L.; Kostka, A.; Ostendorf, A.; Laplanche, G. Laser metal deposition of refractory high-entropy alloys for high-throughput synthesis and structure-property characterization. *Int. J. Extrem. Manuf.* **2021**, *3*, 015201. [CrossRef]
35. Moorehead, M.; Bertsch, K.; Niezgoda, M.; Parkin, C.; Elbakhshwan, M.; Sridharan, K.; Zhang, C.; Thoma, D.; Couet, A. High-throughput synthesis of Mo-Nb-Ta-W high-entropy alloys via additive manufacturing. *Mater. Des.* **2020**, *187*, 108358. [CrossRef]
36. Li, Q.; Zhang, H.; Li, D.; Chen, Z.; Huang, S.; Lu, Z.; Yan, H. WxNbMoTa Refractory High-Entropy Alloys Fabricated by Laser Cladding Deposition. *Materials* **2019**, *12*, 533. [CrossRef]
37. Zhang, H.; Zhao, Y.; Huang, S.; Zhu, S.; Wang, F.; Li, D. Manufacturing and Analysis of High-Performance Refractory High-Entropy Alloy via Selective Laser Melting (SLM). *Materials* **2019**, *12*, 720. [CrossRef]
38. Vock, S.; Klöden, B.; Kirchner, A.; Weißgärber, T.; Kieback, B. Powders for powder bed fusion: A review. *Prog. Addit. Manuf.* **2019**, *4*, 383–397. [CrossRef]
39. Sutton, A.T.; Kriewall, C.S.; Leu, M.C.; Newkirk, J.W. Powder characterisation techniques and effects of powder characteristics on part properties in powder-bed fusion processes. *Virtual Phys. Prototyp.* **2017**, *12*, 3–29. [CrossRef]
40. Balbaa, M.A.; Ghasemi, A.; Fereiduni, E.; Elbestawi, M.A.; Jadhav, S.D.; Kruth, J.-P. Role of powder particle size on laser powder bed fusion processability of AlSi10mg alloy. *Addit. Manuf.* **2021**, *37*, 101630. [CrossRef]
41. Huber, F.; Papke, T.; Kerkien, M.; Tost, F.; Geyer, G.; Merklein, M.; Schmidt, M. Customized exposure strategies for manufacturing hybrid parts by combining laser beam melting and sheet metal forming. *J. Laser Appl.* **2019**, *31*, 022318. [CrossRef]
42. Yadroitsev, I.; Krakhmalev, P.; Yadroitsava, I. Titanium Alloys Manufactured by In Situ Alloying During Laser Powder Bed Fusion. *JOM* **2017**, *69*, 2725–2730. [CrossRef]
43. Fischer, M.; Joguet, D.; Robin, G.; Peltier, L.; Laheurte, P. In situ elaboration of a binary Ti-26Nb alloy by selective laser melting of elemental titanium and niobium mixed powders. *Mater. Sci. Eng. C* **2016**, *62*, 852–859. [CrossRef] [PubMed]
44. Sonawane, A.; Roux, G.; Blandin, J.-J.; Despres, A.; Martin, G. Cracking mechanism and its sensitivity to processing conditions during laser powder bed fusion of a structural aluminum alloy. *Materialia* **2021**, *15*, 100976. [CrossRef]
45. Rasch, M.; Heberle, J.; Dechet, M.A.; Bartels, D.; Gotterbarm, M.R.; Klein, L.; Gorunov, A.; Schmidt, J.; Körner, C.; Peukert, W.; et al. Grain Structure Evolution of Al–Cu Alloys in Powder Bed Fusion with Laser Beam for Excellent Mechanical Properties. *Materials* **2019**, *13*, 82. [CrossRef] [PubMed]
46. Zou, Y.; Okle, P.; Yu, H.; Sumigawa, T.; Kitamura, T.; Maiti, S.; Steurer, W.; Spolenak, R. Fracture properties of a refractory high-entropy alloy: In situ micro-cantilever and atom probe tomography studies. *Scr. Mater.* **2017**, *128*, 95–99. [CrossRef]
47. Mercelis, P.; Kruth, J. Residual stresses in selective laser sintering and selective laser melting. *Rapid Prototyp. J.* **2006**, *12*, 254–265. [CrossRef]
48. Kruth, J.-P.; Deckers, J.; Yasa, E.; Wauthlé, R. Assessing and comparing influencing factors of residual stresses in selective laser melting using a novel analysis method. *Proc. Inst. Mech. Eng. Part B J. Eng. Manuf.* **2012**, *226*, 980–991. [CrossRef]
49. Soni, V.; Senkov, O.N.; Couzinie, J.-P.; Zheng, Y.; Gwalani, B.; Banerjee, R. Phase stability and microstructure evolution in a ductile refractory high entropy alloy $Al_{10}Nb_{15}Ta_5Ti_{30}Zr_{40}$. *Materialia* **2020**, *9*, 100569. [CrossRef]
50. Hooper, P.A. Melt pool temperature and cooling rates in laser powder bed fusion. *Addit. Manuf.* **2018**, *22*, 548–559. [CrossRef]
51. Boussinot, G.; Döring, M.; Hemes, S.; Stryzhyboroda, O.; Apel, M.; Schmidt, M. Laser powder bed fusion of eutectic Al–Ni alloys: Experimental and phase-field studies. *Mater. Des.* **2021**, *198*, 109299. [CrossRef]
52. Kou, S. *Welding Metallurgy*; John Wiley & Sons, Inc.: Hoboken, NJ, USA, 2002; ISBN 0471434914.
53. Lippold, J.C. *Welding Metallurgy and Weldability*; John Wiley & Sons, Inc.: Hoboken, NJ, USA, 2015; ISBN 9781118960332.
54. Kimura, T.; Nakamoto, T.; Mizuno, M.; Araki, H. Effect of silicon content on densification, mechanical and thermal properties of Al-xSi binary alloys fabricated using selective laser melting. *Mater. Sci. Eng. A* **2017**, *682*, 593–602. [CrossRef]

Discussion of the publication's findings in the context of this thesis:

Building upon the results of chapter 4 and especially the publication *"Laser Powder Bed Fusion (PBF-LB/M) process strategies for in-situ alloy formation with high-melting elements"* [92] the derived process strategies for in-situ alloy formation were applied to refractory metal high entropy alloys. It is shown that the strategies developed in [92] can be applied not only to Ti alloys, but are also successful for a high entropy alloy consisting of five basic elements. This substantiates the transferability of the developed strategies and shows that the underlying assumptions and principles are not only valid for Ti-alloys, but are also applicable to other in-situ alloy formation tasks. Hence, it can be assumed that the findings regarding PBF-LB/M in-situ alloy formation strategies are valuable for other future material development and multi-material projects.

The initial working hypotheses formulated in chapter 3 are confirmed by the experimental results presented in chapter 6:

Discussion of initial hypotheses:

The findings prove a successful in-situ formation of a WMoTaNbV high entropy alloy by PBF-LB/M. As intended, the samples entirely consist of a single bcc-phase without formation of intermetallic compounds. Compared to vacuum arc melting, which is commonly employed for preparing high entropy alloys in literature, a finer grain structure and less composition differences between inter- and intradentritic areas are evident. Hence, it is concluded that the high cooling rates in the range of 10^6 K/s inherent to PBF-LB/M are beneficial for forming the refractory metal high entropy alloy WMoTaNbV.

It is confirmed that the PBF-LB/M process strategies presented in chapter 4.2 support the in-situ formation of the alloy WMoTaNbV and the dissolution of high-melting elements. PBF-LB/M parameter sets comprising low scan speeds of up to 100 mm/s and accordingly reduced laser powers result in a strongly reduced number of undissolved high-melting particles. This supports the assumption that the relationships described in chapter 4.2 do not only apply for Ti-alloys but are also transferable to the in-situ formation of refractory metal high entropy alloys. However, despite the strong reduction of undissolved high melting particles for certain parameter combinations, cracking along grain boundaries could not entirely be prevented. This is however not related to in-situ alloy formation but is rather material specific and can be mitigated by using less cracking susceptible alloys or by additional technical measures like high temperature heating during PBF-LB/M.

The results demonstrate that a variation of the PBF-LB/M process parameter affects the cooling and solidification rates strongly enough to have an impact on the micro hardness and the solidification mode of the WoMoTaNbV high entropy alloy. Process parameter sets resulting

in smaller growth rates and/or higher temperature gradients shift the solidification mode towards cellular solidification, while higher growth rates and/or smaller temperature gradients in the liquid favor columnar dendritic solidification. These changes in the microstructure also affect the mechanical properties of the material. Hardness measurements show a higher hardness of 614±21 HV0.1 for the more cellular solidified material compared to 561±17 HV0.1 for dendritic microstructure. With respect to future applications, this demonstrates the possibility to adjust the microstructure and mechanical properties in a certain range only by altering the PBF-LB/M process parameters. This allows for parts with material properties tailored to the specific loads in different part sections.

7 Summary and outlook

The aim of this thesis is a comprehensive investigation of in-situ alloy formation of refractory metal alloys by PBF-LB/M. The main focus rests on Ti-alloys, as these are the most common refractory metal alloys. In contrast to conventional PBF-LB/M pre-alloyed powder is replaced by mixtures of elemental powders, which are fused to a homogeneous alloy by melting with the laser beam. There are two motivations for this approach. If done globally for the whole build envelope, in-situ alloy formation supports future high throughput studies for material development for PBF-LB/M by providing a possibility to test a vast number of alloy compositions without the necessity of atomizing many batches of pre-alloyed powders. If done locally, in-situ alloy formation holds the potential to create parts with locally adjusted material properties, which would be a major breakthrough for several engineering disciplines such as tool making or chemical industry.

Although the approach of in-situ alloy formation by PBF-LB/M is already used by several research groups, there is still a lack of basic understanding and transferrable process strategies. This is therefore the first sub-goal of this work. It is shown that:

- The PBF-LB/M parameter combination severely influences the homogeneity of the in-situ alloyed material and the number of undissolved particles, while parameter combinations with slow scan speeds and accordingly low laser powder are in general beneficial for successful in-situ alloys formation.
- Adjusting the particle size of the high melting particle fraction potentially further reduces the amount of undissolved material, however interactions with the chosen laser parameter set and the resulting process dynamics need to be taken into account.
- The melting point difference of the alloying elements is a useful first indicator to estimate the feasibility of in-situ alloys formation by PBF-LB/M. Melting point differences of up to 450 K will most likely result in a successful in-situ alloy formation.

The applicability of the derived strategies is subsequently verified for the modification of Ti-based alloys with minor element addition and for formation of refractory metal high entropy alloys comprising up to five components. With regard to Ti-alloys the following main findings were identified:

- The addition of β-phase stabilizing elements with melting point differences smaller than 450 K compared to Ti (such as Fe and V) result in a successful in-situ alloy formation and a homogeneous microstructure. The resulting material properties can be varied over a large range.
- The Molybdenum equivalent is suitable to give a first estimation of the resulting β-phase content of the alloy following PBF-LB/M. It is shown, that a Mo_{eq} of 10 is sufficient to retain more than 90 % β-phase in as built condition. Following a heat-treatment with

much slower cooling rates than during PBF-LB/M a Mo_{eq} of at least 20 is required for the same amount of retained β-phase.
- With respect to the idea of creating parts with locally adjusted material properties it is successfully shown that a defect-free combination of a near-α base alloy and an in-situ formed highly β-stabilized Ti-alloy in a single part is feasible.

Finally, the transferability of the developed process strategies for in-situ alloy formation using PBF-LB/M of titanium alloys to other applications is examined. To this end, in-situ alloy formation of the refractory metal high entropy alloy WMoTaNbV consisting of equal amounts of the five elements is investigated with the following findings:

- The in-situ alloy formation of the alloy WMoTaNbV by PBF-LB/M is feasible.
- The developed PBF-LB/M process strategies are also applicable to this complex task and the number of undissolved high-melting particles (mainly W) are strongly reduced compared to a less favorable PBF-LB/M process strategy.
- The PBF-LB/M process parameters not only affect in-situ alloy formation, but also allow the variation of the resulting microstructure and the resulting material properties for this alloy.

Overall, process strategies to support in-situ alloy formation of refractory metal alloys were derived based on own experimental work and literature. The applicability of these strategies was examined for β-stabilized Ti-alloys and more complex refractory metal high entropy alloys. It is shown that the developed strategies in both cases support in-situ alloy formation by reducing the number of undissolved high melting particles or even dropping it close to zero. These results are a valuable addition to future PBF-LB/M material development projects relying on in-situ alloy formation to investigate different alloy combinations.

Moreover, first results on PBF-LB/M of metastable β-Ti-alloys and the refractory metal high entropy alloy WoMoTaNbV are presented. Due to their properties, especially metastable β-Ti-alloys are of high interest for applications in the aerospace or motorsport industry. More work to industrialize these alloys is needed, but the results regarding processability and achievable properties are very promising.

Thinking even further, first experiments in this work demonstrate a defect free transition between a near-α base alloy and a metastable β-Ti-alloy. Combined with recent developments regarding selective placement of metal powders in the build chamber, e.g. nozzle-based or with electrophotographic powder deposition, this finding demonstrates the possibility of creating PBF-LB/M parts with locally adjusted material properties. This would allow resolving contradicting material requirements at different positions and hence the fabrication of highly optimized parts.

While most of this thesis's results are of a rather fundamental nature, they clearly contribute to important developments to expand the possibilities of PBF-LB/M, such as novel alloys and parts with locally adjusted properties. Further research and development projects are needed for a proper industrialization, but the results demonstrate promising possibilities to manufacture future high-performance parts for demanding sectors like aerospace- or chemical-industry, thus increasing resource efficiency and competitiveness.

Literature

[1] OECD, Towards a more resource-efficient and circular economy, OECD Publ. Paris. 73 (2021) 1–53. www.oecd.org/environment/waste/OECD-G20-Towards-a-more-Resource-Efficient-and-Circular-Economy.

[2] Statistisches Bundesamt, Energiepreise: Hohe Steigerungen auf allen Wirtschaftsstufen, (n.d.). https://www.destatis.de/DE/Presse/Pressemitteilungen/2022/03/PD22_N016_61.html (accessed April 23, 2023).

[3] ZDF, EU verschärft Regeln für CO2-Preise, (n.d.). https://www.zdf.de/nachrichten/politik/co2-zertifikat-emission-treibhausgase-eu-klima-100.html (accessed April 23, 2023).

[4] European Parliament, EU ban on the sale of new petrol and diesel cars from 2035 explained, (n.d.). https://www.europarl.europa.eu/news/en/headlines/economy/20221019STO44572/eu-ban-on-sale-of-new-petrol-and-diesel-cars-from-2035-explained (accessed April 23, 2023).

[5] Clean Aviation, Clean Aviation, (n.d.). https://www.clean-aviation.eu/ (accessed April 23, 2023).

[6] DIN EN ISO/ASTM 52900:2022-03, (2022).

[7] General Electric, New manufacturing milestone: 30,000 additive fuel nozzles, (2018). https://www.ge.com/additive/blog/new-manufacturing-milestone-30000-additive-fuel-nozzles (accessed November 28, 2018).

[8] S.A. Niknam, M. Mortazavi, D. Li, Additively manufactured heat exchangers: a review on opportunities and challenges, Int. J. Adv. Manuf. Technol. 112 (2021) 601–618. https://doi.org/10.1007/s00170-020-06372-w.

[9] SLM Solutions GmbH, NXG XII 600, (n.d.). https://www.slm-pushing-the-limits.com/specs (accessed April 23, 2023).

[10] DAP Aachen, Projektabschluss IDAM, (n.d.). https://dap-aachen.de/2022-06-22-idam (accessed April 23, 2023).

[11] Wohlers Associates, Wohlers Report 2019, Wohlers Associates, Inc., 2019.

[12] ISO/ ASTM 52900 Standard Terminology for Additive Manufacturing – General Principles – Terminology, (n.d.). https://doi.org/10.1520/ISOASTM52900-15.

[13] F. Huber, T. Papke, C. Scheitler, L. Hanrieder, M. Merklein, M. Schmidt, In Situ Formation of a Metastable β-Ti Alloy by Laser Powder Bed Fusion (L-PBF) of Vanadium and Iron Modified Ti-6Al-4V, Metals (Basel). 8 (2018) 1067. https://doi.org/10.3390/met8121067.

[14] K. Wei, F. Li, G. Huang, M. Liu, J. Deng, C. He, X. Zeng, Multi-laser powder bed fusion of Ti–6Al–4V alloy: Defect, microstructure, and mechanical property of overlap region, Mater. Sci. Eng. A. 802 (2021) 140644. https://doi.org/10.1016/j.msea.2020.140644.

[15] M. Horn, M. Schmitt, M. Schafnitzel, A. van Husen, P. Wagenblast, S. Auernhammer, J. Heyder, C. Hauck, J. Barz, M. Ott, G. Schlick, C. Seidel, Powder Bed Fusion of highly filigree copper features using a green laser, Procedia CIRP. 111 (2022) 81–86. https://doi.org/10.1016/j.procir.2022.08.135.

[16] J. Grünewald, V. Blickle, M. Allenberg-Rabe, P. Wagenblast, K. Wudy, Flexible and highly dynamic beam shaping for Laser-Based Powder Bed Fusion of metals, Procedia CIRP. 111 (2022) 65–70. https://doi.org/10.1016/j.procir.2022.08.124.

[17] R. Rothfelder, F. Huber, M. Schmidt, Influence of beam shape on spatter formation during PBF-LB/M of Ti6Al4V and tungsten powder, Procedia CIRP. 111 (2022) 14–17. https://doi.org/10.1016/j.procir.2022.08.105.

[18] M. Rasch, C. Roider, S. Kohl, J. Strauß, N. Maurer, K.Y. Nagulin, M. Schmidt, Shaped laser beam profiles for heat conduction welding of aluminium-copper alloys, Opt. Lasers Eng. 115 (2019) 179–189. https://doi.org/10.1016/j.optlaseng.2018.11.025.

[19] S.A. Khairallah, A.T. Anderson, A. Rubenchik, W.E. King, Laser powder-bed fusion additive manufacturing: Physics of complex melt flow and formation mechanisms of pores, spatter, and denudation zones, Acta Mater. 108 (2016) 36–45. https://doi.org/10.1016/j.actamat.2016.02.014.

[20] E. Eschner, T. Staudt, M. Schmidt, Correlation of spatter behavior and process zone formation in powder bed fusion of metals, CIRP Ann. 69 (2020) 209–212. https://doi.org/10.1016/j.cirp.2020.04.092.

[21] M.J. Matthews, G. Guss, S.A. Khairallah, A.M. Rubenchik, P.J. Depond, W.E. King, Denudation of metal powder layers in laser powder bed fusion processes, Acta Mater. 114 (2016) 33–42. https://doi.org/10.1016/j.actamat.2016.05.017.

[22] P. Bidare, I. Bitharas, R.M. Ward, M.M. Attallah, A.J. Moore, Fluid and particle dynamics in laser powder bed fusion, Acta Mater. 142 (2018) 107–120. https://doi.org/10.1016/j.actamat.2017.09.051.

[23] J. Reijonen, A. Revuelta, T. Riipinen, K. Ruusuvuori, P. Puukko, On the effect of shielding gas flow on porosity and melt pool geometry in laser powder bed fusion additive manufacturing, Addit. Manuf. 32 (2020) 101030. https://doi.org/10.1016/j.addma.2019.101030.

[24] J.P. Oliveira, A.D. LaLonde, J. Ma, Processing parameters in laser powder bed fusion metal additive manufacturing, Mater. Des. 193 (2020) 1–12. https://doi.org/10.1016/j.matdes.2020.108762.

[25] ISO/ASTM, ISO/ASTM TS 52930:2021 Additive manufacturing — Qualification principles — Installation, operation and performance (IQ/OQ/PQ) of PBF-LB equipment, 2021. (n.d.). https://www.iso.org/standard/79527.html (accessed September 17, 2023).

[26] K. Kassym, A. Perveen, Atomization processes of metal powders for 3D printing, Mater. Today Proc. 26 (2019) 1727–1733. https://doi.org/10.1016/j.matpr.2020.02.364.

[27] L.V.M. Antony, R.G. Reddy, Processes for production of high-purity metal powders, Jom. 55 (2003) 14–18. https://doi.org/10.1007/s11837-003-0153-4.

[28] A. Asgarian, Z. Tang, M. Bussmann, K. Chattopadhyay, Water atomisation of metal powders: effect of water spray configuration, Powder Metall. 63 (2020) 288–299. https://doi.org/10.1080/00325899.2020.1802558.

[29] 3D LAB sp. z o.o, ATO Lab+, (n.d.). https://metalatomizer.com/.

[30] D. Herzog, V. Seyda, E. Wycisk, C. Emmelmann, Additive manufacturing of metals, Acta Mater. 117 (2016) 371–392. https://doi.org/10.1016/j.actamat.2016.07.019.

[31] S.L. Sing, S. Huang, G.D. Goh, G.L. Goh, C.F. Tey, J.H.K. Tan, W.Y. Yeong, Emerging metallic systems for additive manufacturing: In-situ alloying and multi-metal processing in laser powder bed fusion, Prog. Mater. Sci. 119 (2021) 100795. https://doi.org/10.1016/j.pmatsci.2021.100795.

[32] D. Bartels, T. Novotny, O. Hentschel, F. Huber, R. Mys, C. Merklein, M. Schmidt, In situ modification of case-hardening steel 16MnCr5 by C and WC addition by means of powder bed fusion with laser beam of metals (PBF-LB/M), Int. J. Adv. Manuf. Technol. 120 (2022) 1729–1745. https://doi.org/10.1007/s00170-022-08848-3.

[33] P.A. Rometsch, Y. Zhu, X. Wu, A. Huang, Review of high-strength aluminium alloys for additive manufacturing by laser powder bed fusion, Mater. Des. 219 (2022) 110779. https://doi.org/10.1016/j.matdes.2022.110779.

[34] C. Zhang, J. Zhu, C. Ji, Y. Guo, R. Fang, S. Mei, S. Liu, Laser powder bed fusion of high-entropy alloy particle-reinforced stainless steel with enhanced strength, ductility, and corrosion resistance, Mater. Des. 209 (2021) 109950. https://doi.org/10.1016/j.matdes.2021.109950.

[35] O. Hentschel, L. Siegel, C. Scheitler, F. Huber, D. Junker, A. Gorunow, M. Schmidt, Processing of AISI H11 Tool Steel Powder Modified with Carbon Black Nanoparticles for the Additive Manufacturing of Forging Tools with Tailored Mechanical Properties by Means of Laser Metal Deposition (LMD), Metals (Basel). 8 (2018) 659. https://doi.org/10.3390/met8090659.

[36] P. Krakhmalev, I. Yadroitsev, I. Yadroitsava, O. de Smidt, Functionalization of biomedical Ti6Al4V via in situ alloying by Cu during laser powder bed fusion manufacturing, Materials (Basel). 10 (2017). https://doi.org/10.3390/ma10101154.

[37] M. Fischer, D. Joguet, G. Robin, L. Peltier, P. Laheurte, In situ elaboration of a binary Ti-26Nb alloy by selective laser melting of elemental titanium and niobium mixed powders, Mater. Sci. Eng. C. 62 (2016) 852–859. https://doi.org/10.1016/j.msec.2016.02.033.

[38] D. Zhao, C. Han, J. Li, J. Liu, Q. Wei, In situ fabrication of a titanium-niobium alloy with tailored microstructures, enhanced mechanical properties and biocompatibility by using selective laser melting, Mater. Sci. Eng. C. 111 (2020) 110784.

https://doi.org/10.1016/j.msec.2020.110784.

[39] R. Duan, S. Li, B. Cai, W. Zhu, F. Ren, M.M. Attallah, A high strength and low modulus metastable β Ti-12Mo-6Zr-2Fe alloy fabricated by laser powder bed fusion in-situ alloying, Addit. Manuf. (2020) 101708. https://doi.org/10.1016/j.addma.2020.101708.

[40] I. Polozov, A. Popovich, Microstructure and Mechanical Properties of NiTi-Based Eutectic Shape Memory Alloy Produced via Selective Laser Melting In-Situ Alloying by Nb, Materials (Basel). 14 (2021) 2696. https://doi.org/10.3390/ma14102696.

[41] F. Huber, D. Bartels, M. Schmidt, In situ alloy formation of a wmotanbv refractory metal high entropy alloy by laser powder bed fusion (Pbf-lb/m), Materials (Basel). 14 (2021) 1–12. https://doi.org/10.3390/ma14113095.

[42] T. Ron, A. Leon, V. Popov, E. Strokin, D. Eliezer, A. Shirizly, E. Aghion, Synthesis of Refractory High-Entropy Alloy WTaMoNbV by Powder Bed Fusion Process Using Mixed Elemental Alloying Powder, Materials (Basel). 15 (2022). https://doi.org/10.3390/ma15124043.

[43] J. Xu, R. Duan, K. Feng, C. Zhang, Q. Zhou, P. Liu, Z. Li, Enhanced strength and ductility of laser powder bed fused NbMoTaW refractory high-entropy alloy via carbon microalloying, Addit. Manuf. Lett. 3 (2022) 100079. https://doi.org/10.1016/j.addlet.2022.100079.

[44] M.H. Mosallanejad, B. Niroumand, A. Aversa, A. Saboori, In-situ alloying in laser-based additive manufacturing processes: A critical review, J. Alloys Compd. 872 (2021) 159567. https://doi.org/10.1016/j.jallcom.2021.159567.

[45] I. Yadroitsev, P. Krakhmalev, I. Yadroitsava, Titanium Alloys Manufactured by In Situ Alloying During Laser Powder Bed Fusion, Jom. 69 (2017) 2725–2730. https://doi.org/10.1007/s11837-017-2600-7.

[46] J. von Liebig, Handbuch der Chemie mit Rücksicht auf Pharmacie, Acad. Verlagsbuchhandlung von C. F. Winter, Heidelberg, 1843.

[47] W. Kroll, Method for manufacturing titanium and alloys thereof, US2205854A, 1937. https://worldwide.espacenet.com/patent/search/family/007990019/publication/US2205854A?q=pn%3DUS2205854.

[48] A.E. van Arkel, J.H. de Boer, Darstellung von reinem Titanium-, Zirkonium-, Hafnium- und Thoriummetall, Zeitschrift Für Anorg. Und Allg. Chemie. 148 (1925) 345–350. https://doi.org/10.1002/zaac.19251480133.

[49] United States Geological Survey, Titanium in the fourth quarter 2018, 2018. https://prd-wret.s3-us-west-2.amazonaws.com/assets/palladium/production/atoms/files/mis-2018q4-titan.pdf.

[50] R.R. Boyer, An overview on the use of titanium in the aerospace industry, Mater. Sci. Eng. A. 213 (1996) 103–114. https://doi.org/10.1016/0921-5093(96)10233-1.

[51] B. Dutta, F.H. Froes, Markets, Applications, and Costs, Addit. Manuf. Titan. Alloy. (2016) 61–73. https://doi.org/10.1016/b978-0-12-804782-8.00006-9.

[52] F.H. (Sam) Froes, Titanium for medical and dental applications—An introduction, Elsevier Inc., 2018. https://doi.org/10.1016/b978-0-12-812456-7.00001-9.

[53] G. Lütjiering, J.C. Williams, Titanium, 2nd ed., Springer, Heidelberg, 2007.

[54] C. Leyens, M. Peters, Titanium an Titanium Alloys, 2003. https://doi.org/10.1002/3527602119.

[55] R. von Mises, Mechanik der plastischen Formänderung von Kristallen, Zeitschrift Für Angew. Math. Und Mech. 8 (1928) 161–184. https://doi.org/https://doi.org/10.1002/zamm.19280080302.

[56] C.W. Hume-Rothery, William Smallman, R. Haworth, The Structure of Metals and Alloys, The Metals and Metallurgy Trust of the Institute of Metals and the Institution of Metallurgists, 1969.

[57] B.E. Tegner, L. Zhu, G.J. Ackland, Relative strength of phase stabilizers in titanium alloys, Phys. Rev. B - Condens. Matter Mater. Phys. 85 (2012) 3–6. https://doi.org/10.1103/PhysRevB.85.214106.

[58] L.F. Huang, B. Grabowski, J. Zhang, M.J. Lai, C.C. Tasan, S. Sandlöbes, D. Raabe, J. Neugebauer, From electronic structure to phase diagrams: A bottom-up approach to understand the stability of titanium–transition metal alloys, Acta Mater. 113 (2016) 311–319. https://doi.org/10.1016/j.actamat.2016.04.059.

[59] R.P. Kolli, A. Devaraj, A review of metastable beta titanium alloys, Metals (Basel). 8 (2018) 1–41. https://doi.org/10.3390/met8070506.

[60] H.W. ROSENBERG, TITANIUM ALLOYING IN THEORY AND PRACTICE, in: Sci. Technol. Appl. Titan., Elsevier, 1970: pp. 851–859. https://doi.org/10.1016/B978-0-08-006564-9.50095-6.

[61] I. Weiss, S.L. Semiatin, Thermomechanical processing of alpha titanium alloys - An overview, Mater. Sci. Eng. A. 263 (1999) 243–256. https://doi.org/10.1016/s0921-5093(98)01155-1.

[62] W.R. Division, M. Division, Performance of high chromium stainless steels and titanium alloys in Arabian Gulf seawater, 120 (1998) 73–81.

[63] RTI International Metals Inc., Titanium alloy guide, 2000.

[64] B.M. Peters, J. Kumpfert, C.H. Ward, C. Leyens, Titanium Alloys for Aerospace Applications, (2003) 419–427. https://doi.org/10.1002/adem.200310095.

[65] O.M. Karasevskaya, O.P. Ivasishin, S.L. Semiatin, Y.V. Matviychu, Deformation behavior of beta-titanium alloys, 354 (2003) 121–132. https://doi.org/10.1016/S0921-5093(02)00935-8.

[66] H. Yang, X.G. Fan, Z.C. Sun, L.G. Guo, M. Zhan, Recent developments in plastic forming technology of titanium alloys, Sci. China Technol. Sci. 54 (2011) 490–501. https://doi.org/10.1007/s11431-010-4206-y.

[67] D. Liu, Y. Zhang, M. Luo, D. Zhang, Investigation of Tool Wear and Chip Morphology in Dry Trochoidal Milling of Titanium Alloy Ti–6Al–4V, Materials (Basel). 12 (2019) 1937. https://doi.org/10.3390/ma12121937.

[68] H.H. Dutta, B. Froes, Additive Manufacturing of Titanium Alloys, Elsevier, 2015. http://s1.iran-mavad.com/pdf96/Additive Manufacturing of Titanium Alloys_iran-mavad.com.pdf.

[69] P.I. Pradeep, A. Akhilesh, V.A. Kumar, P. Manikandan, K.N. Kumar, T. Venkateswaran, A. Sahu, S.K. Singh, P.R. Narayanan, Characterization of Titanium Alloy Ti6Al4V-ELI Components made by Laser Powder Bed Fusion Route for Space Applications, Trans. Indian Natl. Acad. Eng. 6 (2021) 1071–1081. https://doi.org/10.1007/s41403-021-00254-7.

[70] EOS GmbH / Liebherr Aerospace, Airbus A380 nutzt erstmals 3D-gedrucktes Bauteil, (n.d.). https://www.eos.info/de/presscenter/case-studies/aerospace_liebherr_ventilblock.

[71] N. Sharma, D. Ostas, H. Rotar, P. Brantner, F.M. Thieringer, Design and Additive Manufacturing of a Biomimetic Customized Cranial Implant Based on Voronoi Diagram, Front. Physiol. 12 (2021) 1–12. https://doi.org/10.3389/fphys.2021.647923.

[72] S. Tunchel, A. Blay, R. Kolerman, E. Mijiritsky, J.A. Shibli, 3D Printing / Additive Manufacturing Single Titanium Dental Implants : A Prospective Multicenter Study with 3 Years of Follow-Up, 2016 (2016).

[73] V. Kumar, P. Kumar, P. Kalra, R. Kumar, Annals of 3D Printed Medicine Additive manufacturing for metallic spinal implants : A systematic review, Ann. 3D Print. Med. 3 (2021) 100021. https://doi.org/10.1016/j.stlm.2021.100021.

[74] EOS GmbH, Ti64, Ti64ELI und TiCP Titan für die additive Fertigung, (n.d.). https://www.eos.info/de/additive-fertigung/3d-druck-metall/eos-metall-werkstoffe-dmls/titan-ti64-hl-cp.

[75] SLM Solutions Group AG, Qualifiizerte Metallpulver und Materialparameter, (n.d.). https://www.slm-solutions.com/de/produkte-und-loesungen/materialien/.

[76] GE Additive, Concept Laser M2 Series 5, (2022). https://www.ge.com/additive/additive-manufacturing/machines/m2series5.

[77] Trumpf SE + Co. KG, Additive Manufacturing: Pulver und Parameter, (n.d.). https://www.trumpf.com/de_AT/produkte/maschinen-systeme/additive-fertigungssysteme/pulver-und-parameter/.

[78] J.C. Colombo-Pulgarín, C.A. Biffi, M. Vedani, D. Celentano, A. Sánchez-Egea, A.D. Boccardo, J.P. Ponthot, Beta Titanium Alloys Processed By Laser Powder Bed Fusion: A Review, J. Mater. Eng. Perform. 30 (2021) 6365–6388. https://doi.org/10.1007/s11665-021-05800-6.

[79] B. Vrancken, L. Thijs, J.P. Kruth, J. Van Humbeeck, Heat treatment of Ti6Al4V produced by Selective Laser Melting: Microstructure and mechanical properties, J. Alloys Compd. 541 (2012) 177–185. https://doi.org/10.1016/j.jallcom.2012.07.022.

[80] J. Yang, H. Yang, H. Yu, Z. Wang, X. Zeng, Corrosion Behavior of Additive Manufactured Ti-6Al-4V Alloy in NaCl Solution, Metall. Mater. Trans. A Phys. Metall. Mater. Sci. 48 (2017) 3583–3593. https://doi.org/10.1007/s11661-017-4087-9.

[81] A. Cutolo, C. Elangeswaran, G.K. Muralidharan, B. Van Hooreweder, On the role of building orientation and surface post-processes on the fatigue life of Ti-6Al-4V coupons manufactured by laser powder bed fusion, Mater. Sci. Eng. A. 840 (2022) 142747. https://doi.org/10.1016/j.msea.2022.142747.

[82] C. Fleißner-Rieger, T. Pfeifer, T. Jörg, T. Kremmer, M. Brabetz, H. Clemens, S. Mayer, Selective Laser Melting of a Near-α Ti6242S Alloy for High-Performance Automotive Parts, Adv. Eng. Mater. 23 (2021). https://doi.org/10.1002/adem.202001194.

[83] S. Patel, M. Keshavarz, M. Vlasea, Challenges during laser powder bed fusion of a near-alpha titanium alloy - Ti-6242Si, (2021) 1104–1117.

[84] C. Cai, X. Wu, W. Liu, W. Zhu, H. Chen, J.C.D. Qiu, C.N. Sun, J. Liu, Q. Wei, Y. Shi, Selective laser melting of near-α titanium alloy Ti-6Al-2Zr-1Mo-1V: Parameter optimization, heat treatment and mechanical performance, J. Mater. Sci. Technol. 57 (2020) 51–64. https://doi.org/10.1016/j.jmst.2020.05.004.

[85] C. Xu, F. Sikan, S.E. Atabay, J.A. Muñiz-Lerma, O. Sanchez-Mata, X. Wang, M. Brochu, Microstructure and mechanical behavior of as-built and heat-treated Ti–6Al–7Nb produced by laser powder bed fusion, Mater. Sci. Eng. A. 793 (2020). https://doi.org/10.1016/j.msea.2020.139978.

[86] G.C. Li, J. Li, X.J. Tian, X. Cheng, B. He, H.M. Wang, Microstructure and properties of a novel titanium alloy Ti-6Al-2V-1.5Mo-0.5Zr-0.3Si manufactured by laser additive manufacturing, Mater. Sci. Eng. A. 684 (2017) 233–238. https://doi.org/10.1016/j.msea.2016.11.084.

[87] C. Qiu, Q. Liu, Multi-scale microstructural development and mechanical properties of a selectively laser melted beta titanium alloy, Addit. Manuf. 30 (2019) 100893. https://doi.org/10.1016/j.addma.2019.100893.

[88] H. Schwab, F. Palm, U. Kühn, J. Eckert, Microstructure and mechanical properties of the near-beta titanium alloy Ti-5553 processed by selective laser melting, Mater. Des. 105 (2016) 75–80. https://doi.org/10.1016/j.matdes.2016.04.103.

[89] M.J. Bermingham, D.H. StJohn, J. Krynen, S. Tedman-Jones, M.S. Dargusch, Promoting the columnar to equiaxed transition and grain refinement of titanium alloys during additive manufacturing, Acta Mater. 168 (2019) 261–274. https://doi.org/10.1016/j.actamat.2019.02.020.

[90] C.L. Yang, Z.J. Zhang, S.J. Li, Y.J. Liu, T.B. Sercombe, W.T. Hou, P. Zhang, Y.K. Zhu, Y.L. Hao, Z.F. Zhang, R. Yang, Simultaneous improvement in strength and plasticity of Ti-24Nb-4Zr-8Sn manufactured by selective laser melting, Mater. Des. 157 (2018) 52–59. https://doi.org/10.1016/j.matdes.2018.07.036.

[91] F. Huber, T. Papke, M. Kerkien, F. Tost, G. Geyer, M. Merklein, Customized exposure strategies for manufacturing hybrid parts by combining laser beam melting and sheet metal forming Customized exposure strategies for manufacturing hybrid parts by

combining laser beam melting and sheet metal forming, 022318 (2019). https://doi.org/10.2351/1.5096115.

[92] F. Huber, M. Rasch, M. Schmidt, Laser Powder Bed Fusion (PBF-LB/M) Process Strategies for In-Situ Alloy Formation with High-Melting Elements, Metals (Basel). 11 (2021) 336. https://doi.org/10.3390/met11020336.

[93] F. Huber, T. Papke, C. Kauffmann, R. Rothfelder, P. Krakhmalev, M. Merklein, M. Schmidt, Systematic exploration of the L-PBF processing behavior and resulting properties of β-stabilized Ti-alloys prepared by in-situ alloy formation, Mater. Sci. Eng. A. 818 (2021) 141374. https://doi.org/10.1016/j.msea.2021.141374.

[94] F. Huber, M. Rasch, L. Butzhammer, M. Karg, M. Schmidt, Strahlschmelzen von Metallen mit unterschiedlichen Intensitäten und Belichtungsstrategien, in: D. Drummer (Ed.), 5. Ind. Des Sonderforschungsbereichs 814 - Addit. Fert., Sonderforschungsbereich 814 - Additive Fertigung, 2017.

[95] M.-T. Tsai, Y.-W. Chen, C.-Y. Chao, J.S.C. Jang, C.-C. Tsai, Y.-L. Su, C.-N. Kuo, Heat-treatment effects on mechanical properties and microstructure evolution of Ti-6Al-4V alloy fabricated by laser powder bed fusion, J. Alloys Compd. 816 (2020) 152615. https://doi.org/10.1016/j.jallcom.2019.152615.

[96] H.-J. Bargel, G. Schulze, eds., Werkstoffkunde, Springer Berlin Heidelberg, Berlin, Heidelberg, 2012. https://doi.org/10.1007/978-3-642-17717-0.

[97] S.P. Kopp, T. Stichel, S. Roth, M. Schmidt, Investigation of the electrophotographic powder deposition through a transfer grid for efficient additive manufacturing, Procedia CIRP. 94 (2020) 122–127. https://doi.org/10.1016/j.procir.2020.09.024.

[98] L.S. Aota, P. Bajaj, H.R.Z. Sandim, E.A. Jägle, Laser powder-bed fusion as an alloy development tool: Parameter selection for in-situ alloying using elemental powders, Materials (Basel). 13 (2020). https://doi.org/10.3390/MA13183922.

[99] W.M. Haynes, Handbook of Chemistry and Physics, 2017.

[100] P. Chen, S. Li, Y. Zhou, M. Yan, M.M. Attallah, Fabricating CoCrFeMnNi high entropy alloy via selective laser melting in-situ alloying, J. Mater. Sci. Technol. 43 (2020) 40–43. https://doi.org/10.1016/j.jmst.2020.01.002.

[101] A. Grigoriev, I. Polozov, V. Sufiiarov, A. Popovich, In-situ synthesis of Ti2AlNb-based intermetallic alloy by selective laser melting, J. Alloys Compd. 704 (2017) 434–442. https://doi.org/10.1016/j.jallcom.2017.02.086.

[102] National Institute of Standards and Technology, NIST Chemistry WebBook, (n.d.). https://doi.org/ttps://doi.org/10.18434/T4D303.

[103] I. Polozov, V. Sufiiarov, A. Popovich, D. Masaylo, A. Grigoriev, Synthesis of Ti-5Al, Ti-6Al-7Nb, and Ti-22Al-25Nb alloys from elemental powders using powder-bed fusion additive manufacturing, J. Alloys Compd. 763 (2018) 436–445. https://doi.org/10.1016/j.jallcom.2018.05.325.

[104] S. Huang, R.L. Narayan, J.H.K. Tan, S.L. Sing, W.Y. Yeong, Resolving the porosity-

unmelted inclusion dilemma during in-situ alloying of Ti34Nb via laser powder bed fusion, Acta Mater. 204 (2021) 116522. https://doi.org/10.1016/j.actamat.2020.116522.

[105] A. van Teijlingen, S.A. Davis, S.R. Hall, Size-dependent melting point depression of nickel nanoparticles, Nanoscale Adv. 2 (2020) 2347–2351. https://doi.org/10.1039/D0NA00153H.

[106] I.M. Kusoglu, B. Gökce, S. Barcikowski, Use of (nano-)additives in Laser Powder Bed Fusion of Al powder feedstocks: research directions within the last decade, Procedia CIRP. 94 (2020) 11–16. https://doi.org/10.1016/j.procir.2020.09.003.

[107] O. Hentschel, L. Siegel, C. Scheitler, F. Huber, D. Junker, A. Gorunow, M. Schmidt, Processing of AISI H11 tool steel powder modified with carbon black nanoparticles for the additive manufacturing of forging tools with tailored mechanical properties by means of laser metal deposition (LMD), Metals (Basel). 8 (2018). https://doi.org/10.3390/met8090659.

[108] D.B. Miracle, O.N. Senkov, A critical review of high entropy alloys and related concepts, Acta Mater. 122 (2017) 448–511. https://doi.org/10.1016/j.actamat.2016.08.081.

[109] G. Ghazal, P. Chapelle, A. Jardy, J. Jourdan, Y. Millet, Dissolution of high density inclusions in titanium alloys, ISIJ Int. 52 (2012) 1–9. https://doi.org/10.2355/isijinternational.52.1.

[110] H. Chen, W. Yan, Spattering and denudation in laser powder bed fusion process: Multiphase flow modelling, Acta Mater. 196 (2020) 154–167. https://doi.org/10.1016/j.actamat.2020.06.033.

[111] P.J. Bania, Beta titanium alloys and their role in the titanium industry, Jom. 46 (1994) 16–19. https://doi.org/10.1007/BF03220742.

[112] J. Ye, S.A. Khairallah, A.M. Rubenchik, M.F. Crumb, G. Guss, J. Belak, M.J. Matthews, Energy Coupling Mechanisms and Scaling Behavior Associated with Laser Powder Bed Fusion Additive Manufacturing, Adv. Eng. Mater. 21 (2019) 1–9. https://doi.org/10.1002/adem.201900185.

[113] JMatPro, (n.d.). https://www.sentesoftware.co.uk/jmatpro.

[114] C.F. Tey, X. Tan, S.L. Sing, W.Y. Yeong, Additive manufacturing of multiple materials by selective laser melting: Ti-alloy to stainless steel via a Cu-alloy interlayer, Addit. Manuf. 31 (2020) 100970. https://doi.org/10.1016/j.addma.2019.100970.

[115] M. Rasch, D. Bartels, S. Sun, M. Schmidt, AlSi10Mg in Powder Bed Fusion with Laser Beam: An Old and Boring Material?, Materials (Basel). 15 (2022). https://doi.org/10.3390/ma15165651.

[116] J.F. Hagen, M. Rasch, S. Kohl, M. Schmidt, Geometry dependent microstructures: bug or feature?, Procedia CIRP. 74 (2018) 724–727. https://doi.org/10.1016/j.procir.2018.08.024.